CALIBRATION OF HIGH-FREQUENCY PRESSURE SENSORS USING LOW-PRESSURE SHOCK WAVES

A Thesis

Submitted to the Faculty

of

Purdue University

by

Mark P. Wason

In Partial Fulfillment of the

Requirements for the Degree

of

Master of Science

May 2019

Purdue University

West Lafayette, Indiana

THE PURDUE UNIVERSITY GRADUATE SCHOOL
STATEMENT OF THESIS APPROVAL

Dr. Steven P. Schneider, Chair

School of Aeronautics and Astronautics

Dr. Sally P. Bane

School of Aeronautics and Astronautics

Dr. Rudolph A. King

NASA Langley Research Center

Approved by:

Dr. Weinong Wayne Chen

Head of the School Graduate Program

To my Mom and Dad.

ACKNOWLEDGMENTS

The Air Force Office of Scientific Research provided funding for this work under grant number FA9550-16-10407.

I would like to thank Dr. Steven Schneider for this opportunity, as well as all the support and guidance he has provided during my time at Purdue. I would also like to thank my committee members, Dr. Sally Bane of Purdue University and Dr. Rudolph King of NASA Langley Research Center, for their suggestions and insight. Thanks also go to Dr. King for his guidance during my brief time at NASA Langley.

I would like to thank the machinists Jim Younts, Jerry Hahn, and Robin Snodgrass, along with the electronic specialist John Phillips. Their advice, suggestions, and immaculate craftsmanship made this work possible.

I would like to thank both Dennis Berridge and Amanda Chou for their continued help with solving shock-tube-related problems. Amanda Chou also provided valuable insight during my brief time at NASA Langley.

There would be no way to complete this project without the support of all the members of the extended family of the Schneider lab group. Thanks go to Brandon, Greg, Josh, Drew, Katie, Cameron, Phil, Varun, Liz, and Carson. Thanks to Ross Carlson for training me to run the shock tube and helping solve mechanical issues. Thanks to Ines Esteban for helping me run the shock tube, perform maintenance, and train new recruits while I wasn't there.

Finally, thank you to all my family and friends for supporting me during my time at graduate school. My parents and sister have always supported me, and continue to do so during my studies. Special thanks to my loving girlfriend, Natalia Narvaez, for her support and acceptance of someone who wakes up much too early.

TABLE OF CONTENTS

Page

LIST OF TABLES

LIST OF FIGURES

Figure Page

Figure Page

Figure Page

Figure Page

Figure Page

SYMBOLS

a	speed of sound
b	diaphragm petal width
d	diameter
$\mathcal{F}\{\}$	Fourier transform
f	frequency
L	cavity depth
l	mean free path
M	Mach number
n	number of elements
p	pressure
s	slope
T	temperature
t	time
u	velocity
v	input signal
x	axial position, measured from the diaphragm
y	output signal
$\delta()$	Dirac delta function
δ_{shock}	shock standoff distance
Δ	thickness
Δp	pressure step
ϵ	percent change
γ	ratio of specific heats
Ω	Ohm
ψ	shock-skew angle

ρ	density
τ	diaphragm thickness
$\theta()$	Heaviside step function

Subscripts

0	stagnation condition
1	pre-shock driven condition
2	condition between incident shock and contact surface
4	pre-shock driver condition
d	diaphragm
$driven$	pre-shock driven condition
$driver$	pre-shock driver condition
Hg	Mercury
i	counter index
j	counter index
max	maximum
off	roll-off
p	contact surface
$peak$	peak value
$rise$, $pitot$	pitot-mode rise time
$rise$, $static$	static-mode rise time
s	shock condition
$sens$	sensor
$step$	condition change
$stop$	stop-band
$tube$	shock tube

ABBREVIATIONS

AEDC	Arnold Engineering Development Complex
AFOSR	Air Force Office of Scientific Research
BAM6QT	Boeing/AFOSR Mach-6 Quiet Tunnel
CUBRC	Calspan-University at Buffalo Research Center
DAQ	Data Acquisition Device
DLR	German Aerospace Center
DNS	Direct Numerical Simulation
FIR	Finite Impulse Response
FLDI	Focused Laser Differential Interferometry
FWHM	Full Width at Half-Maximum
GUI	Graphical User Interface
HEG	High Enthalpy Shock Tunnel Göttingen
HIEST	High Enthalpy Shock Tunnel
HWT	Hypersonic Wind Tunnel
ID	Internal Diameter
JAXA	Japan Aerospace Exploration Agency
NASA	National Aeronautics and Space Administration
NI	National Instruments
P3IST	Purdue 3-Inch Shock Tube
PCB	PCB Piezotronics
PI	Proportional Integral
PSD	Power Spectral Density
RMS	Root-mean-square
SNR	Signal-to-Noise Ratio
VISA	Virtual Instrument Software Architecture

ABSTRACT

Wason, Mark P. MSAAE, Purdue University, May 2019. Calibration of High-Frequency Pressure Sensors Using Low-Pressure Shock Waves. Major Professor: Steven Schneider.

Many important measurements of low-amplitude instabilities related to hypersonic laminar-turbulent boundary-layer transition have been successfully performed with 1-MHz PCB132 pressure sensors. However, there is large uncertainty in measurements made with PCB132 sensors due to their poorly understood response at high frequency. The current work continues efforts to better characterize the PCB132 sensor with a low-pressure shock tube, using the pressure change across the incident shock as an approximate step input.

New vacuum-control valves provide precise control of pre-run pressures in the shock tube, generally to within 1% of the desired pressure. Measurements of the static-pressure step across the shock made with Kulite sensors showed high consistency for similar pre-run pressures. Skewing of the incident shock was measured by PCB132 sensors, and was found to be negligible across a range of pressure ratios and static-pressure steps. Incident-shock speed decreases along the shock tube, as expected. Vibrational effects on the PCB132 sensor response are significantly lower in the final section of the driven tube.

Approximate frequency responses were computed from pitot-mode responses. The frequency-response amplitude varied by a factor of 5 between 200–1000 kHz due to significant resonance peaks. Measurements with blinded PCB132 sensors indicate that the resonances in the frequency response are not due to vibration.

Using the approximate frequency response measured with the shock tube to correct the spectra of wind-tunnel data produced inconclusive results. Correcting pitot-mode

PCB132 wind-tunnel data removed a possible resonance peak near 700 kHz, but did not agree with the spectrum of a reference sensor in the range of 11–100 kHz.

1. LITERATURE REVIEW

1.1 Introduction

Hypersonic boundary-layer transition can be a major consideration for vehicle design. Heating can vary dramatically depending on the boundary layer state. Inaccurate or conservative prediction of boundary layer transition may result in vehicles that are too heavy. Moments and drag can change depending on boundary layer state, and can cause vehicle failure if not accounted for properly. Transition is often difficult to predict. To improve hypersonic vehicle-design methods, new transition-prediction methods must be developed. In order to develop new methods, improved transition measurements must be acquired.

Hypersonic boundary layers can transition from laminar to turbulent through a number of different mechanisms. One path to boundary-layer transition is through second-mode instability waves, an acoustic wave with frequencies often on the order of 100–500 kHz. Only some sensors are able to measure this range. These sensors include Kulite XCQ series ultraminiature pressure transducers, which can measure pressure fluctuations in the 100 kHz range but are limited by sensor resonance. Many XCQ sensors have a natural resonance at a frequency on the order of 100 kHz, depending on the sensor range. This is problematic because the frequencies of interest for hypersonic boundary-layer transition studies can be near 500 kHz.

In 2006, Fujii measured second-mode waves in a hypersonic boundary layer with PCB132A31 pressure sensors [1]. Since then, PCB132 pressure sensors have been widely used in hypersonic boundary-layer studies. PCB132 sensors are capable of measuring pressure fluctuations at frequencies up to 1 MHz, but have a frequency response which is not well understood. PCB132 sensors were originally designed for time-of-arrival measurements [2], and so were not thoroughly calibrated by the

manufacturer [3]. Additionally, the sensing element location varied between sensors, leading to spatial uncertainties. Recently, PCB began manufacturing a new version of the sensor with a circular, centrally-placed sensing element. Despite the improvement, the sensor frequency response remains uncertain.

Because the use of PCB132 sensors in hypersonic boundary-layer transition studies is so widespread, it is necessary to develop a better understanding of the sensor. This work is a continuation of a calibration approach that uses a low-pressure shock tube to generate a pressure-step input to the PCB132 sensor. The shock tube is capable of producing low-pressure shocks at moderate Mach numbers. This allows for the creation of steep steps with low-pressure rises, within the pressure range relevant for hypersonic boundary-layer transition measurements.

The calibration approach used for PCB132 sensors could also be useful for other high-frequency pressure sensors developed for hypersonic boundary-layer transition in the future. Evaluation of other pressure sensors will require similar inputs to PCB132 sensors, and so could be studied with a shock tube.

1.2 Measurements with PCB132 Sensors

PCB132 pressure transducers have been used in numerous hypersonic boundary-layer transition studies. Early measurements of the second-mode boundary-layer instability were made by Estorf et al. on a 7° half-angle sharp cone [4]. Measurements were made at Mach 6 in the Boeing/AFOSR Mach-6 Quiet Tunnel (BAM6QT) and in the conventional Mach-6 wind tunnel in Braunschweig. Data were acquired by an array of PCB132A31 sensors mounted flush to the model surface. Successful measurements of second-mode instability waves were possible in both facilities across a range of Reynolds numbers. No evidence of downstream effects due to the surface-mounted sensors was observed. It should be noted that a typo in [4] reports the sensors as PCB131A32, when in actuality the correct model number is PCB132A31 [5].

Chynoweth studied second-mode waves on a flared cone under quiet flow at Mach 6 [6]. The maximum second-mode pressure fluctuations prior to breakdown were nearly 30%, and more than double the magnitude predicted by a correlation for noisy flow. Second-mode harmonics were clearly visible in the power spectral density (PSD) calculated from measurements made with PCB132 sensors. Harmonics were present at frequencies up to 1MHz. Edelman measured the crossflow instability on a straight 7° half-angle cone using PCB132 sensors and temperature-sensitive paint [7]. PSDs computed from PCB132 measurements show secondary instability frequencies in excess of 400 kHz.

Tanno et al. measured the surface pressure fluctuations due to the second-mode instability on a 7° half-angle cone in the Japan Aerospace Exploration Agency (JAXA) high enthalpy shock tunnel (HIEST) [8]. Mechanical vibrations posed an issue for piezoelectric sensors in HIEST, and so a modified mounting technique using silicone caulk was employed. Vibration modes up to 340 kHz were observed from a hammer test and from data obtained during runs. Surface-pressure measurements appeared to show second-mode instabilities.

PCB132 pressure sensors were used for free-stream noise measurement in a variety of conventional hypersonic facilities including the Hypersonic Ludweig Tube Braunschweig at Mach 6, the NASA 20-Inch Mach 6, the Sandia Hypersonic Wind Tunnel (HWT-8) at Mach 8, and the Arnold Engineering Development Complex (AEDC) Tunnel 9 at Mach 14 [9]. PSDs of these data all generally fit to a slope of $f^{-3.5}$ in the frequency domain. Good agreement was demonstrated between direct numerical simulation (DNS) results and measurements taken with PCB132 sensors in the BAM6QT, Sandia HWT, and AEDC Tunnel 9.

Wagner et al. studied free-stream disturbances at Mach numbers ranging from 3–7.4 [10]. Testing was performed at the German Aerospace Center (DLR) High Enthalpy Shock Tunnel Göttingen (HEG), the DNW-RWG Ludweig tube, and the TU Braunschweig Ludweig tube. Disturbances were measured with PCB132 and Kulite pressure transducers flush-mounted to a wedge. Silicone sleeves were used to

mount PCB132 sensors to reduce vibration contamination. Measured static pressure root-mean-square (RMS) was converted to total pressure using a relation for Mach numbers higher than 2.5. The converted RMS levels agree with separate pitot-probe data for measurements made at Mach 6 and 7.4.

1.3 Dynamic Sensor Calibration

Numerous methods for dynamic pressure calibration exist. Sensors can be calibrated directly at certain frequencies using a periodic pressure generator, a chamber which generates a sinusoidal pressure input to a sensor under investigation. Aperiodic pressure generators such as shock tubes or fast-opening devices create a pressure change close to a step input, allowing the sensor impulse response to be computed from the measured step response. The sensor response depends on the pressure input, possibly making both the shock thickness and speed important factors. The lowest frequency a sensor can be calibrated at will depend on the flow duration, determined by the time between the arrival of the shock and the arrival of the contact surface [11].

Gregory et al. presented a comparison of dynamic calibration methods, showing that shock tubes produce the fastest pressure rise [12]. PCB132 sensors have a manufacturer-quoted rise time of less than 1 μs, and so dynamic calibration methods must use a faster rise time to properly evaluate the sensor. Other aperiodic pressure generators like solenoid valves generate pressure changes orders of magnitude slower than a typical shock tube. Periodic pressure generators are limited by maximum frequencies in the 100 kHz range, making them unsuitable for PCB132 calibration at higher frequencies.

Janza & Hicks provide a number of methods for performing dynamic calibration of piezoelectric pressure sensors with a shock tube [13]. The first method uses the rise time measured by two sensors to determine the shock speed and from this calculate the pressure rise. A second method uses a relation for reflected and incident pressure rise along with a reference gauge to check the other calibration methods. Janza & Hicks

also discuss possible noise sources including sensor resonance, acceleration, ground loops, and temperature variation. The effect of the rise time on the calibration of piezoelectric gauges is discussed.

Knight presented results of piezoelectric sensor testing in a shock tube [14]. The sensors and electronics were only designed for time-of-arrival measurements. Because of this, quantitative voltage data was not taken. Knight emphasized the importance of mechanical isolation for improving signal-to-noise ratio since the sensors are sensitive to vibration, similar to PCB132 sensors.

Gavrilenko & Nikelaev also tested a piezoelectric pressure sensor in a shock tube [15]. The sensor had a rise time of 3 μs and a step-like response. Additionally, the sensor could be statically calibrated. They showed linear behavior for both static and dynamic calibrations, and only 3% difference between the calibrations.

Matthews et al. applied system identification procedures to data obtained from a piezoelectric pressure sensor tested in the Cranfield shock tube [16]. The authors do not include the model of the piezoelectric sensor used. The Cranfield shock tube has a 7.3 m driven section with an 8.13 cm ID. A range of 6.9–8.3 MPa burst pressures were used. A model was developed for the sensor from a second-order system coupled with a sixth-order Butterworth low-pass filter. The estimates of model parameters were consistent between runs, but could not capture all of the sensor's behavior. In particular, the model diverged from the sensor response after about 15 μs after shock arrival. Using only the first 15 μs of the trace produced a model that more closely matched the measured data.

Matthews et al. also compare expected shock tube performance to that of a drop-weight calibration system. The drop-weight system has a much smaller bandwidth due to rise times on the order of 1 ms. Because of this, drop-weight systems are not suitable for calibration of high-frequency pressure sensors that require evaluation at frequencies up to 1 MHz.

Mohammed et al. used a shock tube for dynamic calibration of temperature probes by utilizing the temperature step across the shock [17]. The shock tube had

a 5 cm ID and a 4.25 m long driven section. Helium was used as the driver gas and CO_2 and air were used for driven gas. Diaphragm pressure ratios ranged from 10–200 and pre-run temperatures were nominally ambient. Pre-run pressures were not included. Temperature probes were mounted in the end-cap of the shock tube. The temperature rise was found to decrease along the length of the shock tube, but change little at different locations in the end-cap. Temperature rise increased with shock Mach number, as expected from the perfect gas relations.

1.4 Shock Tube Physics

As discussed previously, the fast rise time of high-frequency pressure sensors necessitates the use of a calibration system with a fast input rise time. Shock tubes are one of the only calibration systems capable of producing a pressure step that is fast enough [12]. Shock tubes have also been studied extensively, and are capable of producing consistent flow conditions.

1.4.1 Basic Shock Tube Principles

A shock tube is a device which creates a normal shock followed by a region of approximately uniform flow. Shock tubes generally have well understood flows, and so are often employed for evaluation or characterization of sensor dynamic response. The pressure step across the normal shock is often used as a step input to the sensor under consideration.

A shock tube works by bursting a diaphragm separating two gases at different pressures. As the diaphragm bursts, a shock wave travels into the lower pressure gas, or driven gas. At the same time, an expansion wave travels into the higher pressure gas, or driver gas. The shock wave can act as a step input to a sensor located in the driven section, as the flow changes temperature, pressure, and density across the shock. Depending on flow conditions, this change can take place in less than 0.1 μs. Upstream of the shock is a section where the driven gas flows with a roughly uniform

velocity profile, followed by the interface between the gases originally on either side of the diaphragm. This interface is called the contact surface, and acts like a piston, pushing the driven gas behind the shock [18]. A schematic of shock tube flow is shown in Figure 1.1.

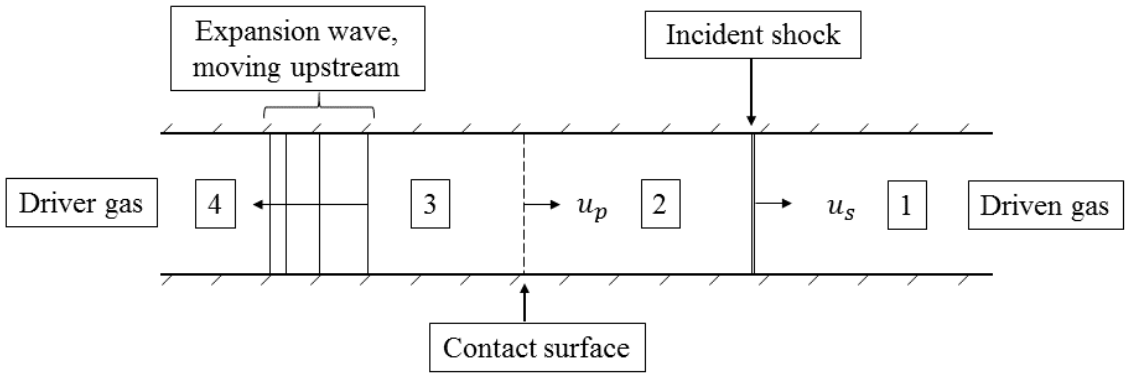

Figure 1.1.: Schematic of shock tube flow. Flow is from left to right.

The relative motion of the contact surface, expansion wave, and incident shock as predicted by perfect gas relations is shown in figure 1.2. Since the relevant test time for most experiments is the time between the arrival of the shock and the contact surface, increasing the shock tube length should increase test time. Test time will not indefinitely increase with shock tube length, and is ultimately determined by viscous effects [19].

Because of the nature of the shock tube, flow between the shock and contact surface is unsteady. As the driven gas is accelerated downstream, a boundary layer forms on the shock tube walls. The run time is determined by the time difference in the arrival of the incident shock and the arrival of the contact surface. Due to the run time limit imposed by arrival of the contact surface, the boundary layer is changing over the course of a run. This is in contrast to most wind tunnels, where flow occurs for long enough to set up a steady boundary layer on the tunnel and test article before data is acquired.

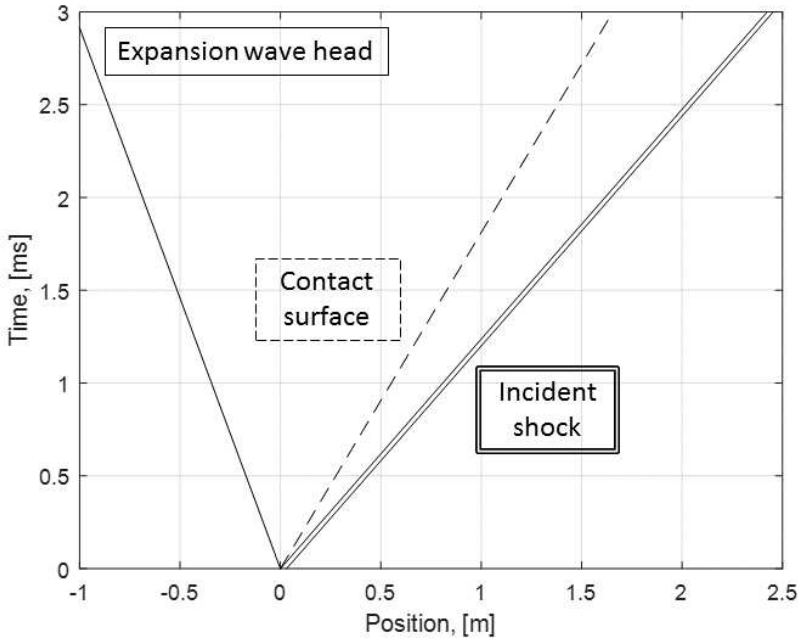

Figure 1.2.: Nominal X-T diagram of shock tube flow showing relative motion of shock, contact surface, and expansion wave.

Typical quantities of interest in a shock tube include the pressure, temperature, and velocity upstream of the shock, as well as the velocity of the shock into the driven gas. These quantities of interest can be computed using normal shock and perfect gas relations, following the derivation presented in [20]. The pressure ratio across the shock, p_2/p_1, can be found using Equation 1.1 with the pre-shock pressure ratio, p_4/p_1, ratio of sound speeds, a_4/a_1, and ratio of specific heats, γ. Subscripts refer to quantities at the locations shown in Figure 1.1.

$$\frac{p_4}{p_1} = \frac{p_2}{p_1}\left\{1 - \frac{(\gamma_4 - 1)(a_1/a_4)(p_2/p_1 - 1)}{\sqrt{2\gamma_1[2\gamma_1 + (\gamma_1 + 1)(p_2/p_1 - 1)]}}\right\}^{-2\gamma_4/(\gamma_4 - 1)} \tag{1.1}$$

Since the quantity of interest is typically the pressure jump across the shock, Equation 1.1 must be solved implicitly. The Mach number of the shock moving into the quiescent gas, M_s, can be found with Equation 1.2.

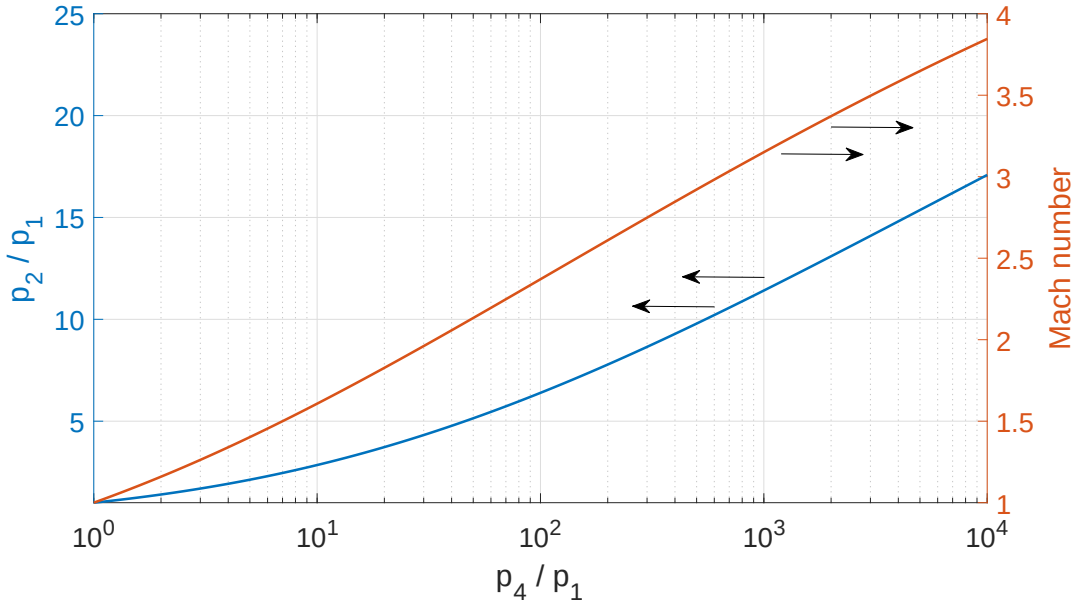

Figure 1.3.: Incident shock pressure ratio and Mach number predicted by shock-tube relations; p_1 refers to driven pressure, p_2 refers to pressure between incident shock and contact surface, and p_4 refers to driver pressure. Pre-run gas at 295 K; $\gamma = 1.4$.

$$M_s = \sqrt{\frac{\gamma_1 + 1}{2\gamma_1}\left(\frac{p_2}{p_1} - 1\right) + 1} \tag{1.2}$$

The temperature ratio across the shock, T_2/T_1, can be calculated with Equation 1.3.

$$\frac{T_2}{T_1} = \frac{p_2}{p_1}\left(\frac{\frac{\gamma_1+1}{\gamma_1-1} + \frac{p_2}{p_1}}{1 + \frac{\gamma_1+1}{\gamma_1-1}\frac{p_2}{p_1}}\right) \tag{1.3}$$

The Mach number and pressure step variation with pre-shock pressure ratio as predicted by shock-tube relations are shown in Figure 1.3. The Mach number and pressure step ratio both increase with increasing pre-shock pressure ratio. This means that increasing the pre-shock pressure ratio will generally result in a faster and stronger shock.

1.4.2 Diaphragm Effects

Diaphragm opening is often idealized when analyzing shock tube flow. In certain applications, diaphragm opening times can be significant. Improper diaphragm rupture can result in flow that is not well understood or characterized. There are numerous ways to burst the diaphragm and initiate flow in a shock tube. Commonly, the diaphragm is cut or broken in an "X" pattern, similar to the patterns shown in Figure 1.4. These patterns result in four "petals" of diaphragm material which are supposed to lie flat to the shock tube walls during a run.

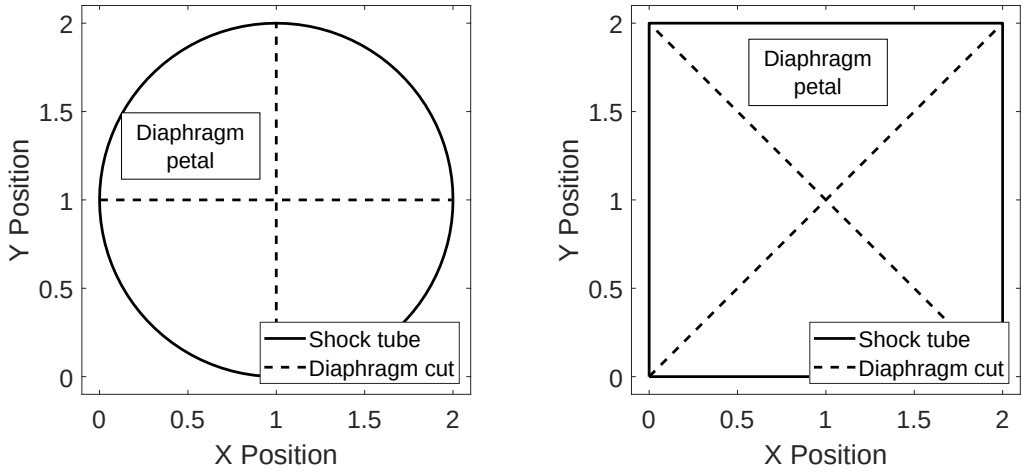

(a) Circular cross-section

(b) Square cross-section

Figure 1.4.: Typical cut patterns in circular and square cross-sectional shock tubes.

Drewry & Walenta developed a theoretical relation for diaphragm opening time based on the diaphragm material density, ρ_d, diaphragm thickness, τ, base width of each diaphragm petal after rupture, b, and driver pressure, p_4 [21]. The time for diaphragm rupture is given in μs in Equation 1.4.

$$t = 4.73(\rho_d b \tau / p_4) \times 10^4 \tag{1.4}$$

The relation was developed with the assumption of instantaneous diaphragm rupture, with an equal application of forces and moments to each of the four petals. A square cross-section diaphragm was assumed. The model had the same form as a model developed independently at NASA Ames Research Center, with only around a 5% difference in constants. The model was compared to separate measurements of diaphragm opening times made with a microphone and photodiode. Both measurement techniques showed opening times around 800 μs, compared to 400 μs predicted by the model developed by Drewry & Walenta. The authors state this could be due to oversimplifications in the model.

Rothkopf & Low characterized the diaphragm opening process in shock tube flow for diaphragms of different metals and shapes, using photographic systems to measure the pre-run diaphragm deformation [22]. The shock tube had a square cross section, 5×5 cm in the driver section and 5.4×5.4 cm in the driven section. The driven section tapered from the square cross section to a 5.2 cm diameter rounded tube. The driver section was 60 cm long and the driven section was 14 cm. They used aluminum, copper, and brass diaphragms of varying thickness with round and square cross-sections. All diaphragms were stamped with an "X" shape to aid in diaphragm rupture. The authors do not describe exactly how the "X" shape was stamped, but note that the stamping force was kept constant between diaphragms. A knife-blade system was mounted directly downstream of the diaphragm at an adjustable distance. They found that the knife-blade system did not decrease opening times compared to the "X" stamp, but did produce a more consistent burst. Material ductility seemed to determine the pre-burst shape and diaphragm thickness determined burst pressure. The measured breaking times could be significant, up to 0.4 ms for some configurations. The experimental results compared favorably to the model developed by Drewry & Walenta in [21].

Liepmann et al. measured the diaphragm opening process in a low-density shock tube [23]. The shock tube had an ID of 17 inches (0.43 m), and a 67.9–72 ft (20.7–21.9 m) long driven section, depending on the setup. The shock tube was designed

for quick turn-around with a diaphragm loading system that reduced time and the number of required operators. An adjustable blade-cutting system was used to burst the diaphragm. Shock arrival after diaphragm cutting was measured with a sensor on the blade system and a downstream film gauge. It was found that at low cutter distance, where the blades were positioned close to the diaphragm, a decrease in diaphragm opening time was observed. This was likely due to diaphragm tearing dominating the opening process. The opening time increased with cutter distance until the point where rupture due to pressure dominated the process.

Persico et al. experimentally and computationally investigated shock tube flows due to partially opened diaphragms and their effect on dynamic pressure calibrations [24]. Computations were performed assuming a perfect gas with an instantaneous, partial diaphragm opening. No structural dynamics were included, so the flow was modeled as around a thin wall partially intruding into the shock tube. To duplicate this experimentally, a metal ring of varying dimension was placed inside the shock tube immediately downstream of the diaphragm. This allowed the center of the diaphragm to burst, while the outer portion stayed intact. The shock tube was made of Plexiglas and exhausted to atmospheric, allowing continuous optical access from the sides and downstream of the diaphragm rupture. Diaphragms were naturally burst and made of DCfix™ plastic. The pre-shock pressure difference was around 1 atmosphere.

The results computed by Persico et al. show a separation region immediately downstream of the partially ruptured diaphragm section, leading to pressure fluctuations far downstream. The simulation results were confirmed by total pressure measurements made with a Kulite pressure sensor which closely matched predicted pressure fluctuations. The pressure fluctuation frequency increased with distance downstream, ranging from 5–15 kHz.

1.4.3 Test-Time Limitation

The test time in a shock tube is generally defined as the difference in the arrival times of the incident shock and contact surface at an axial location. When flow is initiated in a shock tube, the shock moves faster than the contact surface. Inviscid analysis of shock tube flow shows that increasing the length of the shock tube increases the test time indefinitely. However, due to the formation of the boundary layer between the shock and contact surface, the shock is decelerated and the contact surface is accelerated. This imposes a maximum test time limitation, especially acute for low-pressure shock tubes [25].

Anderson analytically computed the reduction in test time [19]. Reduction in test time is due to mass loss into the boundary layer upstream of the contact surface. Anderson assumed the shock Mach number was constant to show the change in test time for 2 shock tube sizes. This is not a realistic assumption, but was used to show the effects of the boundary layer on shock tube performance.

Spence reviewed some theoretical models of shock attenuation [26], concluding that Mirels's model [27] is more accurate than Trimpi and Cohen's model [28]. Mirels's formulation appears more accurate due to the inclusion of a mass addition term, absent in Trimpi and Cohen's model. Both models assume one-dimensional flow and that the boundary layer is small compared to the tube radius. Demyanov used the same formulation as Mirels and obtained a closed-form solution [29]; however it compared poorly with experiments. A possible cause is an inconsistency, in that variables outside of the boundary layer were treated as independent of radial position.

Mirels analytically investigated the reduction in flow time for shock tubes with fully turbulent boundary layers [25]. Mirels's analysis examined the mass flow through the boundary layer at the contact surface and found the variation in test time. Boundary layer thickness was defined based on displacement thickness. The maximum possible test time is affected by the shock tube ID, d, and the driven pressure, p_1. For turbulent cases, the maximum test time scaled with $d^{5/4} \cdot p_1^{1/4}$ and for laminar cases

it scaled with $d^2 \cdot p_1$. Mirels also found that in the shock Mach number range of 3 to 8, laminar theory applies for $d \cdot p_1$ less than 0.5 in·$\mathrm{cm_{Hg}}$ and turbulent theory applies for $d \cdot p_1$ greater than 5 in·$\mathrm{cm_{Hg}}$. This was based on previously reported transition Reynolds numbers from shock tubes in the shock Mach number range of 1 to 9. Reynolds number was defined based on the separation distance between the shock and contact surface. The boundary layer completely filled the tube for laminar cases when the shock Mach number was less than 12 and for turbulent cases when the shock Mach number was less than 3. This occurred for a long shock tube, or a shock tube long enough to reach a maximum test time.

Martin performed an experimental study of the boundary layer between the incident shock and the contact surface for pressure ratios across the incident-shock of 2.75 and 8.0 [30]. Martin used air and helium for the driver gases and air for the driven gas, with initial driven pressures of 400 and 160 mbar. Velocity profiles were found by measuring densities from boundary-layer interferograms and assuming constant pressure in the boundary layer. Martin compared velocity profiles to a 1/7 power law and found a 1/5 power law produced a better fit.

Singh & Reddy characterized two shock tubes based on an interaction length determined by the distance between the incident shock and contact surface at the end of the shock tube [31]. Data were acquired from one shock tube with a 0.165 m ID and 10–14 m long driven section, and another with a 0.05 m ID and 5.12 m driven section. For a given length to ID ratio, the change in interaction length with incident-shock Mach number showed a similar trend to 1-D shock tube theory but shifted to a lower normalized interaction length. Scaling the interaction length proportionally to the laminar boundary layer thickness caused all curves to collapse. This allowed for a test-time evaluation method based on Mach number alone.

1.4.4 Low-Pressure Shock Tubes

Duff investigated shock tube performance in a 2.86 cm ID shock tube at driven pressures from 0.3–6.7 mbar with argon as the driven gas [32]. Density was measured with an electron beam densitometer. The test time was calculated from density measurements by comparing the increase in density due to the arrival of the incident shock and contact surface. The shock speed was measured by piezoelectric gauges located near the test window. The test time was found to decrease non-linearly with increasing Mach number for Mach numbers from 1.2–7.0. Severe attenuation compared to values predicted by perfect gas relations was observed for higher Mach numbers. The shock velocity also decreased with distance downstream. Duff defined a lower limit to the shock strength by assuming the shock velocity and flow from the expansion wave would be equal and by assuming that deceleration between the shock and contact surface is isentropic. The measured shock strength fell between the ideal relation and this lower limit.

Roshko studied the reduction in test time in small, low-pressure shock tubes [33]. A 2-inch (5.1 cm) ID shock tube and a 3-inch (7.6 cm) square shock tube were tested at initial driven pressures between 0.13–13.33 mbar. Flow duration was measured using the heating to a constant-current hot wire as a result of the flow between the incident shock and contact surface. The flow duration was measured at locations up to 7.0 m from the diaphragm section using nitrogen and helium as driver gases, and air and argon as driven gases.

Roshko compared experimental results to a similarity solution derived from mass motion past the contact surface. Roshko assumed a laminar boundary layer, a constant shock speed, and constant conditions between the incident shock and contact surface. The resulting maximum test time can be found for air with Equation 1.5, where the test time in seconds, t_{max}, is a function of the driven pressure in Pa, p_1, the ID in m, d, and G, a function of the incident shock Mach number, M_s, arrived at through the similarity solution.

$$t_{max} = \frac{p_1 d^2}{G(M_s)} \times 9.7 \cdot 10^{-5} \tag{1.5}$$

Since the function G increases monotonically with shock Mach number, the test time will be longest for large shock tubes with high driven pressures operated at low Mach numbers. This shows how small, low-pressure shock tubes, like the shock tube used for the current work, often have a flow duration much shorter than ideal predictions.

Duff & Young measured curvature of the shock wave in a 2.86 cm ID shock tube operated at a driven pressure of 0.45 mbar with piezoelectric pressure sensors mounted in the end plate [34]. The piezoelectric sensors were custom-made from barium titanate discs. The sensor rise time and frequency response are not presented. The tilt of the shock wave was negligible, as measured by the difference in shock-arrival times at the end plate. The measured shock curvature was independent of shock strength for Mach numbers from 1.8 to 6.3. The magnitude of the axial "bulge" varied approximately with the reciprocal square root of the initial pressure. The authors note that some uncertainty in the measurements may be reduced with a longer shock tube.

Lin & Fyfe investigated shock tube flow for strong shocks ($12 < M_s < 22$) at low densities in a 24-inch (61 cm) ID shock tube [35]. The test time was measured using various optical techniques, and was approximately 30% of the ideal predicted value. The shock thickness was measured with an ultraviolet absorption technique, and was significantly higher than the thickness predicted by the Thomas or Mott-Smith shock-thickness models. The disagreement with the models was likely due to curvature or tilt of the incident shock. Significant scatter was observed in the shock thickness measurements, indicating the curvature or tilt could be caused by asymmetrical disturbances.

Chigullapalli et al. investigated low-pressure shock tube flows by solving the Boltzmann model kinetic equations for both one and two-dimensional shock tube flows [36]. Conditions included a diaphragm pressure ratio of 10, no temperature gradient, and idealized diaphragm opening. The initial pressures were 1 and 10 Pa.

The simulation did not have a large enough grid to show the complete trend of shock deceleration. However, the simulation did show that the maximum entropy generation was in the interaction of the boundary layer and the shock wave. This implies the flow between the contact surface and incident shock is non-isentropic.

1.4.5 Shock Curvature

Hartunian developed an analytic model for the shock curvature in a shock tube, assuming a two-dimensional shock wave and laminar boundary layer [37]. The resulting shock shape is a function of Mach number and initial pressure. Experimental data compared reasonably well for data taken in air by Lin & Fyfe [35], but showed significant differences for data taken in argon by Duff & Young [34]. These differences could be due to the 2-dimensional assumption in Hartunian's analysis. The data from Lin & Fyfe were obtained in a shock tube with an ID of 61 cm, while the data from Duff & Young was obtained in a shock tube with an ID of 2.86 cm. Hartunian notes that the smaller diameter of the shock tube used for Duff & Young's data set could have significantly changed the shock shape from that predicted by the 2-D shock-curvature model.

De Boer extended Hartunian's shock curvature theory to shock tubes of square and circular cross-section, with both laminar and turbulent flow [38]. De Boer found that shock curvature decreased with increasing driven pressure and increasing Mach number. De Boer compared the model to the same data sets, obtained by Lin & Fyfe [35] and Duff & Young [34]. Both data sets compared favorably with De Boer's model.

1.5 Pressure Sensor Spatial Resolution

Corcos evaluated the effect of transducer size on signal attenuation in the presence of turbulence [39]. By assuming a stationary, homogeneous turbulent flow, Corcos computed the signal attenuation due to the finite transducer size for both circular and

square transducers. Corcos used the computed attenuation values to correct pressure data collected under turbulent flow on a flat plate. Correction was possible, but it was observed that higher-frequency content existed in the flow that was unable to be recovered from the signal.

White extended Corcos's theory to ellipses, rectangles, and diamonds [40]. He found more attenuation for shapes with the major axis aligned with the flow direction. This was due to more area to average the pressure fluctuations, and thus more attenuation. When the three shapes were normalized by their areas, similar attenuation was observed, while the circular element had significantly less attenuation. White also stated that at very low and very high frequencies the attenuation curves are similar regardless of sensor shape. White also extended the work of Gilchrist and Strawderman on hydrophones with variable sensitivity [41] to a more general approach, showing that a variable sensitivity can show less attenuation than a uniform sensitivity for the same sensor size.

1.6 Calibration Efforts for PCB132 Sensors and Other High-Frequency Pressure Sensors

There is little in the literature about the calibration of PCB132 sensors despite their widespread use in hypersonic wind-tunnel testing. As of 2015, PCB132 sensors are calibrated by the manufacturer by generating a pressure step with a shock tube of approximately 1 psi [3]. The sensors are assumed to have a 0 V offset and a linear calibration slope. The first external effort to calibrate PCB132 sensors was reported in 2010 when Berridge used a shock tube to perform a dynamic calibration of PCB132A31 sensors [42]. Berridge noted that most shock-tube measurements used pressure steps with magnitudes that are much higher than measured instability-pressure amplitudes. Because of this, a new low-pressure shock tube was built at Purdue.

Berridge reported additional calibration efforts in 2015 using the Purdue 3-Inch Shock Tube (P3IST) [3]. Berridge defined a maximum relevant pressure-step limit of 0.1 psi (7 mbar), based on the measured maximum amplitudes of second-mode instability waves before breakdown. Berridge used the P3IST to generate low-pressure shock waves with amplitudes less than the 7 mbar limit. Linear calibrations were obtained for PCB132 sensors by correlating the peak voltage with the measured pressure step, for sensors in both pitot and static modes. Berridge's calibration methods will be discussed in further detail in Chapters 3 and 6. Berridge evaluated the flow quality using PCB132 sensors as well as other reference sensors. The current work is a continuation of Berridge's work with the P3IST.

Recently, Ort & Dosch of PCB Piezotronics evaluated PCB132 sensors further using a shock tube and an acoustic calibrator [2]. They used a variation of the PCB132 sensor not commercially available, designated as PCBX132B38. This sensor is a type of PCB132B38 sensor, a newer version of the PCB132A31 sensor used by Berridge. PCB132 sensor types will be discussed in more detail in Section 2.4.1. The fundamental difference between the PCBX132B38 sensor and other PCB132 sensors is the built-in high-pass filter has a much lower cutoff frequency. This results in a step response which is roughly steady state after the initial oscillations damp. Because of this, an acoustic calibrator could be used to evaluate the sensor frequency response at 250 Hz.

The shock tube used by Ort & Dosch was a 2 inch (5.08 cm) ID shock tube with a 12 inch (0.31 m) driver section and a 72 inch (1.90 m) driven section. Shocks were created by naturally bursting a 0.001 inch (0.025 mm) aluminum diaphragm to create a static-pressure step of approximately 4 psi (276 mbar), well above the maximum second-mode range. They found the frequency response of the PCB132 sensor using the pitot-mode step response to the shock wave and compared effects of mounting methods, including neoprene durometer and mounting-hole size. The frequency response varied the most with hole size. Nearly all frequency responses

showed a reasonably flat response between 10–100 kHz, with large peaks evident at frequencies higher than 200 kHz.

The sensitivities of the PCBX132B38 sensor measured with the acoustic calibrator at 250 Hz and the approximately steady-state level agree well. The sensitivity of the frequency response at 20 kHz did not compare to the other sensitivities well. This implies the frequency response is not constant between 250–20,000 Hz, although it is unclear why.

Ort & Dosch also evaluated the sensing area of a PCB132B38 sensor. The piezoelectric sensing element is mounted at the sensor face covered in a layer of epoxy. The size of the sensing element is known, but the epoxy layer makes the effective sensing area unclear. The PCB132 sensor was mounted with the sensor face flush to the shock-tube wall. A shock wave was generated at a Mach number close to Mach 1.1, so a relatively low-speed pressure change could be measured by the PCB132 sensor. By fitting the PCB132 response to the theoretical pressure change acting on a circular element, the effective sensing area could be estimated. They found that the effective sensing area of a PCB132B38 sensor was only 19% larger than the sensing area of the piezoelectric crystal. This analysis used a theoretical pressure change without the influence of shock thickness, and so the accuracy of sensing area measurement is unclear.

The main uncertainties present in Ort & Dosch's work include the pressure step magnitude and the specific PCB132 sensor used. The pressure step generated by their shock tube was around 40 times larger than the upper limit defined by Berridge for second-mode measurements. Because of this, it is unclear if the frequency-responses presented by Ort & Dosch are accurate at lower pressures relevant to hypersonic boundary-layer transition.

It is also unclear if the responses measured by Ort & Dosch are representative of PCB132 sensors in general. Sensitivities were obtained for only three PCBX132B38 sensors and the frequency response for only a single PCB132B38 was presented. Additionally, the relationship between the responses of a PCB132B38 and a PCBX132B38

are not evaluated. Because of this, there is still uncertainty in the behavior of PCB132 sensors in general.

2. APPARATUS

2.1 Purdue 3-Inch Shock Tube

The Purdue 3-inch Shock Tube (P3IST) is designed to produce low-pressure steps for calibrating high-frequency pressure sensors. A schematic of the P3IST is shown in Figure 2.1. The P3IST has an internal diameter of 3.5 inches (8.89 cm), a driver-tube length of 1.43 m, and a driven-tube length of 3.95 m. The shock tube is made of 4 sections of 4-foot (1.22 m) 304 stainless-steel pipe machined together so the internal diameters match. No measurements of the interior-surface roughness or joint-step height were made, although it is believed the step height is less than 0.001 inches. A carbon steel transition section connects the driver and driven sections. Pipe sections are joined with a Marman-clamp assembly. Additional details of P3IST construction are available in [3].

The P3IST is now able to produce consistent run conditions through the use of automated vacuum control valves and an electrical burst system. Previously, uncer-

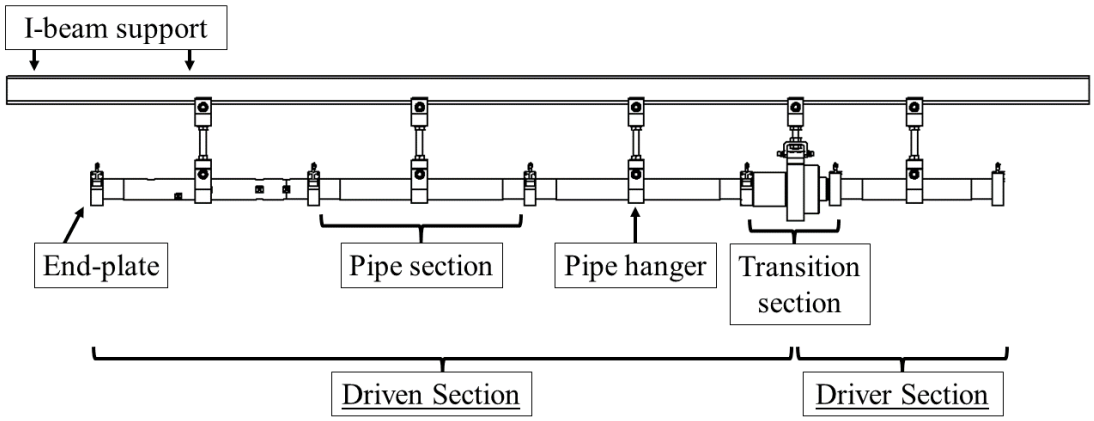

Figure 2.1.: P3IST schematic.

tainties of pre-run pressure were as high as 24% [3]. Currently, automated valves control the driver and driven pressures to typically within 0.5% of the desired values prior to initiating a run. Mylar and polyethylene diaphragms are used with thicknesses ranging from 0.31–2 mil. The diaphragm is ruptured by discharging a capacitor bank across bare nickel chromium (nichrome) wires contacting the diaphragm. The current heats the wires, breaks the diaphragm, and initiates a run. The "X" shape of the wires causes the diaphragm to petal, similar to shock tubes that use scored diaphragms with natural bursts. Because the diaphragm does not break naturally, the pre-run pressures can generally be controlled much more precisely than in a natural-burst shock tube.

The transition section is designed as a hydraulic press and collar, as shown in Figure 2.2. Hydraulic fluid at 1000 psi (68.9 bar) compresses the two sides of the transition section together to form a vacuum seal. Diaphragms are held between the two sides of the transition section by compressed o-rings.

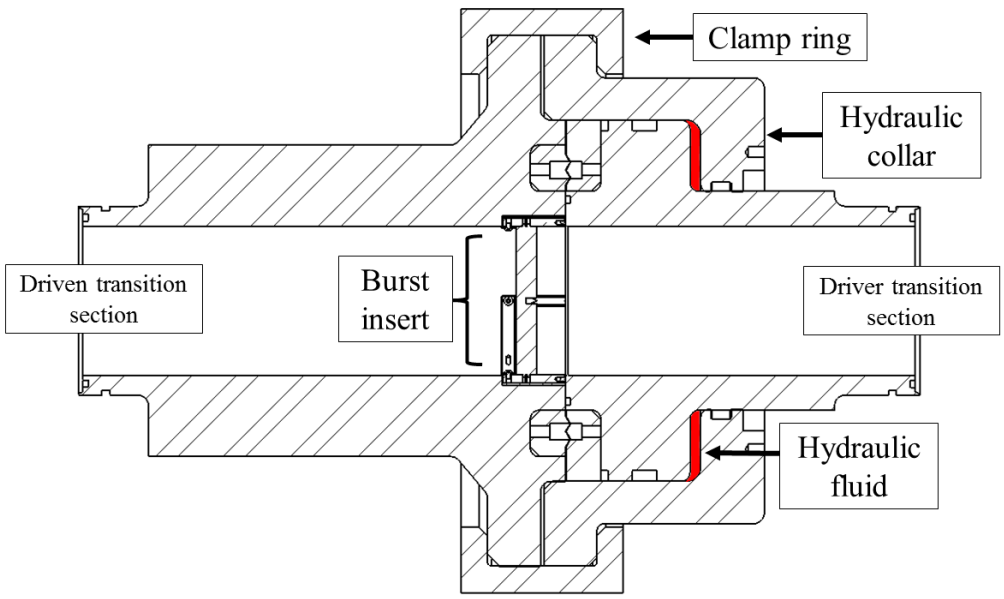

Figure 2.2.: P3IST transition section cross-sectional schematic. Figure adapted from work done by Berridge [3] and Kerlo [43].

The P3IST can be operated at present with a maximum driver pressure of 1000 mbar and a minimum driven pressure of 0.05 mbar. The minimum driven pressure is highly sensitive to leaks, so actual minimum pressures can be higher depending on the specific setup. A conservative estimate of the typical minimum driven pressure is 0.2 mbar. The driver section is designed to be capable of operating at up to 1000 psi (68.9 bar), but the maximum safe pressure of the automated vacuum control valves limits the maximum driver pressure to atmospheric pressure.

2.1.1 Shock Tube Improvements

The initial mechanical design and drafting of the P3IST was provided by Kerlo [43]. Berridge worked with Kerlo and modified the P3IST design as necessary [3]. Improvements were made to the electrical-burst system by Dally with a new design that reduced the frequency of issues related to electrical contact [44]. The shock tube was improved after the work of Dally with the integration of higher-accuracy pressure gauges, automated control valves, and LabVIEW system operation, as described in section 2.1.2. Assistance with the mounting and interface of the automated valves was provided by Carlson, as discussed in [45]. Assistance with shock-tube maintenance and investigation of vibrational reduction methods was provided by Esteban [46].

In previous work with the P3IST, pre-shock pressure measurement uncertainty was estimated as 0.7-24% in the driver section and 6-30% in the driven section [3]. These relatively large uncertainties were likely the result of previous operational procedures, in which the operator had to manually close the vacuum valve and then initiate the run. This also required the operator to read two separate pressure gauges immediately prior to initiating the run. At low pressures the leak rate can be significant, meaning that the pressures would be changing up until the start of the run. This added additional uncertainty to the measured pre-shock pressures.

In the new configuration, pressures are controlled using the integrated proportional-integral (PI) controllers in the automated isolation and control valves. The ramping

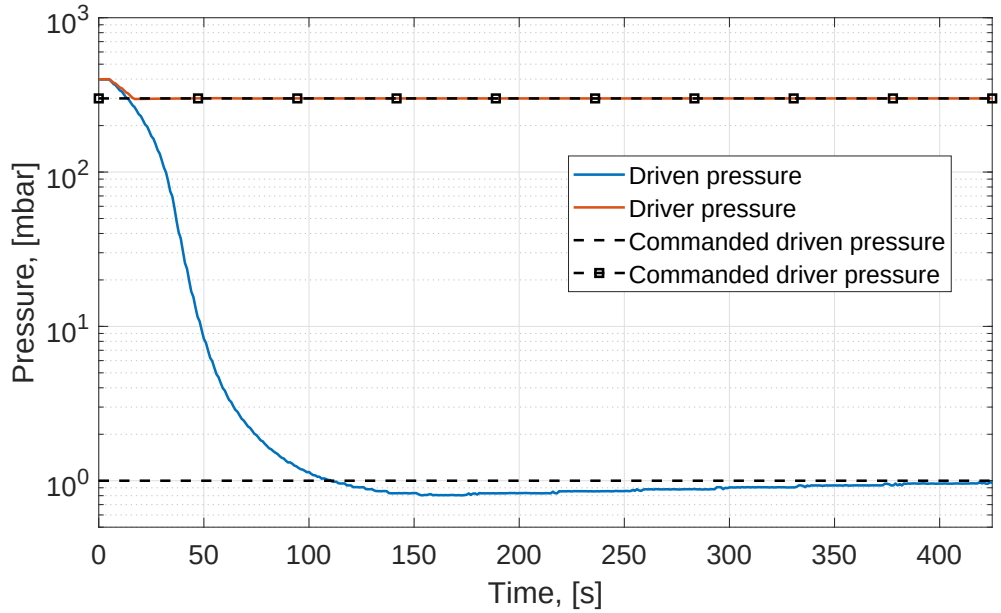

Figure 2.3.: Pressure ramp via automated valves for desired pressures $p_{driven} = 1$ mbar, $p_{driver} = 300$ mbar.

feature allows for a gradual decrease in pressure before the PI controller becomes active. Figure 2.3 shows the pressure change after desired pressures have been commanded. The driver pressure is reached quickly since the initial pressure is closer to the desired. The driven pressure decreases for approximately a minute and then settles. The controller overshoots somewhat, shown by the measured driven pressure decreasing below the desired pressure. This overshoot is not an issue, since the pressure increases due to the settling of the driven gas and the presence of small leaks.

The pressure-system integration also allows for a much more streamlined burst procedure. When a burst is commanded, an automated procedure closes both valves, records and writes pressures to a file, and then sends the burst signal to the capacitor bank. The pre-shock pressures are estimated to be measured within 1 second of the burst command, dramatically reducing the uncertainty in recorded pressures. Figure 2.4 shows that the time from when a burst is commanded to the shock reaching a sensor 3.66 m downstream is less than 15 ms. The shock speed can be measured from

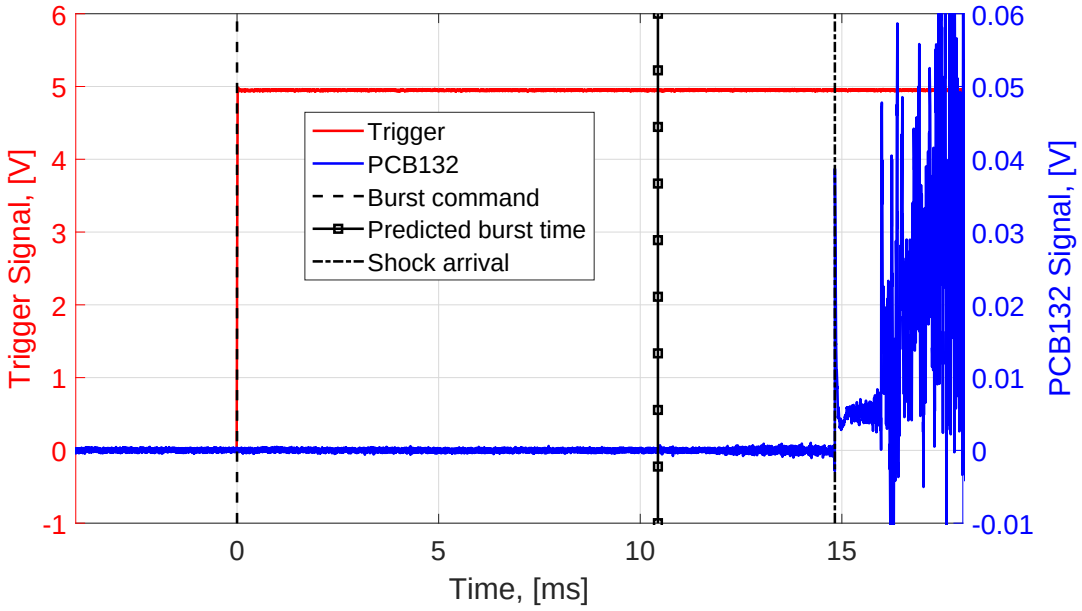

Figure 2.4.: Trigger signal sent to burst capacitor and sensor response located 3.66 meters downstream of the diaphragm. Predicted burst time based on sensor location and measured shock speed. $p_{driven} = 3.00$ mbar, $p_{driver} = 568.0$ mbar, $u_s = 833.5$ m/s.

the arrival times of two PCB132 sensors statically mounted in the P3IST. Based on the measured shock speed and sensor location, the predicted diaphragm burst time is close to 10 ms after the command was sent. The time between the capacitor beginning to discharge and the diaphragm rupturing varies slightly between runs, but is low enough to assume the pressure does not significantly change after the burst is commanded.

In addition to reduced uncertainty in pressure measurements, pressures can now be controlled much more precisely. Figure 2.5 shows the average percent difference of the measured pre-shock pressure from the commanded pressure with error bars indicating standard deviation. With the exception of the runs with driver pressure 50 mbar and driven pressure 0.05 mbar, averages were taken from sets of at least 6 runs.

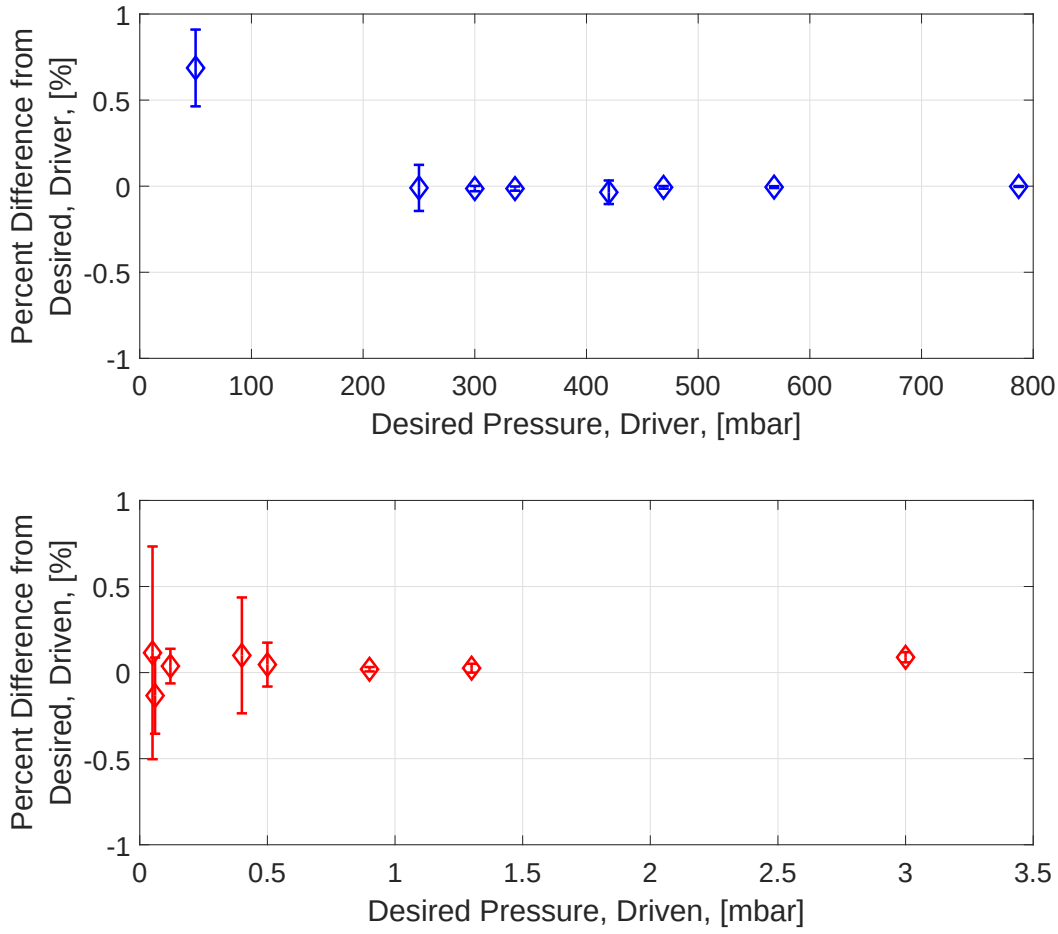

Figure 2.5.: Pre-shock pressure measurement percent difference from commanded pressure. Error bars indicate standard deviation.

The set of runs at driver pressure 50 mbar and driven pressure 0.05 mbar only had 3 runs due to difficulties associated with leaks. Significantly more variation is observed at lower driver and driven pressures due to the increased influence of leaks. Even so, all points have an average percent error of less than 1% from the commanded pressure. This is an order-of-magnitude improvement in pressure-control precision from the apparatus used by Berridge [3].

2.1.2 Shock Tube Operation

Both driver and driven sections are connected to a Leybold TRIVAC D 25 B vacuum pump. The pump has a minimum pressure of 0.002 mbar and a manufacturer-quoted pumping speed of 30.8 m^3/hr.

Driver and driven pressures are controlled independently in the driver and driven sections with VAT Series 615 butterfly control and isolation valves. The VAT valves have a maximum differential pressure of 1 atmosphere, so pressurizing the shock tube above ambient pressure could damage the valves in the current configuration. The valves have integrated PI controllers, along with a direct pressure sensor interface. The PI controllers are tuned for each section and have a ramp functionality, causing the valve to slowly open and allow a lower flow rate to the pump. The vacuum pump can be damaged by excessive flow-rates, so this serves as a safety measure. The VAT valve pressure-control accuracy is quoted as 0.05% of the sensor full-scale output. The valves have a position resolution of more than 28,000 increments from fully closed to fully open. Complete opening and closing times are 0.6 seconds.

The P3IST is operated using a LabVIEW code to command the valves and monitor pressures. The system can set specific valve opening ratios or target pressures for the PI controller. The electrical burst system is also controlled through the LabVIEW program using the National Instruments (NI) data acquisition device (DAQ). Before the run is initiated, the burst-system capacitor bank is charged by sending a 5 Volt signal from the DAQ to the capacitor bank unit, switching a circuit to begin charging from an external power supply. When the switch is toggled again or the 5 Volt signal is absent, the circuit switches to discharging the capacitor bank across an internal resistor. This is a safety precaution to prevent the capacitor bank from storing charge while not in use. When the burst is commanded, another signal is sent to the capacitor, causing it to discharge across the nichrome wires to initiate the run. The capacitor bank is charged to 35 Volts, and has a total capacitance of approximately 1 Farad.

Pre-run pressures are measured in the driven section with two Leybold CERAVAC CTR 101 N active pressure sensors with full scale ranges of 1000 Torr and 1 Torr (1333 mbar and 1.33 mbar). The CERAVAC sensors are capable of gas-independent pressure measurements by measuring a change in capacitance of a diaphragm as it is deflected by changing pressure [47]. The sensors are internally heated to 45 °C to eliminate the requirement for temperature compensation. The sensors have a quoted measurement uncertainty of 0.12% for pressures above 0.1 Torr (0.13 mbar) and 0.15% for pressures below 0.1 Torr. The overpressure limit is 3.1 bar. The sensors output an analog signal between 0 and 10 Volts directly to the VAT valve. The sensors are powered through the VAT valve.

Pre-run pressures are measured in the driver section with a Paroscientific Model 745 Digiquartz® pressure transducer. The transducer has a range of 0-15 psia (0-1034 mbar) and an accuracy of 0.008% of the full scale, or 0.082 mbar. The Paroscientific sensor outputs a digital signal through an RS-232 interface port. In order to properly interface with the driver section VAT valve, the digital signal is converted to analog through a NI USB-6343 DAQ. The DAQ operates at 500 kS/s with 16 bit resolution.

2.1.3 Electrical Burst System

The electrical burst system consists of 4 Delrin and brass inserts held together in a cross-pattern by bus bars and support blades, as shown in Figure 2.6. The assembly is placed in grooves in the transition section and connected to the capacitor bank wires via alligator clips. Wires are fed through Conax compression seal fittings located in the transition section. Solid core wires are used to minimize leaks through the wire insulation. Bus bars carry current to brass posts insulated in Delrin housing. The bus bars are wrapped in electrical tape to prevent electrical contact with the shock tube walls. The structural support blades are insulated from the brass core of the posts by electrical tape. Nichrome wires are attached to the brass posts by tightening the screw around a length of wire.

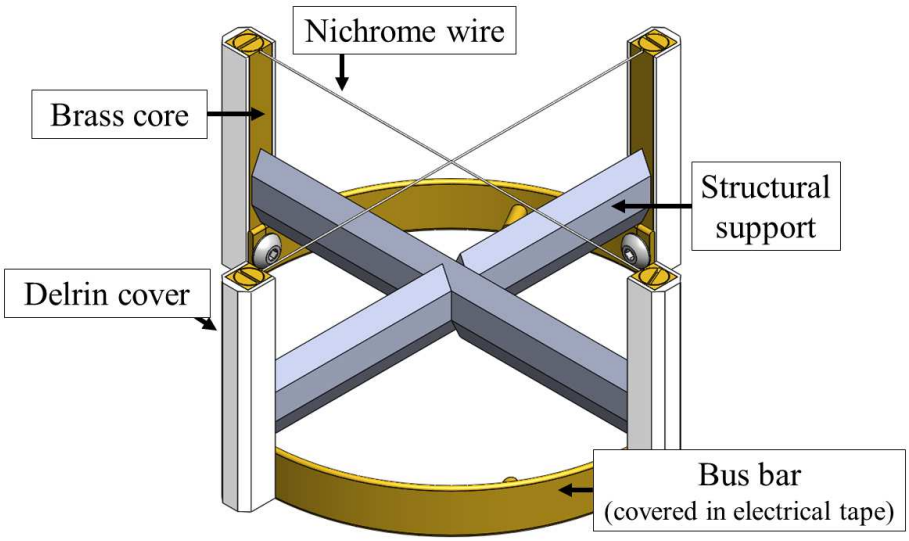

Figure 2.6.: Electrical burst system schematic.

If the nichrome wires heat different amounts, the diaphragm could burst asymmetrically, possibly leading to an asymmetric flow. A difference in heating could be caused by small differences in resistance of the nichrome-wire circuit. Since the time scales associated with the diaphragm burst and shock tube flow are so small, it is important to have minimal variation in electrical resistance between the two nichrome wires. Berridge recommended less than 0.1-0.2 Ω difference in each arm of the circuit for the electrical burst system to function properly [3]. Improper diaphragm rupture could lead to a flow condition not suitable for calibration purposes. Diaphragms can be visually inspected after a run to determine if a proper burst was achieved. Currently, there is no way to evaluate diaphragm burst during a run, and so some uncertainty in diaphragm rupture exists.

Four types of diaphragms are typically used with the P3IST, with the appropriate differential pressures summarized in Table 2.1. The pressure ranges are based on recommendations given by Berridge [3] and Dally [44]. In the current work, the 2-mil Mylar diaphragms were difficult to properly burst, often not bursting completely or showing significant tearing. Additionally, pressures high enough to necessitate the

2-mil diaphragms were rarely needed. Because of this, the 2-mil diaphragms were not used frequently.

Table 2.1.: Useful diaphragm pressure differentials

Diaphragm Type	Typical Useful Pressure Differential, [mbar]
0.31-mil Polyethylene	35 - 200
1-mil Mylar	200 - 415
1.5-mil Mylar	415 - 700
2-mil Mylar	> 700

2.2 Boeing/AFOSR Mach-6 Quiet Tunnel

The Boeing/AFOSR Mach-6 Quiet Tunnel (BAM6QT) is a Ludwieg tube designed to produce low-noise hypersonic flow. It is one of several hypersonic quiet tunnels in the world [48]. A schematic is shown in Figure 2.7.

Prior to initiating a run, the driver tube is pressurized to the desired pressure and the vacuum tank is evacuated. A pair of aluminum diaphragms downstream of the nozzle are burst to start the run. A shock wave travels downstream and an expansion wave travels upstream. The expansion wave reflects between the nozzle and the end of the driver tube. This happens approximately every 200 ms, after which the pressure

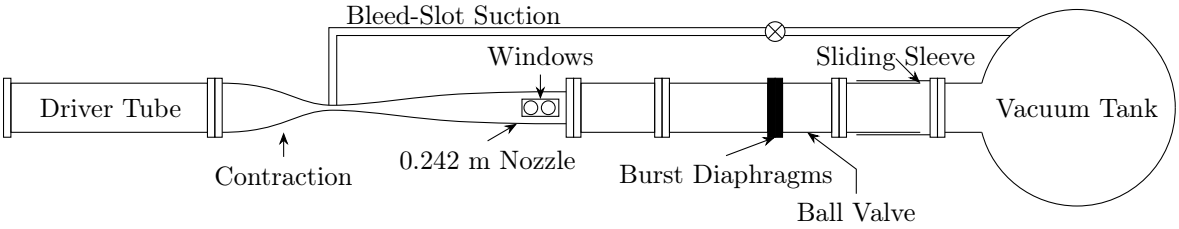

Figure 2.7.: BAM6QT schematic.

drops by around 1%. During the 200 ms, the flow is quasi-steady. Useful run duration is typically around 5 seconds long.

The BAM6QT uses a number of features to maintain laminar flow on the nozzle wall. The first is a bleed slot located immediately upstream of the nozzle throat. This is connected to the vacuum tank and is used to remove the incoming boundary layer to allow a laminar boundary layer to form. The tunnel can be run with the bleed slot opened or closed, thereby operating as either a quiet or conventional hypersonic tunnel.

Other important features of the BAM6QT include filters which remove particles larger than 0.01 μm from the air used to fill the driver tube. The nozzle is polished to a mirror finish to reduce surface roughness that could cause transition of the nozzle-wall boundary layer. The nozzle also has a long concave section to slow the growth of Görtler vortices. Measured free-stream noise levels are less than 0.05 % [49]. Currently, quiet flow is achievable at a maximum stagnation pressure of 155 psia (10.7 bar) and a unit Reynolds number of 11.9×10^6 m^{-1}.

2.3 Sensor Mounting

2.3.1 Static Mounting

Sensors are mounted in the P3IST in both static and pitot configurations. Here, static refers to a mounting where the sensor face is parallel to the flow direction, so as to measure static pressure. Pitot configuration refers to a mounting where the sensor face is normal to the flow direction, so as to measure post-shock stagnation pressure. Statically-mounted sensors use mounts which are machined flush to the shock tube inner diameter. Three different static-mount designs are used in the P3IST, shown in Figure 2.8. These mounts interface with wall-ports or ports in the driven-section wall.

PCB132 sensors were previously mounted in the P3IST directly to metal ports using nail polish as adhesive, shown in Figure 2.8(a). Nail polish was applied so that

the sensor sides were covered, electrically isolating the PCB132 sensor from the shock tube. This is common practice for PCB132 mounting in models in the BAM6QT. PCB132 sensors are vibration sensitive [3], but this mounting typically does not pose an issue for wind tunnel testing since start-up vibrations will often diminish during a relatively short time before data is collected. Vibrations do pose an issue for shock tubes and shock tunnels however, since flow durations are so short. Vibrational noise is especially problematic in the P3IST since pressure jumps are commonly very low. The low pressure jumps are necessary for calibration at amplitudes relevant for hypersonic boundary-layer transition. If the sensor measures any pre-shock noise due to acoustic waves traveling through the shock tube structure, it can substantially affect the measurement.

To reduce vibrational contamination, Berridge used the modified mounting design shown in Figure 2.8(b). The new mount reduced vibrational noise with a neoprene sleeve with nail polish used as adhesive. This allowed for mounting without any metal contact, similar to noise reduction techniques used in shock tunnels at Calspan-University at Buffalo Research Center (CUBRC) [3]. The new mount provided significant vibration reduction from the previous mount, but posed some new problems. Because the neoprene was not matched to the curvature of the shock tube, the addition of the sleeve created larger gaps from the shock tube curvature, as shown in Figure 2.9. Sensors mounted in these mounts often produced a downward spike immediately before the shock was detected, which Berridge proposed was due to these gaps.

Ort & Dosch recently showed the downward spike immediately before shock arrival was actually due to the deflection of the neoprene sleeve housing the PCB132 [2]. Piezoelectric sensors function by converting strain to charge. This means that a lateral compression of the sensing element can result in a change in voltage. Immediately before the shock arrives at the sensor face, it moves over the neoprene housing and compresses it. This in turn compresses the PCB132 sensor, causing a negative voltage spike and changing the effective sensing area. The effects of this response caused by

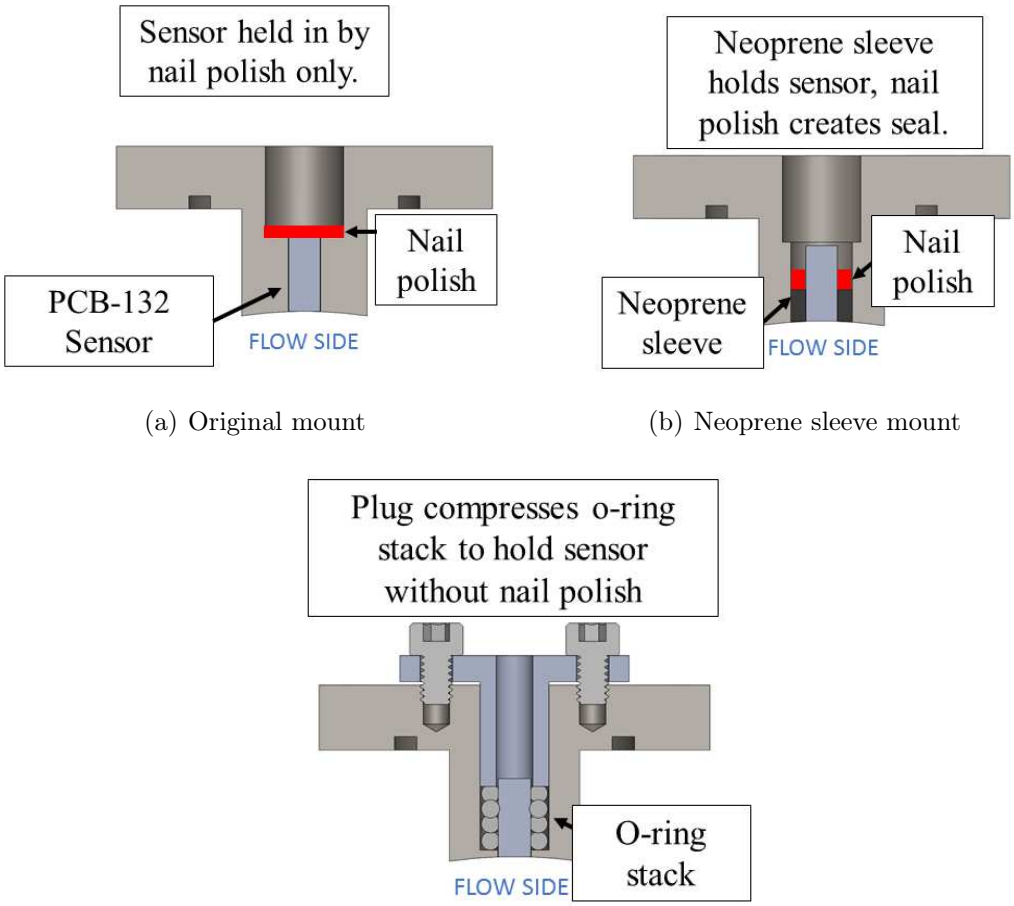

(a) Original mount

(b) Neoprene sleeve mount

(c) Compression mount

Figure 2.8.: Cross-sectional views of different static-mounting designs for PCB132 in P3IST.

the compression of the neoprene sleeve have not been extensively studied, and it is unclear if measurements of arrival time or sensor sensitivity are significantly affected. Because of this, it is unclear if this neoprene sleeve design is feasible for future shock tube measurements with PCB132 sensors. Experiments for this work were concluded by the time the findings made by Ort & Dosch were published, so some measurements made with PCB132 sensors mounted in neoprene sleeves are included here.

To counter these issues, a new mount was designed, shown in Figure 2.8(c). The new mount holds the PCB132 sensor by compressing a stack of o-rings with a metal

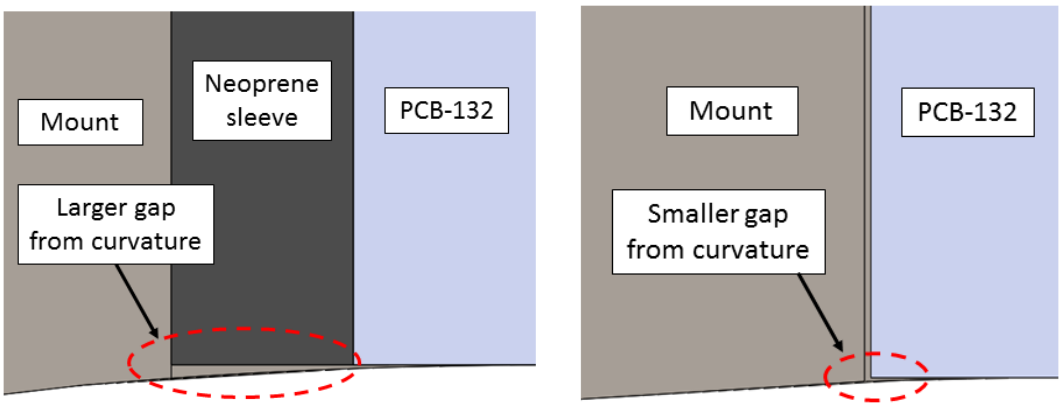

(a) Neoprene sleeve mount (b) Original mount

Figure 2.9.: Gap from sensor mount to shock tube curvature caused by introduction of neoprene sleeve.

piece. When properly mounted, the PCB132 sensor does not contact the metal mount at any point, and vibration is reduced by the o-rings. The gap between the sensor and the mount is 1.5 mil (0.04 mm). Contact could occur between the sensor and the mount due to vibration during a run, however this effect is not believed to be significant. No further measures to electrically isolate the sensor were taken. Since this design does not use nail polish or other adhesives, mounting is much quicker. Additionally, there is no risk of ruining or changing the sensor with nail polish or acetone as with the other mounting techniques. No further reduction in vibrational noise was observed with the new mount. Only some experiments were conducted that show similar vibrational noise to the previous neoprene mounting technique, but extensive testing was not conducted. Drawings of the new mount are included in Appendix G.

2.3.2 Pitot Mounting

PCB132 sensors were mounted in a pitot configuration in the P3IST by interfacing with either the end plate or the wall ports. Pitot refers to a mounting configuration

where the the sensor face is normal to the flow direction, so as to measure pitot pressure during a run. Figure 2.10 shows a pitot probe used for mounting in the P3IST end-plate. The probe is an aluminum tube 0.15 inches (0.38 cm) in diameter, beveled at the end near the sensor face. The PCB132 sensor was held in the tube with room-temperature-vulcanizing silicone (RTV). The end of the probe was filled with RTV and nail polish to form a seal. Due to the amount of RTV and nail polish needed to fill the backside of the probe to make a seal, it is often difficult or impractical to uninstall PCB132 sensors from this mount. The probe body was mounted to the P3IST end-plate with a Conax compression seal fitting.

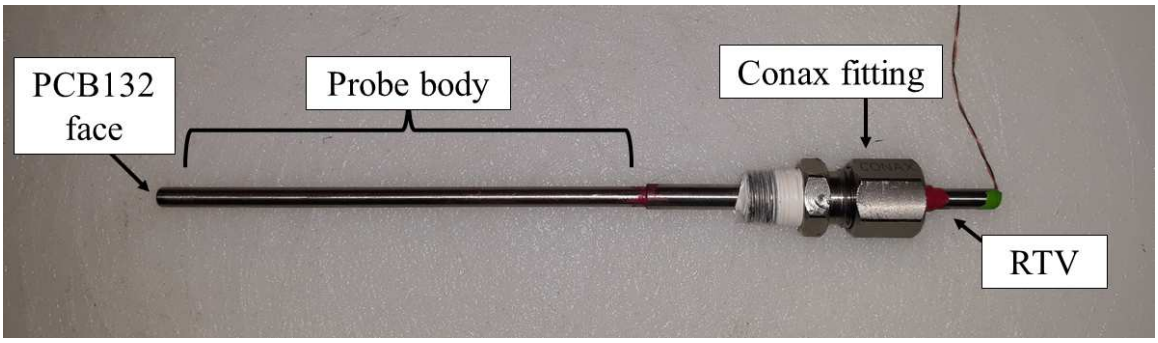

Figure 2.10.: PCB132 mounted in pitot-probe for end-plate mounting in P3IST.

Figure 2.11 shows a pitot probe that interfaces with a wall-port in the P3IST. The probe is designed to fit into the shock tube from a wall-port and seal with a Conax compression seal fitting. The PCB132 was held in the probe with RTV, but did not require RTV or nail polish to fill the backside to make a vacuum seal. The wall-port pitot-probes are generally easier to install since they interface with the wall ports, which are easier to access. Due to the small amount of RTV required, PCB132 sensors can be easily pushed through the mount to uninstall.

The pitot probes shown in Figures 2.10 and 2.11 were already constructed when the current work began. Unfortunately, the original drawings of these probes could not be located for inclusion in this document.

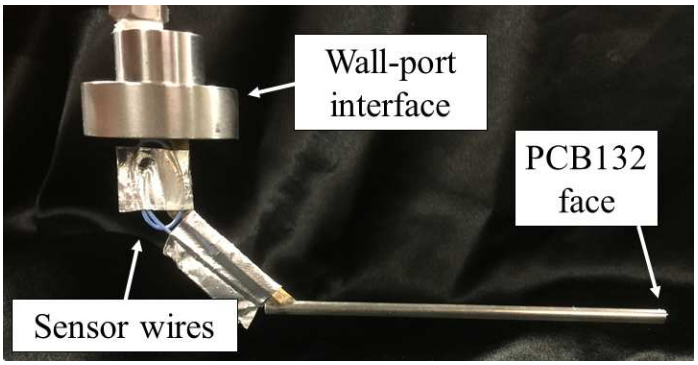

Figure 2.11.: PCB132 mounted in pitot-probe for wall-mounting in P3IST.

2.4 Sensors

2.4.1 PCB132 Pressure Sensors

PCB132 pressure sensors are ceramic piezoelectric pressure transducers. They were developed as a time-of-arrival sensor with a fast response time [2]. PCB132 sensors found use in boundary layer transition studies in 2006 [1] due to the ability to measure frequencies up to 1 MHz. PCB132 sensors have a quoted measurement range of 50 psi (3.45 bar) and a typical sensitivity of 2.03 mV/mbar. Their rise time is quoted as less than 3 μs. PCB132 sensors are high pass filtered at 11 kHz with the built-in amplifier. PCB132B38 sensors have -0.45 dB attenuation at 11 kHz and -3 dB attenuation at 3.5 kHz [2]. The high-frequency response limit is quoted as 1 MHz. Measurements made by Ort & Dosch indicate the high-frequency resonance is close to 700 kHz [2].

Two types of PCB sensors are commonly used: PCB132A31 and PCB132B38. These sensors will be referred to further as PCB132A and PCB132B, respectively. Both sensors are cylindrical and have the same outer dimensions of 0.30 inches (7.62 mm) long and 0.125 inches (3.18 mm) in diameter. PCB132A sensors have a simple twisted cable and the PCB132B sensors have a more durable coaxial cable. Both sensors have a layer of epoxy covering the face.

PCB132A sensors are the older version of the sensor, only designed for time-of-arrival measurements. The sensing element is a 0.762×0.762 mm square on the sensor face. The sensing element is not centered and the element position differs between sensors. This adds uncertainty to measurements, especially those that require high spatial precision. Figure 2.12 shows a microscope image of a PCB132A sensor with the epoxy layer removed from the face.

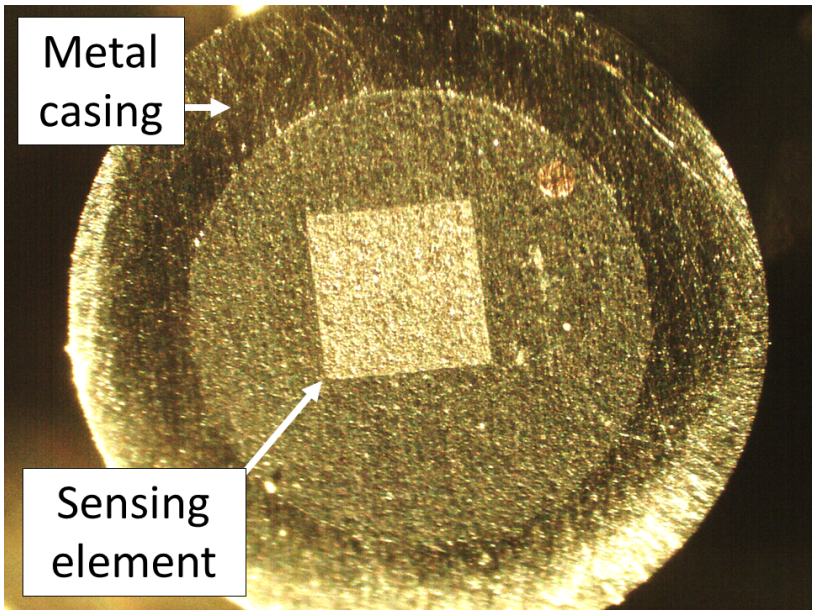

Figure 2.12.: PCB132A31 microscope image with epoxy face removed.

To improve sensing-element placement and size, PCB132B sensors were designed with boundary-layer transition measurements in mind. The sensing element is a centered 0.89-mm-diameter cylindrical piezoelectric crystal. Ort & Dosch estimated the effective sensing diameter of a PCB132B sensor as 0.97 mm, based on data acquired in a shock tube [2]. Since this is only for a single sensor, it is unclear how much the effective sensing area varies between sensors. It is also unclear how much the epoxy layer affects the PCB132 sensor face. Significant variations have been observed in the

epoxy layer thickness and surface roughness. It is unclear if this could affect local sensitivity or even boundary-layer behavior.

2.4.2 PCB606B01 Acceleration Sensors

PCB606B01 sensors were used to characterize vibrations in the P3IST. PCB606B01 sensors [50] are ceramic piezoelectric accelerometers, pictured in Figure 2.13. They have a measurement range of ± 490 m/s^2 and a resolution of 3.434 mm/s^2. Their frequency range, or the range of frequencies for which the output signal is within ± 3 dB, is 0.5–10,000 Hz. The resonant frequency is quoted as 25 kHz, although testing in the P3IST indicates this may differ for individual sensors. The sensors have a non-linearity of ± 1%. The accelerometers have a bolt which can be used to easily mount the sensor to a manufacturer-supplied mounting pad. The accelerometer senses acceleration normal to the mounting surface, or in the vertical direction for the accelerometer shown in Figure 2.13. The manufacturer-quoted transverse sensitivity, or the sensitivity to acceleration in directions not normal to the mounting surface is less than 7%.

Figure 2.13.: PCB606B01 from [50].

2.4.3 Kulite Pressure Sensors

Kulite XCQ-062-15A pressure transducers were used to measure the static pressure step in the P3IST. The Kulite sensors were the only reference sensor used in this work. Previously, measurements of the static-pressure step have been made in the P3IST with other sensors, such as the PCB102B18 piezoelectric pressure sensor. Only Kulite sensors were used due to a lower manufacturer-quoted uncertainty. A limitation of the current work is an absence of any comparison between Kulite sensors and other reference sensors.

Kulite XCQ-062-15A pressure transducers are cylindrical pressure sensors 1.7 mm in diameter and 9.5 mm long. The sensor uses an etched silicon diaphragm exposed to the measurement pressure on one side and a reference pressure on the other side. Piezoresistive strain gauges on the diaphragm are placed in a Wheatstone bridge configuration to measure the diaphragm strain due to pressure. The strain is converted to voltage by the sensor and external amplifier, and the measured pressure is inferred from a linear calibration.

Two variations of Kulite sensors were used in this work: A-screens and B-screens. A-screen Kulite sensors have no protective covering over the silicon diaphragm. Instead, the diaphragm is recessed 0.025 inches (0.64 mm) from the edge of the casing and is otherwise open. The diaphragm can be delicate, and so care must be taken to not damage it. B-screen Kulite sensors have a porous covering to protect the diaphragm from damage. The screen reduces the useful frequency range of the sensor. The burst system in the P3IST often causes wire or diaphragm fragments to fly downstream during or after a run. Despite this, no damage to the A-screen Kulites used in the P3IST has been observed during this or previous work.

The Kulite sensors have a measurement range of 0–15 psia and can measure static pressure. Because of this, Kulite sensors were calibrated in situ in the P3IST before each section of testing. Kulite sensors are mechanically stopped to prevent damage and have a quoted maximum pressure of 300 psi (20.7 bar). The combined non-

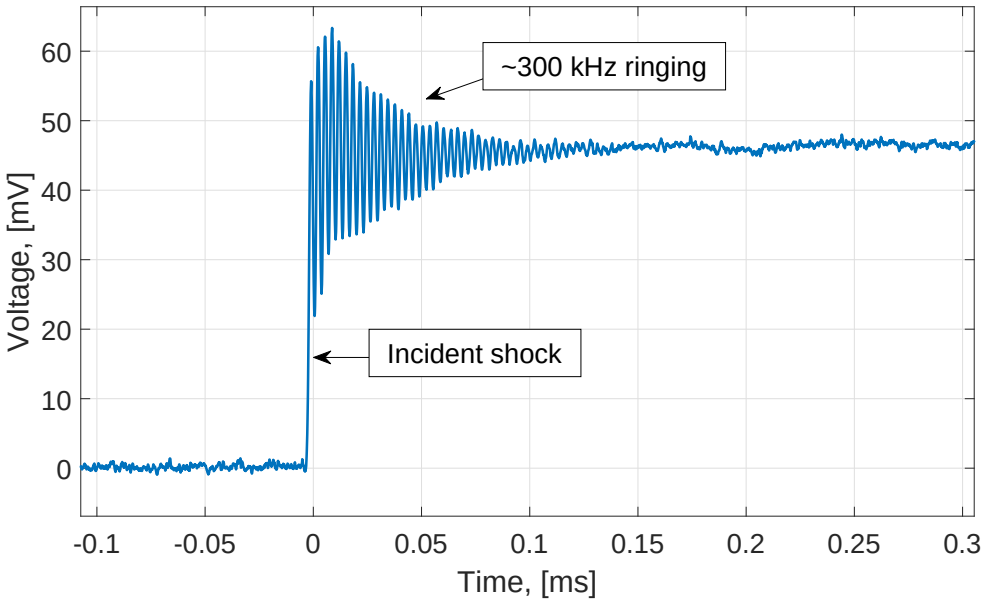

Figure 2.14.: Sample Kulite trace; $p_{driven} = 2.81$ mbar, $p_{driver} = 37.0$ mbar.

linearity, hysteresis, and repeatability is quoted as ± 0.1% of the full-scale output, or 1.0 mbar. The sensor resolution is quoted as infinitesimal.

The Kulite sensors used in this work have a strong resonance at around 300 kHz, as shown in Figure 2.14. The transient response to the shock passage dies off fairly quickly, but the ringing continues for a significant portion of the response. The ringing can be averaged to compute the pressure step due to the shock, as done by Berridge [3]. This will be discussed further in Section 3.1.

2.5 Data Acquisition

Data were acquired with Tektronix MDO3014 oscilloscopes. The oscilloscopes have a maximum sample rate of 2.5 GS/s and a vertical resolution of 8 bits. Data were acquired using the Hi-Res mode on the oscilloscopes. This mode averages data at the highest sample rate of the digitizer to record a waveform at the desired sample

frequency. This results in reduced noise and an effective vertical resolution of about 11 bits. PCB132 sensors were sampled at frequencies in excess of 10 MHz, PCB606B01 sensors were generally sampled at frequencies in excess of 100 kHz, and Kulite sensors were generally sampled at frequencies in excess of 1 MHz. All signals were DC coupled.

Two models of signal conditioners were used with PCB sensors: PCB model 482C05 and PCB model 482A22. The model 482C05 is a newer version of model 482A22. There are no noticeable functional differences between the two signal conditioners. Both devices are four-channel signal conditioners used with PCB manufactured ICP® piezoelectric sensors. The signal conditioners output ± 10 V and have a high frequency response greater than 1 MHz. Signals from Kulite sensors were amplified 100 times with INA103 amplifier chips. The amplifier chips were used with amplifier boxes custom-built at Purdue. The amplifier boxes also have an AC output with a total gain of 10,000 times. Only the DC output was used for the current work.

3. DATA PROCESSING

The primary goal of this work is to develop a better understanding of PCB132 sensors and high-frequency pressure sensors relevant to hypersonic boundary-layer transition in general. Calibration efforts of PCB132 sensors will be discussed in Section 3.4, but difficulties associated with these efforts should be noted here. Since the transfer function of the PCB132 sensor is unknown, much of this work is approximate. Because of this, the accuracy of the calibration methods presented here are unclear. A complete understanding of the pressure-input signal generated by the P3IST is also not available, and so uncertainties exist in any frequency analysis of the sensor response.

3.1 Kulite Processing

Kulite pressure sensors were used as reference sensors to measure the static-pressure step across the incident shock in the P3IST. Here, static-pressure step refers to the change in static pressure in the driven section of the P3IST due to the arrival of the incident shock wave. As discussed previously, Kulite sensors were the only type of reference sensor used to measure the static-pressure step.

Static pressure steps are measured in the P3IST by averaging the Kulite trace between 0.25–0.75 ms after incident shock arrival. The averaging interval was chosen such that the Kulite signal would approach steady-state before an average was computed. Kulite sensors show oscillations due to the sensor-diaphragm resonance after passage of the shock. These oscillations can be averaged to compute the step level if the sensor rise has completed. Rotea et al. showed that a Kulite XCQ-062-25A pressure sensor had a rise-time close to 0.1 ms [51]. Since similar Kulite sensors were used in this work, it is thought that the rise-time should be close to 0.1 ms. Starting

the averaging interval at 0.25 ms after shock passage ensures the voltage rise of the Kulite sensor has completed before averaging the trace.

Figure 3.1 shows a Kulite trace for a typical run. The raw signal shows oscillations up until around 0.8 ms after the incident shock passes the sensor. The signal low-pass filtered at 300 kHz shows the oscillations are largely at higher frequencies, likely due to the Kulite diaphragm resonance. The filtered trace appears to settle quickly after the incident shock passage. Setting the start of the averaging interval at 0.25 ms ensures the measured step will not be influenced by the rise time.

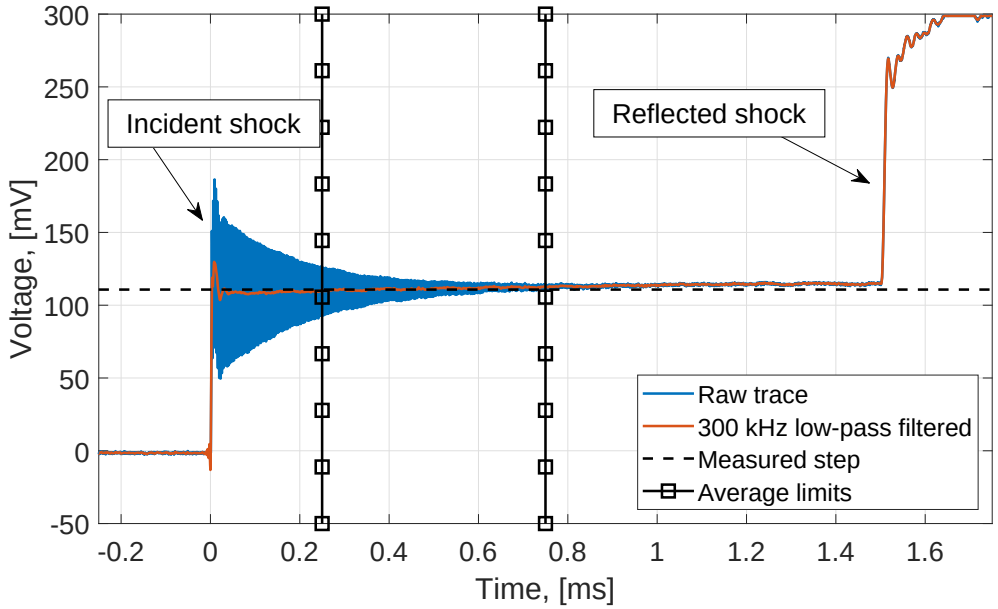

Figure 3.1.: Sample voltage Kulite trace; p_{driven} = 9.72 mbar, p_{driver} = 75.23 mbar.

3.2 Mach Number Measurement

The velocity of the incident shock wave was measured by comparing the arrival times at two statically-mounted PCB132 sensors. The distance between the sensors was divided by the difference in arrival times to calculate the incident shock speed.

The incident-shock Mach number was computed by dividing the measured shock speed by the speed of sound.

Temperature was not generally measured in the P3IST. Room temperature was controlled by climate control in the room. Some variation in the room temperature was common. The maximum temperature variation is estimated as between 293–300 K. This produces a variation in Mach number of 1.2%. Based on typical climate-control settings in the room, the gas temperature in the P3IST was assumed to be 295 K.

3.3 Calculation of Stagnation-Pressure Step

The pressure step experienced by pitot-mounted PCB132 sensors was calculated from the measured shock speed and the measured static-pressure step using perfect gas and normal shock relations. The stagnation-pressure step was calculated this way because pitot-mode Kulite mounting was not always possible with a pitot-mounted PCB132 sensor in the P3IST. The static-pressure step across the incident shock was measured by Kulite sensors, as discussed in Section 3.1, and the shock speed was measured by statically-mounted PCB132 sensors, as discussed in Section 3.2. The density ratio across the shock wave can be found using Equation 3.1, where γ is the ratio of specific heats, and the subscript 1 refers to the region downstream of the shock and subscript 2 refers to the region immediately upstream of the shock. The subscripts also refer to conditions shown in Figure 1.1.

$$\rho_2/\rho_1 = \frac{1 + \frac{\gamma+1}{\gamma-1}\frac{p_2}{p_1}}{\frac{\gamma+1}{\gamma-1} + \frac{p_2}{p_1}} \tag{3.1}$$

The density ratio and measured shock velocity, u_s, can be used to find the velocity upstream of the shock, u_2, with Equation 3.2.

$$u_2 = u_s(1 - \rho_1/\rho_2) \tag{3.2}$$

The temperature upstream of the shock can be found using perfect gas relations across the incident shock, in a similar manner to the density. Using the upstream temperature (Equation 1.3), the speed of sound and Mach number of the gas upstream of the shock can be calculated. If the upstream Mach number is subsonic, the total pressure can be calculated with Equation 3.3, where $p_{0,2}$ is the total pressure in the flow upstream of the shock.

$$p_{0,2} = p_2\big(1 + \frac{\gamma - 1}{2} {M_2}^2\big)^{\gamma/(\gamma-1)} \tag{3.3}$$

If the flow is instead supersonic upstream of the shock, a bow shock will form in front of the probe. The pitot pressure in supersonic flow including the influence of the bow shock can be found using Equation 3.4.

$$p_{t,2} = p_2 \frac{\big(\frac{\gamma+1}{2} {M_2}^2\big)^{\gamma/(\gamma-1)}}{\big(\frac{2\gamma}{\gamma+1} {M_2}^2 - \frac{\gamma-1}{\gamma+1}\big)^{1/(\gamma-1)}} \tag{3.4}$$

Since the PCB132 measures the differential pressure across the shock, the pressure step is given in Equation 3.5 as net pressure increase due to the shock.

$$p_{step} = p_{0,2} - p_1 \tag{3.5}$$

The derivation of equations used for calculating the stagnation-pressure step can be found in references [20] and [18].

3.4 PCB132 Sensor Calibration

As mentioned previously, accurate calibrations of PCB132 sensors are difficult to obtain due to the dearth of knowledge of the sensor itself. The transfer function of the PCB132 sensor is unknown. Additionally, the exact shape of the shock-wave input generated in the P3IST is unknown. Well-understood surface-pressure sensors with a higher frequency response than PCB132 sensors are not currently available, making quantification of the pressure-input signal difficult.

Two methods of determining the sensitivity of PCB132 sensors are presented here: peak correlation and frequency response approximation. The peak-correlation method was previously used by Berridge to generate linear calibrations of PCB132 sensors by correlating the voltage peak of the PCB132 sensor response with the measured pressure step. An example of two PCB132 sensor responses, normalized by their respective voltage peaks, is shown in Figure 3.2. The voltage rises in response to the shock passage and rolls off quickly due to the high-pass filter in the sensor. This results in a single, narrow peak in the sensor signal which can be correlated with the measured pressure step. The peak-correlation method was used for both statically-mounted and pitot-mounted sensors to generate linear calibrations. Differences between responses obtained from PCB132 sensors in pitot and static-modes are evident from Figure 3.2, and will be discussed in Section 6.1.

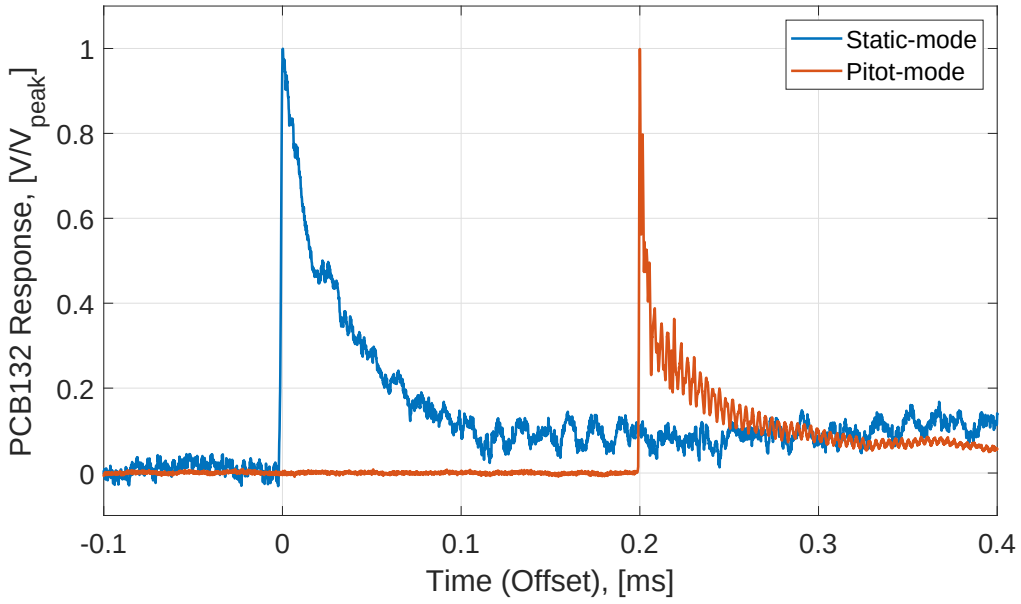

Figure 3.2.: PCB132 responses normalized by peak height for sensors statically-mounted (SN 7516) and pitot-mounted (SN 8247); $p_{driven} = 1.34$ mbar, $p_{driver} = 65.04$ mbar. Time axis artificially offset to show detail.

A second method of determining the sensor sensitivity uses the response obtained from pitot-mounted PCB132 sensors tested in the P3IST. This method assumes the pitot-response is approximately a step response of the PCB132 sensor, and uses it to calculate the approximate frequency response. This method also assumes the pressure-input signal to the PCB132 sensor is a perfect step input, which is untrue. Only pitot-mounted sensors are used with this method due to the faster rise time of the pressure-input signal. The effects of the pressure-input rise time will be discussed further in Section 6.2. Because uncertainties exist in the pressure-input signal, uncertainties are introduced into the calculation of the approximate frequency response. This method will be discussed further in Section 3.4.2.

3.4.1 PCB132 Static-Mode Calibrations

Previous calibrations of PCB132 sensors were obtained with the P3IST by correlating the peak PCB132 voltage to the static-pressure step measured with Kulites. Since the transfer function of the PCB132 sensor is unknown, it is unclear how accurate this calibration method is. In order to quickly perform calibrations, the shock response must be quickly and reliably located in the voltage trace. Berridge designed a shock detection method to locate the shock arrival in a PCB132 trace acquired in the P3IST. Berridge's method measures the width of voltage peaks in the PCB132 signal with a criterion defined as the full width at half-maximum (FWHM). An example of a FWHM measurement of a PCB132 response generated with the P3IST is shown in Figure 3.3. To detect a shock, the minimum FWHM and minimum peak height are specified. These values are set based on run conditions, and are changed by the operator if the trace is not processed properly. The first peak that exceeds the specified peak height and FWHM is reported as the incident shock. Berridge showed that this method successfully identified the incident shock in most PCB132 traces.

To improve shock detection, noise was reduced with a moving-average filter. Vibration can contaminate data acquired with PCB132 sensors in the P3IST, and must

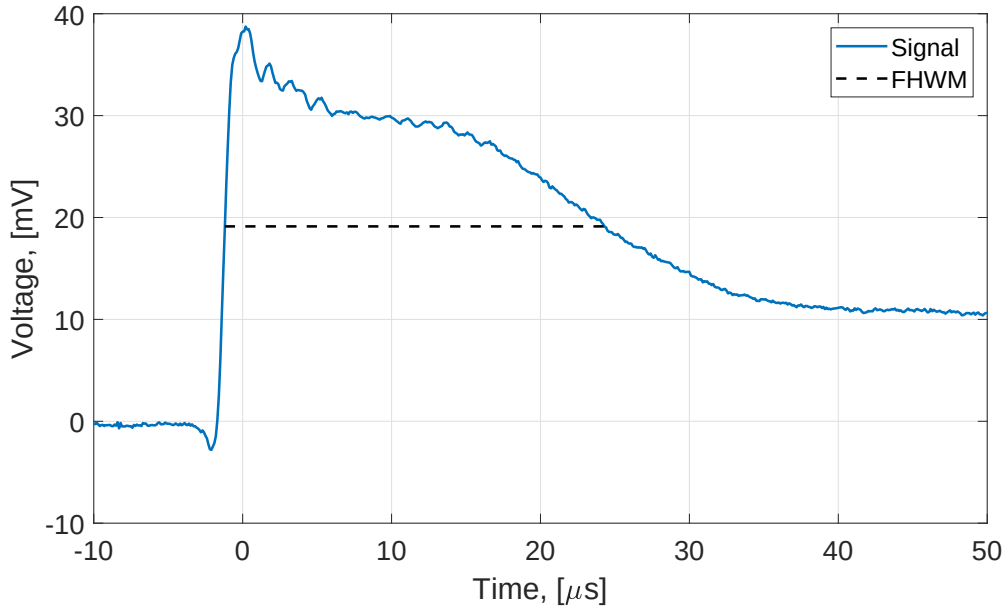

Figure 3.3.: PCB132 trace FWHM measurement example; $p_{driven} = 3.00$ mbar, $p_{driver} = 568.0$ mbar.

be reduced to reliably measure the voltage peak. Measurement of structural vibration of the P3IST will be discussed further in Chapter 4. Berridge applied the filter in two stages, first with a down-sampling moving-average filter, and then with a typical moving-average filter. The down-sampling moving-average filter is a filter where each element in the output is the average of n elements of the input. Each input point is only included in an average once, such that the output vector is smaller than the input vector by a factor of the averaging interval. This is described in Equation 3.6, where y is the output signal, v is the input signal, and n is the averaging interval.

$$y_j = \frac{1}{n} \sum_{i=(j-1)n+1}^{jn} v_i \tag{3.6}$$

To detect a shock, the down-sampling filter was applied to the entire trace. The FWHM criteria was applied and a shock was located in the trace. A window around the shock location in the original trace was then filtered with a typical moving-

average filter and the shock was found again with the FWHM criteria. In this way, computational time was reduced by not having to apply the typical moving-average filter to the entire data trace.

In the current work, using a typical filter on an entire data trace does not significantly increase computational time. The down-sampling filter method is still used, but is no longer strictly necessary, due to improved computer performance. The shock detection algorithm is used for reliable location of the incident shock in PCB132 traces. In the current work, a different filter is used in place of the typical moving-average to locate the shock, as will be discussed presently.

New Filtering Techniques

Properly filtering PCB132 data is important for shock detection and peak-amplitude measurements. Depending on the run and mounting conditions, significant amounts of pre-shock vibration may be present in the PCB132 signal. Filtering PCB132 traces is not trivial due to the variation of responses across run conditions and sensors. Figure 3.4 shows PSDs computed from pre-shock noise measured by four PCB132 sensors during the same run. Sensor positions are shown as x/d, or the axial location from the diaphragm normalized by the shock-tube ID. PSDs were computed from data sampled at 10 MHz using Welch's method, implemented with the Matlab function `pwelch` with a window size of 5000 points. Figures 3.4(B) and 3.4(C) show significant frequency content at lower frequencies, close to 30 kHz, while other PSDs show more power at higher frequencies. Some common peaks are evident between the different sensors, but most of the frequency content is fairly dispersed. The variability in PCB132 frequency content indicates a single filter may not work well for all PCB132 traces.

To account for the variability in run conditions and sensor behavior, Berridge allowed the user to vary filter parameters including filter frequency and averaging intervals. Allowing user definition of these parameters for amplitude measurement could

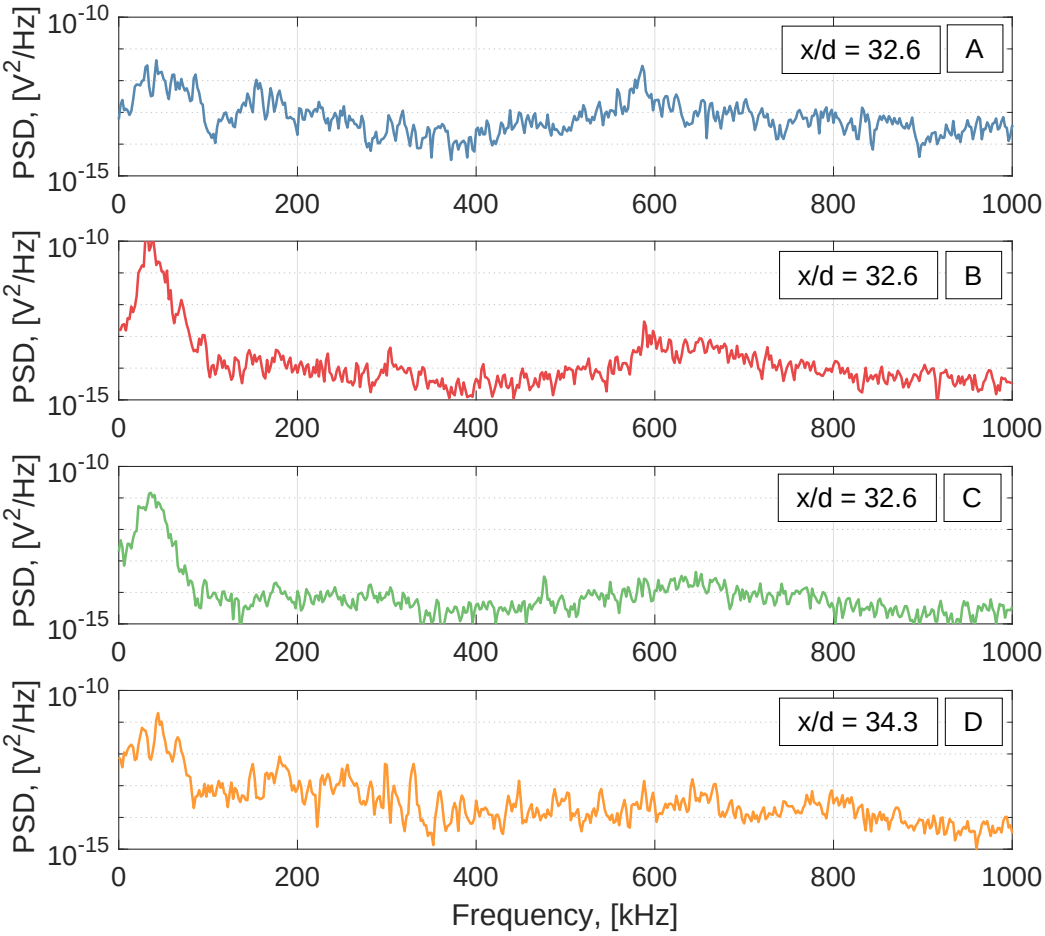

Figure 3.4.: PSD computed from 150 μs of pre-shock noise measured by 4 PCB132 sensors in P3IST; 2 kHz frequency resolution; $p_{driven} = 0.321$ mbar, $p_{driver} = 754.83$ mbar.

introduce inconsistencies in data processing. This is shown in Figure 3.5 where the same data PCB132 data is processed with moving-average filters of varying averaging-window sizes. Varying window sizes changes the calibration significantly, while all data sets have high R^2 values. With only subjective criteria to determine filter settings, significantly different calibrations could easily be obtained from the same data

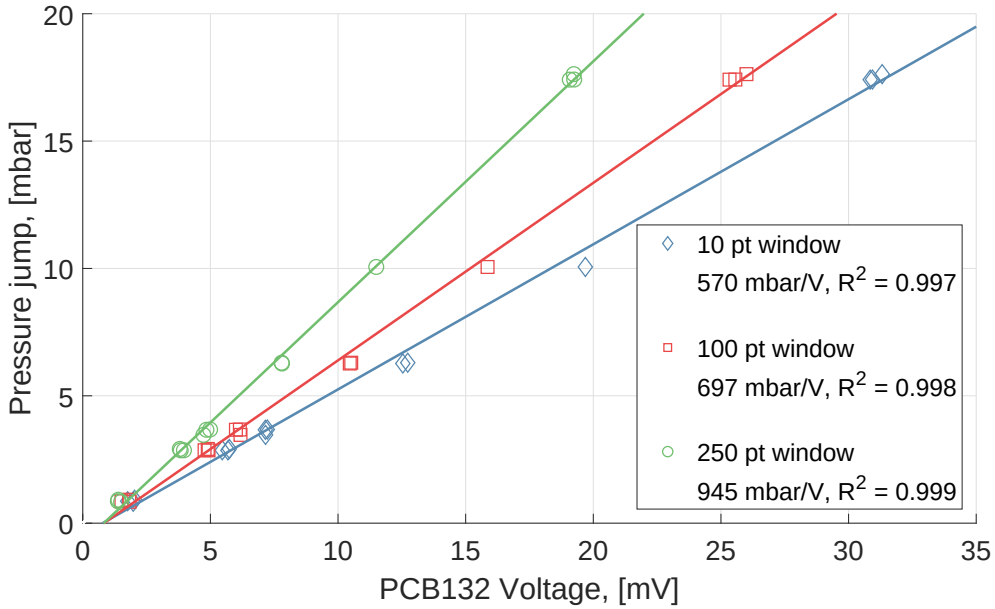

Figure 3.5.: PCB132 calibrations produced with different moving-average filter window sizes; PCB132 sampled at 25 MS/s.

set. In order to reduce uncertainty in peak measurement, filter settings should be automatically determined.

An improved method of filtering PCB132 data was desired to improve consistency in data processing. Since the sensor response to shock passage is aperiodic, the shock response will act somewhat like an impulse input to a filter. Because of this, there is no simple way to attenuate only the noise, and any filter will change the peak somewhat.

Efforts were made to remove noise using a noise-prediction filter. These efforts were largely unsuccessful, but are discussed briefly for the sake of completeness. The noise-prediction filter was an application of a Wiener optimum linear filter. The method works by using the Wiener-Hopf equations to design a filter that would predict the pre-shock noise a short time ahead of the current value. This predicted trace could then be subtracted in the time domain to remove the influence of vibration from the

voltage amplitude measurement [52]. In practice, this filter worked well for some traces that showed strongly periodic noise components. Issues arose when the filter was applied to traces with more random vibration. Often, the noise prediction filter would add more noise to the trace, adding more uncertainty to any measurements. Ultimately, this approach was not used due to the increased uncertainty.

A finite impulse response (FIR) low-pass filter was selected as the basis for the new design. This is similar to the previous filtering approach since a moving-average filter is a type of FIR filter. To evaluate the filter's performance, a known signal was filtered. Since the application of a filter is a convolution process in the time domain, a clean signal can be treated separately from any noise components if the signal and noise components are uncorrelated. This analysis enables direct comparison of the signal attenuation.

Three artificial signals were created based on representative PCB132 traces, shown in Figure 3.6. The representative traces were chosen so that there was variation in signal-to-noise ratio (SNR) and response shape. The artificial signals are constructed from a combination of undamped and damped sine waves, roughly matching the peak magnitude and rise time seen in the data. A damped sine wave is a sinusoidal function multiplied by an exponential decay such that it approaches zero as time increases. This assumes the noise is constant across the response.

An FIR filter was designed using the Parks-McClellan optimal filter-design method. The transition region was 100 kHz wide with a pass-band ripple of 0.2 dB and a stop-band attenuation of 100 dB. The frequency response of a sample filter with similar specifications is shown in Figure 3.7. The transition region was chosen to provide a gradual change between the pass and stop bands in order to minimize the filter order. If the transition region were expanded, a higher-order filter would be required, which could significantly increase computation time. The constructed signals in Figure 3.6 were passed through this filter for varying stop-band frequencies. The difference in the peak amplitude of the artificial signal and the filtered signal is shown in Figure 3.8. This is compared to the 1 MHz moving-average filter used previously.

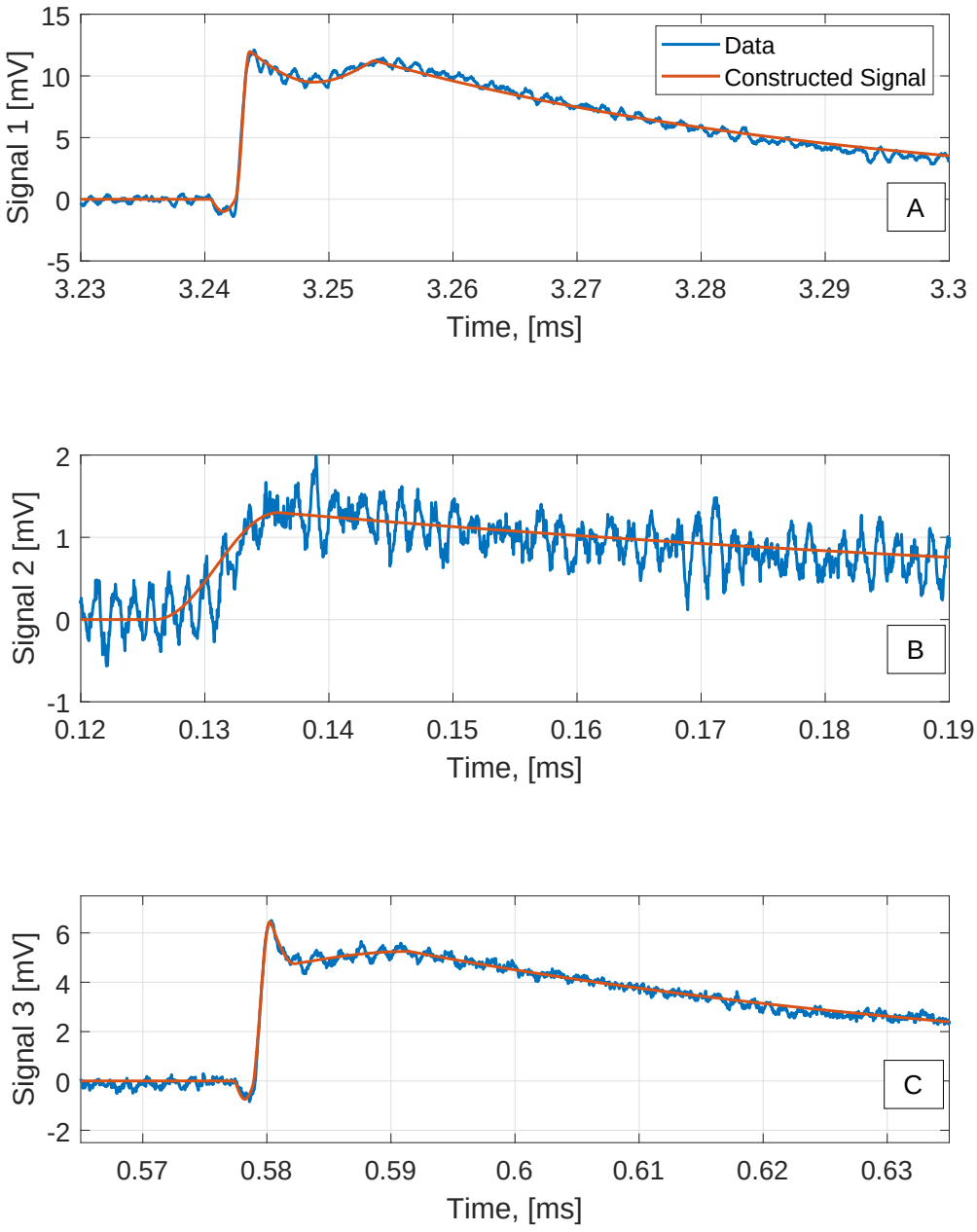

Figure 3.6.: Artificial constructed signals based on actual PCB132 signals.

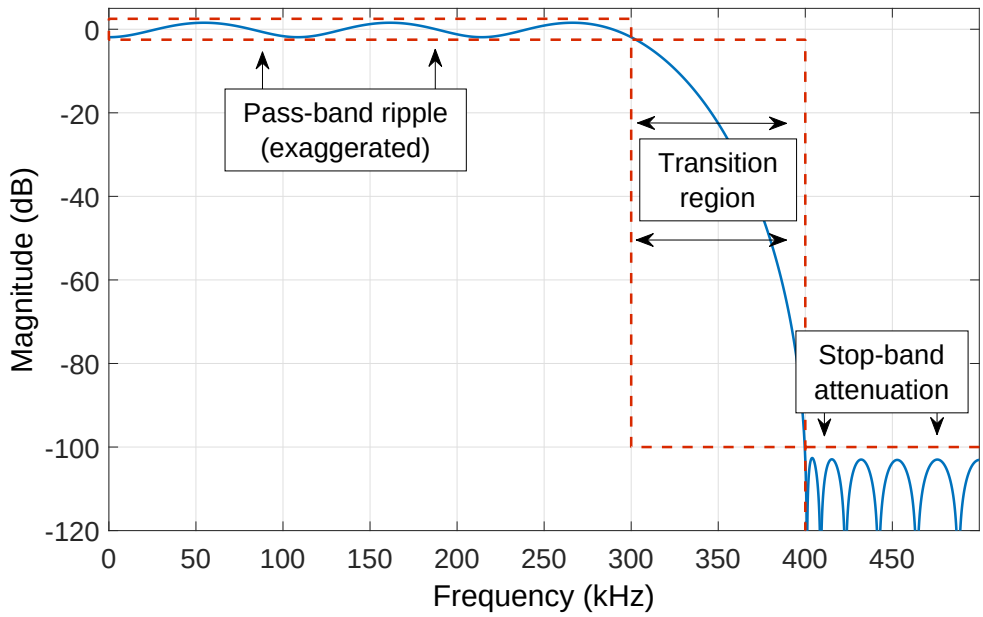

Figure 3.7.: Sample low-pass FIR filter with a stop-band frequency of 400 kHz. Pass-band ripple is increased to 5 dB to show clearly.

Signal 1 shows some amplification for higher stop-band frequencies. This is likely due to a ringing in the filter caused by the steep slope of the signal. The difference in peaks is around 1% for stop-band frequencies near 300 kHz, and at frequencies less than 300 kHz, the filter attenuates the peak as expected. The amplification at higher filter frequencies indicates that the filter parameters may need to be fine tuned to achieve the lowest difference from the signal peak. Signal 2 shows a much lower difference between actual and filtered peaks than signal 1. This is likely because Signal 2 has a lower rise-time and wider peak. Signal 3 shows much more attenuation than either signal 1 or 2. This is likely because the peak is so narrow. Using a stop-band frequency of 600 kHz produces an attenuation of around 1%.

It is desirable to set the filter stop-band frequency as low as possible to remove the most noise, but not change the magnitude of the voltage peak appreciably. From Figure 3.8, a stop-band frequency of around 300 kHz produces a peak change of around

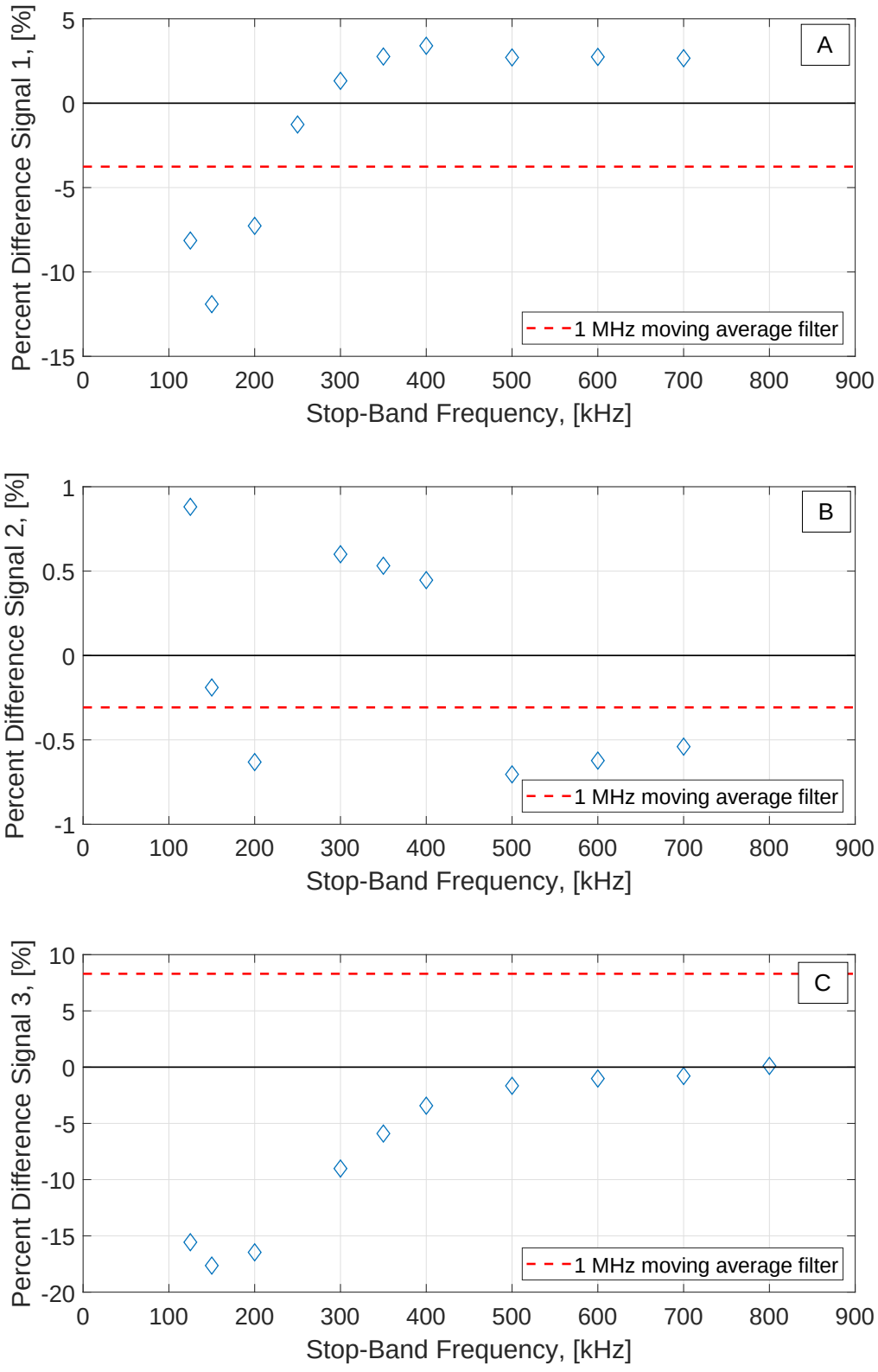

Figure 3.8.: Percent difference between peaks in artificial signals before and after passing through the FIR low-pass filter.

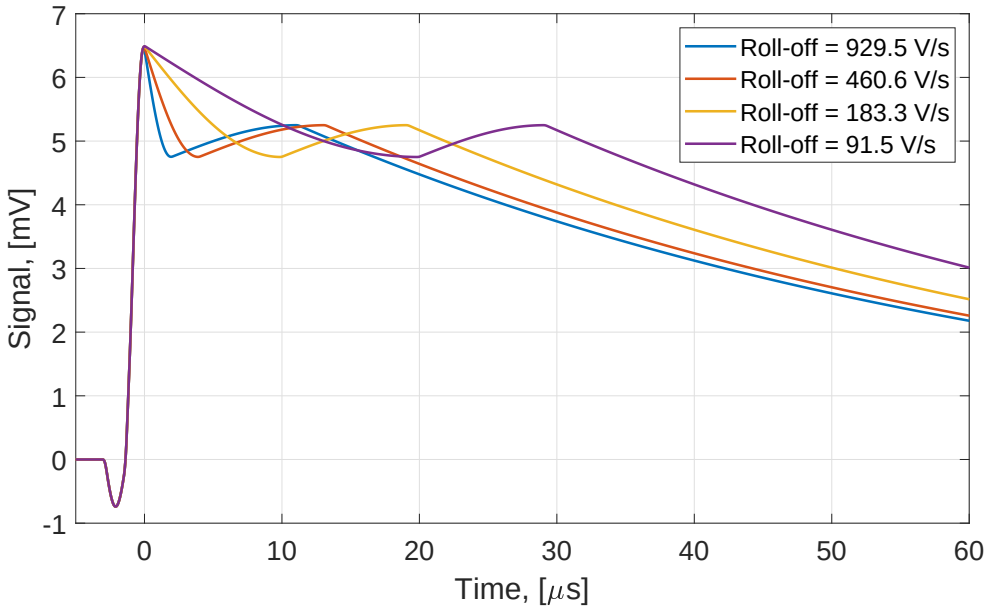

Figure 3.9.: Different roll-offs for artificial signal

1% in Signal 1. Signal 2 does not change by more than 1% when passed through the filter for any of the frequencies tested. Signal 3 is only within 1% difference between the peaks for stop-band frequencies higher than 600 kHz. If a metric of the signal characteristic was developed, it could be possible to adjust the filter frequency for each trace.

A correlation between the PCB132 response shape and the appropriate stop-band frequency was developed to systematically modify the filter. The response shape was quantified by a measurement of the roll-off immediately after the peak. To determine a relationship, Signal 3 was modified by compressing or expanding the peak, as shown in Figure 3.9. This would change the peak width and roll-off. The roll-off was calculated as the average slope over the roughly linear portion immediately after the peak. The low-pass FIR filter was then applied to the trace and the stop-band frequency modulated until peak was attenuated or amplified by no more than one percent.

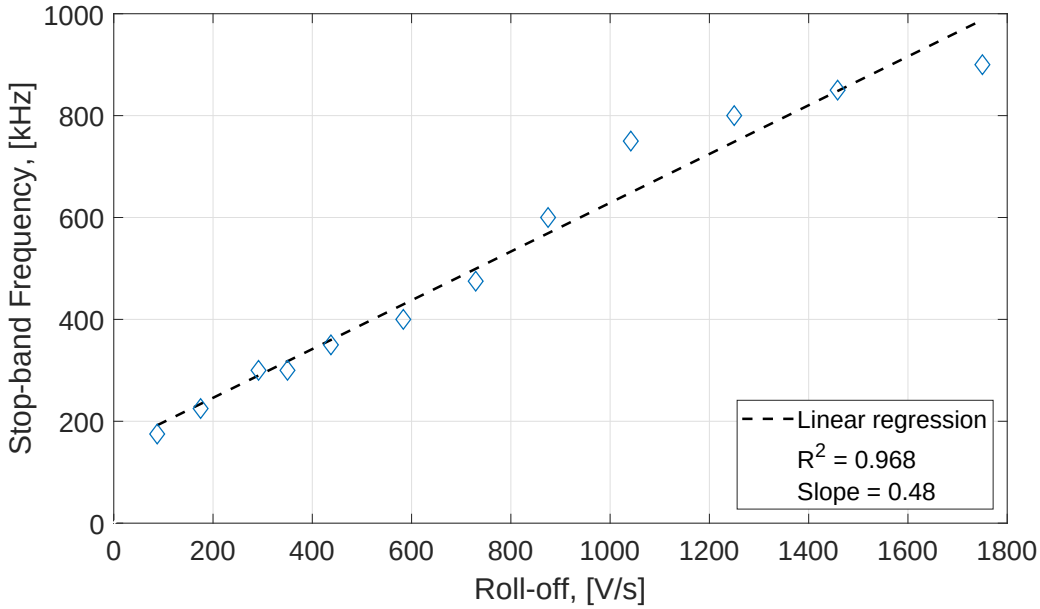

Figure 3.10.: Stop-band frequency that produces less than 1% change in peak height of artificial signal, as a function of signal roll-off.

The selected stop-band frequency is plotted against the roll-off in Figure 3.10. The appropriate stop-band frequency increases with roll-off approximately linearly. A linear regression can be used to calculate the filter frequency for a given roll-off slope. This results in the simple correlation shown in Equation 3.7, where f_{stop} is the stop-band frequency in kHz and s_{off} is the roll-off in V/s.

$$f_{stop} = 0.48 s_{off} + 150 \tag{3.7}$$

Applying this relation to actual data requires a calculation of the roll-off slope. Since the immediate roll-off can be much steeper than the roll-off later in the trace, it is important to measure the roll-off after the peak in as few samples as possible. However, the roll-off measurement will be affected by the presence of noise, so must be averaged over a time after the peak. Before the roll-off is calculated, the data are filtered by a low-pass filter, with a pass-band frequency of 1 MHz and a stop-band frequency of 1.5 MHz. This is intended to only reduce electronic noise, making roll-off

calculation more reliable. The roll-off is then computed from 3 μs of data after the voltage peak as the slope of a linear regression through the points. The 3 μs data length was chosen based on qualitative comparison of actual PCB132 responses.

When implementing the filter, it was found that processing would take too long for low filter frequencies. Therefore, a minimum pass-band limit of 300 kHz was imposed. Figure 3.11 shows the results of this adjusting filter design applied to the three signals used in the previous analysis. From visual inspection, the filter appears to appropriately filter the data. The largest difference between the raw and filtered signals is in Figure 3.11(C), at around 6% attenuation. This is much larger than the 1% difference used with the artificial signals, but is still reasonably low. The filter is not perfect for every PCB132 trace, but provides a more consistent approach to filtering than previous work.

It should be noted that the uncertainties associated with the sensor transfer function or pressure-input signal were not reduced by this improved data processing method. The new data processing method automates filter design for the processing of PCB132 data. It does not address the fact that neither the sensor transfer function or pressure-input signal are known. As previously discussed, a well-understood reference sensor with a higher-frequency response than the PCB132 sensor is not available, making characterization of the exact pressure-input signal difficult. Because of this, it is still unclear how accurate this calibration method is.

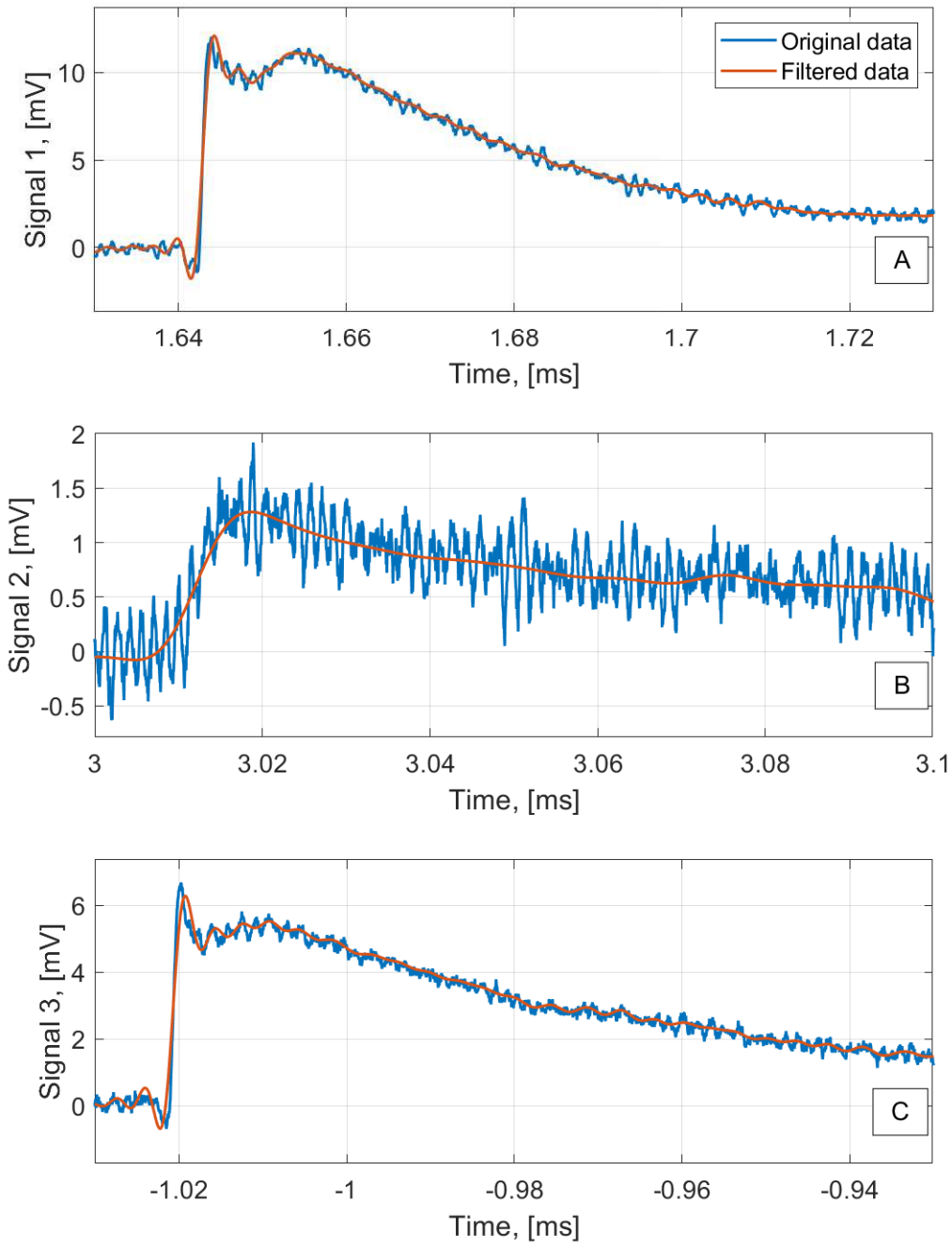

Figure 3.11.: PCB132 data traces filtered with adjusting FIR low-pass filter.

3.4.2 PCB132 Frequency Domain Processing

The frequency response of a system is the ratio of the output spectrum to the input spectrum. The frequency response of a sensor is of interest since it can be used to obtain the calibrated amplitude and phase at different input frequencies. The frequency response of a system can be computed if its step response is known. The approximate step response of a PCB132 sensor was experimentally obtained through testing in the P3IST by approximating the pressure step across the shock as a step input. As mentioned previously, this is only an approximation because it is impossible to generate a perfect pressure-step input with the P3IST. The actual shape of the pressure-input signal generated with the P3IST is unknown. As such, frequency responses calculated this way assume an ideal input signal, resulting in some amount of unquantified error.

Frequency Response Calculation

The frequency response of a system can be computed by dividing the frequency content of the step response by the frequency content of a step input. The Heaviside step function, $\theta(t)$, is defined in Equation 3.8 as a function of time, t. The frequency content of a step input is given in equation 3.9 as the Fourier transform of the Heaviside step function, and is a function of the frequency, f, and the Dirac delta function, δ. The Dirac delta function is the impulse function, and is defined as 0 for frequency not equal to 0. Because of this, the Dirac delta function portion of Equation 3.9 is excluded from implementation of the step function frequency content.

$$\theta(t) = \begin{cases} 0 & t < 0, \\ 1/2 & t = 0, \\ 1 & t > 0 \end{cases} \tag{3.8}$$

$$\mathcal{F}\{\theta(t)\} = \frac{1}{2\pi i f} + \frac{\delta(f)}{2} \tag{3.9}$$

An approximate frequency response can be calculated from an approximate step response by assuming an ideal input signal. For PCB132 responses obtained in the P3IST, the input is not an ideal step signal, and so errors are introduced by assuming this. This assumption is made because independent measurements of the input signal generated in the P3IST are not currently possible. To find the frequency content of the PCB132 response, the discrete Fourier transform is computed. All discrete Fourier transforms of PCB132 data were computed with the fast Fourier transform algorithm implemented with the Matlab function `fft`. This is then divided by the frequency content of the ideal-step signal.

Pitot-Mode Response Shapes

The frequency response was computed only for PCB132 sensors mounted in pitot mode. This is because PCB132 sensors experience a faster input-rise time when mounted in pitot mode in the P3IST. The effects of input rise time and sensor-mounting orientation on the PCB132 response will be discussed further in Section 6.2.

Before computing the frequency content of the step response, the time trace must be properly truncated and windowed. To compute the frequency response, only the region due to the incident shock can be used. So if other flow features are observed, sections of the trace must be removed.

Figure 3.12 shows some examples of PCB132 pitot traces with different reasons for signal contamination. These traces result from different mounting techniques used in the P3IST. Figure 3.12(A) is from a wall-mounted pitot probe, while Figures 3.12(B) and 3.12(C) are from end-plate-mounted pitot probes. Data shown in Figure 3.12(B) was measured from a PCB132 mounted in a longer pitot probe than the probe used for Figure 3.12(C).

Figure 3.12(A) shows an increase in noise after 200 μs not usually observed in PCB132 sensor step responses. Based on other experimental results [2], the PCB132

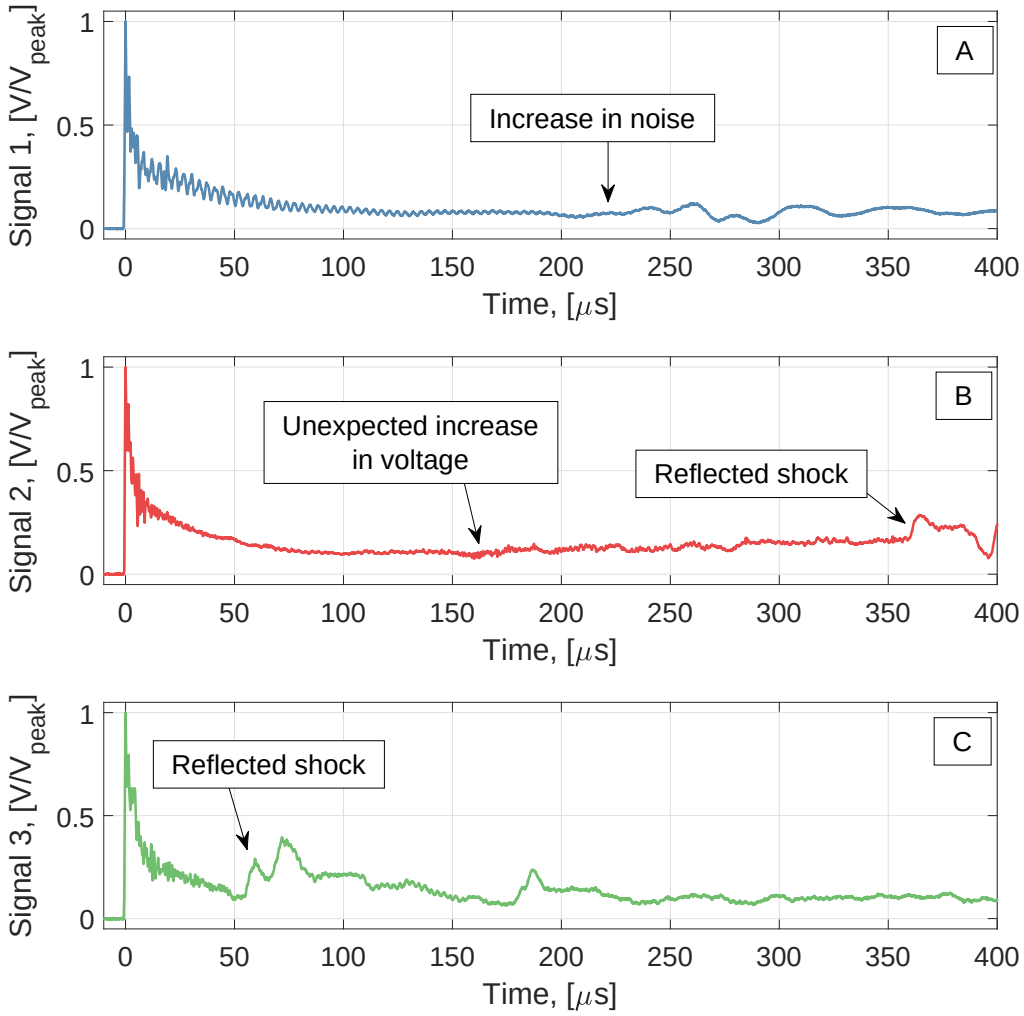

Figure 3.12.: Representative pitot-responses for three PCB132 sensors.

response is expected to roll off to zero amplitude, and not show low-frequency oscillations long after shock passage. Based on observations of PCB132 sensors in the P3IST, the increase in noise is likely due to vibration contaminating the signal.

Figure 3.12(B) shows an increase in voltage at around 150 μs, which could be due to the arrival of the contact surface. Figure 3.12(B) also shows a clear peak near 350

μs, likely due to the shock reflecting off the end-plate of the P3IST. Figure 3.12(C) shows a similar peak, but much sooner after incident shock arrival, at around 60 μs. This peak is also likely a reflected shock from the end-plate, but occurs much sooner because the pitot-probe in Figure 3.12(C) was mounted much closer to the end-plate. The predicted arrival time of the reflected shock at the pitot probe for the trace shown in Figure 3.12(C) is 79 μs, supporting the conclusion that the increase in voltage is due to the reflected shock.

The three mounting techniques used to measure data shown in Figure 3.12 may explain the different reasons for signal contamination. Figure 3.12(A) is from a PCB132 mounted in a wall-mounted pitot probe, which could be why it is contaminated by vibration. Based on observations of data taken with the P3IST, wall-mounted PCB132 sensors generally measure higher vibration than those mounted in the end-plate. Figure 3.12(B) is from a PCB132 mounted in a long pitot-probe in the end-plate. The reflected shock is visible, but occurs late in the trace. Figure 3.12(C) is from a PCB132 mounted in a much shorter pitot-probe in the end-plate, and so the reflected shock passes the sensor sooner.

The length of usable PCB132 data is also significantly influenced by run conditions. The clearest example is that for runs with faster shocks the useful length of PCB132 response will be shorter. If the incident shock is faster, the reflected shock will also be faster, contaminating the flow sooner and shortening the usable PCB132 data. Additionally, for runs with higher vibration, vibration contamination may be more pronounced. Because of this, it is necessary to individually select the data window for each trace. Data windows are kept consistent when comparing two frequency responses.

Windowing

It is necessary to exclude data taken before the incident shock arrives and after the signal becomes contaminated. Truncating the time trace immediately before

the signal becomes contaminated generally produces a non-zero end-point, which adds artificial ringing to the frequency domain. These oscillations can be reduced by applying certain window functions to the time-domain signal. Any window function will affect the frequency domain values somewhat. Figure 3.13 shows a comparison of Hamming and Hann windows. Figure 3.13 also shows half versions of these windows, or the same window function starting from the midpoint. Since the PCB132 step response is non-symmetric, Hann and Hamming windows will significantly change the shape of the time trace. A half-Hann or half-Hamming window will change the time trace shape much less, possibly modifying the frequency domain values less.

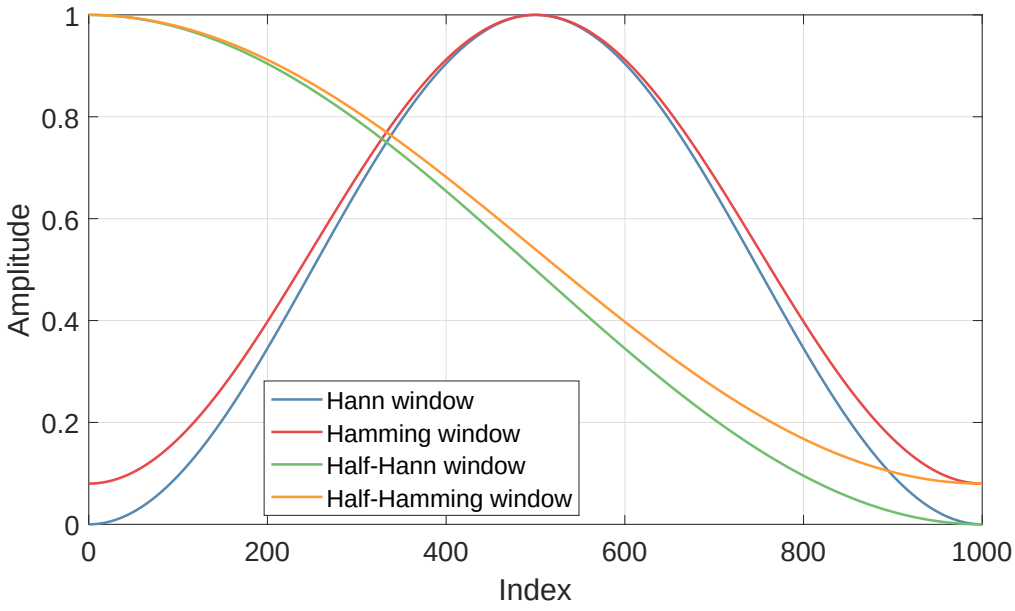

Figure 3.13.: Comparison of different window types.

Figure 3.14 shows a PCB132 pitot-response trace scaled with different window functions. The PCB132 response was selected to begin immediately before the shock arrival and end 50 μs later, excluding any contaminated portions of the signal. As expected, the Hann and Hamming windows change the shape of the time trace significantly. The half-Hann and half-Hamming windows both change the time domain signal less, while keeping the end-points close to zero.

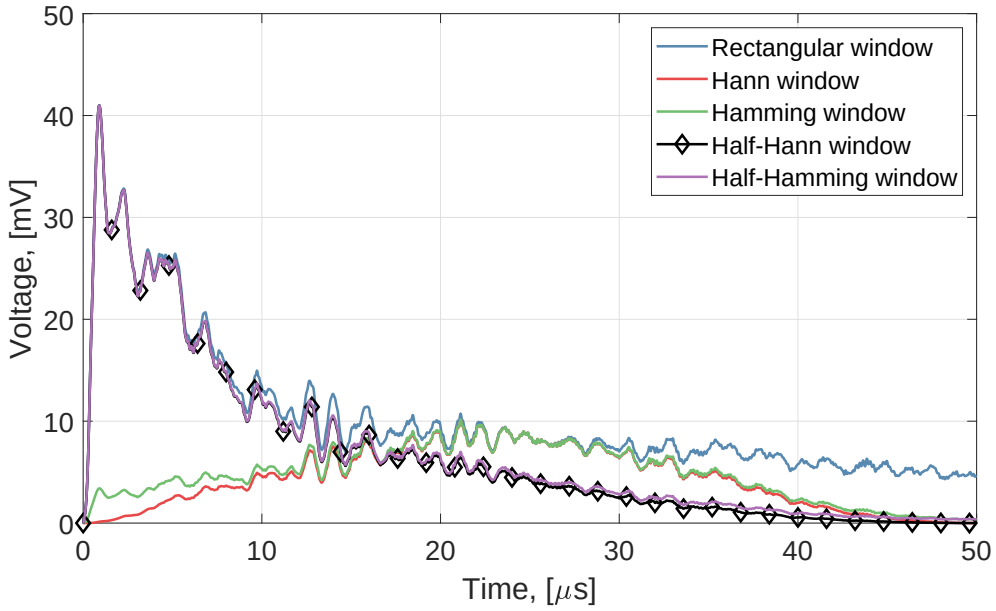

(a) Time Domain

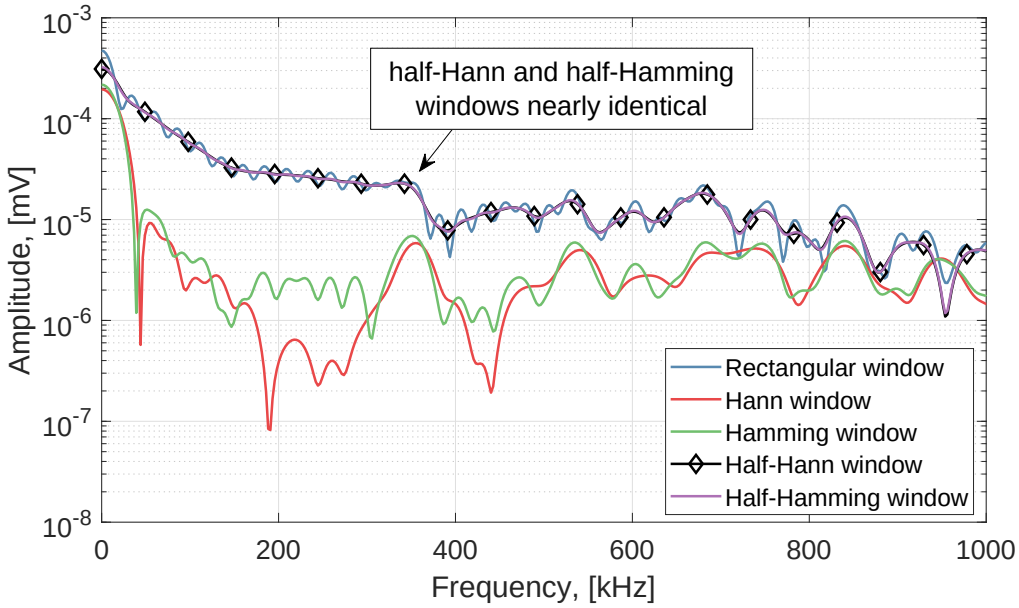

(b) Frequency Domain

Figure 3.14.: Comparison of windows used with pitot-response of SN 6994, time trace low-pass filtered at 3 MHz; $p_{driven} = 2.81$ mbar, $p_{driver} = 37.02$ mbar.

Figure 3.14(b) shows that the frequency content of the rectangular window has apparent ringing throughout, as expected due to the non-zero end-point. The data windowed with half-Hann and half-Hamming windows have nearly identical frequency content, and agree reasonably well with the rectangular window. The data windowed with the Hann and Hamming windows have dramatically different frequency content from the data windowed with the rectangular, half-Hann, or half-Hamming windows. The half-Hann and half-Hamming windows appear to produce the best results for this application, with minimal ringing and fair agreement with the rectangular window. A half-Hann window was used for computing all PCB132 frequency responses.

Effect of Data Length on Frequency Response

As mentioned previously, the frequency response can be calculated by dividing the frequency content by the step input signal, assuming an ideal input signal. When calculating the frequency response, data can be zero-padded to increase the resolution in the frequency domain. The frequency resolution is the spacing of points in the frequency domain and is changed based on the sampling frequency and the number of points in the time domain signal. While the frequency resolution can easily be kept consistent, information is still lost by not using the entire PCB132 step response to calculate the frequency response. The effect of truncating a PCB132 trace on the calculated frequency response can be evaluated by comparing the results using different amounts of truncation. Figure 3.15(a) shows the same signal with different data lengths, windowed with a half-Hann window and zero-padded to 200 μs. The PCB132 signal is divided by the stagnation-pressure step to result in a sensitivity measurement. Data are truncated before the window is applied, so the shape of the time trace is changed by the window function for the different amounts of truncation. The frequency response calculated from these signals is shown in Figure 3.15(b). The apparent effect of shortening the data trace is smoothing of frequency peaks.

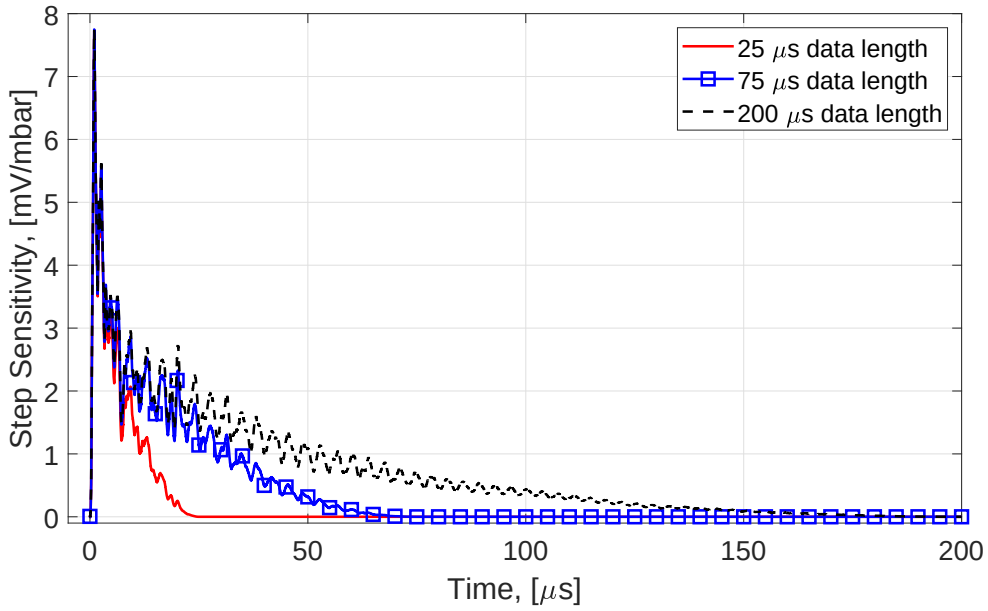

(a) Time Domain

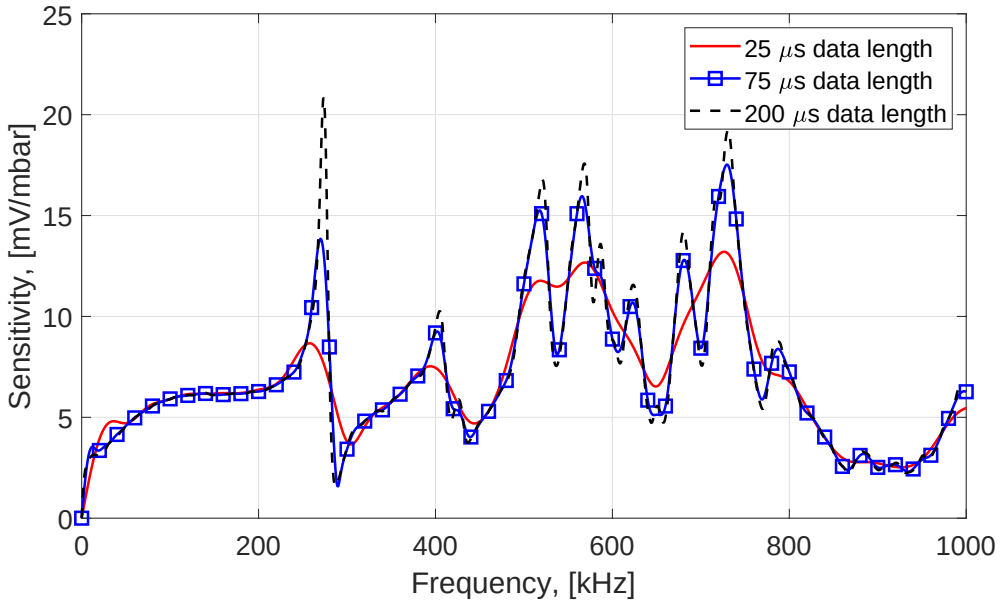

(b) Frequency Domain

Figure 3.15.: Comparison of signal truncation on frequency response; time trace low-pass filtered to 3 MHz; $p_{driven} = 1.31$ mbar, $p_{driver} = 438.84$ mbar.

For qualitative analysis of the frequency response, this is not a major concern. The same peaks are clearly visible in the frequency response of the shortened data traces, but are smoothed. Some peaks are shifted or smeared out, however this is only evident for the shortest data length. The peak locations and relative magnitude can still be compared despite the smoothing effect. However, a truncated data trace could pose issues if the frequency response were used to calibrate a PCB132 signal. Some peak magnitudes vary by nearly a factor 3 due to truncating the time trace, causing any calibration to have significant errors.

Future step-response measurements of PCB132 sensors in the P3IST should seek to maximize data-trace length to minimize this issue. Generally, applying the half-Hann window to a shorter trace will affect the shape more than a longer trace. So longer time traces should be better representations of the PCB132 response than shorter responses. Increasing data-trace length in the P3IST could be accomplished a number of ways including using longer end-plate-mounted pitot probes or better vibration isolation with the wall-mounted pitot probes. Other methods such as the reflected-shock mounting used by Ort & Dosch [2] could be tested as well. The reflected-shock mounting is a mounting configuration where the PCB132 sensor is mounted flush to the end-plate.

Frequency Response Implementation

Data acquired in the BAM6QT is typically analyzed by computing a power spectral density (PSD) using Welch's method of averaging modified periodograms. This method works by averaging modified periodograms computed from overlapping segments of the signal of interest. Here the signal of interest is the signal obtained from testing in the BAM6QT. Each periodogram is computed by windowing a segment of the total signal with a Hann window. The discrete Fourier transform is computed, and then squared to produce a periodogram. A window compensation factor is applied to account for power lost due to the application of the Hann window. Each segment

overlaps with the adjacent segments by 50%. The final PSD estimate is computed by averaging all periodograms.

The approximate frequency response of a PCB132 sensor calculated from measurements in the P3IST can be used to correct a PCB132 signal obtained in the BAM6QT. This can be done by dividing the frequency content of the signal of interest by the frequency response. So after a segment of the signal is windowed and transformed to the frequency domain, it is divided by the approximate frequency response of the sensor. This is then squared and averaged across all segments to compute a PSD with Welch's method. This is equivalent to dividing the uncorrected PSD by the frequency response squared. A custom implementation of Welch's method is used here to apply the frequency-domain correction.

4. VIBRATIONAL EFFECTS

Contamination of data by vibration is an issue for statically-mounted PCB132 sensors in the P3IST. Some contamination of data from mechanical vibration is evident in data acquired from pitot-mounted PCB132 sensors in the P3IST, however it is to a much lesser degree than statically-mounted sensors. Vibration is often detected by PCB132 sensors prior to the shock arrival, as shown in Figure 4.1. Berridge concluded the pre-shock increase in vibration was due to a vibrational wave traveling through the shock tube structure and arriving at the sensor before the shock [3]. Wave speeds in steel are in excess of 3000 m/s [53], which is generally much faster than the incident shock speed produced in the P3IST.

4.1 Vibration Characterization

The driven section of the P3IST is made from three pipe sections, as shown in Figure 4.2. From testing with PCB132 sensors, it was observed that vibrational noise was lower in section 3, or the most downstream section. This is generally unsurprising, as it is expected that the vibration wave damps in amplitude as it moves through the shock-tube structure. If the vibration wave is caused by the diaphragm rupture, the vibration amplitude would be expected to be reduced at more downstream sections. However, the vibration appears to reduce dramatically between sections 2 and 3. The same reduction in vibration was not observed between sections 1 and 2. It is possible that a similar reduction occurs between section 1 and 2, however it was not extensively studied. It is thought the low vibration in section 3 may be due to the joint between sections 2 and 3, but it is unclear. A difference in the joint between section 2 and 3 may contribute to the more dramatic reduction in vibration.

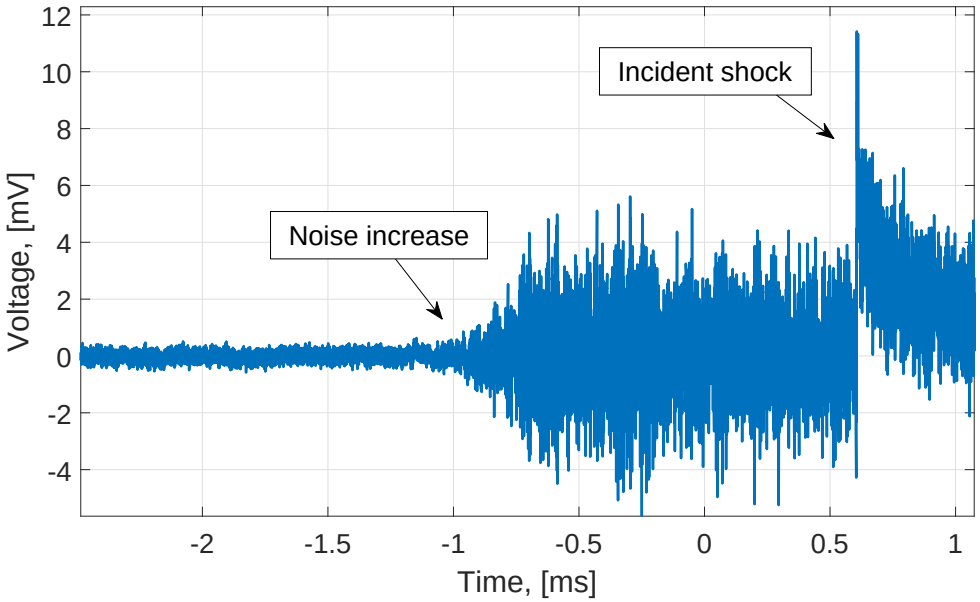

Figure 4.1.: Sample sensor trace from SN 6617; $x/d = 27.4$; $p_{driven} = 0.400$ mbar, $p_{driver} = 335.9$ mbar. Sensor mounted in neoprene jacket.

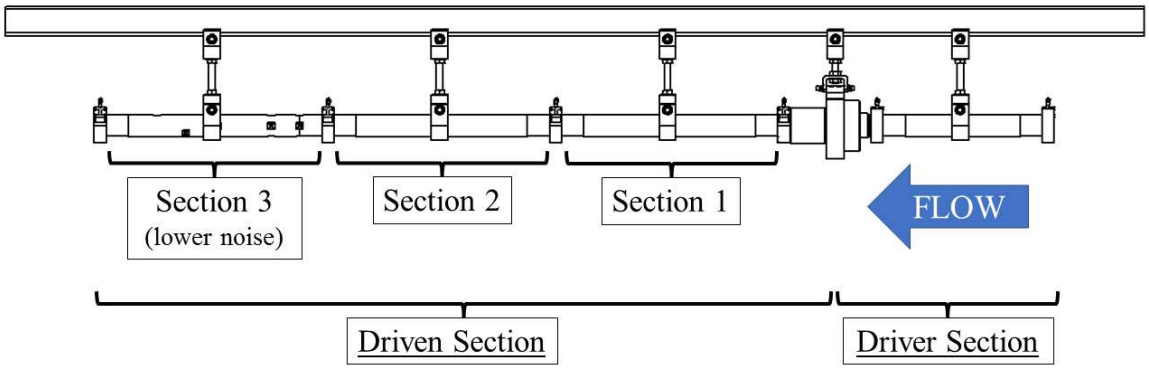

Figure 4.2.: Shock tube pipe section schematic.

To characterize vibration in the P3IST, PCB606B01 piezoelectric accelerometers were mounted to the shock tube structure. The frequency range where the accelerometer is within ±3 dB is quoted as 0.5–10,000 Hz, much lower than the PCB132 maximum frequency range. The accelerometer has a resonant frequency quoted as 25

kHz. No commercially available accelerometers were identified with a frequency range higher than 60 kHz, so it is difficult to characterize vibrations in the P3IST in the complete frequency range of PCB132 sensors.

The accelerometers were mounted by gluing a mounting pad to a blank static mount with a cyanoacrylate-based adhesive, and then bolting the accelerometer to the mounting pad. The mounting pad was kept consistent with each accelerometer to reduce variation from mounting. Figure 4.3 shows the mounting pad glued to a blank P3IST insert.

Figure 4.4 compares the apparent arrival times of the vibration wave measured by a PCB132 sensor and an accelerometer located at the same axial position. Axial position is given as x/d, or the axial distance downstream of the diaphragm normalized by the shock tube ID. By visual inspection, the accelerometer appears to detect the arrival of the vibration wave at around 0.5 ms before the PCB132 sensor. It is unclear why this occurs, but could be due to a number of factors, including the acoustic wave traveling through the PCB132 mounting. This PCB132 sensor was mounted in a neoprene sleeve, so it may have delayed the measurement of vibration somewhat. The accelerometer may also be more sensitive to acceleration than the PCB132 sensor, possibly causing the vibration measured by the PCB132 sensor to be initially indistinguishable from the electronic noise floor. Another possible cause for the apparent difference in arrival times could be due to a phase delay introduced by the PCB132 11 kHz high-pass filter.

A final possible source of the disparity in vibrational-wave arrival times is a difference in directional-vibration sensitivity. As discussed previously, the accelerometer is primarily sensitive to vibration normal to its mounting surface, and so it will be primarily sensitive to shear waves in the shock tube structure. The variation in acceleration sensitivity of the PCB132 sensor with direction is not known because its vibrational response is not characterized. Because of this, it could be possible that the PCB132 sensor has a limited sensitivity to shear waves in the shock tube struc-

ture in its current mounting. This could contribute to the difference in arrival times measured with the PCB132 sensor and the accelerometer.

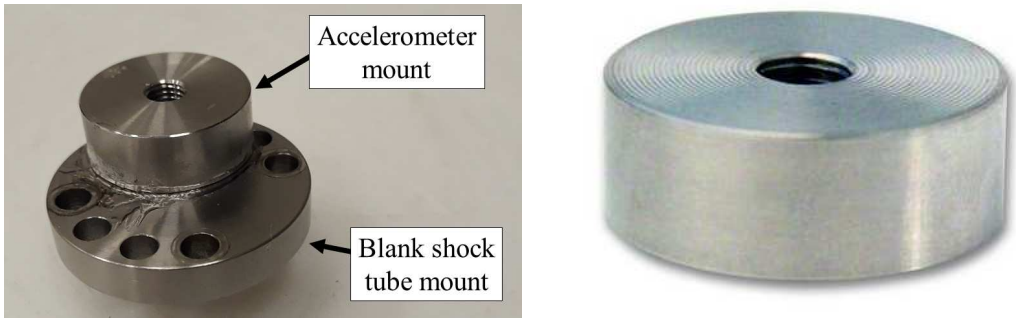

(a) Mounting pad and insert (b) PCB 080A118 mounting pad, from [54]

Figure 4.3.: Mounting pad and insert used for accelerometer testing.

Figure 4.5 compares the PSDs of a PCB132 sensor and an accelerometer located at the same axial position, computed from the pre-shock noise of the data shown in Figure 4.4. PSDs were computed for 2 ms of data using Welch's method with both signals zero-padded to twice their length. The zero-padding was used because the frequencies of interest were small compared to the length of available data. Both the PCB132 and accelerometer have a peak near 10 kHz, possibly the primary frequency in the shock tube structure. PCB132 sensors are high-pass filtered at 11 kHz, but the PSD clearly shows frequency content below this. The accelerometer shows a peak at 30 kHz, possibly due to the sensor's resonance, quoted as 25 kHz.

The PCB132 sensor shows significant content at frequencies higher than 100 kHz. This frequency content does not seem to be present in the accelerometer spectrum at these frequencies. As previously stated, the quoted high-frequency range of the accelerometer is 25 kHz, so it is expected that the magnitude is low in the 100 kHz range. The PCB132 sensor is also not an accelerometer, and its response to vibration is not calibrated or well understood. Previous estimation of PCB132B38 frequency response has shown that the maximum resonance is near 800 kHz [2]. It is

unclear if a similar resonance occurs due to vibration. Since the frequency response of the accelerometer is too low, it is unclear if the peaks visible in the PSD of the PCB132 vibration are due to similarly amplified vibration frequencies in the shock-tube structure.

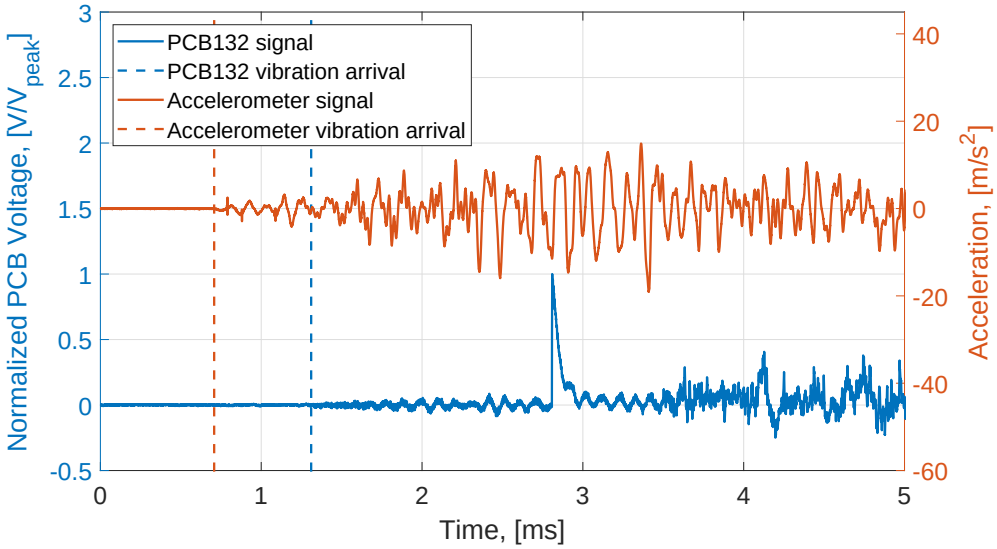

Figure 4.4.: Time trace from PCB132 and accelerometer located at $x/d = 27.4$; $p_{driver} = 786.97$ mbar, $p_{driven} = 1.300$ mbar.

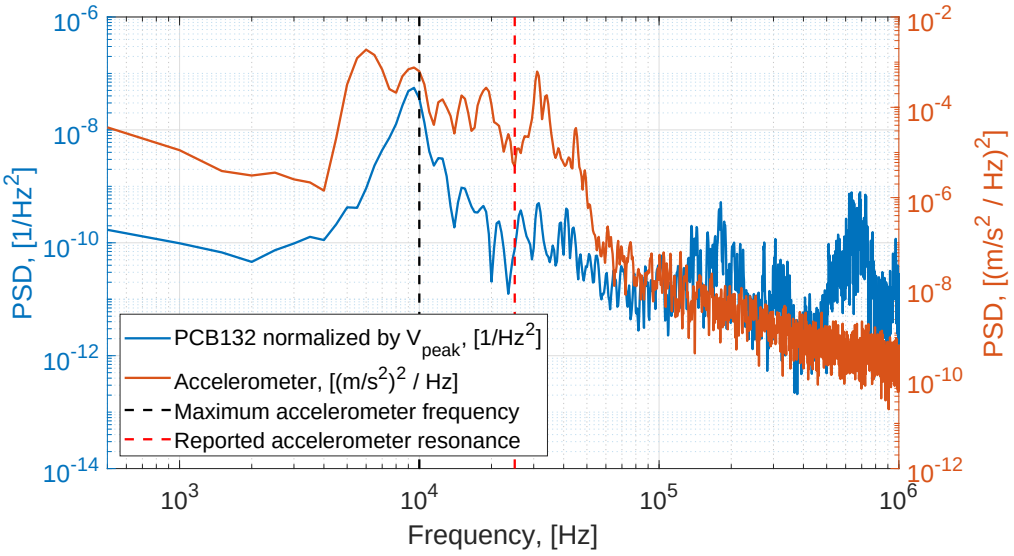

Figure 4.5.: PSD from PCB132 and accelerometer located at $x/d = 27.4$; $p_{driver} = 786.97$ mbar, $p_{driven} = 1.300$ mbar.

Figure 4.6 shows a PSD computed for accelerometer data with both accelerometers at the same axial location. The data were acquired from both sensors with the same oscilloscope. PSDs were computed for a record length of 2 ms from the start of vibration, and zero-padded to twice the original signal length. These PSDs are typical of most measurements made with the accelerometers. While there are clear frequency peaks, the frequency content appears to be fairly dispersed. It appears that the peak frequency measured by both accelerometers is around 10 kHz, and most of the low-frequency content is significantly lower magnitude. There are a number of relatively smaller peaks between 10–25 kHz. Both accelerometers show a peak near the quoted-sensor-resonance frequency of 25 kHz, however the magnitude is lower than the peak at 10 kHz. Frequency content higher than 25 kHz is much lower amplitude.

Figure 4.7 shows a time trace for a similar flow condition to Figure 4.6, but with accelerometer SN 4288 moved downstream to $x/d = 32.6$. Note that SN 4288 is offset by 15 m/s^2 to show both traces clearly. The time trace shows an obvious decrease in acceleration magnitude measured by SN 4288, even though it was only moved

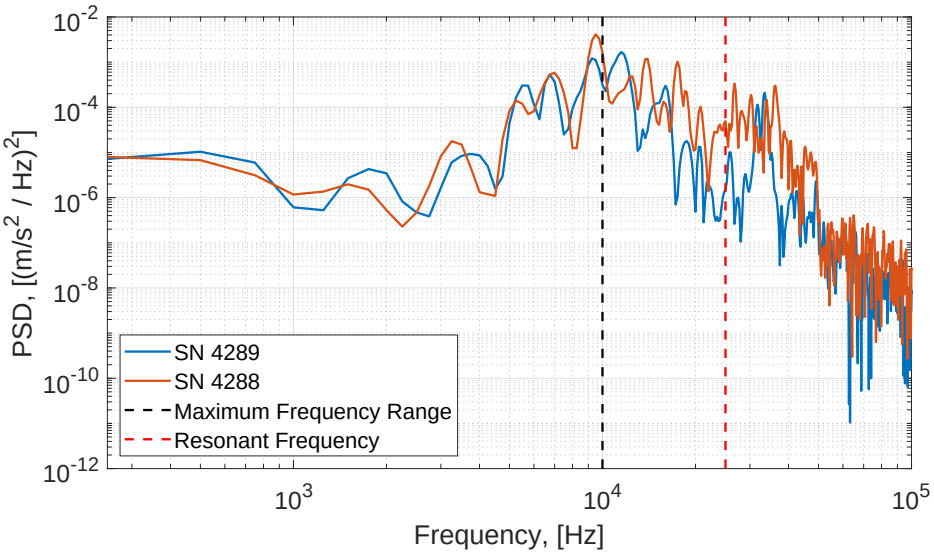

Figure 4.6.: PSD of vibrations measured before shock arrival by two accelerometers located at $x/d = 27.4$; $p_{driver} = 335.96$ mbar, $p_{driven} = 0.400$ mbar.

downstream from SN 4289 by 0.46 m. The likely cause of this drop in acceleration was because SN 4288 was mounted in section 3, while SN 4289 was still mounted in section 2 (as defined in Figure 4.2).

Figure 4.8 shows a PSD computed from data shown in Figure 4.7. The frequency content measured by the two sensors appear qualitatively similar, but with SN 4288 showing a lower magnitude than SN 4289. The reduction in magnitude is expected based on the time trace shown in Figure 4.7. Figure 4.9 shows a similar PSD to Figure 4.8 but with the position of the accelerometers reversed. Again, the sensor in the final pipe section measures lower amplitude vibrations. This indicates the reduction in vibration is physical and not due to differences in the accelerometers or how they were mounted.

RMS acceleration was computed for accelerometer measurements by taking the square root of the integrated PSD for frequencies less than 10 kHz. Figure 4.10 shows the computed RMS for both accelerometers located at the same axial position. RMS

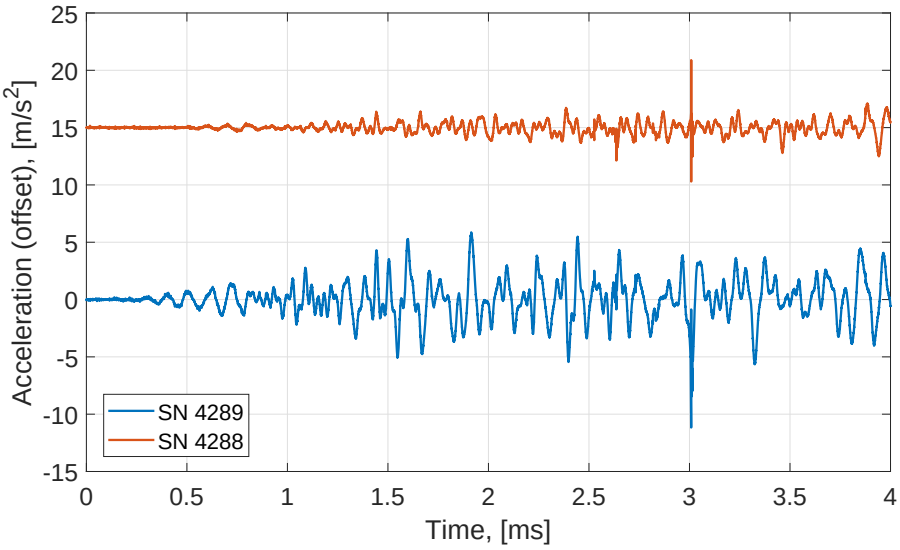

Figure 4.7.: Time trace of vibrations measured before shock arrival by PCB606B01 SN 4288 at $x/d = 32.6$, PCB606B01 SN 4289 at $x/d = 27.4$; $p_{driver} = 336.01$ mbar, $p_{driven} = 0.400$ mbar. Amplitudes offset for clarity

values were averaged over at least 3 runs for each flow condition and error bars show standard deviation of each set. Run conditions for all accelerometer data are included in Appendix A, Table A.1.

Note that RMS values are plotted against the pre-shock pressure differential, or the pressure difference between the driver and driven sections immediately prior to a run. The pre-shock pressure differential appeared to produce a better correlation of acceleration measurements than other shock tube parameters like static pressure step or shock Mach number. This could indicate that the vibration is largely due to diaphragm rupture. Pre-shock pressure differential does not necessarily determine the shock speed or strength, but does generally determine how the diaphragm breaks [21]. The RMS acceleration measured by the accelerometers at the same axial location roughly agree. There is significant scatter, but there seems to be a weak trend of increasing RMS acceleration with increasing pre-shock pressure differential.

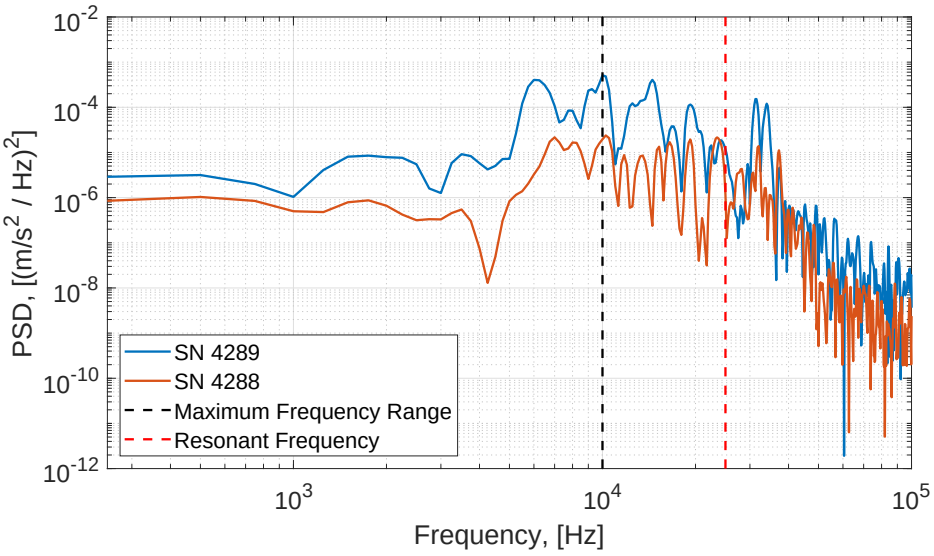

Figure 4.8.: PSD of vibrations measured before shock arrival by PCB606B01 SN 4288 at $x/d = 32.6$, PCB606B01 SN 4289 at $x/d = 27.4$; $p_{driver} = 336.01$ mbar, $p_{driven} = 0.400$ mbar.

Figure 4.11 shows the averaged RMS vibration fluctuations for SN 4288 located in the final pipe section. SN 4288 shows RMS values between 50 and 80% lower than SN 4289. The acceleration measured in the final pipe section has much less variability than the acceleration measured in section 2, as shown by smaller error bars. The acceleration measured in section 3 also doesn't appear to have as strong a trend with pre-shock pressure differential as acceleration measured in section 2.

Figure 4.12 shows the same shape trend as in Figure 4.11 but with the accelerometer position reversed. The measured acceleration is similar to that measured with the previous sensor positions indicating the individual accelerometers behave similarly. Again, the acceleration measured in section 2 has more variability than that measured in the final section.

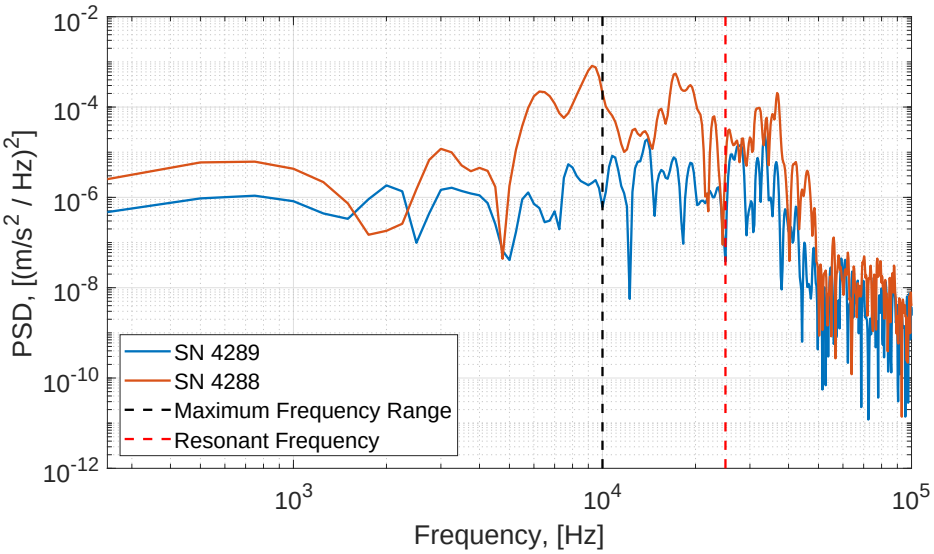

Figure 4.9.: PSD of vibrations measured before shock arrival by PCB606B01 SN 4288 at $x/d = 27.4$, PCB606B01 SN 4289 at $x/d = 32.6$; $p_{driver} = 335.91$ mbar, $p_{driven} = 0.400$ mbar.

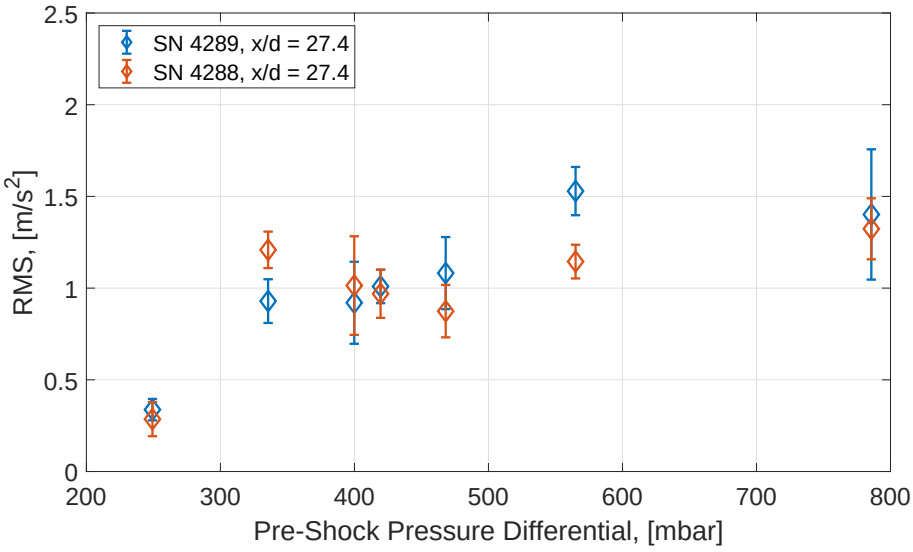

Figure 4.10.: Averaged RMS acceleration fluctuations for both accelerometers located at $x/d = 27.4$; error bars show standard deviation in averaged sets.

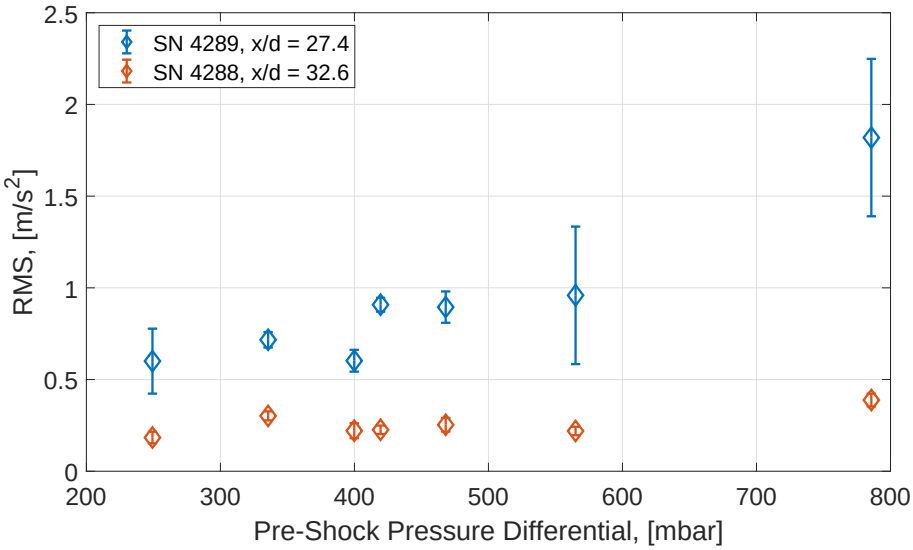

Figure 4.11.: Averaged RMS acceleration fluctuations for PCB606B01 SN 4288 at $x/d = 32.6$, SN 4289 at $x/d = 27.4$; error bars show standard deviation in averaged sets.

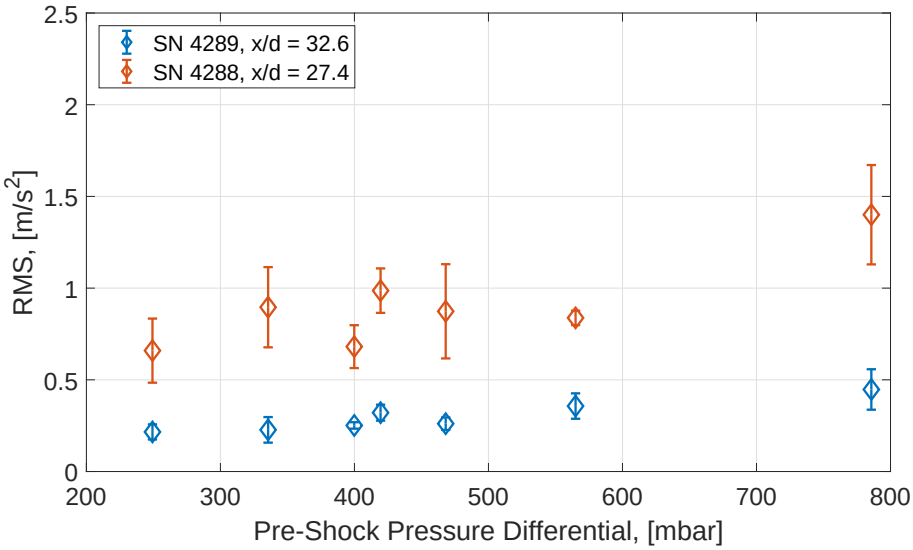

Figure 4.12.: Averaged RMS acceleration fluctuations for PCB606B01 SN 4288 at $x/d = 27.4$, SN 4289 at $x/d = 32.6$; error bars show standard deviation in averaged sets.

4.2 PCB132 Vibration Measurements

PCB132 sensors were mounted in the neoprene sleeve and tested on different sides of the joint between sections 2 and 3 for the same pressure step. Noise was evaluated as the RMS computed from 1 ms of data immediately prior to the shock arrival, normalized by the measured peak voltage. The RMS was computed from the PSD of data for frequencies less than 1 MHz. Table 4.1 shows the vibration levels drop significantly across the joint, as expected based on accelerometer measurements.

Table 4.1.: Normalized RMS of PCB132 vibration measurements

	RMS/$V_{peak} \times 100$, [%] $x/d = 27.4$	RMS/$V_{peak} \times 100$, [%] $x/d = 32.6$	% Reduction across joint
SN 7500	8.48	1.68	80.2
SN 6830	5.24	1.20	77.1

To evaluate the spectral content of the PCB132 signals on either side of the joint, 1 ms of data taken immediately before shock arrival was used to compute a PSD, shown in Figure 4.13. There is a peak close to the 10 kHz peak identified with accelerometer measurements. The upstream location shows much more noise, as expected based on the higher RMS. The downstream location shows noise close to the electronic noise floor, indicating little to no vibrational contamination. This is not always the case for PCB132 sensors mounted in the final section, but this PCB132 trace has negligible vibration.

As with accelerometer measurements, the vibration measured by PCB132 sensors is dramatically reduced in section 3 when compared with section 2. It remains unclear whether the high-frequency PCB132 behavior is due to high-frequency vibration in the shock tube structure. Some further measurements of vibration acquired with blinded, pitot-mounted PCB132 sensors are presented in Section 6.3.

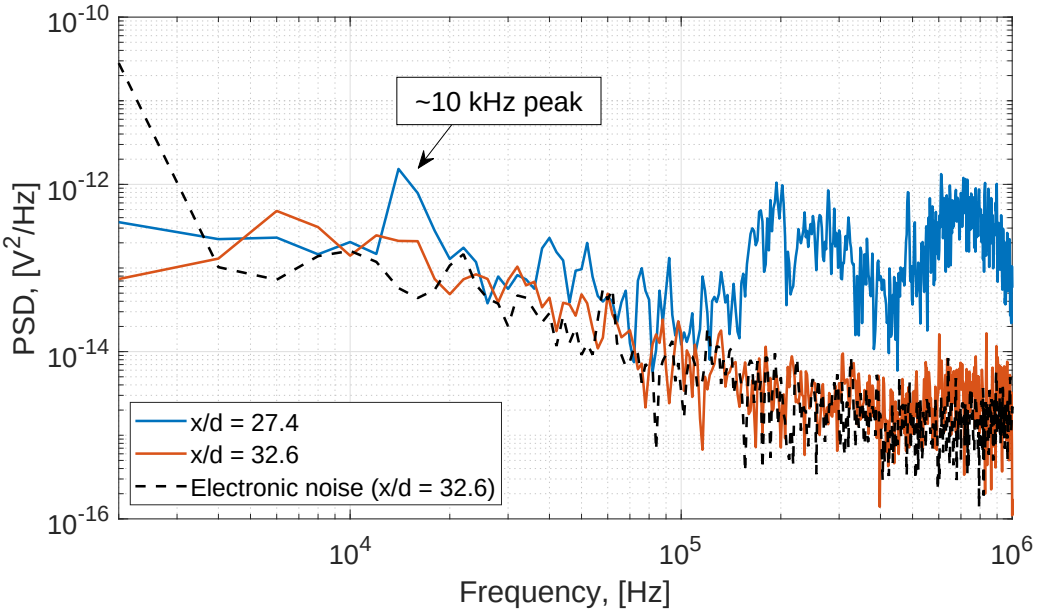

Figure 4.13.: PSD of PCB132 data from either side of the shock tube joint; nominal pressures $p_{driven} = 0.4$ mbar, $p_{driver} = 336$ mbar.

5. FLOW QUALITY

Flow quality was examined in the P3IST to assess the impact of the recent improvements, discussed in Section 2.1.1. The goal was to determine the typical operating conditions of the P3IST with the improved pressure-control system, especially at the new ports located at 2.90 and 3.05 m (x/d = 32.6, 34.3) downstream from the diaphragm. Metrics of interest include the uniformity of the incident shock, repeatability of the static pressure step across the shock, and variability of incident-shock Mach number. As discussed in Section 2.1.1, pre-shock pressures were typically controlled to within 1% of the desired values. This allowed for analysis of the repeatability of the shock tube flow to an extent not possible in previous work.

The effects of different driven pressures and different shock thicknesses were not studied. Shock thickness will affect the speed of the pressure-input signal to the PCB132 sensor, and so could affect the sensor response. Driven pressure will affect the mean free path and shock thickness, among other things. Since the effect of shock thickness on the PCB132 sensor was being studied separately [55], it was not studied here.

5.1 Double-Shock Feature

An easily identifiable flow-quality issue that occurs in the P3IST is the creation of multiple shocks. If the diaphragm does not break completely, a weaker incident shock can form due to partial diaphragm rupture. This weaker shock is followed by a much stronger shock when the diaphragm completely breaks. Partial diaphragm rupture is caused by a difference in resistances in the diaphragm-burst circuit. If there are different resistances across the different sections of the circuit, the nichrome wires will heat differently. This can cause the diaphragm to cut on one axis before the other,

and create the double-shock flow feature. This flow feature is discussed further by Berridge in [3] with evidence supporting the conclusion that this issue is caused by a difference in the burst circuit resistances.

An example of a double shock observed at a single axial location by two Kulite sensors is shown in Figure 5.1. The incident shock is visible at 0 ms, followed soon after by another pressure increase. This second pressure increase is qualitatively similar to the pressure increase caused by the incident-shock passage. The second pressure increase is not due to a reflected shock from the end plate. This conclusion is based on the predicted arrival time of the reflected shock at 2 ms, much later than the second increase in pressure. This pressure increase is likely due to a double-shock flow feature. This behavior is similar to that reported by Berridge for double shocks in the P3IST [3]. Double-shock features are generally easily identifiable from observation of the time trace of Kulite sensors. Because the double-shock feature is not well controlled or understood, data is not used from runs which exhibit a double-shock feature.

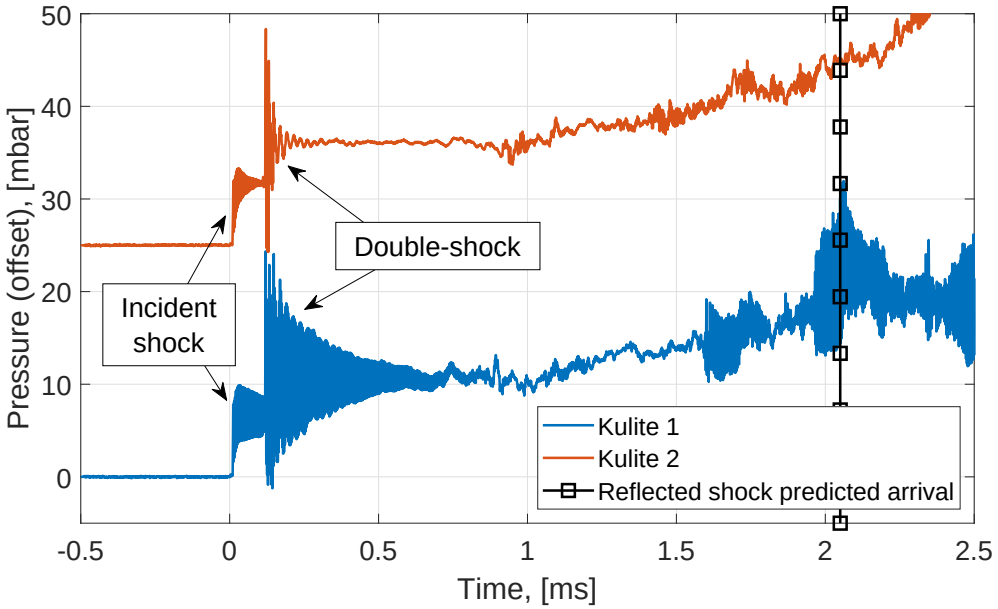

Figure 5.1.: Double-shock feature measured by two Kulite sensors; reflected shock predicted based on measured incident shock speed. Kulite 2 offset for clarity. Sensors at 3.05 m, $x/d = 34.3$. Low-pass filtered at 1 MHz.

5.2 Skewing of Incident Shock

The shock skew is defined as the shock angle measured from the shock tube sidewalls, as depicted in Figure 5.2. The shock wave likely has some degree of bowing which cannot be measured from the sidewalls, so the shock skew is not necessarily a measure of planarity. The shock skew is of interest as a measure of the uniformity of the incident shock wave. The shock skew can be calculated with the measured shock speed, difference in incident-shock arrival times on opposite sides of the shock tube, and the diameter of the shock tube. The shock speed is calculated from the arrival times measured by PCB132 sensors mounted at two different axial locations and the distance between them, as discussed in Section 3.2.

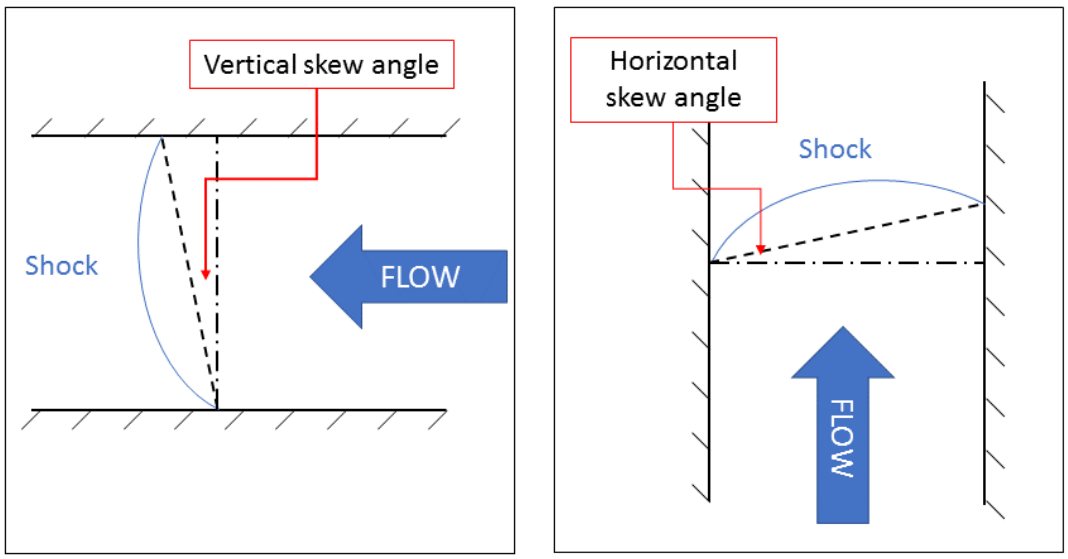

(a) Side view (b) Top view

Figure 5.2.: Shock-skew angle schematic.

Shock skew is defined in equation 5.1, where ψ is the shock-skew angle, t_1 and t_2 are the arrival times at sensors 180° azimuthally apart, u_s is the shock speed, and d_{tube} is the shock-tube inner diameter.

$$\psi = \arctan\left(\frac{(t_1 - t_2)u_s}{d_{tube}}\right) \tag{5.1}$$

Arrival times must be measured before evaluating the shock skew. Shock arrival times were measured at 2.90 and 3.05 m (x/d = 32.6, 34.3) downstream from the diaphragm at four evenly-spaced azimuthal positions. A schematic of port locations is shown in Figure 5.3, where azimuthal angle is defined clockwise starting from the top of the shock tube when looking downstream. The manufacturer-reported rise-time of PCB132 sensors is less than 3 μs, so it is expected that values will fall within 3 μs of each other if the shock arrival-time is azimuthally constant. Additionally, skew can only be resolved when the differences in arrival times are large with respect to the uncertainty in the rise times measured by the PCB132 sensors

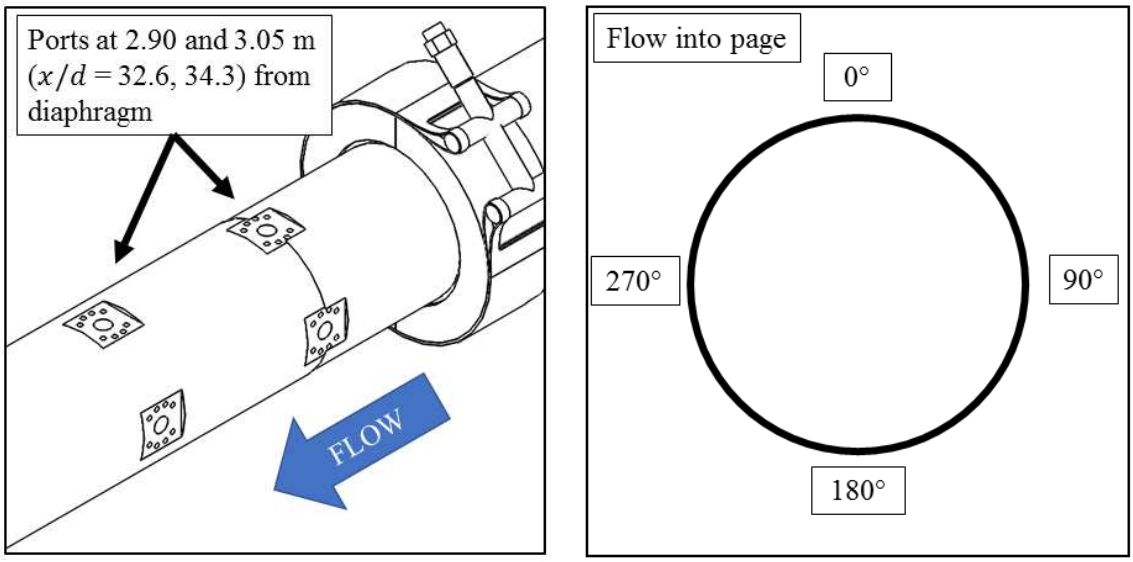

(a) Axial locations (b) Azimuthal locations

Figure 5.3.: Port locations used for shock arrival time measurements.

Some of the PCB132 sensors were mounted in neoprene sleeves that were flush to the inside of the shock tube. As previously discussed, Ort & Dosch showed that the pre-shock downward spike was caused by the neoprene sleeve compressing the sensing element due to the shock moving over the neoprene [2]. This could influence the rise time of these sensors, but it is unclear how much. Additionally, both model A and model B PCB132 sensors were used. Model A PCB132 sensors have a sensing element which is not centrally or precisely placed, which could affect measured arrival time. Model B PCB132 sensors have a centrally placed sensing element, however the tolerance of the sensing-element location is not known. As an attempt to counteract these effects, all PCB132 sensors were rotated 180° in the same sensor port half-way through testing. This was intended to average out the effects of asymmetries due to sensor mounting and sensor-to-sensor variation.

Figure 5.4 shows a comparison of arrival times measured by sensors at $x/d = 32.6$ and 34.3, with error bars showing standard deviation of each averaged point. The

lowest pressure step was excluded from the data taken at the $x/d = 34.3$ location due to difficulties in locating the shock arrival in certain PCB132 traces. All ranges of arrival times are within 1 μs of each other, less than the range of the manufacturer-reported rise time. In this range, any variation in rise time could be due to a specific sensor with a slightly faster rise time. Slightly more scatter is observed in the arrival times measured at $x/d = 32.6$, but the variation is low compared to the sensor rise-time.

Shock speed was measured as the axial distance between port locations divided by the difference in average arrival times, as discussed in Section 3.2. The speed was assumed to be constant over the relatively short distance of 0.15 m between the port locations at $x/d = 32.6$ and 34.3. Shock speeds for this set of experiments varied between 800–1,200 m/s. The uncertainty in shock-skew angle can be calculated with the manufacturer-reported rise time and incident-shock speed using Equation 5.1 as between 1.5–2.3 deg.

Figure 5.5 shows the incident-shock skew angle calculated for both axial locations, with error bars showing standard deviation of each averaged point. It is generally close to zero for $x/d = 34.3$, but appears to show vertical skew at $x/d = 32.6$. While this seems significant, the average incident-shock skew angles are all within 0.5°. This is within the uncertainty of 1.5–2.3 deg, and so is likely insignificant. The skew seems to increase at $x/d = 34.3$ for lower pressure steps. This could be due to a lower SNR. Lower pressure steps produce lower PCB132 signals, and so have lower SNR. If the SNR is too low, the arrival time could be misidentified, influencing the calculated shock skew.

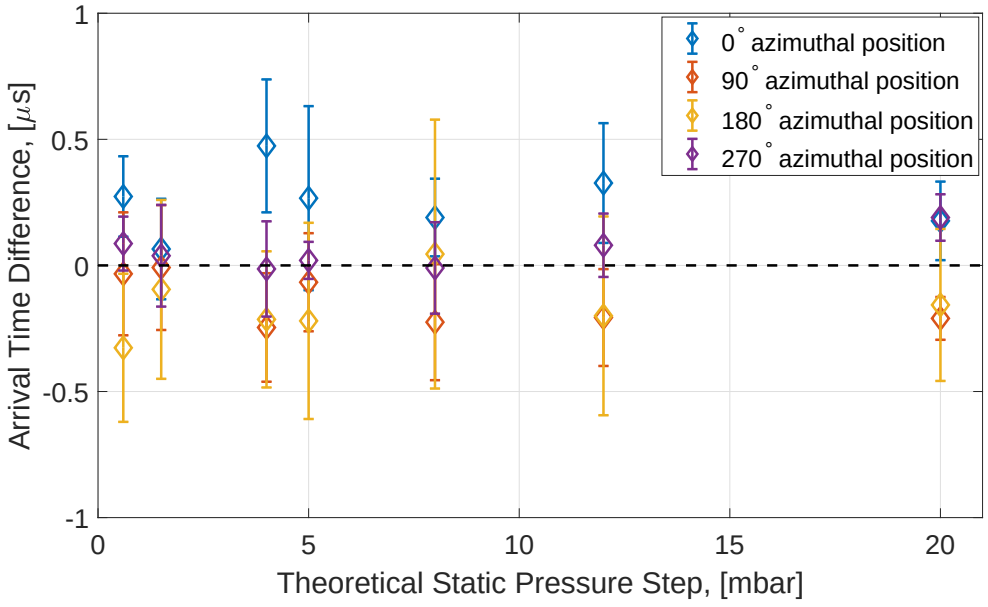

(a) 2.90 m from diaphragm, $x/d = 32.6$

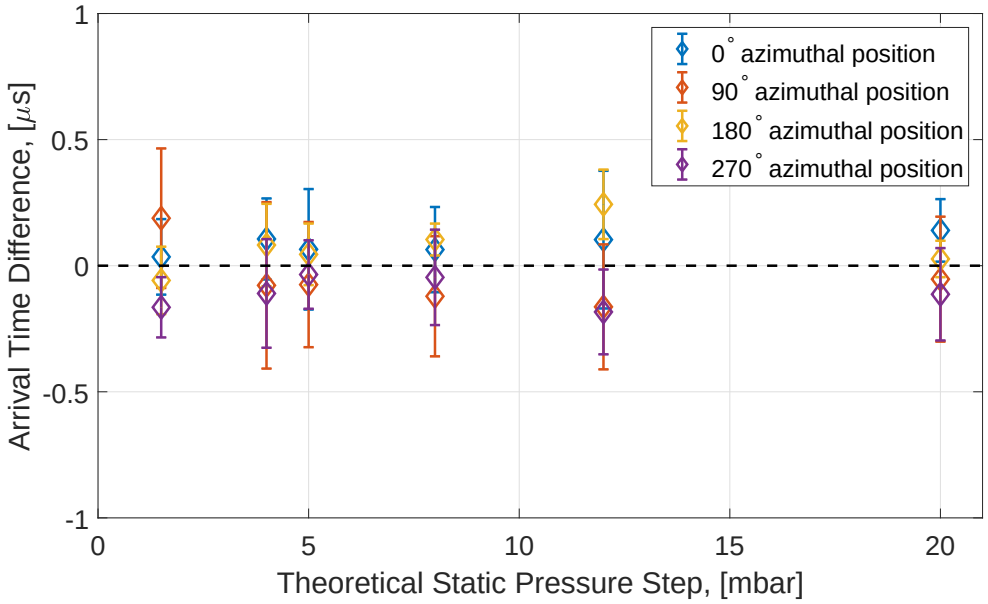

(b) 3.05 m from diaphragm, $x/d = 34.3$

Figure 5.4.: Arrival time comparison for sensors at 4 azimuthal positions at 2.90 and 3.05 m downstream from diaphragm (x/d = 32.6, 34.3). Averaged over 6 runs, error bars show standard deviation. Run conditions available in Appendix A, Table A.2

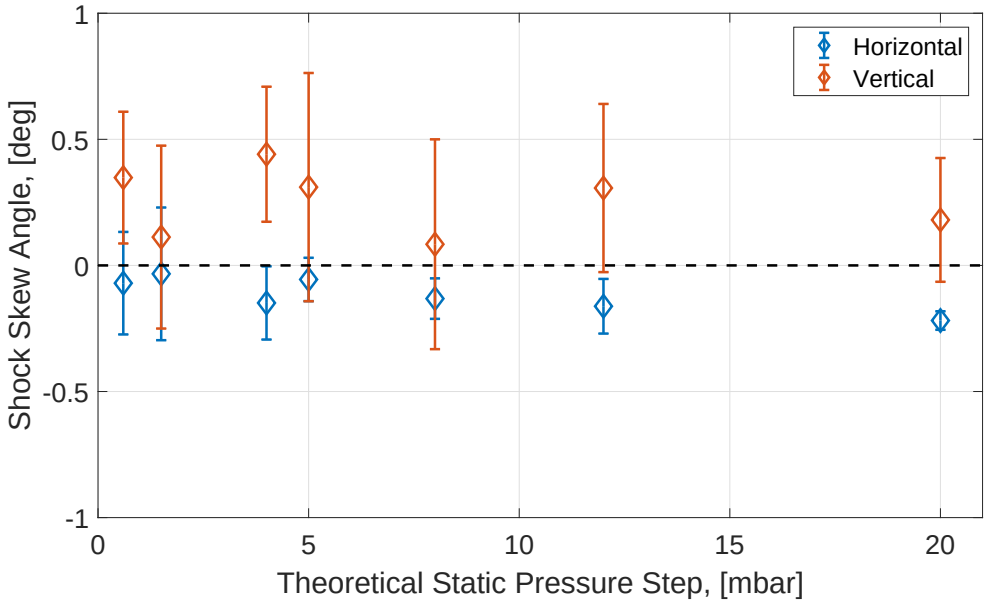

(a) 2.90 m downstream, $x/d = 32.6$

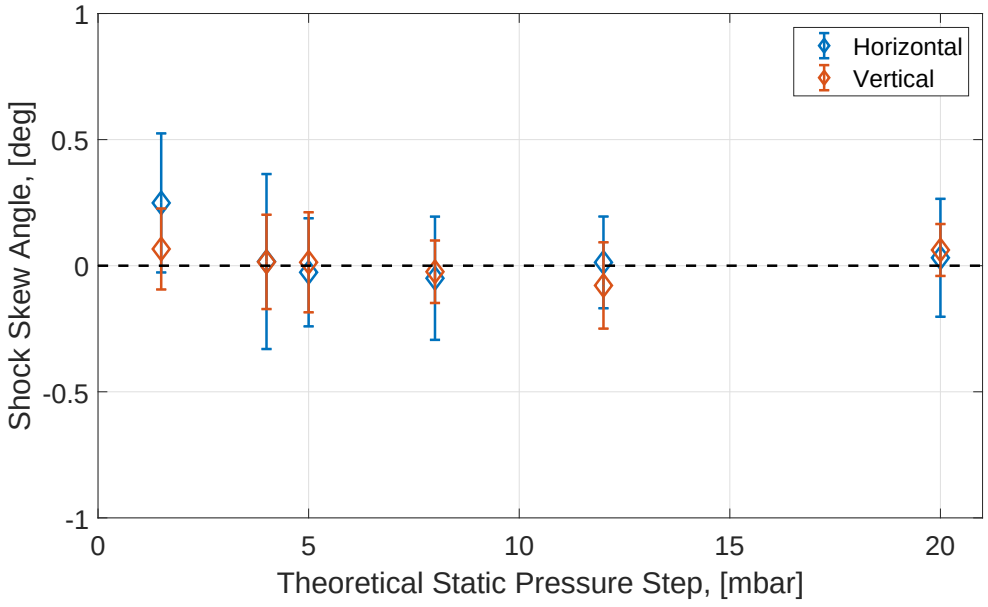

(b) 3.05 m downstream, $x/d = 34.3$

Figure 5.5.: Incident-shock skew angle at 2.90 and 3.05 m downstream from diaphragm ($x/d = 32.6, 34.3$). Averaged over 6 runs, error bars show standard deviation. Run conditions available in Appendix A, Table A.2

5.3 Static Pressure Step

The performance of PCB132 sensors should be evaluated in a pressure range relevant to hypersonic boundary-layer transition studies. Berridge set the upper limit of the relevant pressure range as 0.1 psi (7 mbar), based on the highest measured amplitudes of second-mode instability waves in wind tunnels [3]. Because of this, the generation of pressure steps at amplitudes less than 7 mbar with the P3IST is of interest. PCB calibrates the sensors at pressures much higher than this, reported by Berridge as 1 psi (68.9 mbar) [3]. PCB assumes a linear calibration based on zero offset and the single calibration measurement. The present measurements can thus be used to check the manufacturer's calibration process.

As mentioned previously in Section 2.4, only Kulite sensors were used to measure the static pressure step due to a low quoted uncertainty. A limitation of the current work is that no comparison to Kulite sensors was performed. The average static pressure step measured by two Kulite sensors as a percentage of the theoretical pressure step is show in Figure 5.6. Data were acquired for 38 runs with the Kulites at the same axial location. Each point shown in Figure 5.6 is an average of the two Kulite measurements for a single run. All measurements show attenuation with respect to the pressure step predicted by perfect gas relations. The measured pressure step is reasonably repeatable, for theoretical pressures below the second-mode upper limit. Two points appear to break from the clear trend at the 12 mbar theoretical pressure step. The reason for this disagreement is unclear, but it could be due to an improper diaphragm rupture. If the diaphragm partially ruptured during a run, the blockage from the diaphragm protruding into the flow could make a weaker shock than a proper rupture. The outlier points are likely not the result of a double-shock feature, since these are generally easily identifiable by inspection. There is currently no method of evaluating the quality of diaphragm rupture during a run in the P3IST and so the cause of the weaker measured pressure steps remains unclear.

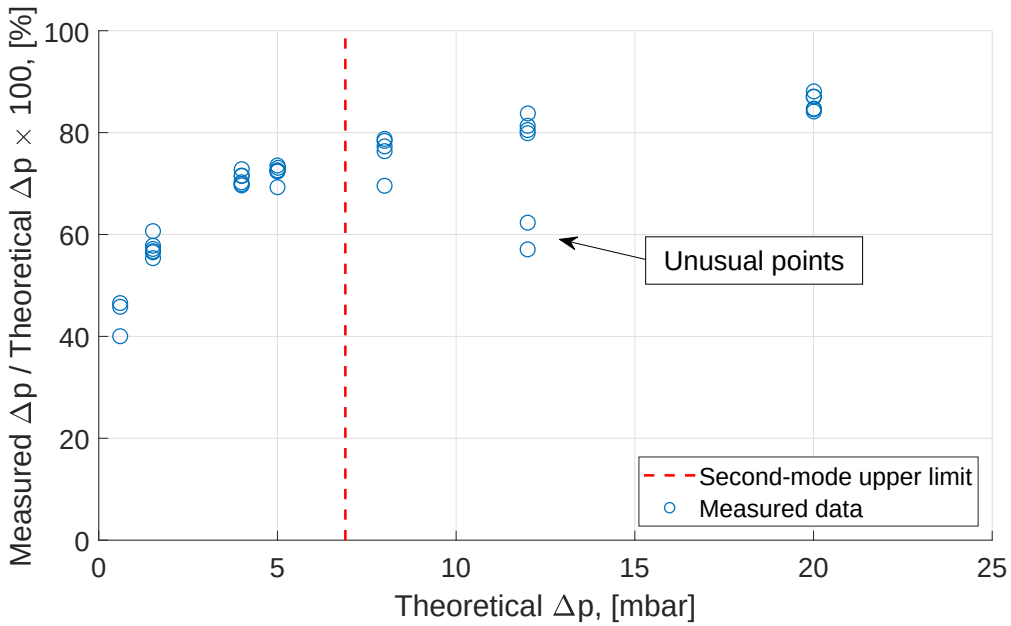

Figure 5.6.: Pressure step measured with Kulite sensors as a percentage of the pressure step predicted with perfect gas relations. Based on data from 38 runs. Sensors at 2.44 m, $x/d = 27.4$. Run conditions available in Appendix A, Table A.2

Figure 5.7 shows the difference in measurements made with two Kulites mounted 180° azimuthally apart at the same axial location. Half way through testing, the Kulite azimuthal positions were swapped to determine if a pressure-step bias existed at one location. In the pressure range lower than the second-mode upper limit, data taken before and after swapping the positions roughly follow the same trend. This indicates that the differences in measurements in this range are likely due to differences in the sensors, and not due to differences in pressure step at the two azimuthal locations. At higher pressure steps however, the data differ depending on position. This indicates there could be a bias in pressure step based on sensor location for higher pressure steps. It is unclear why this occurs, although the possible bias is relatively small compared to the static-pressure step.

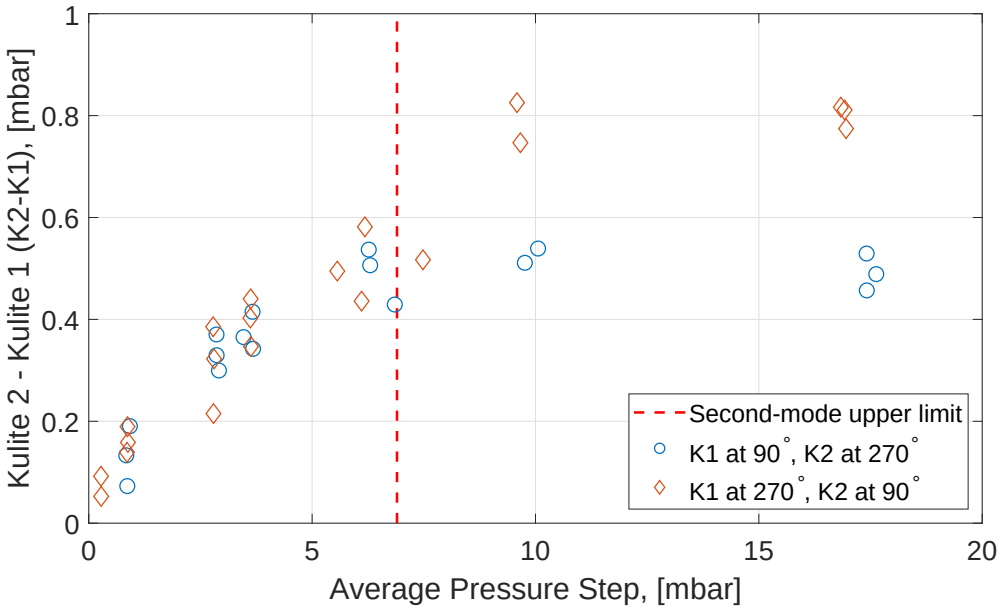

Figure 5.7.: Difference in Kulite measurements when mounted at 2.44 m, $x/d = 27.4$. Run conditions available in Appendix A, Table A.2

5.4 Mach Number

The Mach number was computed based on the room temperature and the measured incident-shock speed, as discussed in Section 3.2. The temperature in the shock tube was not generally measured, and is assumed to remain at a constant 295 K. Figure 5.8 shows the variation in Mach number along the shock tube axis, averaged for at least 5 runs, with error bars indicating standard deviation in each averaged set. Listed pressure ratios refer to the ratio of pre-shock driver and driven pressures. The position of the Mach number measurement is the average distance of the two measurement ports used to calculate the shock speed.

Variation in the averaged Mach number measurements is low, especially for the runs with lower pressure ratio. This could be at least partially due to the lower pressure ratios corresponding to flow conditions that produce higher differential pressure

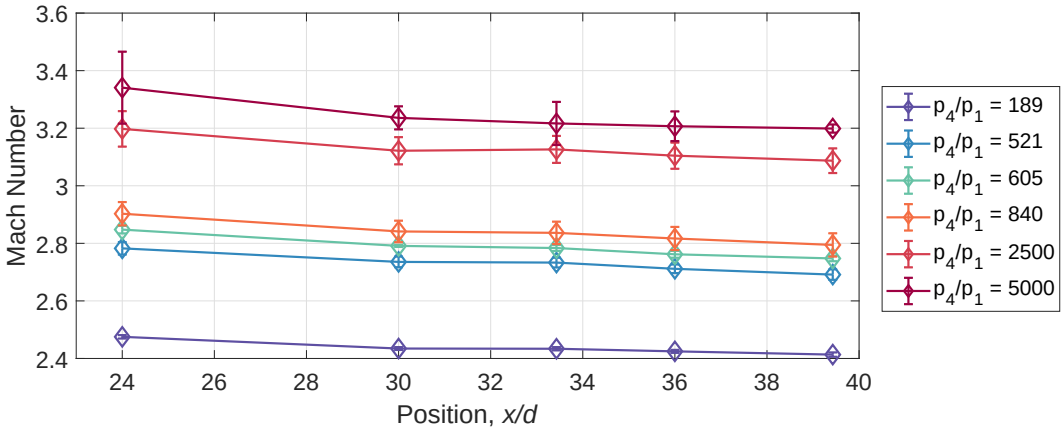

Figure 5.8.: Averaged decrease in Mach number axially at varying pre-shock pressure ratios. Error bars indicate standard deviation of averaged set of runs. Pressure ratios indicate pre-shock pressure ratios. Run conditions available in Appendix A, Table A.3

across the incident shock. This means that for runs with a low ratio of driver to driven pressures, the difference in pressure across the shock was higher. Run conditions for the runs presented in Figure 5.8 are included in Appendix A, Table A.3. This trend is not generally true, but is true for the conditions presented here. The higher pressure steps result in higher SNR in PCB132 signals, meaning the arrival time should be measured somewhat more accurately.

Figure 5.8 indicates the shock is fully formed before $x/d = 24$. The shock formation distance is the distance over which the shock travels before reaching its maximum speed [56]. After this initial formation length, the shock is expected to decelerate relatively slowly as it moves downstream [25]. Because no increase in the incident-shock Mach number is observed, the shock likely forms entirely upstream of the measurement ports.

The Mach numbers towards the beginning and end of the shock tube are compared to theoretical values in Figure 5.9. The perfect gas line refers to the trend based on

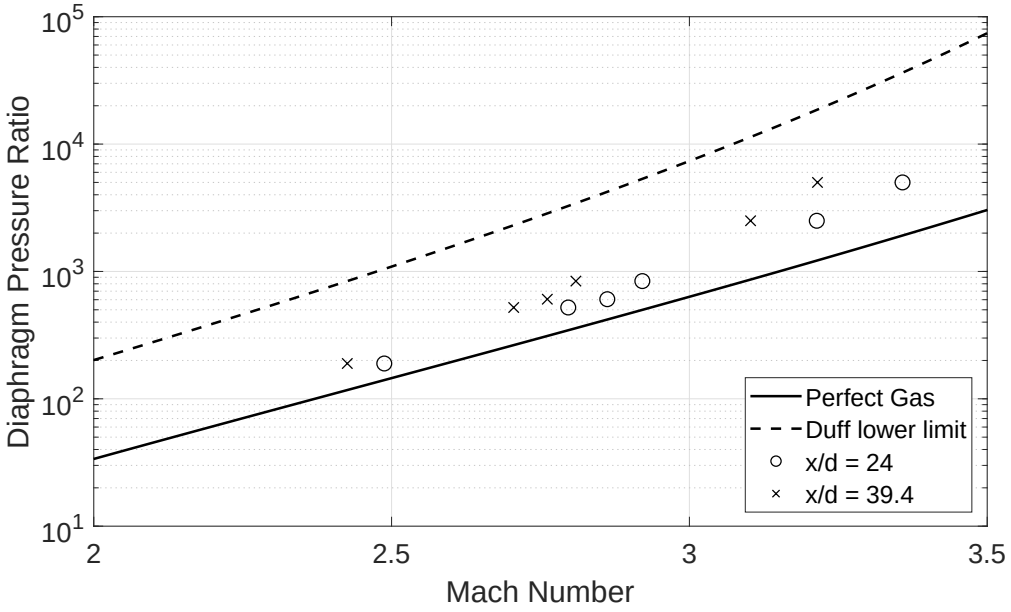

Figure 5.9.: Mach number computed at 2 axial locations based on pre-shock pressure ratio. Compared with ideal gas theory and the lower limit proposed by Duff [32]

.

the typical perfect gas shock tube equations, and the lower limit refers to a relation proposed by Duff for shock attenuation [32]. Duff's relation matches the flow velocity to shock velocity and assumes isentropic flow deceleration between the shock and contact surface. The data follow the expected trend: as the shock moves downstream the shock Mach number decreases, moving towards the lower limit proposed by Duff.

Two pressure steps were tested with the same pre-shock pressure ratio but different predicted static-pressure steps. These conditions should produce the same Mach number at each axial location. This is because the Mach number is based on the pre-shock pressure ratio, and not the pre-shock pressure magnitudes. This is shown in Figure 1.3 and discussed further in Section 1.4.1. Table 5.1 compares the averaged measured Mach numbers for the two run conditions. All axial locations agree to within 0.5% difference, showing repeatable behavior.

Table 5.1.: Mach number comparison for $p_4/p_1 = 840$ for different static pressure steps.

Position	Mach Number		
x/d	$\Delta p = 4$ mbar	$\Delta p = 5$ mbar	% difference
24.0	2.899	2.903	0.14
30.0	2.836	2.841	0.18
33.4	2.833	2.836	0.11
36.0	2.812	2.817	0.18
39.4	2.789	2.795	0.21

6. PCB132 CALIBRATION EFFORTS

6.1 PCB132 Pitot/Static Measurement Comparison

Previously, Berridge generated a PCB132 calibration slope with the P3IST by correlating the peak voltage with the static-pressure step. Because the transfer function of the PCB132 sensor is unknown, the accuracy of this method is unclear. This peak-correlation method was used with both static-mounted and pitot-mounted sensors, showing up to 47% difference from the manufacturer supplied sensitivities for static-mounted sensors and up to 174% difference for pitot-mounted sensors. Berridge also measured significantly higher sensitivities when using the peak-correlation method for PCB132 sensors mounted in pitot mode as opposed to static mode [3]. This difference between the manufacturer calibration and the two P3IST calibrations highlights the uncertainty associated with PCB132 calibration, and why further work is necessary to generate reliable calibrations.

6.1.1 PCB132 Peak Calibrations

Calibrations were performed using the peak-correlation method discussed in Section 3.4. Plots showing sample responses of Kulite and PCB132 sensors are also available in Section 3.4. As previously mentioned, the transfer function of PCB132 sensors is unknown and so the present calibrations are only approximations. The peak-correlation method was used by Berridge to generate linear calibrations for PCB132 sensors, but the accuracy is unclear.

The same PCB132 sensor was mounted in static and pitot configurations in the P3IST. Static-mode calibrations were performed using the PCB132 peak voltage and static-pressure rise measured with Kulites. As previously mentioned, Kulites were the

only reference sensors used due to the fast response and low quoted uncertainty. A comparison with other reference sensors was not performed. Pressure steps for pitot-mounted sensors were calculated with the shock-tube relations using the measured shock speed and static-pressure step, as discussed in Section 3.3.

Figure 6.1 shows a comparison of the PCB132 factory calibration and calibrations performed with the P3IST. All P3IST calibrations show a high degree of linearity. As with calibrations performed by Berridge, the pitot-mounted peak calibrations show a much lower slope than calibrations performed in static-mode. This corresponds to higher sensitivities for pitot mode than static mode.

6.1.2 Effect of Incident-Shock Velocity

To generate a useful pressure-sensor calibration, the PCB132 voltage peak must be only a function of the pressure step across the incident shock generated with the P3IST. In other words, a variation of parameters such as Mach number or density should not change the PCB132 voltage peak if the pressure step is held constant. Berridge generated linear calibrations for pressure steps between 0.07–35 mbar, showing good likelihood that this method is valid. However, since PCB132 sensors have such a fast rise time, it is possible that the shock moves too slowly to act as an approximate step input. If the shock moves slowly enough, the effective pressure-input signal to the PCB132 sensor could become too much like a ramp to reasonably approximate a step input. This would mean the calibration could change based on shock speed.

To determine if this is an issue, PCB132 sensors were statically-mounted and calibrations were performed for similar pressure steps at nominal Mach numbers of 2.1 and 3.4. Pressure step refers to the differential static pressure across the incident shock, or $p_2 - p_1$. In order to generate the similar pressure steps with different Mach numbers, the driven and driver pressures were not constant across runs. Actual Mach numbers varied for each run, but Mach numbers predicted by perfect gas relations

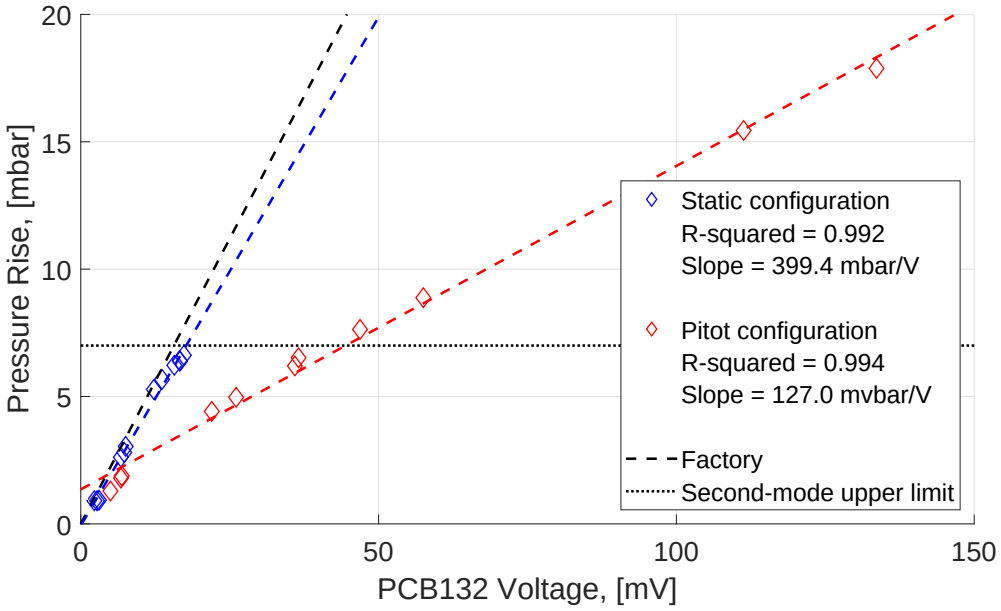

(a) PCB132B SN 8246

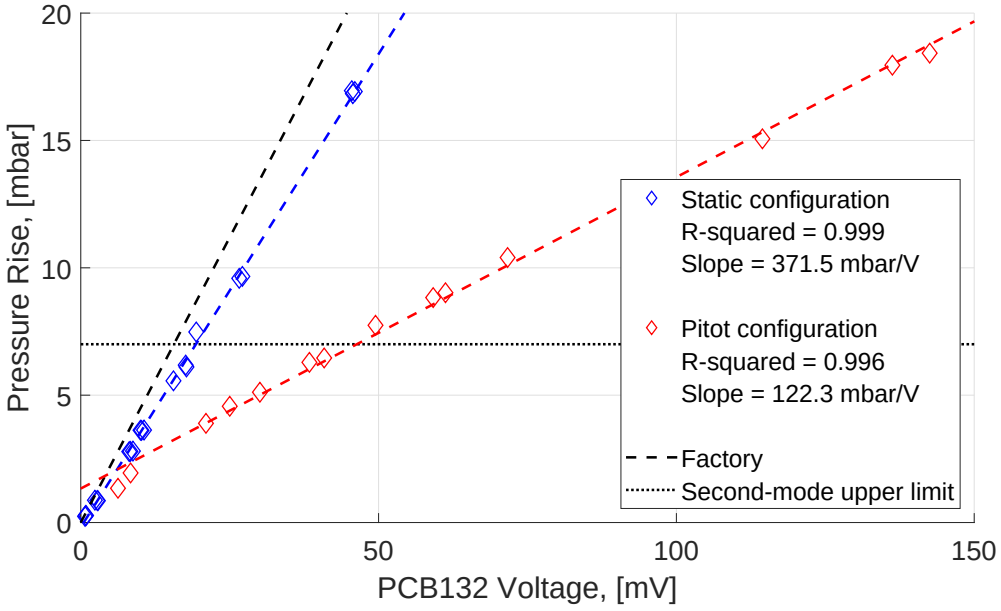

(b) PCB132B SN 8247

Figure 6.1.: Comparison of PCB132B calibrations performed in static and pitot mountings in P3IST. Flow conditions are available in Appendix A, Table A.4.

from pre-run pressures were kept constant. The variation in measured Mach number is summarized in Table 6.1. Conditions for each run are included in Appendix A, Table A.5. Only a limited pressure-step range from approximately 1–4 mbar was tested in the P3IST. This was due to performance limitations of the P3IST including maximum and minimum pressures and useful pressure differentials of the diaphragm. The tested pressure-step range was less than the second-mode upper limit of 7 mbar, so is relevant to low-pressure PCB132 evaluation.

Table 6.1.: Measured Mach-number variation

Theoretical M_s	Mean measured M_s	Max. measured M_s	Min. measured M_s
2.1	1.84	1.90	1.71
3.4	3.20	3.26	3.13

Figure 6.2 shows responses for a single PCB132 sensor subjected to similar pressure steps, but different incident-shock Mach numbers. The run with the faster incident-shock Mach number produces a response with a higher peak than the run with the slower Mach number. This does not seem to be explainable by the difference in static-pressure steps, since the difference in pressure step is around 2% while the difference in the PCB132 voltage peaks is around 23%. The rise times of the responses do not seem to significantly vary, however it is difficult to determine due to the low amplitude of the signals and the presence of noise. The response from the run with the faster Mach number also shows more noise than the slower Mach number. This is likely due to the higher pre-run differential pressure causing more vibrational contamination. As discussed in Chapter 4, vibration appears to be highest in the P3IST for runs with high pre-run diaphragm differential pressure. Higher pressure ratios are required to produce faster Mach numbers, and so runs with faster Mach numbers often have higher vibrational contamination.

The comparison in PCB132 responses due to shocks at different Mach numbers shown in Figure 6.2 can be extended by performing a calibration with the peak-

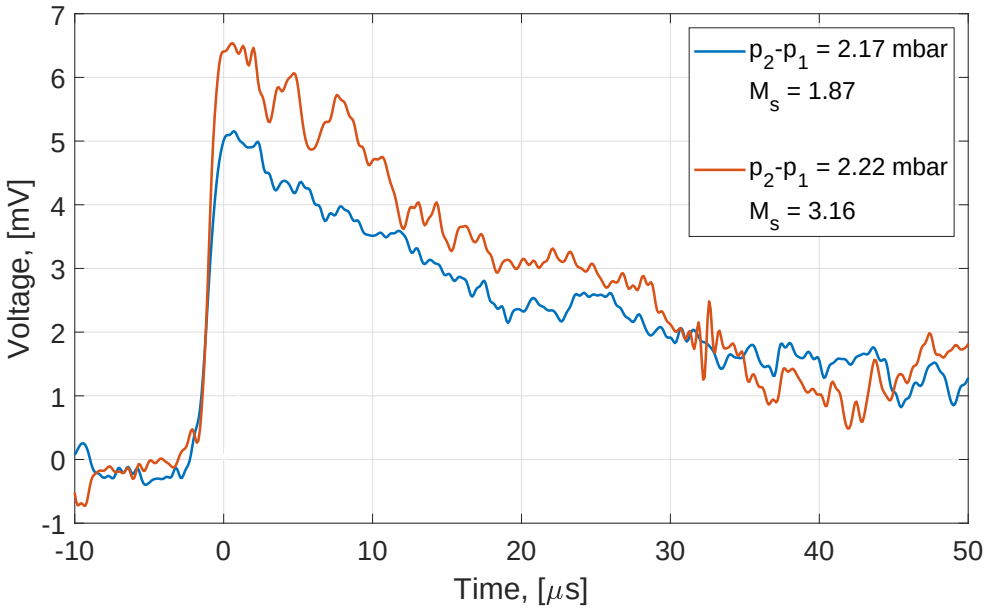

Figure 6.2.: PCB132 response comparison with similar pressure steps and different shock speeds; PCB132 SN 7516; $x/d = 34.3$. Signals low-pass filtered at 1.5 MHz. Full run conditions are available in Appendix A, Table A.5

correlation method. Figure 6.3 shows the difference between the static-mode calibrations performed at different shock Mach numbers for the same sensor. Calibrations were performed by correlating the PCB132 voltage peak with the static-pressure step measured by Kulite sensors, using the method discussed in Section 3.4.1. The difference between the slopes of the two calibrations is approximately 19%. This is higher than the difference between the manufacturer calibration and the Mach 2.1 calibration. This implies that the calibration is not only a function of pressure step, adding uncertainty to the static-mode calibration method.

It should be noted that while Mach numbers were kept nominally constant, other parameters relevant to the shock tube flow changed. In particular, the driven pressure was not held constant. As will be discussed in Section 6.2, the shock thickness varies with a number of parameters including the shock speed and the mean free path of

the driven gas. Since the mean free path of a gas is affected by the pressure, a changing driven pressure results in a changing shock thickness. This will also affect the pressure-input signal to the PCB132 sensor. This effect was not accounted for, and so a changing shock thickness may also be affecting these measurements. Despite this, these data still show a changing calibration with parameters other than pressure step.

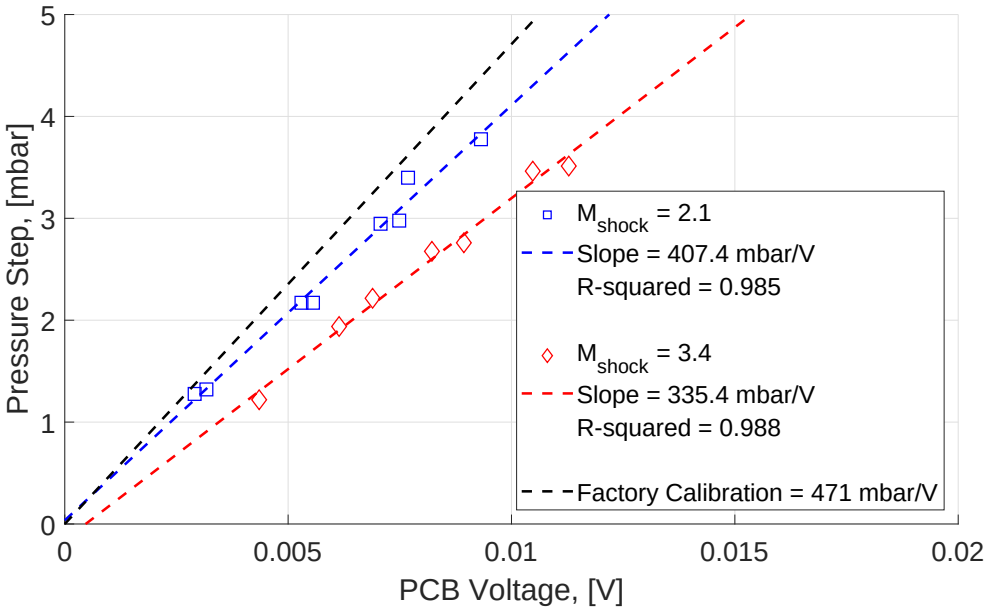

Figure 6.3.: Calibration comparison with different shock speeds; PCB132 SN 7516; $x/d = 34.3$. Full run conditions are available in Appendix A, Table A.5

Static-mode calibrations were obtained using the P3IST for 5 other PCB132 sensors at similar conditions to those shown in Figure 6.3. The percent change in slope was calculated from the linear regression slope obtained from each calibration. Percent change in slope is defined in equation 6.1, where ϵ is the percent change, s_1 is the calibration slope from runs at Mach 2.1 and s_2 is the calibration slope from runs at Mach 3.4.

$$\epsilon = \frac{s_1 - s_2}{(s_1 + s_2)/2} \times 100 \tag{6.1}$$

In order to determine if the change in calibration slope is statistically significant, a two-sample t-test was performed. A t-test is a statistical test that determines the likelihood that two sample sets come from populations with different average values. A p-value represents the probability that the data populations have the same mean sensitivity. A low p-value means that it is likely the different populations have different mean values, while a high p-value means that it is inconclusive whether the populations have different mean values. The t-test was performed using data sets composed of measured sensitives, or the voltage rise divided by the pressure step.

Table 6.2 shows the percent change in slope for six PCB132 sensors between calibrations at Mach 2.1 and Mach 3.4 along with p-values from the t-test. The p-values are scaled by 100 to represent a percentage. All six sensors show a higher slope for the calibration at Mach 2.1 than the calibration at Mach 3.4. Additionally, all p-values are less than 5%, with half much less than 1%. This indicates that the difference in percent change is statistically significant. This also further strengthens the argument that there are methodological problems with static-mounted PCB132 calibration methods. Since different calibrations can be obtained for PCB132 sensors using the P3IST, it is unclear which set of run conditions produces a more accurate calibration.

A possible explanation for the variation in static-mode calibration based on incident-shock Mach number is a change in the rise time of the pressure-input signal. The pressure signal generated by the P3IST has a finite rise time as the pressure changes across the shock. The rise time of the pressure signal will depend on both the shock thickness and shock speed. So the change in calibration slopes could be explained if the faster shocks create a steeper pressure-input signal. If the shock is moving fast enough, the sensor response would be expected to be approximately independent of input rise time. The difference in calibration slopes could be due to the shock moving

too slow to act as an approximate step input to the PCB132 sensor. This will be discussed further in Section 6.2.

Table 6.2.: Percent change and p-value of linear regressions from PCB132 sensors at different Mach numbers.

PCB132 SN	Percent Change (ϵ), [%]	P-value $\times 100$, [%]
6819	20.88	2.13×10^{-2}
7506	18.68	1.12×10^{-3}
7315	12.78	1.82
7516	19.37	3.04×10^{-5}
8245	30.14	1.26
7306	30.03	3.07

6.2 Input Rise Time

For an input to excite the approximate step response of a system, the input must be sufficiently close to a step. In other words, the rise time of the input signal must be sufficiently fast compared to the rise time of the excited system. This poses a unique challenge for PCB132 sensors since the sensor rise time is on the order of 1 μs. Thus, a very fast increase in pressure is needed to excite the step response of PCB132 sensors. Additionally, all experimental excitation will be imperfect, and so it is not possible to achieve a perfect step response. PCB132 sensors are frequently used for hypersonic boundary-layer transition measurements, and so it is necessary to evaluate the PCB132 performance for pressure steps in the relevant amplitude. As previously discussed, the approximate upper limit of this relevant pressure range is 7 mbar. As will be discussed in more detail in Section 6.2.2, the combination of requirements for low-pressure steps and fast, thin shocks are difficult to achieve in the P3IST.

Here, input rise time will be defined as the time it takes for the shock to completely move over the sensor. Rise time for pitot and static-mode are given in equations 6.2 and 6.3, respectively. Rise time is based on the shock thickness, Δ_s, and shock speed, u_s, but also the sensing diameter of the static-mode PCB132, d_{sens}.

$$t_{rise,\ pitot} = \frac{\Delta_s}{u_s} \qquad (6.2) \qquad t_{rise,\ static} = \frac{\Delta_s + d_{sens}}{u_s} \qquad (6.3)$$

In static mode, the input rise time will largely be determined by PCB132 sensor sensing area and shock speed. For PCB132B sensors, the piezoceramic crystal is 0.035 in (0.89 mm) in diameter. Ort & Dosch computed a sensing diameter that was 10% larger than the piezoceramic crystal for a PCB132B sensor. This is an estimate for a single sensor, and so variation in the effective sensing area is expected. The increase in sensing area is likely due to pressure acting on the epoxy surrounding the sensing element transferring stress to the sensing element, effectively increasing the area of sensitivity [2]. The shock thickness is on the order of the mean free path of the driven gas [57]. For a typical driven pressure of 1 mbar, the mean free path is 0.057 mm, about 6% of the effective sensing diameter found by Ort & Dosch. The shock thickness could be comparable to the sensing diameter at low driven pressures, but will generally be smaller for most driven pressures used in the P3IST. Shock thickness effects will be discussed more in Section 6.2.1.

6.2.1 Shock Thickness

Measurements of shock thickness in the P3IST are not available, and so the shock thickness must be estimated to evaluate the rise time of the pressure-input signal in the P3IST. There are two broad categories of analytical solutions of 1D shock flows: approximate solutions of the Navier-Stokes equations, and approximate solutions of the Boltzmann equation. Solutions of the Navier-Stokes equations treat the flow

through the shock as continuous and one-dimensional. Solutions of the Boltzmann equation approach the problem as a molecular process [57].

Two models were used to predict the shock thickness in the P3IST: an approximate solution of the Navier-Stokes equations derived by Shapiro and Kline, and an approximate solution of the Boltzmann equation derived by Mott-Smith. The model derived by Shapiro and Kline is a solution of the exact Navier-Stokes equations for a one-dimensional, viscous region [58]. The shock thickness, Δ_s, is given in Equation 6.4 as a function of viscosity, μ, density, ρ, speed of sound, a, ratio of specific heats, γ, Mach number, M, the function G, and the function D, which is a function of Pr, M^*, and γ. The superscript $(\ )^*$ refers to critical values, or values where $M = 1$. The term n is a constant which equals 0.768 for air. The complete model is in [58, p. 133], Equations 5.39a and 5.39b. The model was implemented using perfect gas relations to find critical values, a look-up table to find the Prandtl number of air, and Sutherland's viscosity law to determine the viscosity.

$$\Delta_s = \frac{\mu_1}{\rho_1 a_1} \frac{D}{(\gamma+1)M^*} \frac{M^*+1}{M^*-1} \left[\frac{\gamma+1}{2} \left(1 - \frac{\gamma-1}{\gamma+1} M^*\right) \right]^{(1/2-n)} G(D, \gamma, M^*, Pr^*) \quad (6.4)$$

The model derived by Mott-Smith is a solution of the Boltzmann equation, and assumes a distribution function to model the temperatures and average velocities of the gases from the upstream and downstream regions. The ratios of the molecules vary based on the distance from the shock. The shock thickness is given in Equation 6.5, where l is the mean free path of the driven gas, and B is a function given in Equation 43 in [59]. The model is implemented using values for B from Table 1 in [59].

$$\Delta_s = 4l/B \quad (6.5)$$

These shock thickness models are compared in Figure 6.4. The shock thickness is normalized by the mean free path. The mean free path will change based on the driven-gas pressure, so the shock thickness is a function of both driven-gas pressure

and incident-shock Mach number. Both shock-thickness models predict a similar trend of decreasing shock thickness with increasing Mach number. The prediction of shock thicknesses on the order of the mean free path agrees with experimental shock-thickness measurements [57]. As a reference, the mean free path in the driven section of the P3IST is 0.057 mm for a typical driven pressure of 1 mbar. Both models show similar trends, and it is unclear which is more accurate for shocks produced in the P3IST.

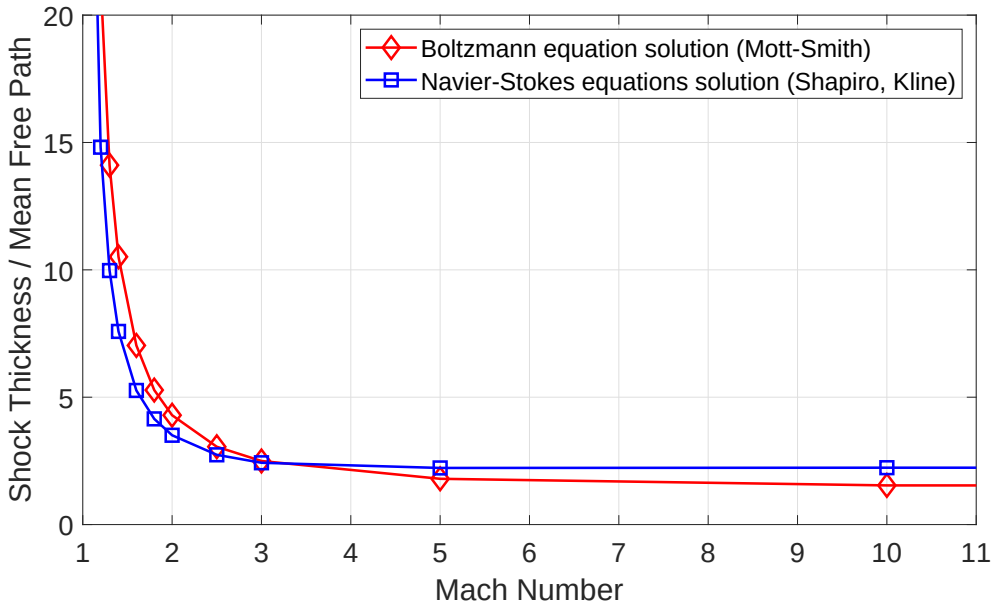

Figure 6.4.: Predicted shock thickness divided by mean free path as a function of incident-shock Mach number.

6.2.2 Shock Tube Performance

Since there are no clear differences between the shock-thickness models, the approximate Navier-Stokes solution presented by Shapiro and Kline was chosen to predict the rise times for shocks in the P3IST. This model will be referred to as the Navier-Stokes-solution model. Currently, shock-thickness measurements in the P3IST

are not available. Work is being performed with focused laser differential interferometry (FLDI) to measure shock thickness in the P3IST, but was not available at the time of writing [60]. In the absence of shock thickness measurements in the P3IST, it is unclear how accurate the models are for this particular application. The shock thickness computed with the Navier-Stokes-solution model is influenced by the temperature, Mach number, and density. Since the initial gas temperature in the P3IST is assumed to be at room temperature, the shock thickness is mainly a result of the density of the driven gas and the Mach number of the incident shock. To examine rise times possible in the P3IST, the shock speed and thickness were calculated based on perfect gas relations from feasible driver and driven pressures.

Figure 6.5 shows the predicted rise time based on the Navier-Stokes-solution model and shock tube relations for both static and pitot modes. Note that colors are shown scaled logarithmically. Areas left blank are where the driven pressure is higher than the driver pressure, i.e. conditions at which a shock tube would not function as intended. Figure 6.5(a) shows that the minimum static-mode rise time occurs for a driven pressure close to 1 mbar and a driver pressure close to 1000 mbar. This minimum is a balance of a low shock thickness and a fast shock. Higher driven pressures reduce the pre-shock pressure ratio, (p_{driver}/p_{driven}), which reduces the shock speed. Lower driven pressures increase the shock thickness. A high driver pressure increases the pre-shock pressure ratio and increases the shock speed. Figure 6.5(a) also shows that the lowest static-mode rise time achievable in the P3IST is slightly less than 1 μs, or close to many measured PCB132 rise times. This implies that the available input rise times for statically-mounted PCB132 sensors in the P3IST are too high to sufficiently evaluate the sensor's frequency response.

Figure 6.5(b) shows that the rise time for pitot-mounted sensors is lowest for large driven pressures because the shock is thinner. There is a slight trend in rise time with increasing driver pressure, but a much stronger decreasing trend with increasing driven pressure. Higher driver pressures generally correlate with higher pre-shock pressure ratios, and thus higher incident shock speeds. Higher driven pressures

correlate with higher driven-gas densities, and thus thinner shocks. The predicted pitot-mode rise time follows an expected trend: the fastest and thinnest shocks will produce the lowest rise times.

While sufficiently fast rise times appear achievable in the P3IST, low-magnitude pressure steps at these conditions are not. This is shown in Figure 6.6, where the pressure steps for both pitot and static mounting are predicted using perfect-gas shock tube relations. The region of flow conditions which generate pressure steps across the shock less than the second-mode upper limit of 7 mbar is shaded. It should be noted that the pressure step is the difference in pitot pressure across the shock for pitot-mode pressure steps and the difference in static pressure across the shock for static-mode pressure steps, as discussed in Section 3.3. Pressure steps in pitot mode are much higher than in static mode. The fastest rise times in pitot-mode correspond to the highest pressure steps. Additionally, pressure steps below the 7 mbar limit correspond with slow rise times for both pitot and static modes.

This illustrates the challenge of calibrating PCB132 sensors with the P3IST: evaluating the PCB132 sensors with higher amplitude pressure steps in the P3IST could have fast enough rise times for calculation of frequency response, but will have pressure steps outside the second-mode range. Thus, calibration of PCB132 sensors with the P3IST is a trade off between evaluation in the useful pressure-amplitude range and evaluation with fast pressure-input signals.

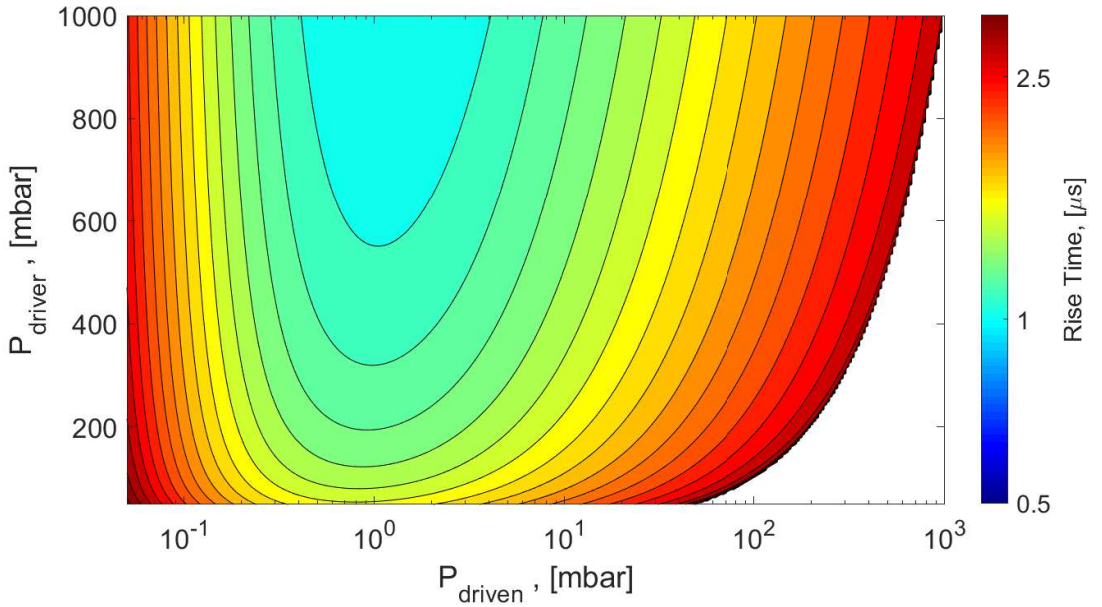

(a) Static-mode rise time

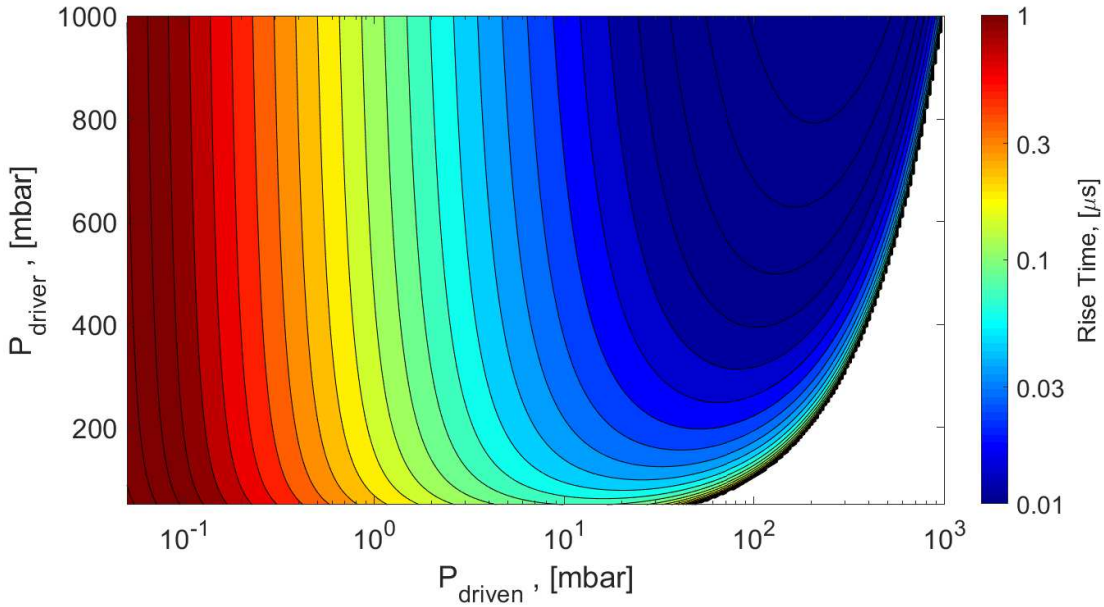

(b) Pitot-mode rise time

Figure 6.5.: Predicted rise time in P3IST based on pre-shock pressures for both static and pitot mounting. Note logarithmic color scaling.

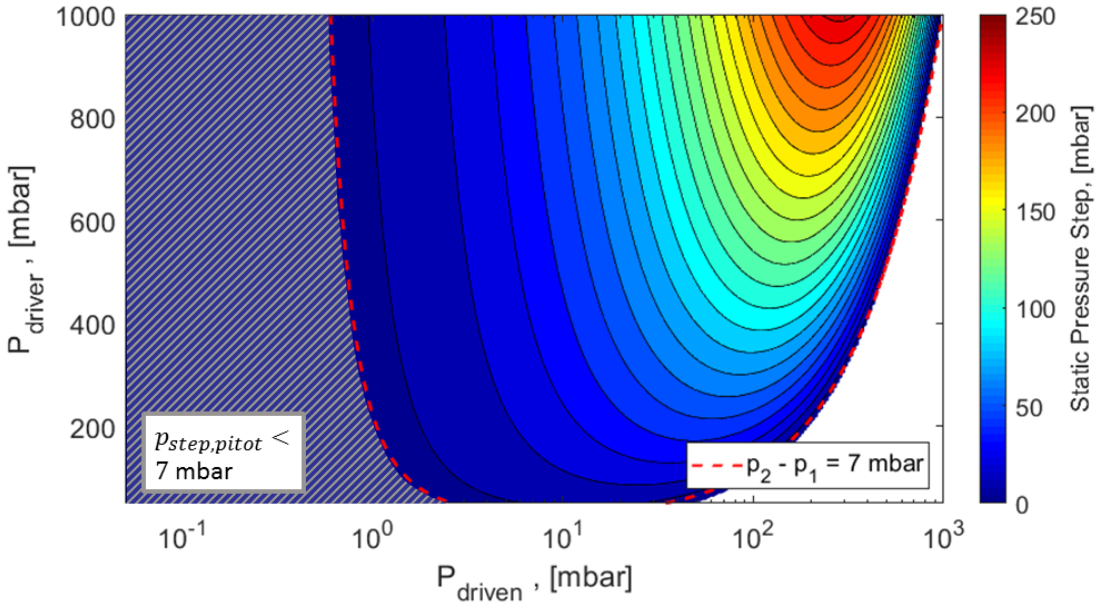

(a) Static-mode pressure step

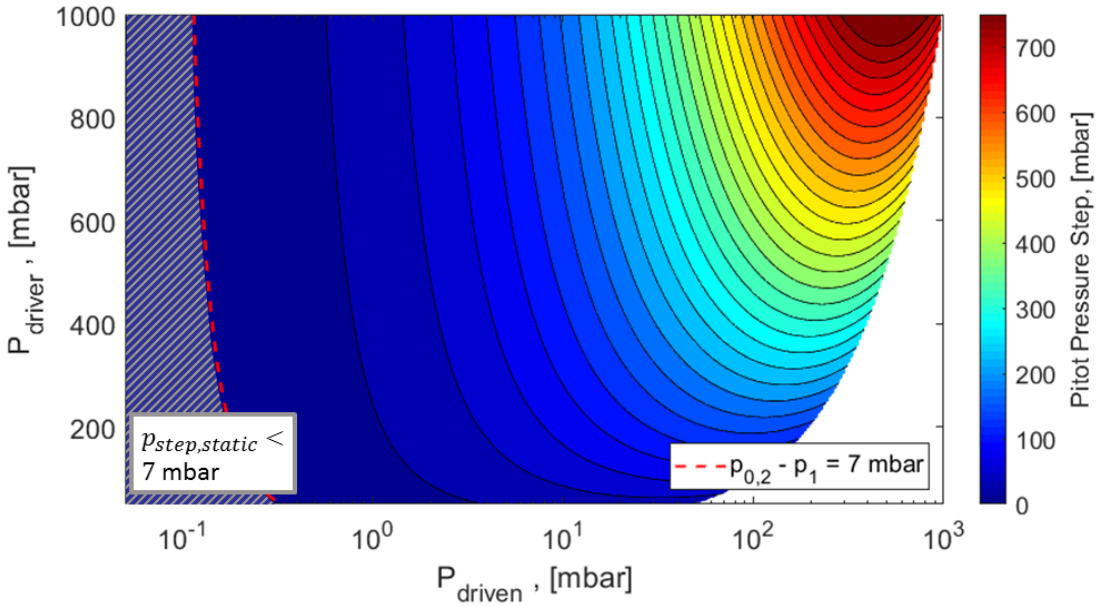

(b) Pitot-mode pressure step

Figure 6.6.: Pressure step for static and pitot mounting calculated with shock tube relations.

6.2.3 PCB132 Sensitivity Comparison

The effect of a slower input rise time can be qualitatively observed by examining the same PCB132 sensor mounted in both pitot and static mode. Berridge measured higher sensitivities for PCB132 sensors in pitot mode than in static mode. This behavior is shown in Figure 6.7(a), where the step sensitivities are compared for the same sensor in both static and pitot modes. Step sensitivity is the PCB132 response divided by the measured pressure step. The two traces show a similar roll-off, but have different peak heights and rise times. The pitot-mounting case also shows more oscillations than the static-mounting case.

This behavior is expected if the pressure-input signal in static mode is not as steep. The static-mounted response behaves similarly to the pitot-mounted response after the shock passes, but exhibits less ringing. This could occur if the step input has less content at the ringing frequency.

Figure 6.7(b) shows the Fourier transform of the responses in Figure 6.7(a). The signals were windowed using a half-Hann window 150 μs long starting immediately before the shock arrival. There is a peak at 272 kHz evident in both Fourier transforms. The static-mounted trace also exhibits a much lower sensitivity than the pitot-mounted trace for almost all frequencies. This could be explained if the static response was subject to slower ramp input than the pitot response. A slower ramp-type input would be expected to exhibit lower-amplitude frequency content than a steeper ramp-type input. This would produce a lower amplitude response from a system, and so could explain the difference in frequency response shapes between static and pitot-mounted sensor responses.

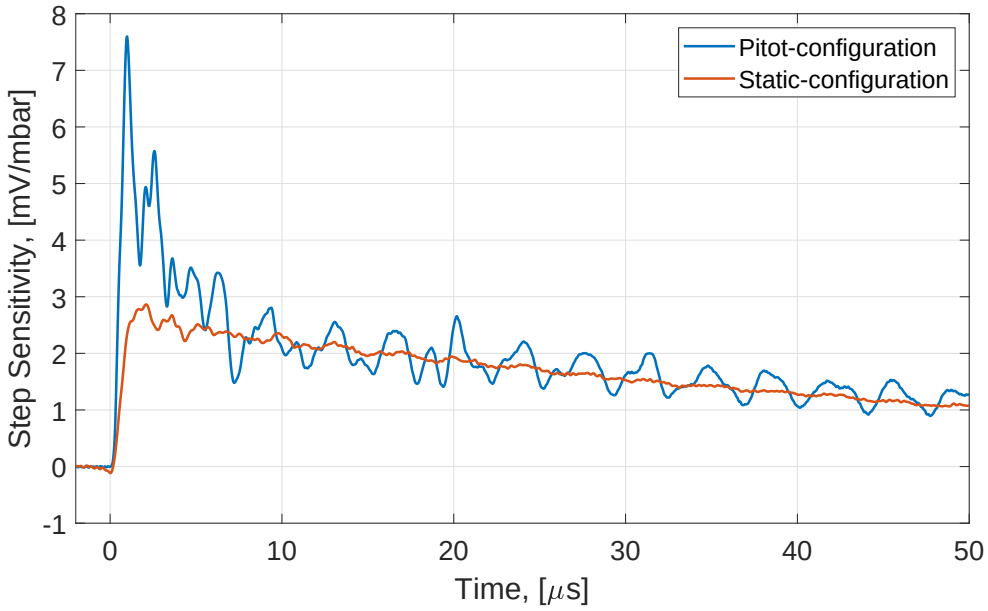

(a) Time domain

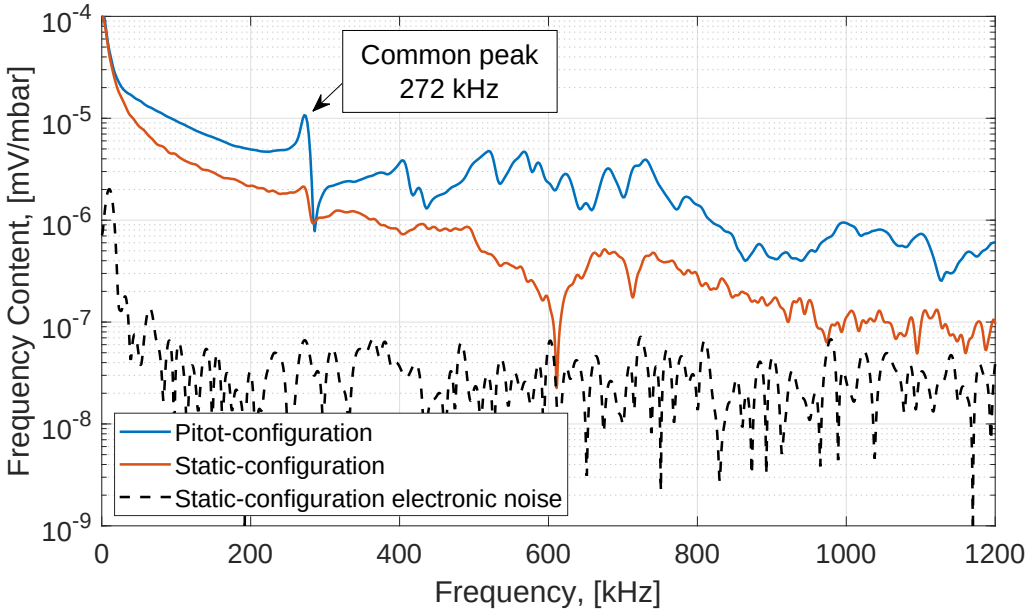

(b) Frequency domain

Figure 6.7.: Step sensitivity for PCB132 SN 8247 mounted in pitot and static mode. Pitot-mode: p_{driven} = 1.31 mbar, p_{driver} = 280.9 mbar. Static-mode: p_{driven} = 0.90 mbar, p_{driver} = 469.0 mbar.

6.2.4 Variation of PCB132 Pitot Responses

It is not possible to set the P3IST to achieve small pressure steps that are also very steep. Low-magnitude pressure steps correspond to slower rise times, as discussed in Section 6.2.2. Attempts to separate the effects of input rise time from step magnitude are discussed by Lay in [55].

Figure 6.8(a) shows the variation in PCB132 pitot-response traces for different input rise times, normalized by the peak height. Normalizing by the peak height allows for observation of the variation of the response shape. The input rise times are predicted based on the measured shock speed and shock thickness predicted by the Navier-Stokes-solution model, as described in Equation 6.2. If the PCB132 sensor is behaving linearly and the pressure inputs are the same shape, the traces should collapse to the same curve. As previously mentioned, the shape of the pressure-input signal is unknown due to the the absence of independent measurements of the pressure change across the shock. The three runs with the fastest input rise times collapse to the same curve fairly well, with small differences in the responses with increasing input rise time. The responses with the fastest input rise times roll off more dramatically from the initial peak than those with slower input rise times. The response appears to exhibit complex, high-frequency oscillations, which repeat consistently between runs with similar input rise times.

Figure 6.8(b) shows the variation in normalized frequency response, or the frequency response divided by the voltage peak. The responses with the lowest input rise times produce thinner, better-defined peaks in the frequency domain. As the input rise time becomes slower, these peaks become lower magnitude and wider. The peaks are still present for the runs with slower input rise times, but with reduced magnitude. For the slowest input rise times, the higher-frequency peaks are close to the electronic noise floor. This could be explained by the slower input signals having less high-frequency content, not exciting the PCB132 sensor at higher frequencies as much as the faster input signals.

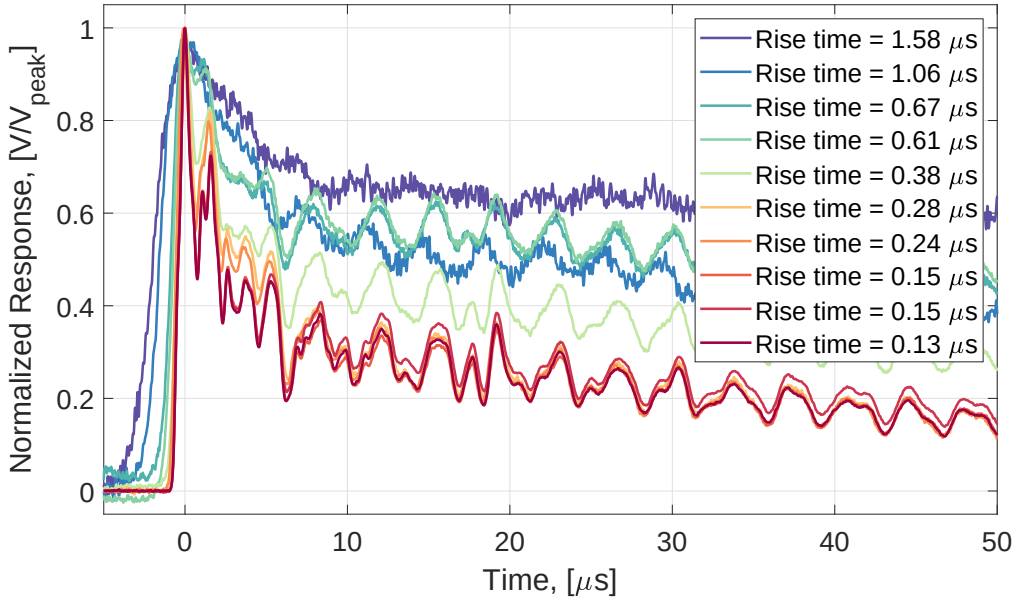

(a) Pitot-mode time traces

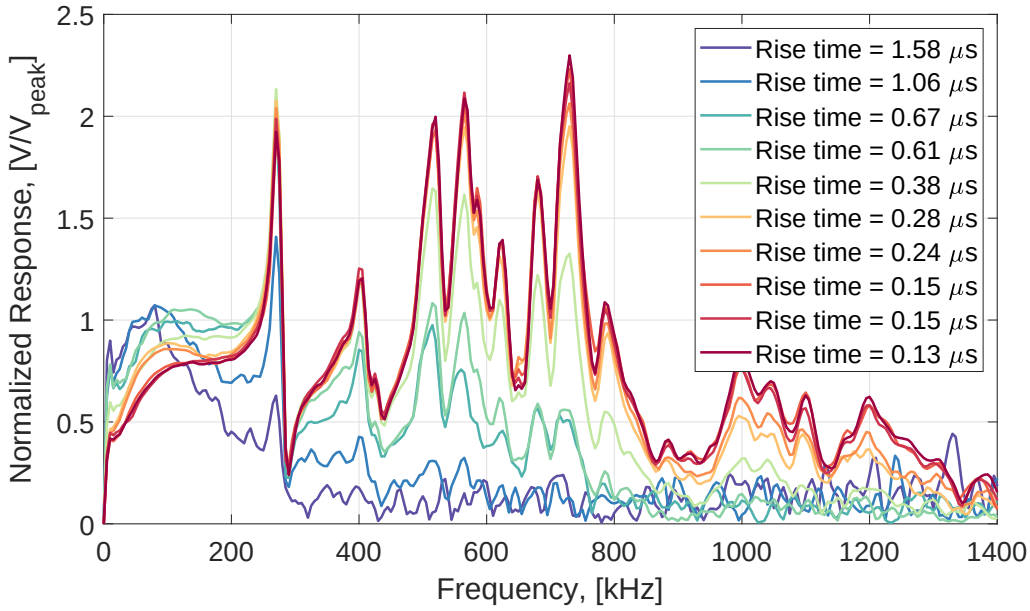

(b) Pitot-mode frequency response

Figure 6.8.: PCB132B SN 8247 pitot-response variation. Time traces lowpass filtered at 5 MHz. Frequency response calculated from 100 μs of data, zero-padded to twice the original length. Rise time calculated from measured shock speed and shock thickness predicted with Navier-Stokes-solution model. Sensor pitot mounted at $x/d = 37.7$.

It should be noted that while a variation in input rise time appears to produce the variation in PCB132 responses shown in Figure 6.8, the pitot pressure step was not kept constant between runs. The pitot-pressure step experienced by the sensors is shown in Figure 6.9, and shows that the pressure step follows a similar trend to input rise time. Because of this, the effects of rise time cannot be separated from the effects of the pressure step. As discussed previously, low-pressure steps at fast input rise times are not achievable with the P3IST. Because of this, the effect of only rise time on PCB132 sensor response is difficult to evaluate at low pressures.

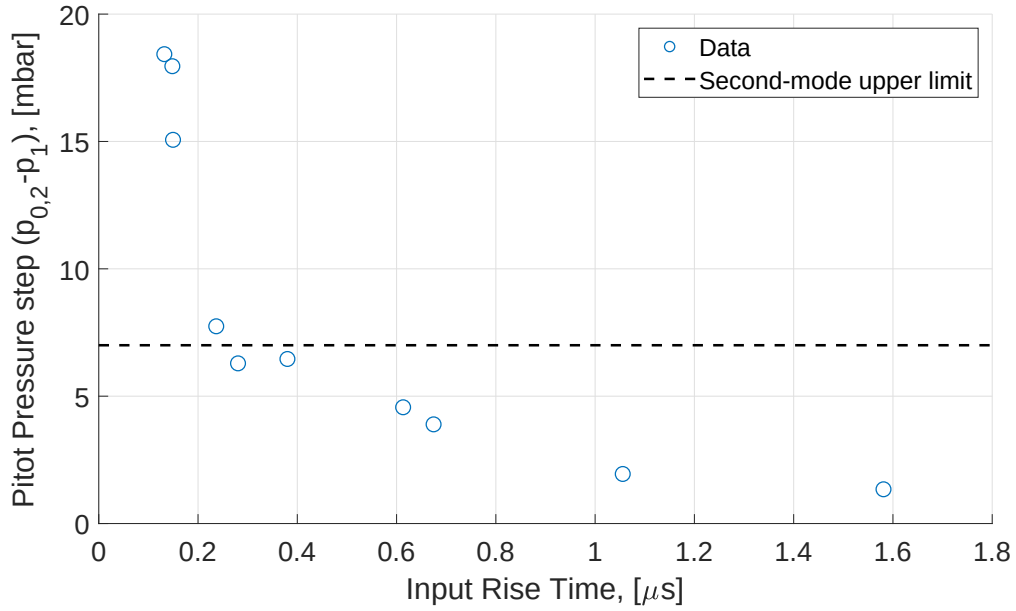

Figure 6.9.: Pitot pressure step $(p_{0,2} - p_1)$ for runs with predicted input rise times shown in Figure 6.8.

A similar trend for a different sensor is shown in Figure 6.10. Similarly, the runs with the fastest input rise times show more defined, complex behavior in the time domain. The frequency response shows larger peaks for responses with faster input rise times, and smaller peaks for slower input rise times, similar to Figure 6.8(b). The peak near 230 kHz is higher magnitude for some responses with slower input rise times, differing from the behavior in Figure 6.8(b). It is unclear why this occurs, but

these responses with the higher peak at 230 kHz appear attenuated at the higher-frequency peaks, as expected.

As with the responses shown in Figure 6.8, the pressure steps used to generate the responses in Figure 6.10 are lower for faster input rise times. This is shown in Figure 6.11, where the pitot pressure steps decrease with increasing input rise time for the conditions tested.

Higher-magnitude pressure steps with faster input rise times were tested with a pitot-mounted PCB132 sensor. Figure 6.12 shows the variation in pitot responses of a PCB132 sensor due to pitot pressure steps from 11–124 mbar with input rise times between 0.01–0.15 μs. Figure 6.12(a) shows some variation in the time trace of the PCB132 responses to the varying pressure step and input rise time. This variation is much less dramatic than the variation shown in Figure 6.10, likely because the input rise times are much faster. The responses vary in magnitude in the roll off after the initial peak, but seem to have the same complex, repeatable response shape.

Similarly, the approximate frequency responses shown in Figure 6.12(b) have little variation in frequency content. Clear disagreement in frequency content between runs occurs at frequencies higher than 700 kHz. The three responses with input rise times less than 0.1 μs have similar frequency content, with slight differences clear for the slower input rise time responses. This agreement between the responses indicates that the PCB132 sensor is likely a linear system in this pressure range. It is thought the slight differences are due to differences in the input rise time, however it is not certain due to the changing pressure step.

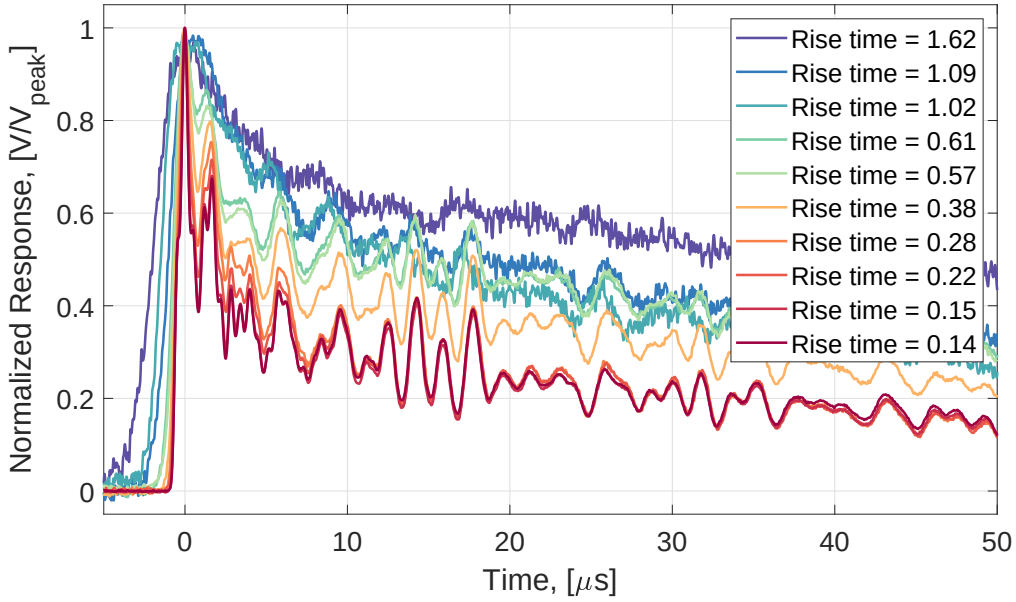

(a) Pitot-mode time traces

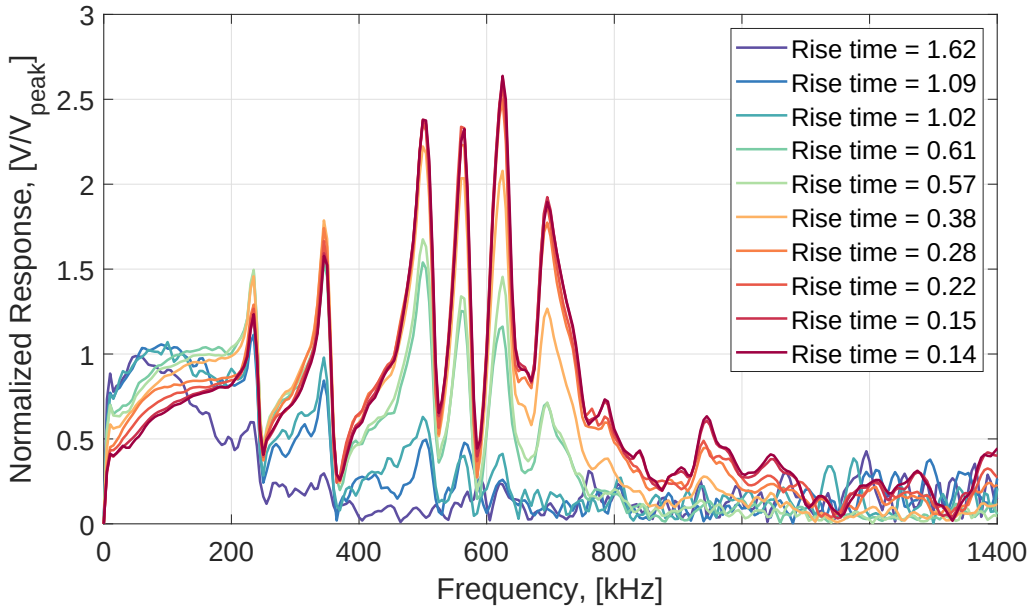

(b) Pitot-mode frequency response

Figure 6.10.: PCB132B SN 8246 pitot-response variation. Time traces lowpass filtered at 5 MHz. Frequency response calculated from 100 μs of data, zero-padded to twice the original length. Rise time calculated from measured shock speed and shock thickness predicted with Navier-Stokes-solution model. Sensor pitot mounted at $x/d = 37.7$.

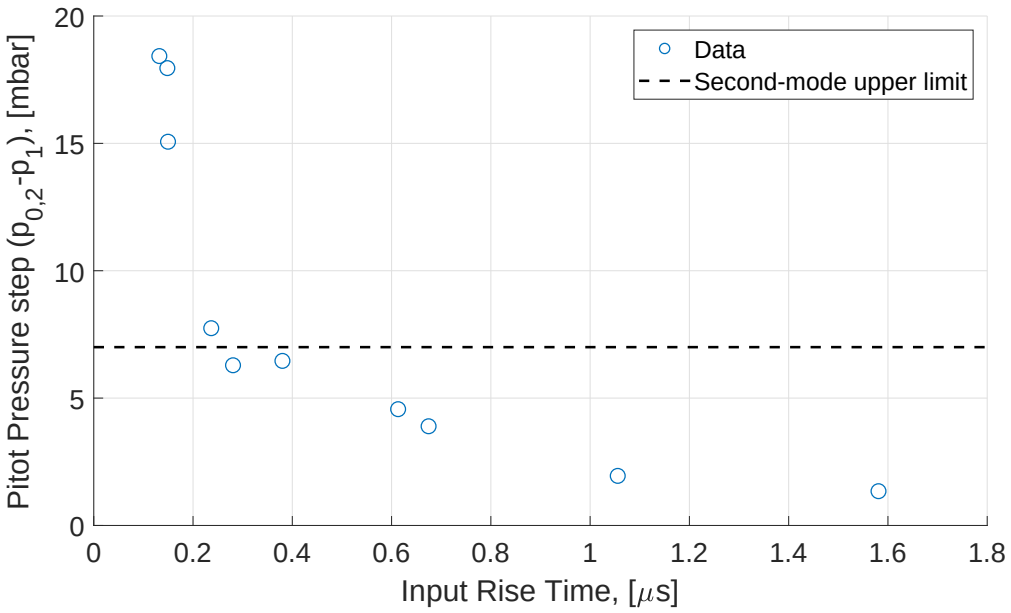

Figure 6.11.: Pitot pressure step $(p_{0,2} - p_1)$ for runs with predicted input rise times shown in Figure 6.10.

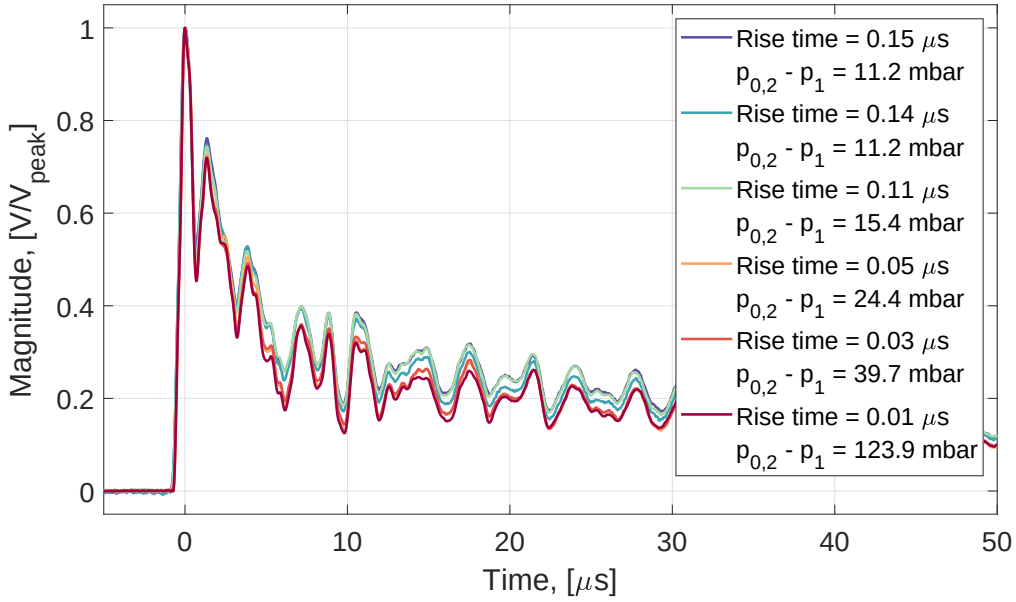

(a) Pitot-mode time traces

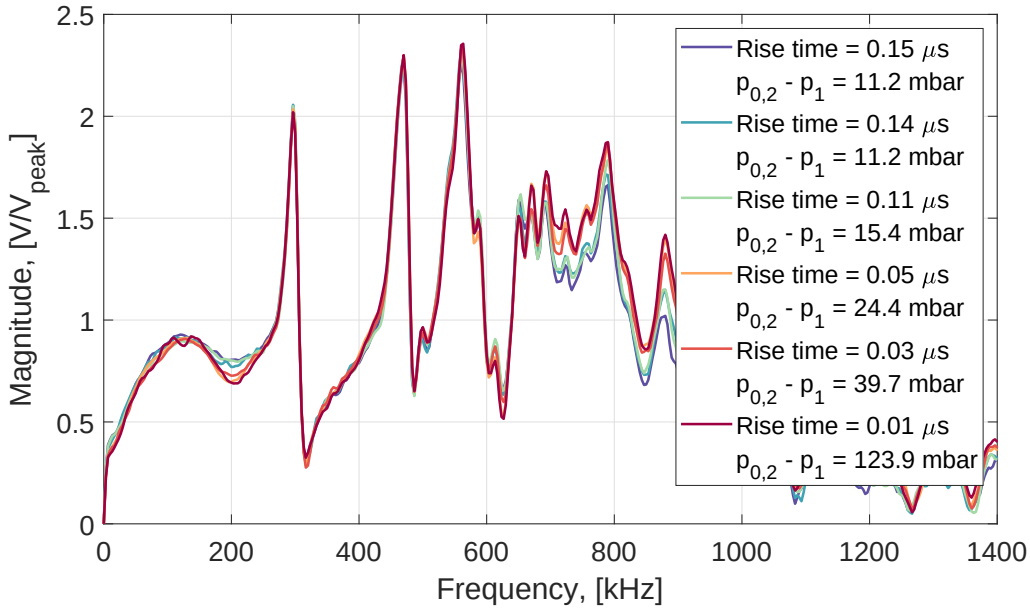

(b) Pitot-mode frequency response

Figure 6.12.: PCB132B SN 8121 pitot-response variation. Time traces lowpass filtered at 5 MHz. Frequency response calculated from 150 μs of data, zero-padded to twice the original length. Rise time calculated from measured shock speed and shock thickness predicted with Navier-Stokes-solution model. Sensor pitot mounted at $x/d = 37.7$.

6.3 Blinded Pitot Sensor

PCB132 sensors are sensitive to vibration, so a measured response could be partially due to vibration excited by the shock passage. If the response were influenced by vibration, the frequency response computed from P3IST measurements resulting from the passing shock could be significantly different from the actual frequency response. To determine if vibration is a factor, a blinded pitot test was performed. The blinded sensor should have a similar vibration response, but no pressure response, showing the dependence of the frequency response on vibration.

Due to the construction of PCB132 sensors, it is difficult to properly blind the sensor without recessing the sensor face; simply adding a layer of tape on the sensor face will cause the sensor to still register some pressure change. To blind a pitot-mounted PCB132, the sensor was slightly recessed, as shown in Figure 6.13(b). The amount the sensor was recessed was not measured, although it is estimated as close to 2.5 mm. The pitot-probe body is about 110 mm long. A small amount of cotton was added as a spacer to damp any pressure change that leaked through the tape. Aluminum tape was applied to the front of the probe. Since PCB132 sensors are high-pass filtered, the tape did not have to make a seal. The tape must only slow the pressure change enough that it is filtered by the built-in 11 kHz high-pass filter in the PCB132 sensor. Because a seal was not made over the sensor, it is more accurate to say the sensor was partially blinded.

Figure 6.14(a) shows a comparison of the un-blinded and blinded pitot responses for the same sensor. The blinded time trace is aligned with the un-blinded time trace based on the predicted shock arrival at the sensor. The blinded response shows a lower amplitude peak with fewer high-frequency oscillations. Figure 6.14(b) shows that the frequency content of the un-blinded response has distinct peaks at frequencies higher than 250 kHz. These peaks in the frequency domain are absent in the blinded case. Most of the frequency content in the blinded sensor response is at a lower frequency, and higher frequency content is close to the electronic noise floor. The un-blinded

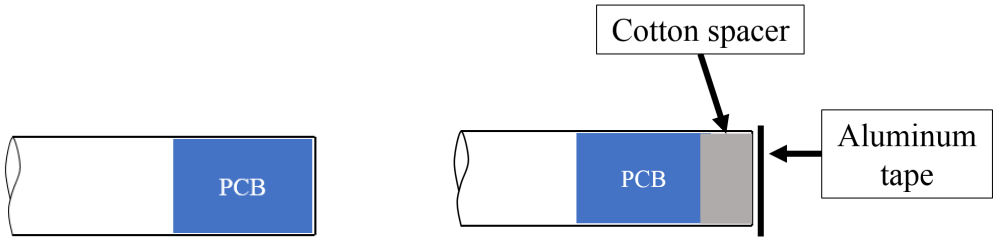

(a) Un-blinded sensor (b) Blinded sensor

Figure 6.13.: Blinded PCB132 schematic.

and blinded responses are expected to be influenced similarly by vibration. This implies that the high-frequency content in the un-blinded response is likely not due to vibration.

Some uncertainty could have been introduced by the blinding method. By using the cotton spacer and aluminum tape, the front of the probe was no longer rigid, possibly damping some vibration. This could have changed the frequency content that would normally be present due to vibration. Because of this, blinded sensor tests should be performed in the future with a more rigid blinded mount.

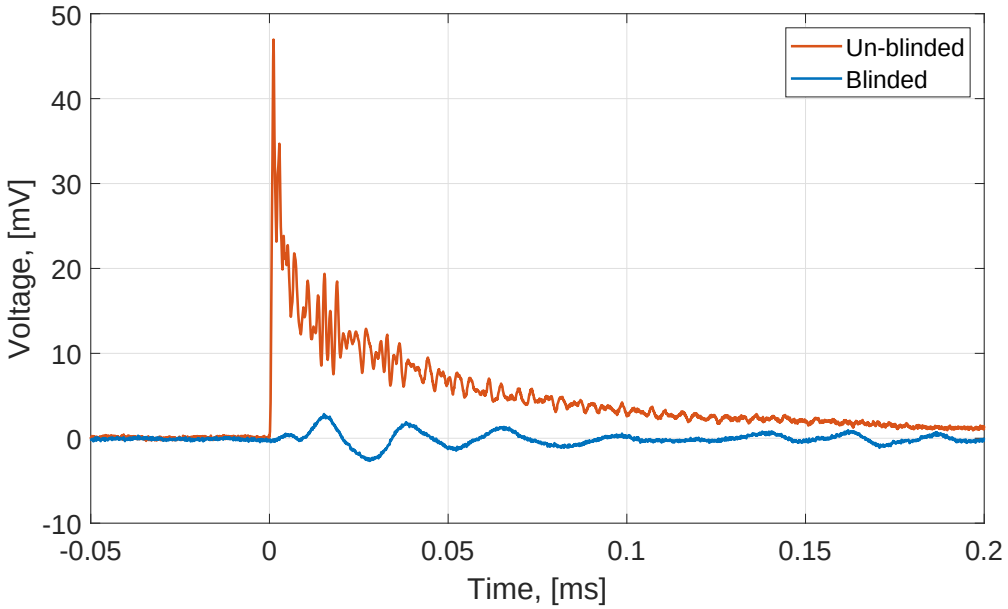

(a) Time Domain

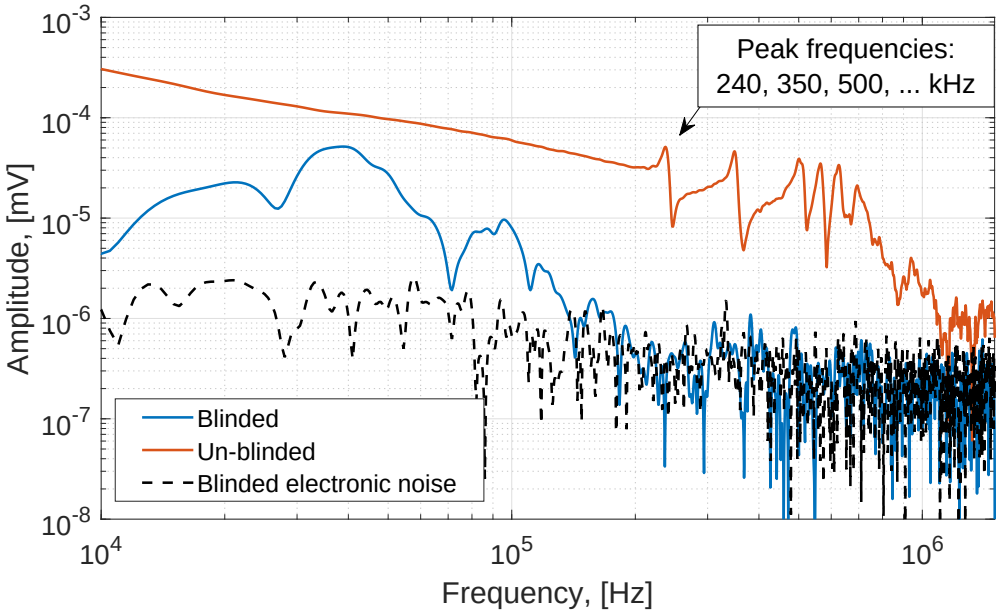

(b) Frequency Domain

Figure 6.14.: Comparison of blinded and un-blinded pitot responses for PCB132B38 SN 8246; p_{driven}= 1.3 mbar, p_{driver}= 66 mbar, nominally. Time trace low-pass filtered at 5 MHz, frequency response calculated with a half-Hann window over 200 μs. Sensor pitot mounted at $x/d = 37.7$.

6.4 Pitot-Mode Response Comparison

The frequency responses calculated from PCB132 step responses measured at similar pressure steps and input rise times were compared for different PCB132 sensors mounted in pitot-mode. Figure 6.15 shows approximate step responses of PCB132 sensors measured in pitot mode in the P3IST normalized by the voltage peak. PCB132 step responses generally show a significant number of oscillations that are repeatable across runs for a given PCB132 sensor. These oscillations are not consistent between different sensors, but similar behavior is evident. Namely, the roll-off after initial response to shock passage is similar. The majority of the oscillations occur immediately after shock passage, and then damp as the response rolls off. The responses also show a similar secondary peak that occurs less than 5 μs after the initial peak. This peak is between 60–85% of the primary peak.

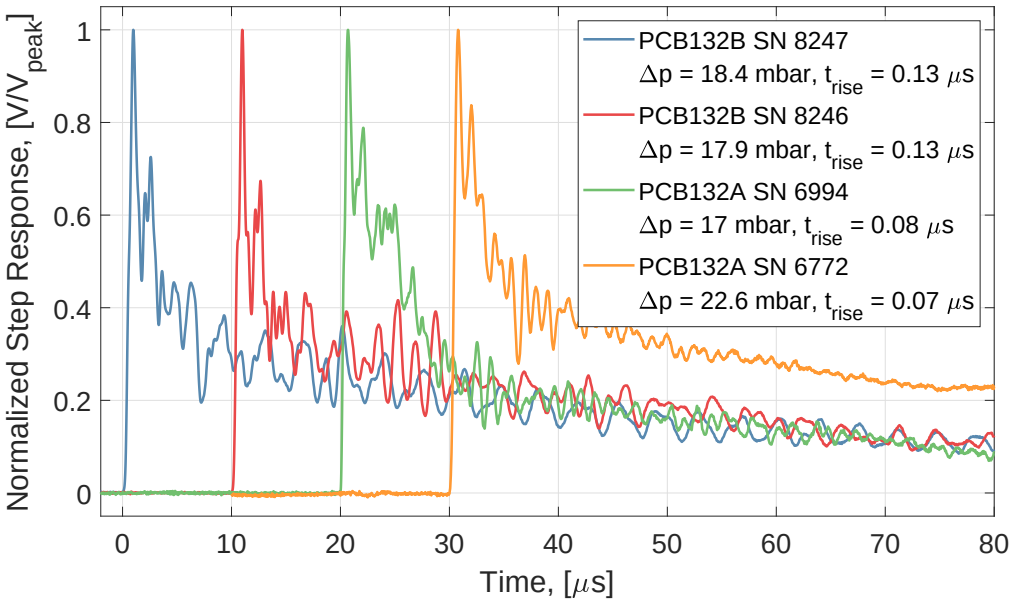

Figure 6.15.: PCB132 step responses normalized by peak voltage peak due to incident shock. Low-pass filtered at 5 MHz. Traces shifted in time for clarity.

A detail view of the initial rise of the responses shown in Figure 6.15 is shown in Figure 6.16. Significant variations between the sensor responses are evident. The secondary peak is present in all responses, however several responses show a smaller peak before this peak occurs. The full rise time of the PCB132 sensor responses in Figure 6.16 appears to vary between 0.6–1 μs. PCB132B SN 8246 shows an inflection point in the initial rise at around -0.5 μs. A similar inflection point was present in pitot-mode responses measured by Berridge [3].

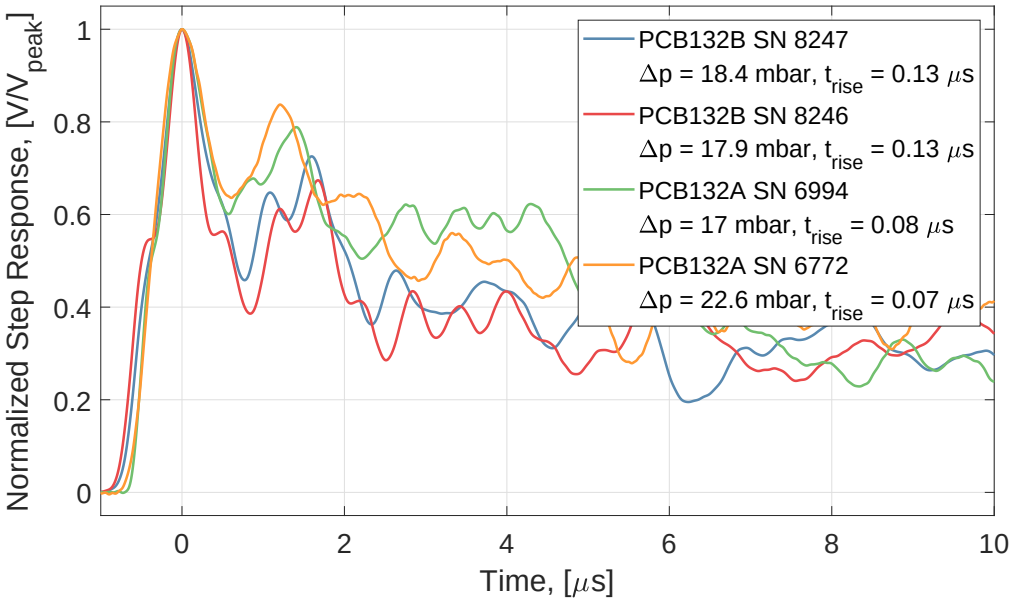

Figure 6.16.: PCB132 step responses normalized by peak voltage peak due to incident shock. Low-pass filtered at 5 MHz.

As discussed in Section 3.4.2, shortening the data traces smooths peaks in the frequency response. To ensure any smoothing effects were consistent between traces, all traces were shortened to the same length. Figure 6.17 shows the approximate frequency responses calculated from the step responses shown in Figure 6.15.

Some behavior is consistent between all four approximate frequency responses. The response is relatively flat for frequencies lower than 200 kHz, and has the first peak in the frequency response between 250–350 kHz. After this peak, the frequency

response shows significant variation across frequencies higher than 400 kHz. The maximum resonance occurs for every sensor at a frequency higher than 600 kHz.

Similar peaks occur in the frequency response for PCB132A and PCB132B sensors, but are shifted to a lower frequency for PCB132B sensors. The first peak in the frequency response occurs for both PCB132A sensors at higher than 300 kHz, while PCB132B sensors show the first peak in the frequency response at around 250 kHz. The PCB132B frequency response seems to roll-off at frequencies higher than 800 kHz, while PCB132A frequency responses show significant content up to 1 MHz. Data from only four sensors are presented here, but the comparison may indicate minor differences between PCB132A and PCB1323B sensors. Additional approximate frequency responses of PCB132 sensors are included in Appendix B.

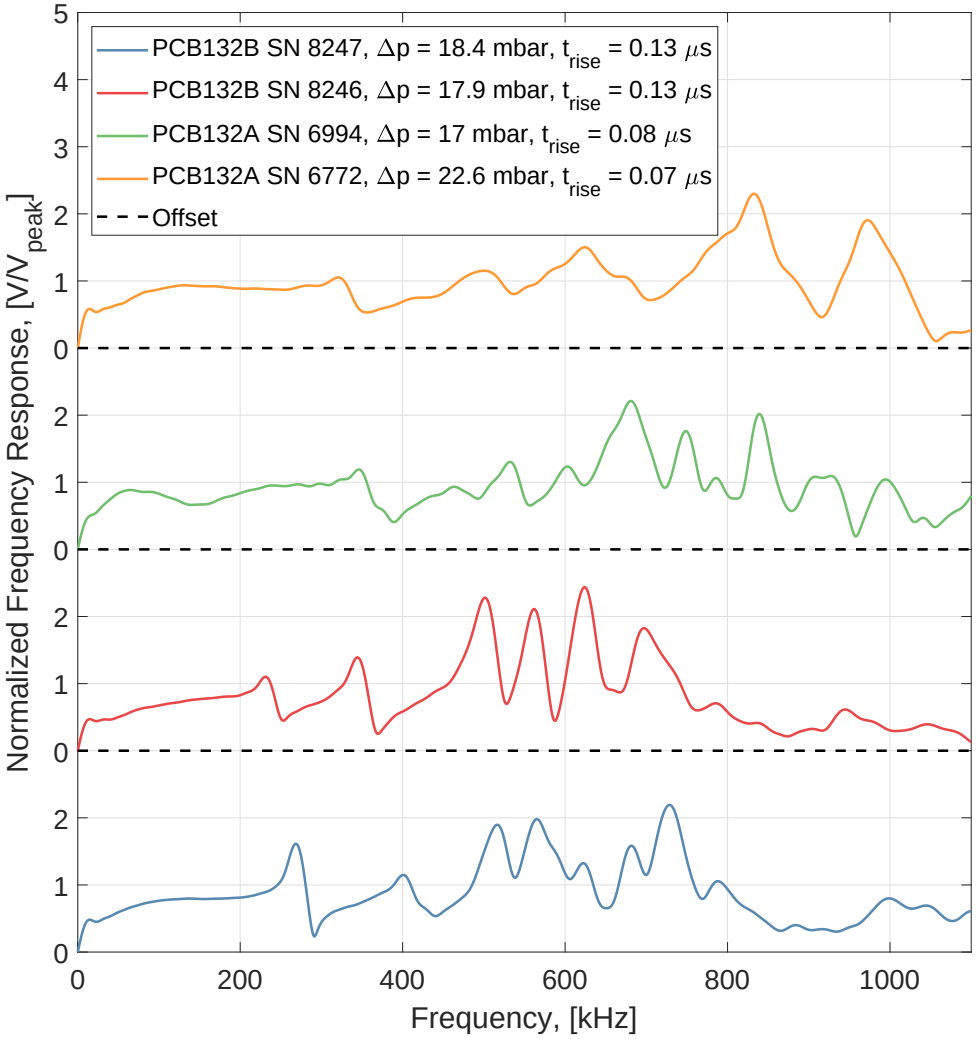

Figure 6.17.: PCB132 frequency responses normalized by peak voltage. Frequency response computed from 60 μs of data windowed with a half-Hann window.

6.5 Experimental Comparison of PCB132 Frequency Response

A PCB132A sensor (SN 6994) and a Kulite XCQ-062-15A A-screen sensor were mounted adjacent to each other in the Boeing AFOSR Mach 6 Quiet Tunnel (BAM6QT) with the goal of comparing the signal power for overlapping frequencies. Unfortunately, the serial number of the Kulite sensor was not recorded. The sensors were mounted in pitot configuration and offset an equal vertical distance from the tunnel centerline, as shown in Figure 6.18. For a Kulite sensor with a diaphragm resonance at 300 kHz, the response should be flat to 90 - 120 kHz [61]. This means the useful overlap region of PCB132 and Kulite sensors is approximately 11 - 100 kHz. The sensors have different sensing areas and probe shapes, both of which will affect the measured pressure fluctuations [48]. Measurements of the probe frontal areas are not available. The Kulite sensor was statically calibrated at eight pressures, producing a linear regression with an R^2 of 1.000, as shown in Figure 6.19.

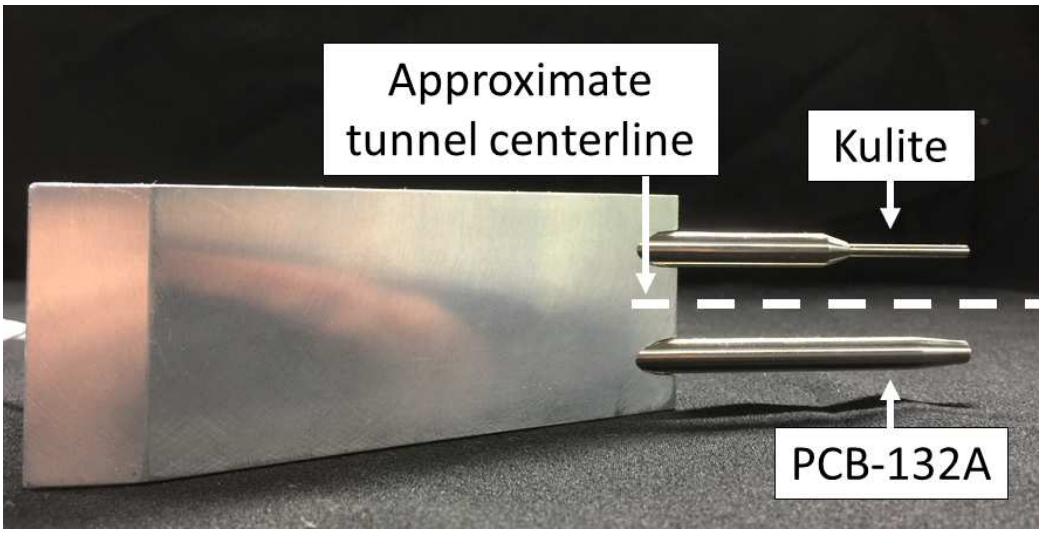

Figure 6.18.: Pitot-probe mounting for testing in BAM6QT.

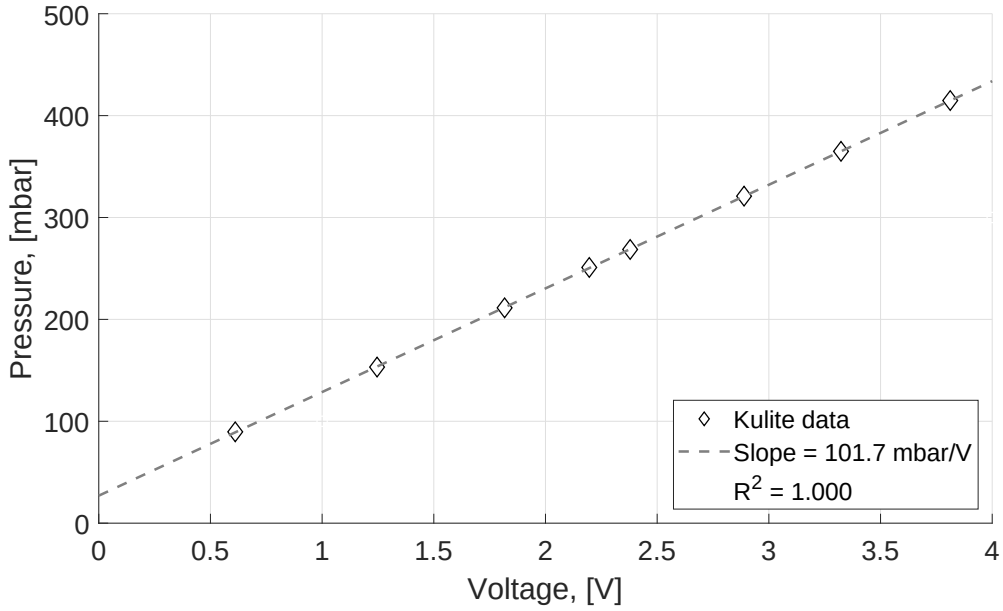

Figure 6.19.: Kulite static in-situ calibration in BAM6QT. Reference pressure measured with a 300 psia Paroscientific Model 740 Digiquartz® Portable Standard pressure gauge.

6.5.1 PCB132 Frequency Response Calculation

Figure 6.20 shows the step sensitivity for PCB132 SN 6994, measured in the P3IST. Step sensitivity is the pitot-step response divided by the pressure step. Step responses were included for pressure steps that produced qualitatively similar responses. Input rise times were predicted with the Navier-Stokes-solution shock-thickness model and the measured shock speed.

Figure 6.21 shows the computed frequency response sensitivity, which is the frequency response divided by the pressure step magnitude. The area between the maximum and minimum frequency response sensitivity is shaded to show the variability in measured responses. The peak resonance of the average frequency response occurs at 681 kHz.

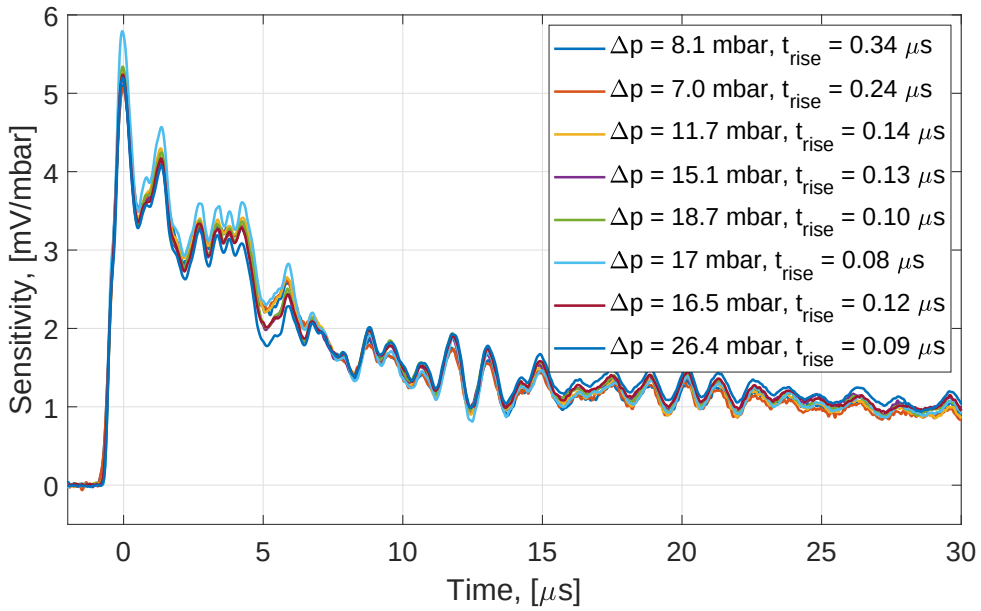

Figure 6.20.: Step sensitivity for PCB132A SN 6994 from P3IST pitot-mode testing.

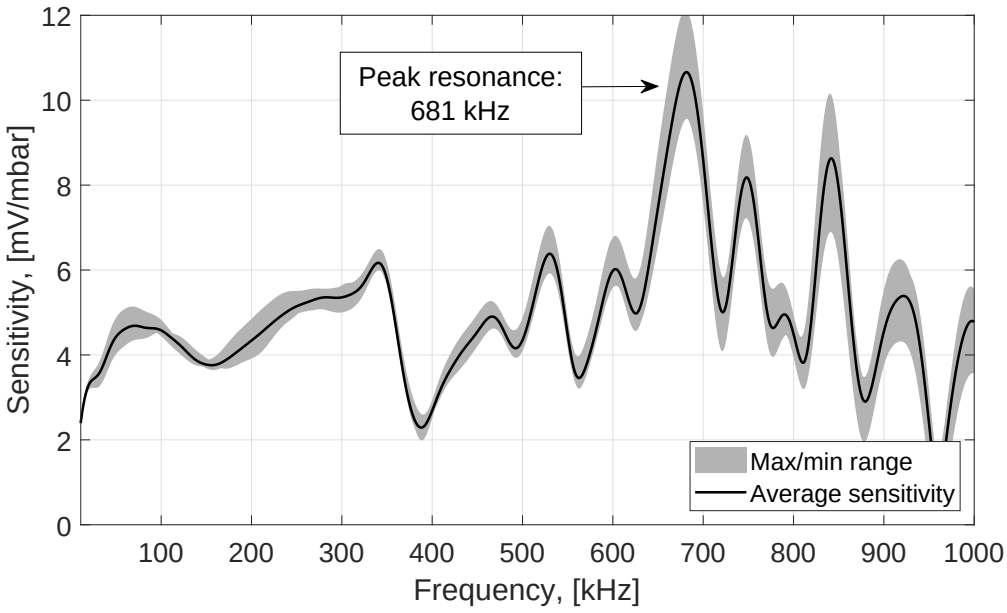

Figure 6.21.: Frequency response computed for SN 6994 from pitot-mounted testing in P3IST, calculated with half-Hann window with 50 μs of data.

6.5.2 BAM6QT Comparison

The average frequency response sensitivity was used to scale the data taken from the BAM6QT. Figure 6.22 shows a comparison of the PSD of Kulite data and the PCB132 data scaled by both the factory calibration and the experimental frequency response. As discussed in Section 3.4.2, the PSD using the approximate frequency response scaling used a custom-implementation of Welch's method of PSD estimation.

The Kulite trace shows a distinct resonance at around 300 kHz, identified as the diaphragm resonance based on similar resonances in other Kulite measurements [62]. Similar peaks are seen in other Kulite PSDs computed from data measured in the BAM6QT [63]. The peak at 60 kHz could be due a Hartmann resonator effect, a resonance caused in a forward-facing cavity. The frequency of this resonance can be calculated using Equation 6.6, where f is the resonance frequency, a_0 is the stagnation speed of sound, L is the cavity depth, and δ_{shock} is the shock standoff distance [64].

$$f = \frac{a_0}{4(L + \delta_{shock})} \tag{6.6}$$

Shock standoff distance was approximated using the experimental correlation for flat-faced cylinders at Mach 5.8 [18, p. 105]. For these tests, the BAM6QT was operated at conditions where the wall boundary layer was turbulent, which effectively decreased the nozzle area and reduced the Mach number to 5.8 [48]. The outer diameter of the Kulite pitot probe was 2.41 mm. The cavity depth used to calculate the resonance was 0.025 inches (0.635 mm), based on the distance from the edge of the sensor housing to the sensing element [65].

The resonant frequency of a Hartmann resonantor for these conditions is calculated as 80.6 kHz, significantly higher than the resonance peak in the PSD near 60 kHz. This difference could be due to an incorrect cavity depth or a difference in the shock standoff distance, but it is unclear. Because of this, the exact cause of the peak near 60 kHz is unknown.

In the range of 11–30 kHz, the PCB132 factory calibration agrees with the Kulite much better than the frequency response found with the P3IST. It is unclear why the pressures from the frequency response calibration found with the P3IST do not match the Kulite well. However, these frequencies are low compared to the frequencies of pressure fluctuations commonly measured with PCB132 sensors in hypersonic boundary-layer transition studies.

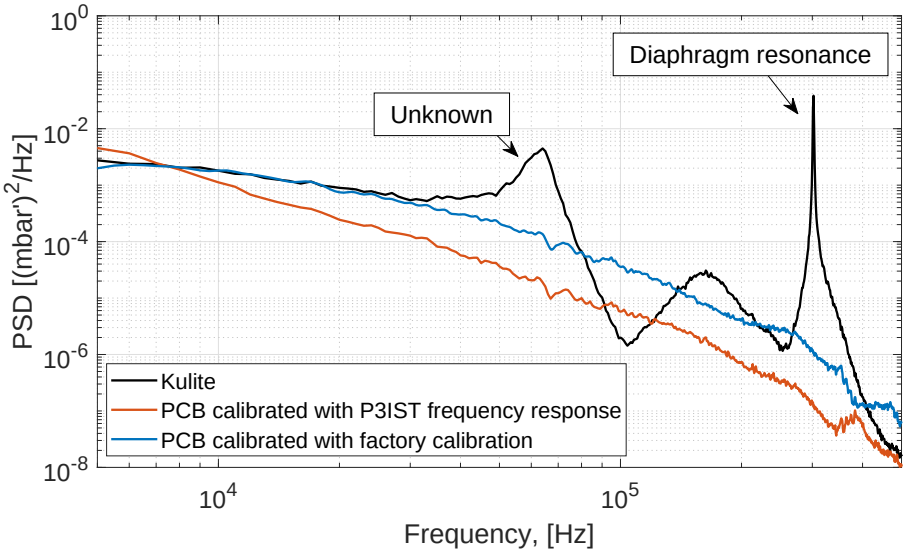

Figure 6.22.: Comparison of PSDs for Kulite and different PCB132 SN 6994 calibrations; $Re_m = 10.35 \times 10^6$, bleeds closed.

Figure 6.23 shows a comparison of PSDs calculated using the PCB132 factory calibration and the present frequency response found using the P3IST. The PSD found with the present calibration does not show the peak near 681 kHz visible in the factory-calibration-scaled PSD. This is the frequency where the maximum sensor resonance was found for PCB132 SN 6994. The overall effect of the frequency response calibration appears to remove peaks from the PSD, however changes are slight.

While this frequency response calibration appears to remove a resonance peak from data obtained from pitot testing in the BAM6QT, other experiments have not shown similar resonance in PCB132 sensors when mounted flush to a model surface.

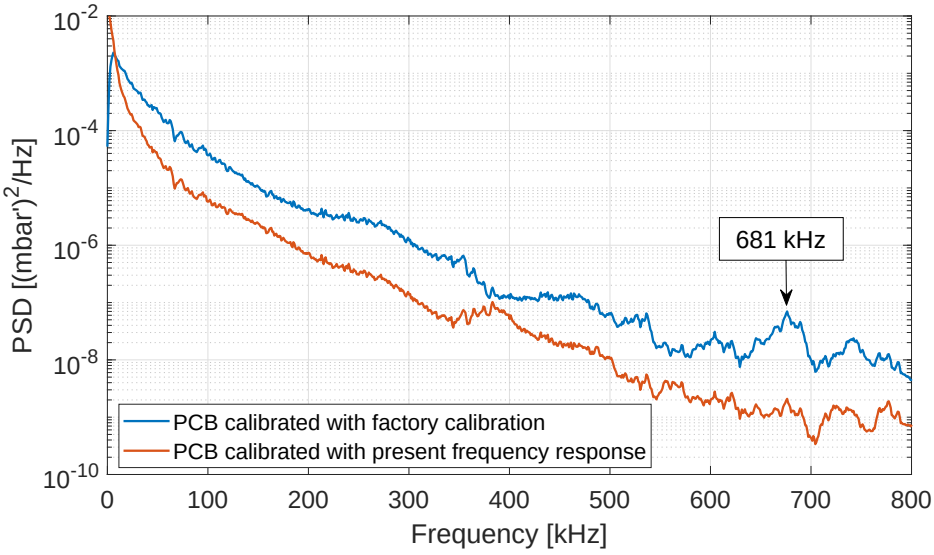

Figure 6.23.: Comparison of PSDs for different PCB132 SN 6994 calibrations; $Re_m = 10.35 \times 10^6$, bleeds closed.

Figure 6.24 shows a comparison of PSDs computed from PCB132A data obtained by Dr. Brandon Chynoweth on a flared cone at varying Reynolds numbers. The PSD shows frequency peaks in the 200-400 kHz range due to the second-mode boundary-layer instability. The first and second harmonics of these peaks appear at frequencies close to the expected multiple of the primary frequency. Some peaks possibly due to a sensor resonance are present, but are at a much lower magnitude than the peaks due to second-mode instability waves. Similarly, other PCB132 measurements made by Chynoweth show little evidence of resonance peaks in the frequency response of PCB132 sensors [6]. It is unclear why these resonances are not in Chynoweth's data, especially at higher frequencies.

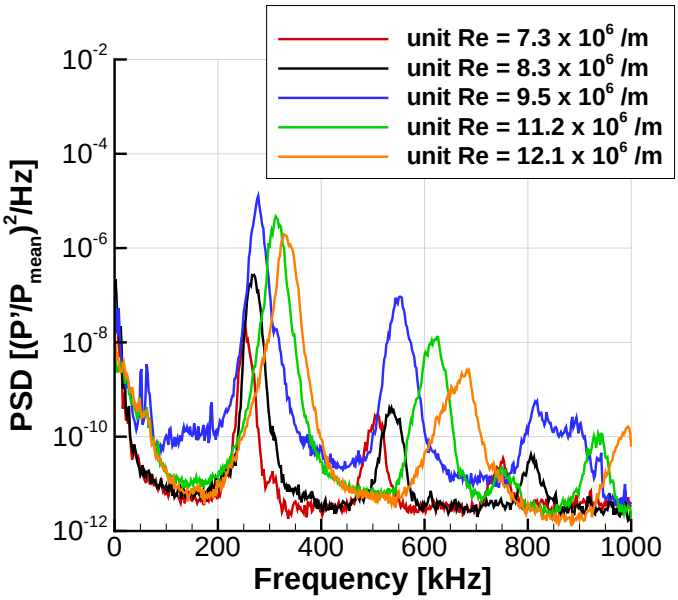

Figure 6.24.: PSD of a single PCB132 sensor at different Reynolds numbers located 0.39 m from the noisetip on a flared cone in quiet flow in the BAM6QT. Plot provided by Dr. Brandon Chynoweth.

An approximate frequency response for another PCB132 sensor run in the BAM6QT was also determined. The PSD of data acquired by Joshua Edelman is shown in Figure 6.25(A), with the frequency response of the PCB132 sensor found with the P3IST shown in Figure 6.25(B). Edelman's data were acquired with the PCB132 sensor flush mounted on a cone at an angle of attack of 6°, 328 mm from the nosetip. The application of the frequency response does not appear to remove peaks in the original PSD, and possibly introduces new peaks. In particular, the peak at around 330 kHz is introduced by scaling the data with the frequency response. This peak does not appear to be a feature of the flow, however it is unclear. The accuracy of the approximate frequency response found with the P3IST is unclear. Future work is needed to better understand PCB132 sensors, especially for static-mode measurements.

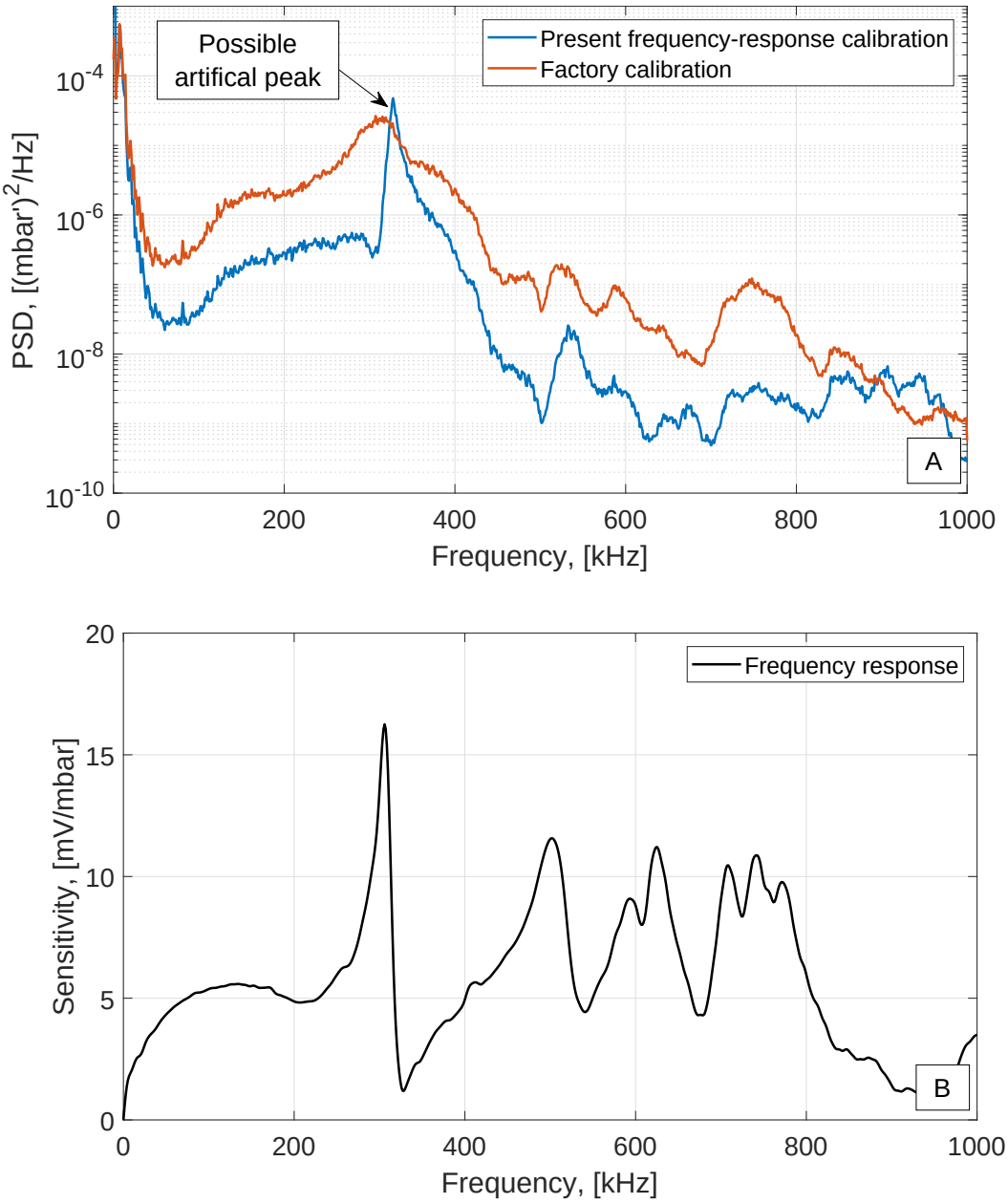

Figure 6.25.: PSD of data acquired by PCB132B (SN7949) in the BAM6QT at $Re_m = 10.6 \times 10^6$, bleeds open (A). Averaged approximate frequency response (SN 7949) found with the P3IST (B); pressure steps range from 10.3–39.2 mbar; data length of 150 μs.

7. CONCLUSIONS

The P3IST has been improved with the addition of automated vacuum-control valves, high-precision pressure sensors, and an automated control system. These additions have dramatically improved repeatability. Pre-shock driven and driver pressures can now be consistently controlled to within 1% of the desired value. New static-sensor ports were also added towards the downstream end of the shock tube.

Vibration was studied in the P3IST with the use of accelerometers. Vibration was found to increase with increasing pre-shock pressure differential, and was lowest in the last section of the shock tube. Some PCB132 sensor measurements of vibration showed similar frequency content to accelerometer measurements, but the comparison was limited by the frequency response of the accelerometers. It remains unclear if the high-frequency PCB132 response to vibration is due to a high-frequency vibration in the P3IST, or a lower-frequency vibration exciting a resonance in the PCB132. It appears that pitot-mounted PCB132 sensors were not significantly affected by pre-shock vibration when mounted in the final section of the P3IST, but these measurements were not conclusive. Future measurements in the P3IST should use sensors mounted in the final tube section to limit contamination from vibration.

Flow characterization studies showed little variation in the measured quantities between runs. The measured shock-skew angle was negligible. The Mach number decreased along the length of the shock tube as expected. Little variation in pressure step measured at a single axial location by Kulite sensors was observed. The improved repeatability of the P3IST shows its usefulness as a calibration tool.

Previous PCB132 calibration methods using static-mounted sensors appear to be affected by the incident-shock speed. This was supported by creating shocks at varying Mach numbers and performing static-mode calibrations. The calibration slope changed based on the Mach number, indicating the PCB132 calibration was a

function of the incident-shock speed. Based on predicted shock-thickness values, the input rise time for static-mounted sensors appears to be close to the sensor rise time. Faster rise times can be generated for pitot-mounted sensors, but these faster rise times generally correlate with higher pressure steps.

The approximate frequency responses of PCB132 sensors were calculated from pitot-mode measurements made in the P3IST. Measurements made with a blinded sensor indicated that vibration was not a significant contribution to the the measured PCB132 pitot response, however these measurements were not conclusive. The evaluated sensors showed a relatively flat response to around 250 kHz, with numerous peaks at higher frequencies. The maximum resonance of the evaluated PCB132 sensors was found to be between 600–800 kHz. The frequency responses of different sensors showed some commonalities, but were dissimilar in detail.

The wind-tunnel frequency response of a PCB132 sensor was evaluated by comparing it to a Kulite sensor, which were both tested in pitot mode in the BAM6QT. The PCB132 frequency content was scaled with the approximate frequency response calculated from pitot-mode measurements in the P3IST. The scaled frequency content showed significant differences from the frequency content measured by the Kulite sensor. This could have been due to a flow feature, but it is inconclusive. Scaling the PCB132 measurements with the approximate frequency response did appear to attenuate a high-frequency peak at the maximum sensor resonance. More testing is necessary to determine the accuracy of the PCB132 frequency response found with the P3IST.

7.1 Future Work Suggestions

More work still needs to be done to fully understand PCB132 sensors. There are also some possible P3IST improvements that may expand capabilities or reduce the time between runs. Some suggestions for future work on this subject are listed below.

1. One of the most significant uncertainties of the current work is a good measurement of the pressure-input signal generated in the P3IST. If high-frequency measurements of this signal were made, it could be possible to calibrate PCB132 sensors with slower input rise times. A better understanding of the input signal could be developed by measuring the change in density across the incident shock with an FLDI. Recent improvements to an FLDI system have made measurements of shock thickness in the P3IST practical [60]. The work of setting up the measurement apparatus is largely complete, but only limited measurements of the shock thickness have been made.

   If the pressure change across the shock can be reliably inferred from density measurements with the FLDI apparatus, the measured input signal could be used to compute the sensor frequency response. This could be supported with a computational study of the shock-tube flow field. By using a measurement of the input signal to compute the PCB132 frequency response, the assumption of an ideal step input is not necessary. This could lead to more accurate calculations of the PCB132 frequency response. Additionally, evaluation of the PCB132 frequency response at lower pressure steps could be possible since a slower input signal could be used. This could also allow for evaluation of the frequency response of static-mounted PCB132 sensors, something that was not feasible in the current work due to the slower input signals.

2. The PCB132 sensor response to vibration was only studied in order to reduce vibration in the P3IST. Work by Wagner shows that vibration caused by an impact hammer excites frequency content in PCB132 sensors that is qualitatively similar to PCB132 frequency responses found with the P3IST [66]. This could be a contributing factor to the apparent errors that occur when the frequency response is applied to wind-tunnel data. It may be useful to investigate the relationship between the PCB132 vibration and pressure responses.

Additionally, a blinded pitot-mode test should be performed with a more rigid mounting. As discussed in Section 6.3, the blinded tests presented here may have been flawed. The method of blinding the PCB132 sensor may have changed its vibrational response significantly. Tests with blinded PCB132 sensors should be performed again to better understand the vibrational response when pitot mounted in the P3IST.

3. The electrical burst system remains one of the less reliable systems in the P3IST. Recently, a new electrical burst system was manufactured, but minor design issues caused reliability concerns. The design of the recent burst system is discussed by Lay in [55]. Some of the main objectives for a redesigned burst system include better insulation from the shock tube structure, use of stock parts for ease of replacement, and quick turnaround time for diaphragm replacement. Making the electrical burst system more robust could reduce operator training time and the time between runs significantly.

4. Some experiments were performed in the P3IST with a PCB132 sensor mounted under a pinhole, with the goal of improving the spatial resolution of PCB132 sensors [46]. Further work was not performed due to unsuccessful initial efforts. Despite this, the pinhole mounting technique may become viable with further research. Some metrics which may affect the PCB132 response in this configuration include the pinhole size, cavity between the PCB132 sensor face and the mount, and the filling material in the cavity.

REFERENCES

REFERENCES

[1] Fujii, K., "Experiment of the Two-Dimensional Roughness Effect on Hypersonic Boundary-Layer Transition," *Journal of Spacecraft and Rockets*, Vol. 43, No. 4, 2006, pp. 731–738.

[2] Ort, D. J. and Dosch, J. J., "Influence of Mounting on the Accuracy of Piezoelectric Pressure Measurements for Hypersonic Boundary Layer Transition," *AIAA Paper 2019-2292*, January 2019.

[3] Berridge, D. C., *Generating Low-Pressure Shock Waves for Calibrating High-Frequency Pressure Sensors*, PhD thesis, Purdue University, West Lafayette, IN, December 2015.

[4] Estorf, M., Radespiel, R., Schneider, S. P., Johnson, H. B., and Hein, S., "Surface-Pressure Measurement of Second-Mode Instability in Quiet Hypersonic Flow," *AIAA Paper 2008-1153*, 1 2008.

[5] Estorf, M., October 2008, Personal communication from Malte Estorf to Steven P. Schneider regarding the typo in AIAA Paper 2008-1153.

[6] Chynoweth, B. C., *Measurements of Transition Dominated by the Second-Mode Instability at Mach 6*, PhD thesis, Purdue University, May 2018.

[7] Edelman, J. B., *Secondary Instabilities of Hypersonic Stationary Crossflow Waves*, Master's thesis, Purdue University, 2016.

[8] Tanno, H., Komuro, T., Sato, K., Itoh, K., Takahashi, M., and Fujii, K., "Measurement of Hypersonic Boundary Layer Transition on Cone Models in the Free-Piston Shock Tunnel HIEST," *AIAA Paper 2009-781*, 2009.

[9] Duan, L., Choudhari, M. M., Chou, A., Munoz, F., Ali, S. R. C., Radespiel, R., Schilden, T., Schröder, W., Marineau, E. C., Casper, K., Chaudhry, R. S., Candler, G. V., Gray, K. A., Sweeney, C. J., and Schneider, S. P., "Characterization of Freestream Disturbances in Conventional Hypersonic Wind Tunnels," *AIAA Paper 2018-0347*, 2018.

[10] Wagner, A., Schülein, E., Petervari, R., Hannemann, K., Ali, S. R. C., Cerminara, A., and Sandham, N. D., "Combined Free-Stream Disturbance Measurements and Receptivity Studies in Hypersonic Wind Tunnels by Means of a Slender Wedge Probe and Direct Numberical Simulation," *Journal of Fluid Mechanics*, Vol. 842, 2018, pp. 495–531.

[11] Damion, J. P., "Means of Dynamic Calibration for Pressure Transducers," *Metrologia*, Vol. 30, 1994, pp. 743–746.

[12] Gregory, J. W., Sakaue, H., and Sullivan, J. P., "Fluidic Oscillator as a Dynamic Calibration Tool," *AIAA Paper 2002-2701*, 2002.

[13] Janza, F. J. and Hicks, C. W., "The Calibrations and Interpretation of Recorded Shock-Tube Pressure Data using Piezoelectric Sensors," Technical documentary report, Air Force Systems Command, Kirtland Air Force Base, 1963, Available on DTIC, No. AD0425990.

[14] Knight, H. T., "Piezoelectric Detector for Low-Pressure Shock Waves," *Review of Scientific Instruments*, Vol. 29, 1958, pp. 174–175.

[15] Gavrilenko, T. P. and Nikolaev, Y. A., "Piezoelectric Pressure Transducer," *Combustion Explosion and Shock Waves*, Vol. 18, 1982, pp. 378–380.

[16] Matthews, C., Pannecchi, F., Eichstädt, S., Malengo, A., Esward, T., Smith, I., Elster, C., Knott, A., Arrhén, F., and Lakka, A., "Mathematical Modelling to Support Traceable Dynamic Calibration of Pressure Sensors," *Metrologia*, Vol. 51, 2014, pp. 326–338.

[17] Mohammed, H. A., Salleh, H., and Yusoff, M. Z., "Dynamic Calibration and Performance of Reliable and Fast-Response Coaxial Temperature Probes in a Shock Tube Facility," *Experimental Heat Transfer*, Vol. 24, 2011, pp. 109–132.

[18] Liepmann, H. W. and Roshko, A., *Elements of Gasdynamics*, Dover, 2001.

[19] Anderson, G. F., "Shock-Tube Testing Time," *Journal of Aerospace Sciences*, 1959, pp. 184–185.

[20] Anderson, J. D., *Modern Compressible Flow*, McGraw Hill Education, 3rd ed., 2012.

[21] Drewry, J. E. and Walenta, Z. A., "Determination of Diaphragm Opening-Times and Use of Diaphragm Particle Traps in a Hypersonic Shock Tube," *UTIAS Technical Note No. 90*, June 1965, NASA-CR-69546, UTIAS-TN-90, NASA STI Document ID: 19660006483.

[22] Rothkopf, E. M. and Low, W., "Diaphragm Opening Process in Shock Tubes," *The Physics of Fluids*, Vol. 17, No. 6, 1974, pp. 1169–1173.

[23] Liepmann, H. W., Roshko, A., Coles, D., and Sturtevant, B., "A 17-Inch Diameter Shock Tube for Studies in Rarefied Gasdynamics," *Review of Scientific Instruments*, Vol. 33, No. 6, 1962, pp. 625–631.

[24] Persico, G., Gaetani, P., and Guardone, A., "Dynamic Calibration of Fast-Response Probes in Low-Pressure Shock Tubes," *Measurement Science and Technology*, Vol. 16, 2005, pp. 1751–1759.

[25] Mirels, H., "Shock Tube Test Time Limitation Due to Turbulent-Wall Boundary Layer," *AIAA*, Vol. 2, No. 1, 1964, pp. 84–93.

[26] Spence, D. A. and Woods, B. A., "A Review of Theoretical Treatments of Shock-Tube Attenuation," *Journal of Fluid Mechanics*, Vol. 19, No. 2, 1964, pp. 161–174.

[27] Mirels, H., "Attenuation in a Shock Tube due to Unsteady-Boundary-Layer Action," Technical Report 1333, National Advisory Committee for Aeronautics, January 1957.

[28] Trimpi, R. L. and Cohen, N. B., "A Theory for Predicting the Flow of Real Gases in Shock Tubes with Experimental Verification," Technical Report 3375, National Advisory Committee for Aeronautics, March 1955.

[29] Demyanov, Y. A., "The Influence of the Boundary Layer on the Gas Flow in a Tube Behind a Moving Shock Wave," *Priklad. Mat. i Mekh.*, Vol. 21, No. 473, 1957.

[30] Martin, W. A., "An Experimental Study of the Turbulent Boundary Layer Behind the Initial Shock Wave in a Shock Tube," *Journal of the Aerospace Sciences*, Vol. 25, No. 10, 1958, pp. 644–652.

[31] Singh, T. and Reddy, K. P. J., "Test Gas Slug Characterization for Large-Scale Shock Tube Facility," *AIAA*, Vol. 55, No. 9, 2017, pp. 2912–2918.

[32] Duff, R. E., "Shock-Tube Performance at Low Initial Pressure," *The Physics of Fluids*, Vol. 2, No. 2, March 1959, pp. 207–216.

[33] Roshko, A., "On Flow Duration in Low-Pressure Shock Tubes," *The Physics of Fluids*, Vol. 3, No. 6, 1960, pp. 835–842.

[34] Duff, R. E. and Young, J. L., "Shock-Wave Curvature at Low Initial Pressure," *The Physics of Fluids*, Vol. 4, No. 7, 1961, pp. 812–815.

[35] Lin, S.-C. and Fyfe, W. I., "Low-Density Shock Tube for Chemical Kinetics Studies," *The Physics of Fluids*, Vol. 4, No. 2, 1961, pp. 238–249.

[36] Chigullapalli, S., Venkattraman, A., and Alexeenko, A. A., "Modeling of Viscous Shock Tube Using ES-BGK Model Kinetic Equations," *AIAA Paper 2009-1317*, January 2009.

[37] Hartunian, R. A., "Shock Curvature due to Boundary-Layer Effects in a Shock Tube," *The Physics of Fluids*, Vol. 4, No. 9, 1961, pp. 1059–1063.

[38] De Boer, P. C. T., "Curvature of Shock Fronts in Shock Tubes," *The Physics of Fluids*, Vol. 6, No. 7, 1963, pp. 962–971.

[39] Corcos, G. M., "Resolution of Pressure in Turbulence," *The Journal of the Acoustical Society of America*, Vol. 35, No. 2, 1963, pp. 192–199.

[40] White, P. H., "Effect of Transducer Size, Shape, and Surface Sensitivity on the Measurement of Boundary-Layer Pressures," *The Journal of the Acoustical Society of America*, Vol. 41, No. 5, 1967, pp. 1358–1363.

[41] Gilchrist, R. B. and Strawderman, W. A., "Experimental Hydrophone-Size Correction Factor for Boundary-Layer Pressure Fluctuations," *The Journal of the Acoustical Society of America*, Vol. 38, April 1965, pp. 298–302.

[42] Berridge, D. C., *Measurements of Second-Mode Instability Waves in Hypersonic Boundary Layers With A High-Frequency Pressure Transducer*, Master's thesis, Purdue University, November 2010.

[43] Kerlo, A.-E., "Design of a 3" Diameter Shock Tube," Unpublished report, Purdue University, May 2010, Purdue AAE590 class project report, available on request from Professor Schneider, pp. 1–73.

[44] Dally, M., "Dynamic Calibration of PCB-132A31 Pressure Transducers in a Three Inch Shock Tube," Unpublished report, Purdue University, June 2015, Purdue AAE590 class project report, available on request from Professor Schneider, pp. 1–62.

[45] Carlson, R., "Automation of the Three-Inch Shock Tube for PCB132A31 Sensor Calibration," Unpublished report, Purdue University, December 2016, Available on request from Professor Schneider, pp. 1–67.

[46] Esteban, I. G., "Calibration of PCB-132 Sensors Using a 3-Inch Shock Tube," Unpublished report, Purdue University, July 2018, Bachelor's thesis, available on request from Professor Schneider, pp. 1–112.

[47] Umrath, W., "Fundamentals of Vacuum Technology," 2016, published online by Leybold.

[48] Gray, K. A., *Flowfield Characterization of the Boeing/AFOSR Mach-6 Quiet Tunnel*, Master's thesis, Purdue University, December 2018.

[49] Juliano, T. J., Schneider, S. P., Aradag, S., and Knight, D., "Quiet-Flow Ludwieg Tube for Hypersonic Transition Research," *AIAA*, Vol. 46, No. 7, 2008, pp. 1757–1763.

[50] "PCB Model 606B01," `http://www.pcb.com/Products.aspx?m=606B01`, Accessed: 2019-02-19.

[51] Rotea, M. A., Randall, L. A., Song, G., and Schneider, S. P., "Model Identification of a Kulite Pressure Transducer," *AIAA Paper 96-2278*, June 1996.

[52] Proakis, J. G. and Manolakis, D. G., *Digital Signal Processing*, Prentice-Hall Inc., 3rd ed., 1996.

[53] Nazarchuk, Z., Skalskyi, V., and Serhiyenko, O., *Acoustic Emission: Methodology and Application*, Springer, January 2017.

[54] "PCB Model 080A118," `http://www.pcb.com/Products/model/080A118`, Accessed: 2019-02-21.

[55] Lay, A. C., "Effect of Varying Shock Thickness on PCB132A31 Sensor Response in the Purdue 3-Inch Shock Tube," Unpublished report, Purdue University, March 2019, Available on request from Professor Schneider, pp. 1–29.

[56] Rothkopf, E. M. and Low, W., "Shock Formation Distance in a Pressure Driven Shock Tube," *The Physics of Fluids*, Vol. 19, No. 12, 1976, pp. 1885–1888.

[57] Pain, H. J. and Rogers, E. W. E., "Shock Waves in Gases," *Reports on Progress in Physics*, Vol. 25, 1962, pp. 287–336.

[58] Shapiro, A. H., *The Dynamics and Thermodynamics of Compressible Fluid Flow*, Vol. 1, Wiley, 1953.

[59] Mott-Smith, H. M., "The Solution of the Boltzmann Equation for a Shock Wave," *Physical Review*, Vol. 82, No. 6, June 1951, pp. 885–892.

[60] Benitez, E. K., "Focused Laser Differential Interferometry for Hypersonic Flow Instability Measurements with Contoured Tunnel Windows," January 2020, To be published in the 2020 AIAA SciTech conference.

[61] Beresh, S. J., Henfling, J. F., Spillers, R. W., and Pruett, B. O. M., "Measurement of Fluctuating Wall Pressures Beneath a Supersonic Turbulent Boundary Layer," *AIAA Paper 2010-305*, January 2010.

[62] Sweeney, C. J., *Characterization of a Hypersonic Quiet Wind Tunnel Nozzle*, Master's thesis, Purdue University, December 2016.

[63] Steen, L. E., *Characterization and Development of Nozzles for a Hypersonic Quiet Wind Tunnel*, Master's thesis, Purdue University, December 2010.

[64] McGilvray, M., Jacobs, P. A., Morgan, R. G., Gollan, R. J., and Jacobs, C. M., "Helmholtz Resonance of Pitot Pressure Measurements in Impulsive Hypersonic Test Facilities," *AIAA*, Vol. 47, No. 10, October 2009, pp. 2430–2439.

[65] Vail, J., January 2019, Personal communication from Jim Vail to Mark Wason regarding the cavity depth of a Kulite A-screen sensor.

[66] Wagner, A., "High Frequency Pressure measurements by means of Piezoelectric Transducers," AIAA Aviation Transition Open Forum Presentation, June 2018, Slides obtained through personal communication.

APPENDICES

A. TABULATED RUN CONDITIONS

Table A.1.: Run conditions for accelerometer measurements

Date	p_1, [mbar]	p_4, [mbar]	$p_4 - p_1$, [mbar]	SN 4288 loc. (x/d)	SN 4289 loc. (x/d)	Diaphragm, [mil]
10/11/18	0.3999	335.96	335.6	27.4	27.4	1
10/11/18	0.3993	335.94	335.5	27.4	27.4	1
10/11/18	0.3995	335.95	335.6	27.4	27.4	1
10/11/18	0.1198	299.93	299.8	27.4	27.4	1
10/12/18	0.1200	299.94	299.8	27.4	27.4	1
10/12/18	0.1200	299.98	299.9	27.4	27.4	1
10/12/18	0.9001	468.99	468.1	27.4	27.4	1.5
10/12/18	0.9002	468.95	468.0	27.4	27.4	1.5
10/12/18	0.9001	468.97	468.1	27.4	27.4	1.5
10/12/18	3.0029	567.95	564.9	27.4	27.4	1.5
10/12/18	3.0024	567.97	565.0	27.4	27.4	1.5
10/12/18	3.0028	567.96	565.0	27.4	27.4	1.5
10/12/18	1.3000	787.00	785.7	27.4	27.4	1.5
10/12/18	1.3001	786.99	785.7	27.4	27.4	1.5
10/12/18	1.3005	786.96	785.7	27.4	27.4	1.5
10/12/18	0.5000	419.92	419.4	27.4	27.4	1
10/12/18	0.5002	419.95	419.4	27.4	27.4	1
10/12/18	0.5001	419.98	419.5	27.4	27.4	1
10/13/18	0.0598	50.47	50.4	27.4	27.4	0.31

10/13/18	0.0600	50.30	50.2	27.4	27.4	0.31
10/13/18	0.0600	50.26	50.2	27.4	27.4	0.31
10/15/18	0.4001	336.01	335.6	32.6	27.4	1
10/15/18	0.4001	335.98	335.6	32.6	27.4	1
10/15/18	0.4031	335.97	335.6	32.6	27.4	1
10/15/18	0.1199	299.96	299.8	32.6	27.4	1
10/15/18	0.1201	299.92	299.8	32.6	27.4	1
10/15/18	0.2189	300.01	299.8	32.6	27.4	1
10/15/18	0.1200	299.97	299.9	32.6	27.4	1
10/15/18	0.9002	468.98	468.1	32.6	27.4	1.5
10/15/18	0.9002	468.98	468.1	32.6	27.4	1.5
10/15/18	0.9006	469.02	468.1	32.6	27.4	1.5
10/15/18	3.0029	568.00	565.0	32.6	27.4	1.5
10/15/18	3.0048	568.01	565.0	32.6	27.4	1.5
10/15/18	3.0028	568.01	565.0	32.6	27.4	1.5
10/16/18	1.3010	787.00	785.7	32.6	27.4	1.5
10/16/18	1.3002	786.97	785.7	32.6	27.4	1.5
10/16/18	1.3001	786.97	785.7	32.6	27.4	1.5
10/16/18	0.5000	419.95	419.5	32.6	27.4	1
10/16/18	0.5000	419.92	419.4	32.6	27.4	1
10/16/18	0.5002	418.90	418.4	32.6	27.4	1
10/16/18	0.0501	249.85	249.8	32.6	27.4	1
10/16/18	0.0494	249.94	249.9	32.6	27.4	1
10/16/18	0.0499	249.91	249.9	32.6	27.4	1
10/17/18	0.0505	249.82	249.8	32.6	27.4	1
10/17/18	0.0963	49.51	49.4	32.6	27.4	0.31
10/17/18	0.4004	335.87	335.5	27.4	32.6	1
10/17/18	0.3996	335.91	335.5	27.4	32.6	1

10/17/18	0.4004	335.95	335.5	27.4	32.6	1
10/17/18	0.4004	335.92	335.5	27.4	32.6	1
10/17/18	0.1201	299.96	299.8	27.4	32.6	1
10/17/18	0.1201	299.89	299.8	27.4	32.6	1
10/17/18	0.1201	299.95	299.8	27.4	32.6	1
10/17/18	0.9002	468.95	468.0	27.4	32.6	1.5
10/17/18	0.9001	468.95	468.0	27.4	32.6	1.5
10/18/18	0.9002	468.99	468.1	27.4	32.6	1.5
10/18/18	0.9002	468.96	468.1	27.4	32.6	1.5
10/18/18	0.9001	468.90	468.0	27.4	32.6	1.5
10/18/18	3.0020	567.96	565.0	27.4	32.6	1.5
10/18/18	3.0025	567.98	565.0	27.4	32.6	1.5
10/18/18	3.0013	567.90	564.9	27.4	32.6	1.5
10/18/18	1.3001	786.99	785.7	27.4	32.6	1.5
10/18/18	1.3005	786.98	785.7	27.4	32.6	1.5
10/18/18	1.3002	786.96	785.7	27.4	32.6	1.5
10/18/18	0.4999	419.89	419.4	27.4	32.6	1
10/18/18	0.5000	419.89	419.4	27.4	32.6	1
10/18/18	0.4999	419.91	419.4	27.4	32.6	1
10/18/18	0.0501	250.79	250.7	27.4	32.6	1
10/19/18	0.0502	249.76	249.7	27.4	32.6	1
10/19/18	0.0501	249.82	249.8	27.4	32.6	1
10/19/18	0.0502	249.91	249.9	27.4	32.6	1
10/19/18	0.1201	299.87	299.7	27.4	32.6	1
10/19/18	0.1201	299.95	299.8	27.4	32.6	1
10/19/18	0.9002	468.90	468.0	27.4	32.6	1.5
10/19/18	0.4999	419.93	419.4	27.4	32.6	1

Table A.2.: Run conditions for incident-shock skew and pressure-jump measurements

Date	p_1, [mbar]	p_4, [mbar]	p_{driver}/p_{driven}	$p_2 - p_1$ (theoretical), [mbar]	Diaphragm, [mil]
10/10/18	0.4003	335.97	839.3	4	1
10/10/18	0.4000	335.98	839.9	4	1
10/10/18	0.9001	469.01	521.1	8	1.5
10/10/18	0.9002	468.97	521	8	1.5
10/10/18	0.9001	469.03	521.1	8	1.5
10/10/18	0.9001	468.97	521	8	1.5
10/10/18	0.9003	468.94	520.9	8	1.5
10/10/18	3.0029	567.97	189.1	20	1.5
10/10/18	3.0029	567.97	189.1	20	1.5
10/10/18	3.0015	567.95	189.2	20	1.5
10/10/18	1.3009	787.01	605	12	1.5
10/10/18	1.3001	787.02	605.3	12	1.5
10/10/18	1.3002	786.99	605.3	12	1.5
10/10/18	0.5002	419.93	839.6	5	1
10/10/18	0.5002	419.92	839.5	5	1
10/11/18	0.5023	419.98	836.1	5	1
10/11/18	0.1203	300.05	2493.4	1.5	1
10/11/18	0.1200	299.99	2499.9	1.5	1
10/11/18	0.1200	300	2499.3	1.5	1
10/11/18	0.3999	335.96	840.1	4	1
10/11/18	0.3993	335.94	841.3	4	1
10/11/18	0.3995	335.95	840.9	4	1
10/11/18	0.1198	299.93	2503.6	1.5	1

10/12/18	0.1200	299.94	2498.6	1.5	1
10/12/18	0.1200	299.98	2499.1	1.5	1
10/12/18	0.9001	468.99	521.1	8	1.5
10/12/18	0.9002	468.95	521	8	1.5
10/12/18	0.9001	468.97	521	8	1.5
10/12/18	3.0029	567.95	189.1	20	1.5
10/12/18	3.0024	567.97	189.2	20	1.5
10/12/18	3.0028	567.96	189.1	20	1.5
10/12/18	1.3000	787	605.4	12	1.5
10/12/18	1.3001	786.99	605.3	12	1.5
10/12/18	1.3005	786.96	605.1	12	1.5
10/12/18	0.5000	419.92	839.9	5	1
10/12/18	0.5002	419.95	839.6	5	1
10/12/18	0.5001	419.98	839.8	5	1
10/13/18	0.0598	50.47	844.4	0.6	0.31
10/13/18	0.0600	50.3	838.6	0.6	0.31
10/13/18	0.0600	50.26	837.6	0.6	0.31

Table A.3.: Run conditions for Mach number comparison

Date	p_1, [mbar]	p_4, [mbar]	p_{driver}/p_{driven}	$p_2 - p_1$ (theoretical), [mbar]	Diaphragm, [mil]
10/15/18	0.4001	336.01	839.8	4	1
10/15/18	0.4001	335.98	839.7	4	1
10/15/18	0.4031	335.97	833.4	4	1
10/15/18	0.1199	299.96	2502.4	1.5	1
10/15/18	0.1201	299.92	2497.7	1.5	1
10/15/18	0.1200	299.97	2499.4	1.5	1

10/15/18	0.9002	468.98	521	8	1.5
10/15/18	0.9002	468.98	521	8	1.5
10/15/18	0.9006	469.02	520.8	8	1.5
10/15/18	3.0029	568	189.1	20	1.5
10/15/18	3.0048	568.01	189	20	1.5
10/15/18	3.0028	568.01	189.2	20	1.5
10/16/18	1.3010	787	604.9	20	1.5
10/16/18	1.3002	786.97	605.3	12	1.5
10/16/18	1.3001	786.97	605.3	12	1.5
10/16/18	0.5000	419.95	839.9	5	1
10/16/18	0.5000	419.92	839.8	5	1
10/16/18	0.5002	418.9	837.5	5	1
10/16/18	0.0501	249.85	4990.6	0.7	1
10/16/18	0.0499	249.91	5006.9	0.7	1
10/17/18	0.0505	249.82	4948.8	0.7	1
10/17/18	0.3996	335.91	840.7	4	1
10/17/18	0.4004	335.95	839	4	1
10/17/18	0.4004	335.92	838.9	4	1
10/17/18	0.1201	299.96	2498.1	1.5	1
10/17/18	0.1201	299.95	2497.8	1.5	1
10/18/18	0.9002	468.99	521	8	1.5
10/18/18	0.9002	468.96	520.9	8	1.5
10/18/18	3.0020	567.96	189.2	20	1.5
10/18/18	3.0025	567.98	189.2	20	1.5
10/18/18	3.0013	567.9	189.2	20	1.5
10/18/18	1.3001	786.99	605.3	12	1.5
10/18/18	1.3005	786.98	605.1	12	1.5
10/18/18	1.3002	786.96	605.3	12	1.5

10/18/18	0.4999	419.89	839.9	5	1
10/18/18	0.5000	419.89	839.7	5	1
10/18/18	0.4999	419.91	839.9	5	1
10/18/18	0.0501	250.79	5006.8	0.7	1
10/19/18	0.0502	249.76	4973.7	0.7	1
10/19/18	0.0501	249.82	4983.2	0.7	1
10/19/18	0.0502	249.91	4982.5	0.7	1
10/19/18	0.9002	468.9	520.9	8	1.5
10/19/18	0.4999	419.93	840	5	1

Table A.4.: Run conditions for peak calibration methods

Date	p_1, [mbar]	p_4, [mbar]	$p_2 - p_1$, [mbar]	PCB132 SN	Mounting	Diaphragm, [mil]
9/13/18	0.4002	336.04	2.805	8246	static	1
9/13/18	0.4005	335.94	2.618	8246	static	1
9/13/18	0.3995	336.06	3.041	8246	static	1
9/13/18	0.1197	300.04	0.908	8246	static	1
9/13/18	0.1201	300.03	0.928	8246	static	1
9/13/18	0.1196	300.03	0.909	8246	static	1
9/14/18	0.9077	469	6.621	8246	static	1.5
9/14/18	0.9001	469.13	5.275	8246	static	1.5
9/14/18	0.9	469.1	6.41	8246	static	1.5
9/14/18	0.9	469.04	5.672	8246	static	1.5
9/14/18	0.9	469.07	6.384	8246	static	1.5
9/14/18	0.9001	469.02	6.226	8246	static	1.5
10/11/18	0.3999	335.96	2.785	8247	static	1
10/11/18	0.3993	335.94	2.805	8247	static	1

10/11/18	0.3995	335.95	2.792	8247	static	1
10/11/18	0.1198	299.93	0.856	8247	static	1
10/12/18	0.12	299.94	0.867	8247	static	1
10/12/18	0.12	299.98	0.877	8247	static	1
10/12/18	0.9001	468.99	5.563	8247	static	1.5
10/12/18	0.9002	468.95	6.107	8247	static	1.5
10/12/18	0.9001	468.97	6.181	8247	static	1.5
10/12/18	3.0029	567.95	16.952	8247	static	1.5
10/12/18	3.0024	567.97	16.836	8247	static	1.5
10/12/18	3.0028	567.96	16.921	8247	static	1.5
10/12/18	1.3	787	9.586	8247	static	1.5
10/12/18	1.3001	786.99	9.662	8247	static	1.5
10/12/18	1.3005	786.96	7.481	8247	static	1.5
10/12/18	0.5	419.92	3.617	8247	static	1
10/12/18	0.5002	419.95	3.63	8247	static	1
10/12/18	0.5001	419.98	3.624	8247	static	1
10/13/18	0.0598	50.47	0.278	8247	static	0.31
10/13/18	0.06	50.3	0.24	8247	static	0.31
10/13/18	0.06	50.26	0.275	8247	static	0.31
11/13/18	1.3071	438.89	8.062	8246	pitot	1.5
11/13/18	1.3088	280.94	7.239	8246	pitot	1
11/13/18	1.3124	86.02	4.774	8246	pitot	0.31
11/13/18	1.3094	65.53	4.282	8246	pitot	0.31
11/13/18	1.3123	48.65	3.646	8246	pitot	0.31
11/13/18	0.4197	279.79	2.804	8246	pitot	1
11/13/18	0.2291	362.82	1.769	8246	pitot	1
11/13/18	0.2264	570.86	1.899	8246	pitot	1.5
11/13/18	0.3355	290.79	1.027	8246	pitot	1

11/13/18	0.1091	70.23	0.564	8246	pitot	0.31
11/14/18	0.2073	48.21	0.933	8246	pitot	0.31
11/12/18	1.0066	699.92	7.513	8247	pitot	1.5
11/12/18	0.4192	279.84	2.756	8247	pitot	1
11/12/18	0.4591	540.83	3.567	8247	pitot	1.5
11/12/18	0.6619	359.78	4.486	8247	pitot	1
11/12/18	1.306	48.33	3.68	8247	pitot	0.31
11/12/18	1.3067	438.84	8.213	8247	pitot	1.5
11/12/18	1.338	65.04	4.324	8247	pitot	0.31
11/12/18	1.324	86.79	4.856	8247	pitot	0.31
11/12/18	1.3096	280.85	7.061	8247	pitot	1

Table A.5.: Run conditions for peak calibration methods

Date	p_1, [mbar]	p_4, [mbar]	$p_2 - p_1$, [mbar]	M_s (nominal)	Diaphragm, [mil]
11/19/18	0.3999	943.84	3.463	3.4	2
11/19/18	0.4004	943.77	3.513	3.4	2
11/19/18	1.3004	53.44	3.776	2.1	0.31
11/19/18	1.3005	54.15	3.398	2.1	0.31
11/19/18	1.0004	45.75	2.947	2.1	0.31
11/19/18	0.3213	754.83	2.760	3.4	1.5
11/19/18	0.7513	35.6	2.171	2.1	0.31
11/19/18	0.2386	565.79	2.215	3.4	1.5
11/20/18	0.1603	376.83	1.219	3.4	1
11/20/18	0.5022	21.92	1.321	2.1	0.31
11/20/18	0.5000	21.6	1.276	2.1	0.31
11/20/18	0.7512	35.15	2.171	2.1	0.31

11/20/18	1.0000	45.96	2.977	2.1	0.31
11/20/18	0.3205	754.85	2.676	3.4	1.5
11/20/18	0.2406	565.85	1.938	3.4	1.5

B. APPROXIMATE PCB132 FREQUENCY RESPONSES

Approximate frequency responses computed from pitot-mode PCB132 responses obtained from testing in the P3IST are shown below. Approximate frequency responses are computed from averaging at least 5 responses with grayed regions indicating the maximum and minimum range of the frequency responses.

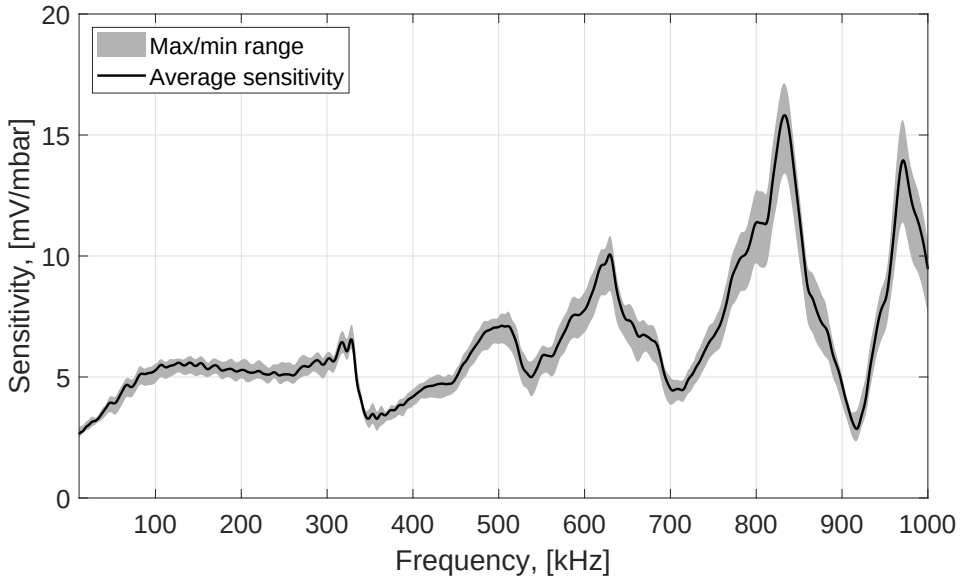

Figure B.1.: PCB132A21 SN 6772. Pressure steps range from 20.1–70.4 mbar. Frequency response calculated from 150μs of data. Grayed area indicates range of sensitivity.

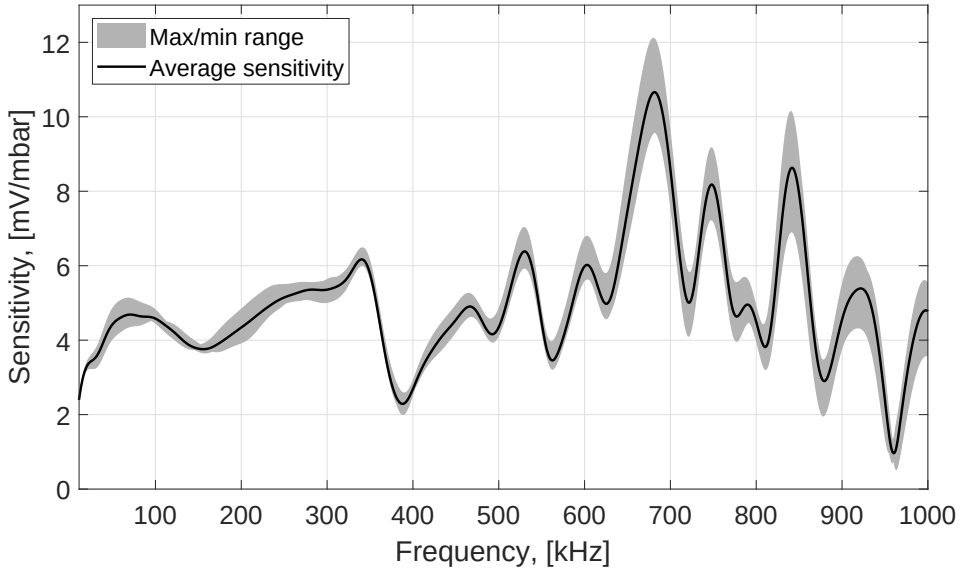

Figure B.2.: PCB132A21 SN 6994. Pressure steps range from 8.1–26.4 mbar. Frequency response calculated from 50μs of data. Grayed area indicates range of sensitivity.

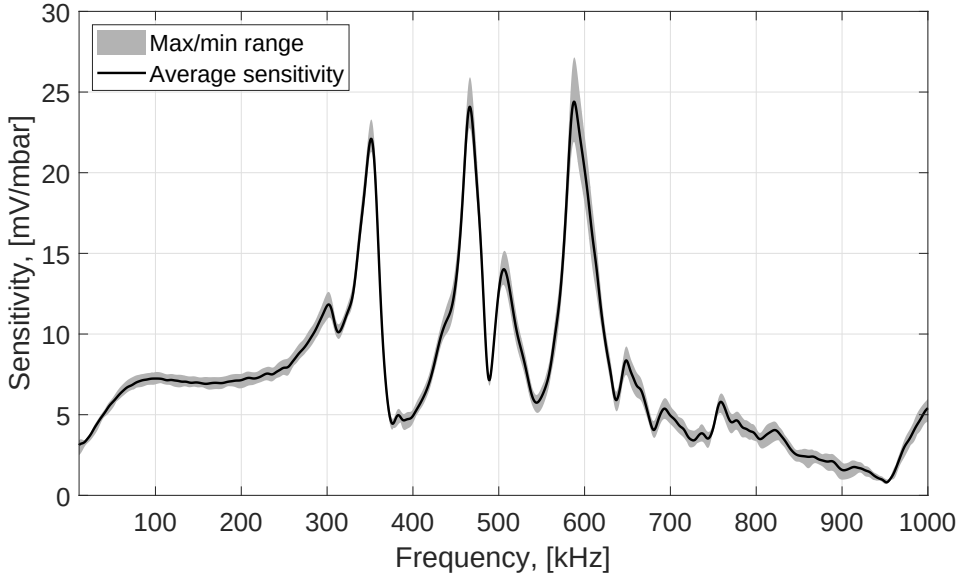

Figure B.3.: PCB132B38 SN 7936. Pressure steps range from 11.7–127.1 mbar. Frequency response calculated from 150μs of data. Grayed area indicates range of sensitivity.

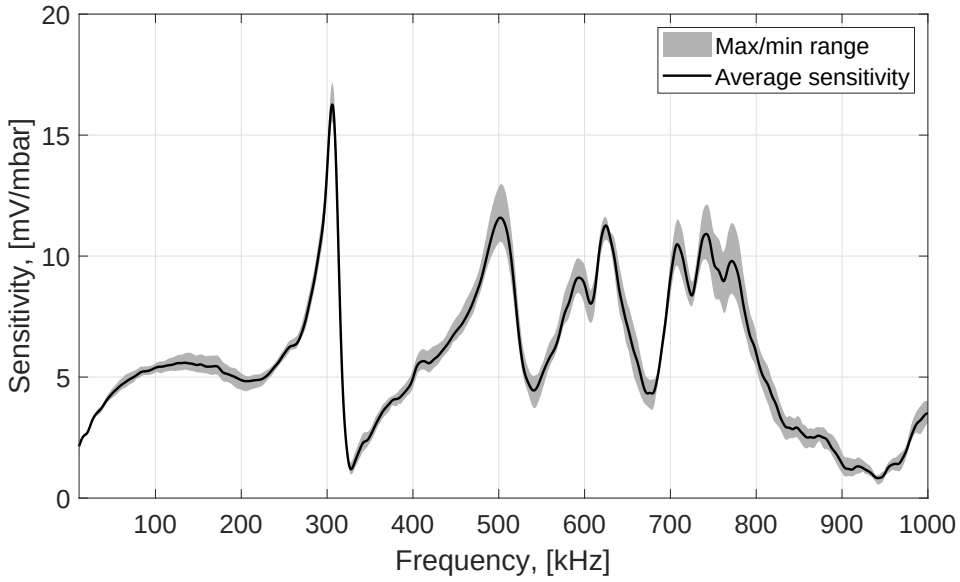

Figure B.4.: PCB132B38 SN 7949. Pressure steps range from 10.3–39.2 mbar. Frequency response calculated from 150μs of data. Grayed area indicates range of sensitivity.

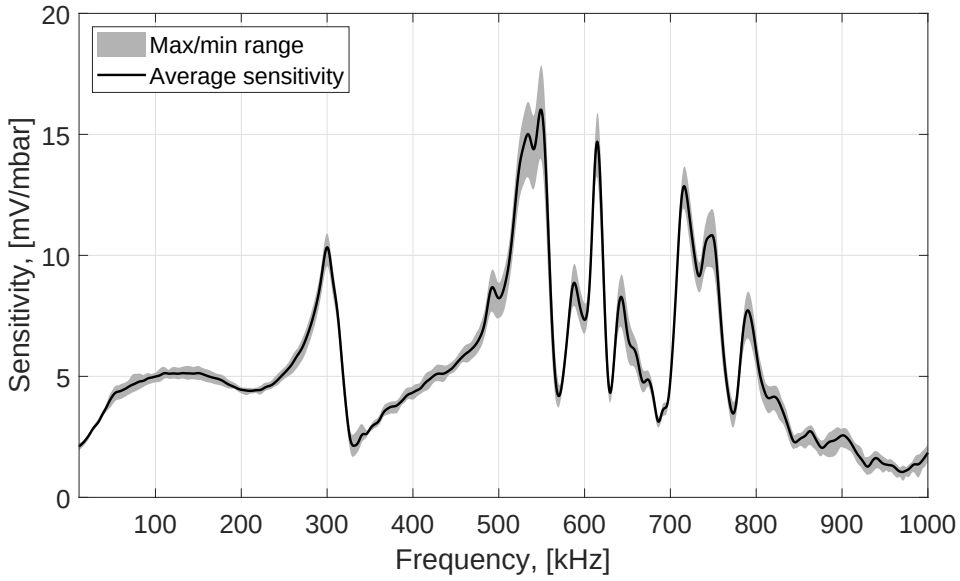

Figure B.5.: PCB132B38 SN 7953. Pressure steps range from 10.8–124.4 mbar. Frequency response calculated from 150μs of data. Grayed area indicates range of sensitivity.

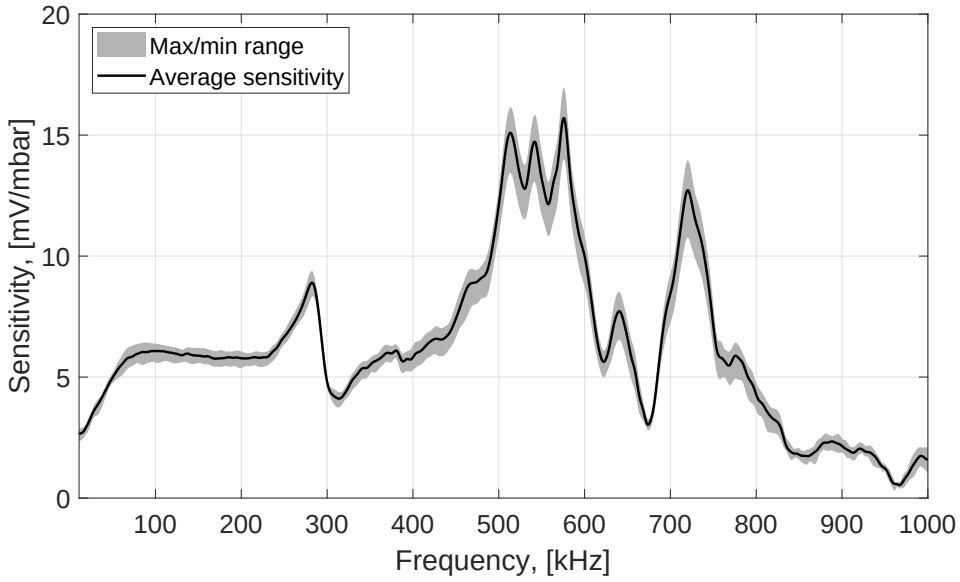

Figure B.6.: PCB132B38 SN 7955. Pressure steps range from 10.7–126.5 mbar. Frequency response calculated from 150μs of data. Grayed area indicates range of sensitivity.

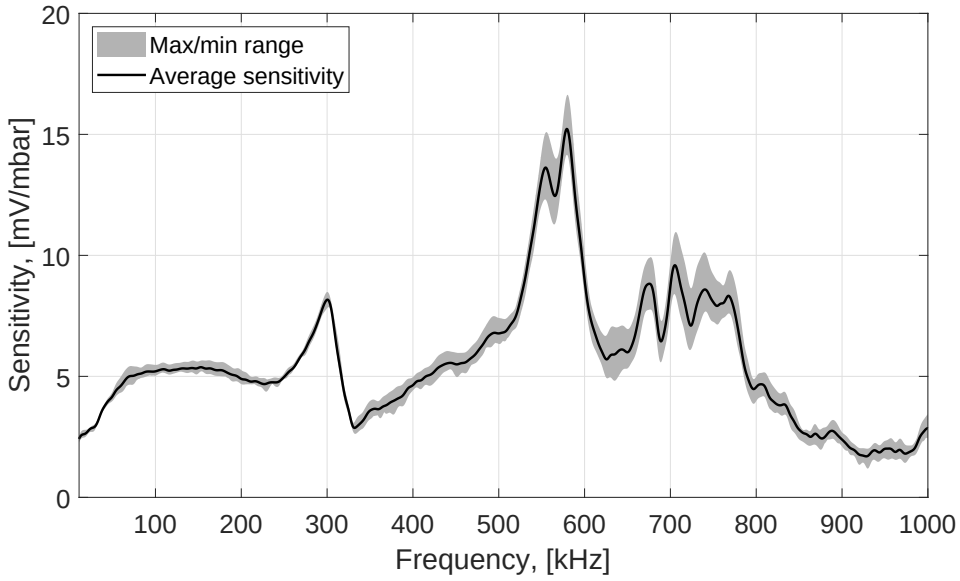

Figure B.7.: PCB132B38 SN 7967. Pressure steps range from 10.1–39.5 mbar. Frequency response calculated from 150μs of data. Grayed area indicates range of sensitivity.

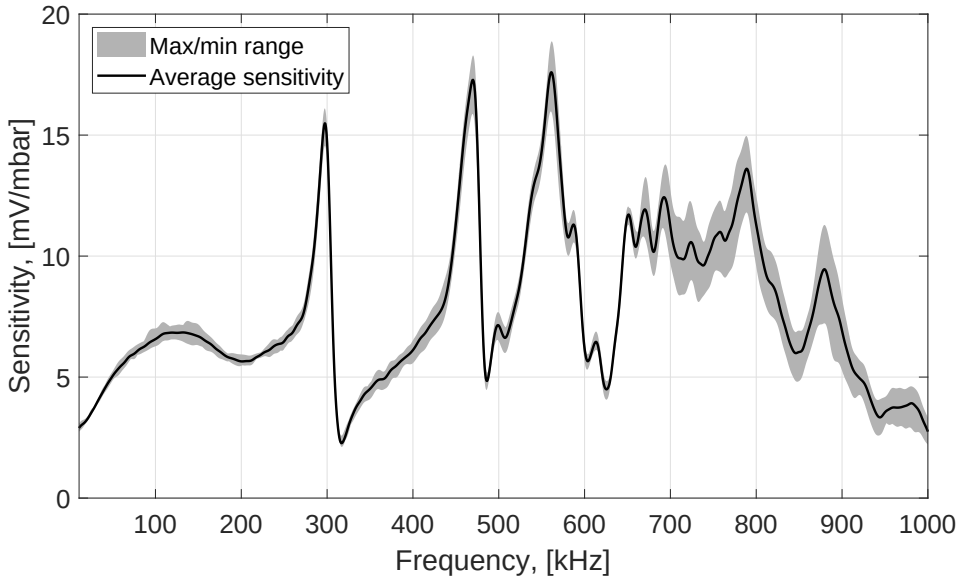

Figure B.8.: PCB132B38 SN 8121. Pressure steps range from 11.2–123.9 mbar. Frequency response calculated from 150μs of data. Grayed area indicates range of sensitivity.

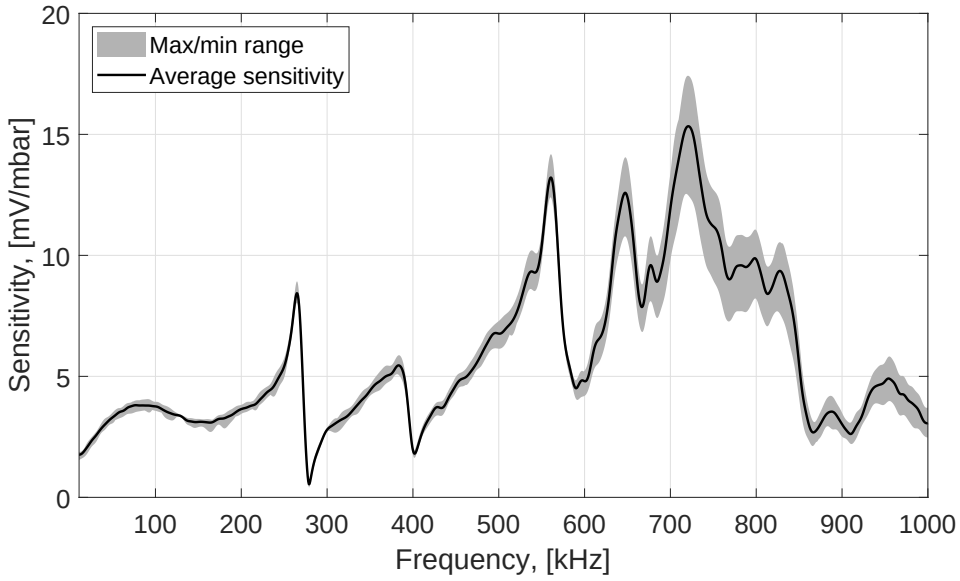

Figure B.9.: PCB132B38 SN 8245. Pressure steps range from 10.8–127.6 mbar. Frequency response calculated from 150μs of data. Grayed area indicates range of sensitivity.

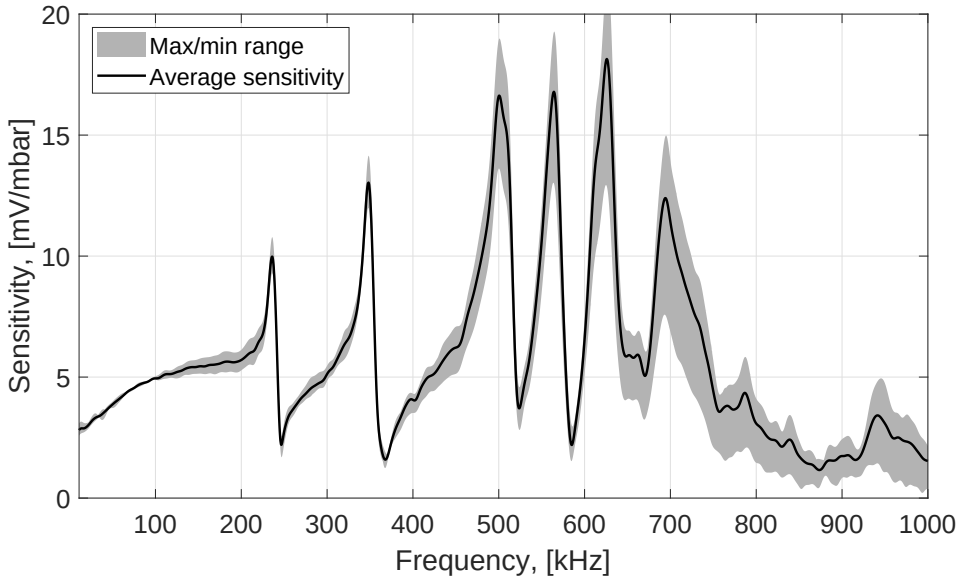

Figure B.10.: PCB132B38 SN 8246. Pressure steps range from 6.5–17.9 mbar. Frequency response calculated from 150μs of data. Grayed area indicates range of sensitivity.

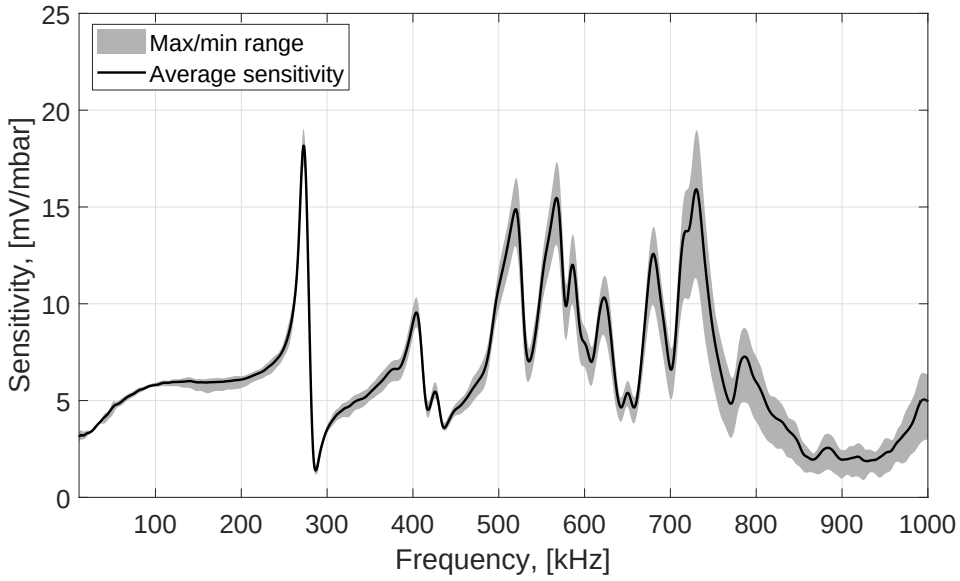

Figure B.11.: PCB132B38 SN 8247. Pressure steps range from 9.0–18.4 mbar. Frequency response calculated from 150μs of data. Grayed area indicates range of sensitivity.

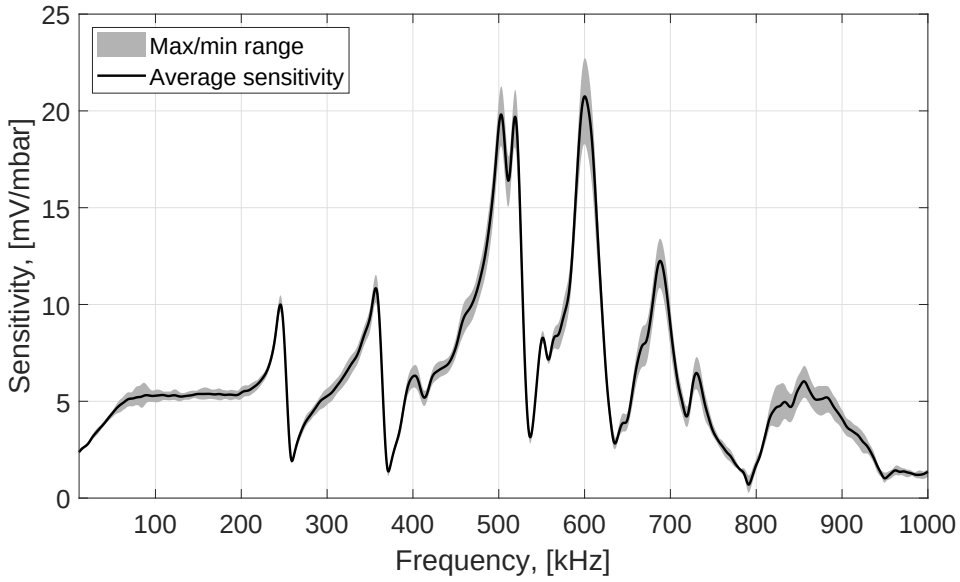

Figure B.12.: PCB132B38 SN 8249. Pressure steps range from 11.0–123.3 mbar. Frequency response calculated from 150μs of data. Grayed area indicates range of sensitivity.

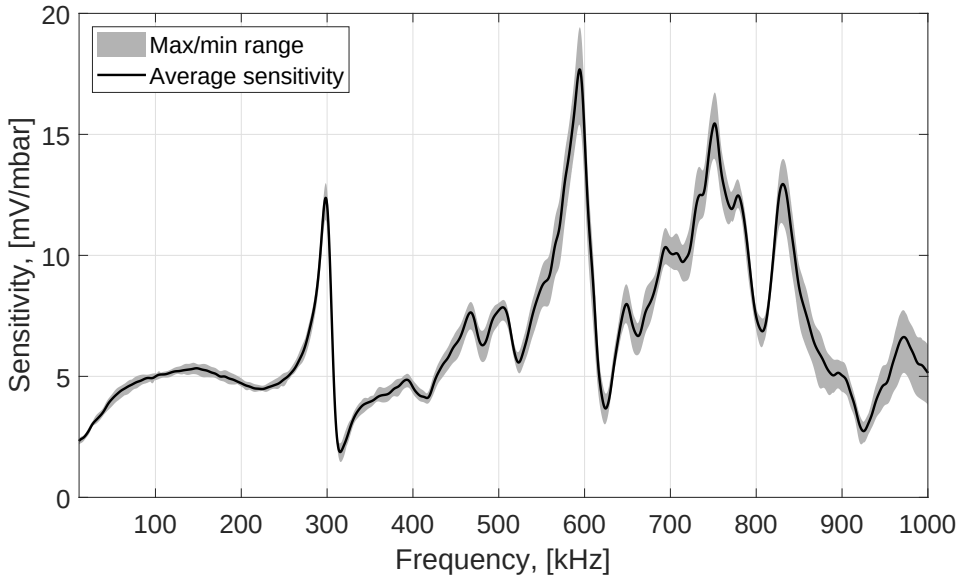

Figure B.13.: PCB132B38 SN 8372. Pressure steps range from 11.0–122.7 mbar. Frequency response calculated from 150μs of data. Grayed area indicates range of sensitivity.

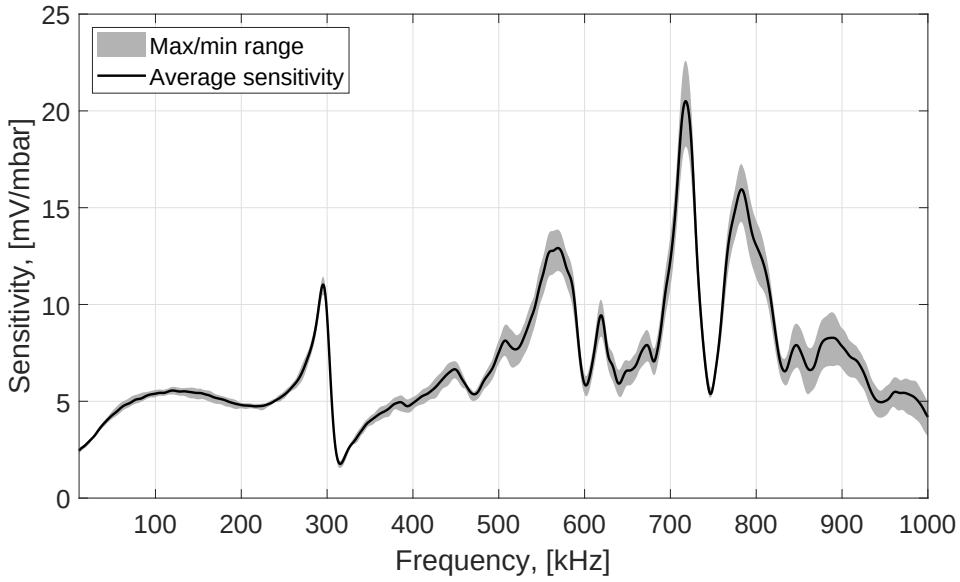

Figure B.14.: PCB132B38 SN 8373. Pressure steps range from 10.9–125.8 mbar. Frequency response calculated from 150μs of data. Grayed area indicates range of sensitivity.

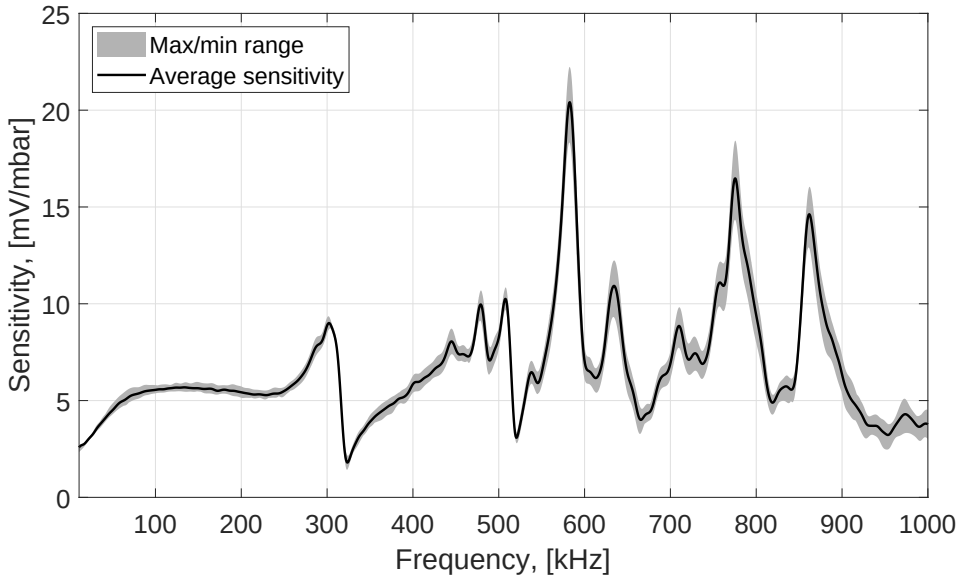

Figure B.15.: PCB132B38 SN 8374. Pressure steps range from 11.2–128.7 mbar. Frequency response calculated from 150μs of data. Grayed area indicates range of sensitivity.

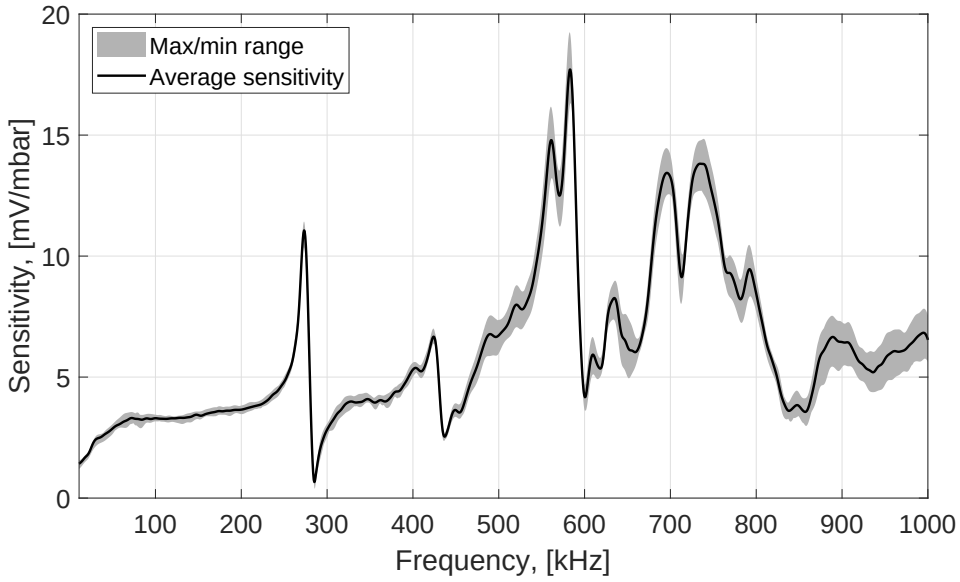

Figure B.16.: PCB132B38 SN 8378. Pressure steps range from 10.9–125.2 mbar. Frequency response calculated from 150μs of data. Grayed area indicates range of sensitivity.

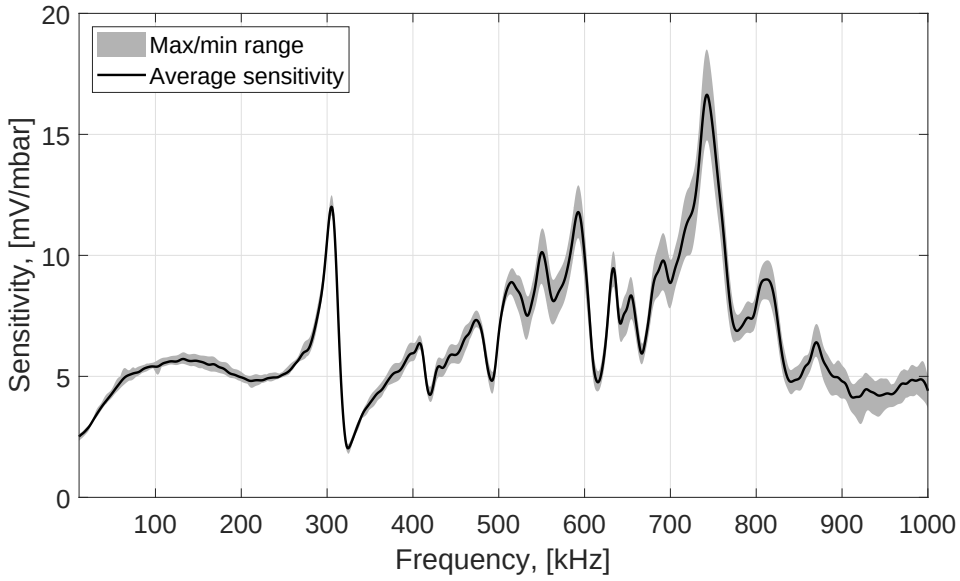

Figure B.17.: PCB132B38 SN 8410. Pressure steps range from 11.1–126.6 mbar. Frequency response calculated from 150μs of data. Grayed area indicates range of sensitivity.

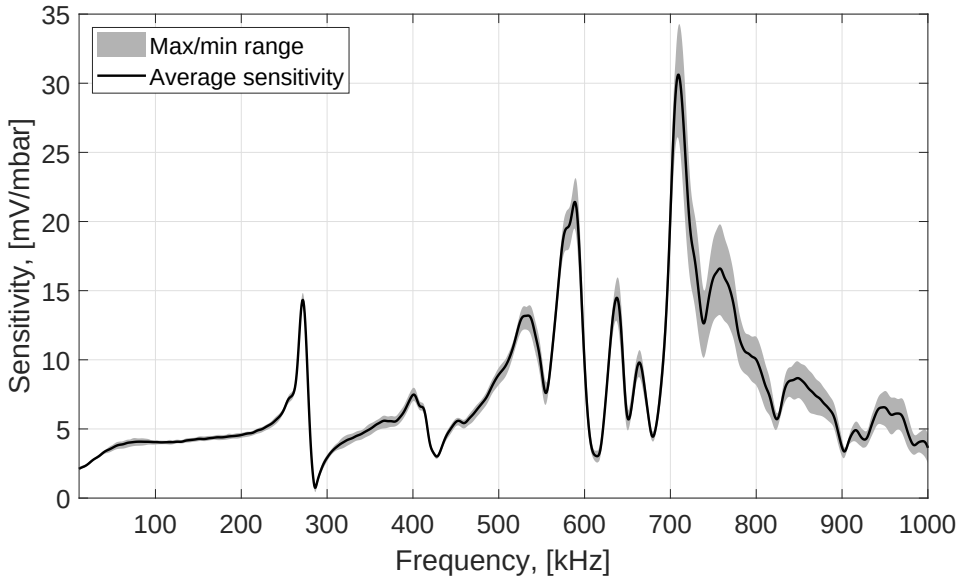

Figure B.18.: PCB132B38 SN 8441. Pressure steps range from 11.0–128.2 mbar. Frequency response calculated from 150μs of data. Grayed area indicates range of sensitivity.

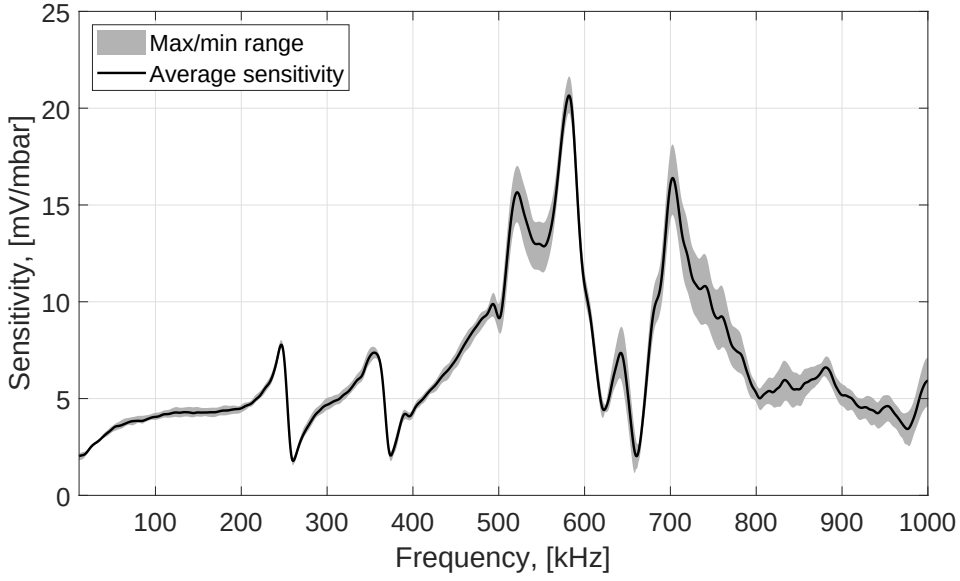

Figure B.19.: PCB132B38 SN 8458. Pressure steps range from 10.2–127.2 mbar. Frequency response calculated from 150μs of data. Grayed area indicates range of sensitivity.

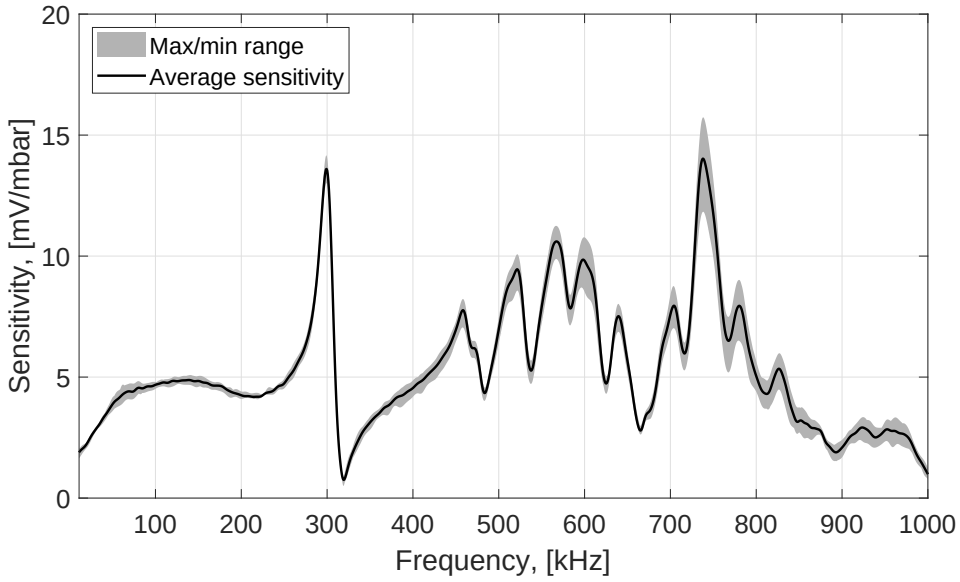

Figure B.20.: PCB132B38 SN 8471. Pressure steps range from 10.8–124.4 mbar. Frequency response calculated from 150μs of data. Grayed area indicates range of sensitivity.

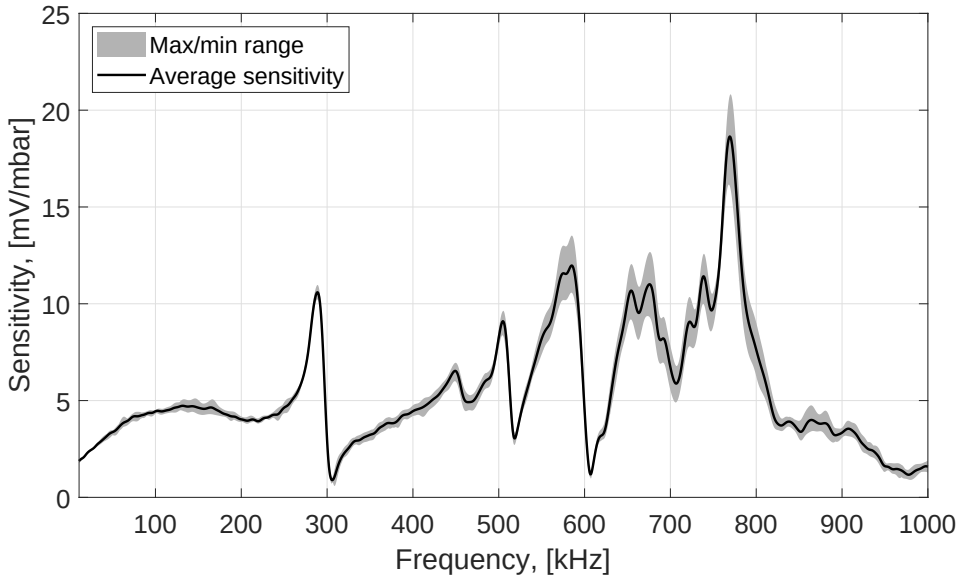

Figure B.21.: PCB132B38 SN 8473. Pressure steps range from 10.9–126.3 mbar. Frequency response calculated from 150μs of data. Grayed area indicates range of sensitivity.

C. SHOCK TUBE OPERATING INSTRUCTIONS

These instructions were modified from the instructions presented in Appendix A in [3] to provide a complete set of operating guidelines for the P3IST.

C.1 Pressure-System Schematic

The P3IST gas system is shown in Figure C.1. Valves numbered 1–5 correspond to the valves shown in Figures C.2, C.3, C.4, and C.5.

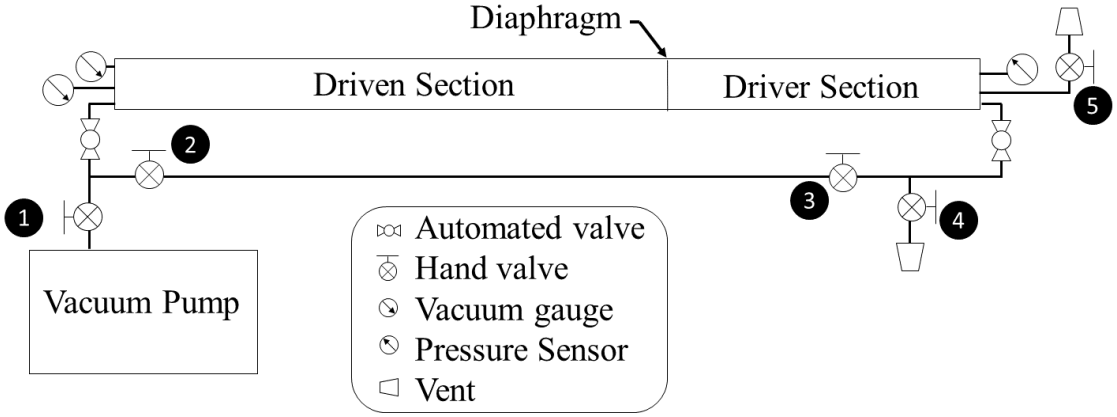

Figure C.1.: P3IST gas system schematic.

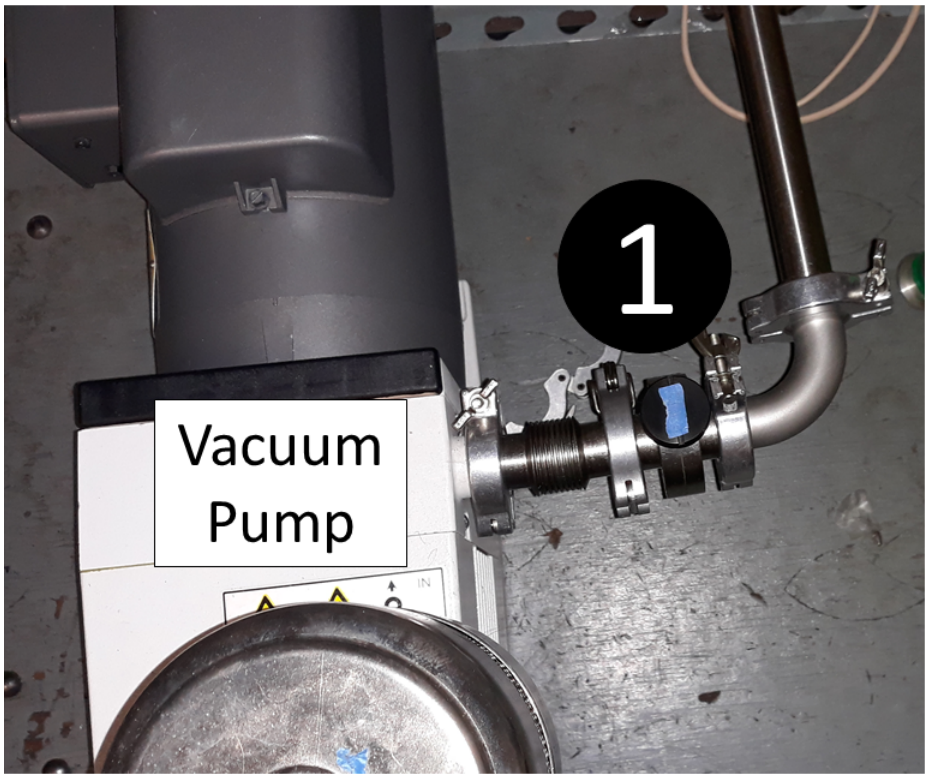

Figure C.2.: Valve 1, as shown in Figure C.1.

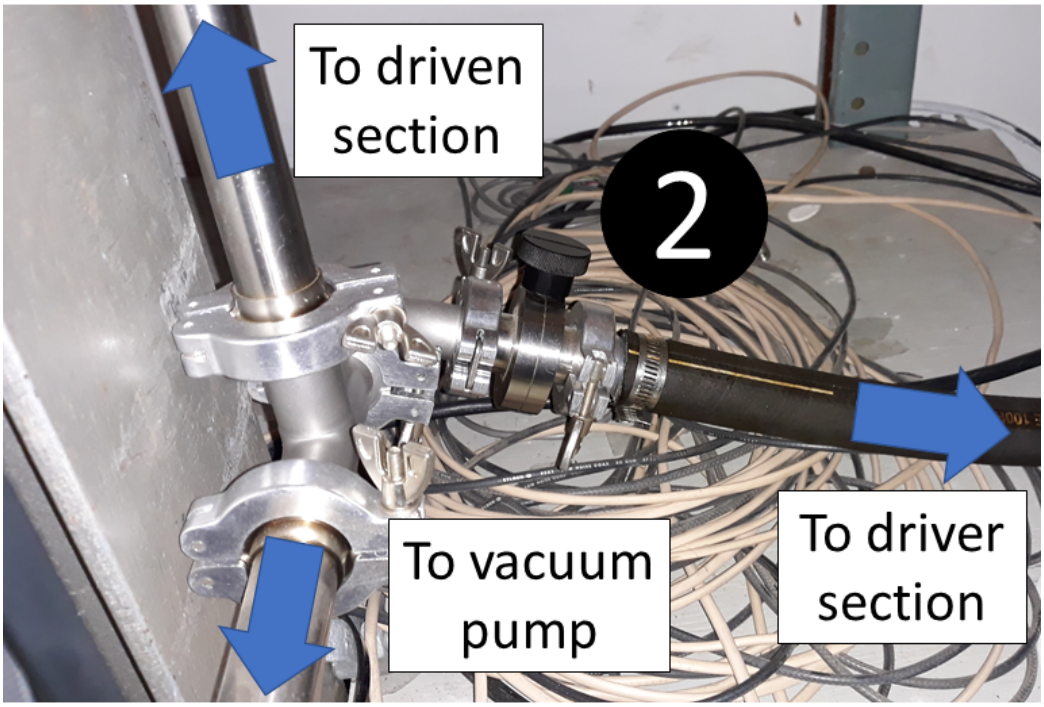

Figure C.3.: Valve 2, as shown in Figure C.1.

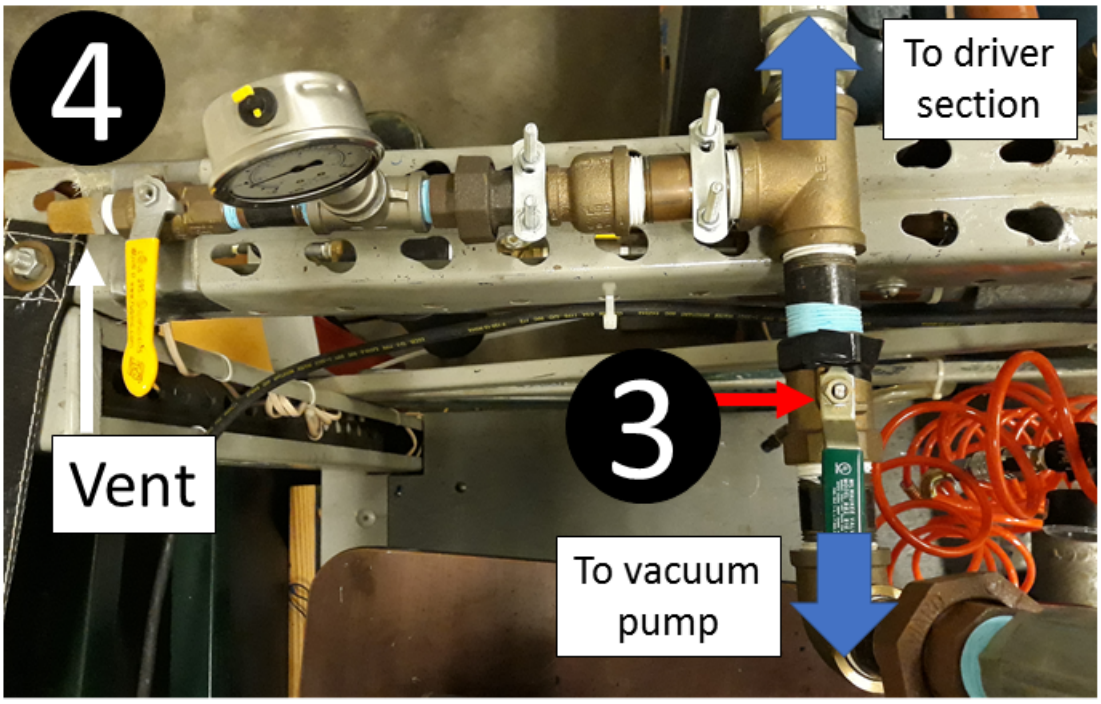

Figure C.4.: Valves 3 and 4, as shown in Figure C.1.

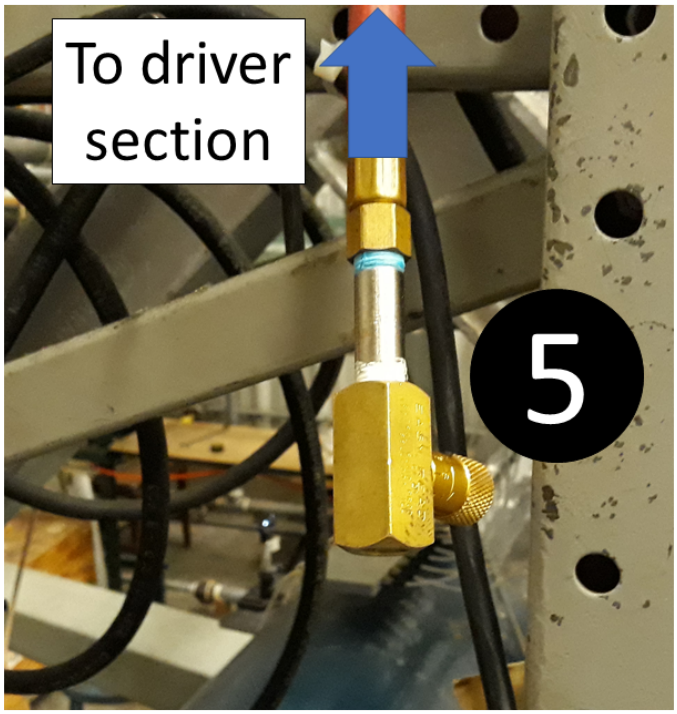

Figure C.5.: Valve 5, as shown in Figure C.1.

C.2 Setup

1. **Turn on vacuum pump 30 minutes prior to use**. Check the oil level before turning on and make sure it is near half full. The vacuum pump draws significant current at start-up, so it should not be plugged into a power strip. Ensure the valve at the vacuum pump inlet (valve 1 in Figure C.1) is fully closed before turning on.

2. **Turn on equipment**. Turn on both VAT valves, and the Paroscientific sensor, DAQ, oscilloscopes, PCB boxes, and Kulite boxes. When turning on the Kulite boxes, ensure the box is turned off before turning on the power supply. Wait until the power supply reads 15 V before turning on the Kulite boxes. The current should increase by around 0.019 amps when each sensor box is turned on and the voltage should stay at 15V. The driven section VAT valve should be turned on at the same time as the vacuum pump. The driven-section vacuum sensors are powered by the driven-section valve and need time to warm up before working properly. Turn the driven-section valve on at least 30 minutes before running the shock tube.

3. **Start LabVIEW program**. Ensure both VAT valves, Paroscientific sensor, and DAQ are properly connected to the laptop. Select the correct Virtual Instrument Software Architecture (VISA) names in the LabVIEW program, and then start the program. Refer to Section C.5 for information on LabVIEW setup. Sometimes, errors can be remedied by changing USB ports, especially for errors with the DAQ. Generally, if the LabVIEW program does not start properly, attempt stopping and restarting a few times. More in depth troubleshooting suggestions are provided in Section D.8.1.

4. **When the pump is warmed up, open the vacuum lines**. Close the yellow hand valve that opens to atmosphere (valve 4 in Figure C.1) and open the green hand valve that opens the black line from the driven side to the driver side (valve 3 in Figure C.1). Open the valve between the driven section tubing and the black

line (valve 2 in Figure C.1). Ensure both automatic valves are closed. Slowly begin to open the valve at the vacuum pump inlet (valve 1 in Figure C.1). Do this slowly until smoke stops coming out the pump indicating that the vacuum lines have been pumped down and the tube can be de-pressurized. Close the small vent-valve in the driver section (valve 5 in Figure C.1).

C.3 Diaphragm Assembly

The electrical burst system schematic is shown again in Figure C.6 for reference.

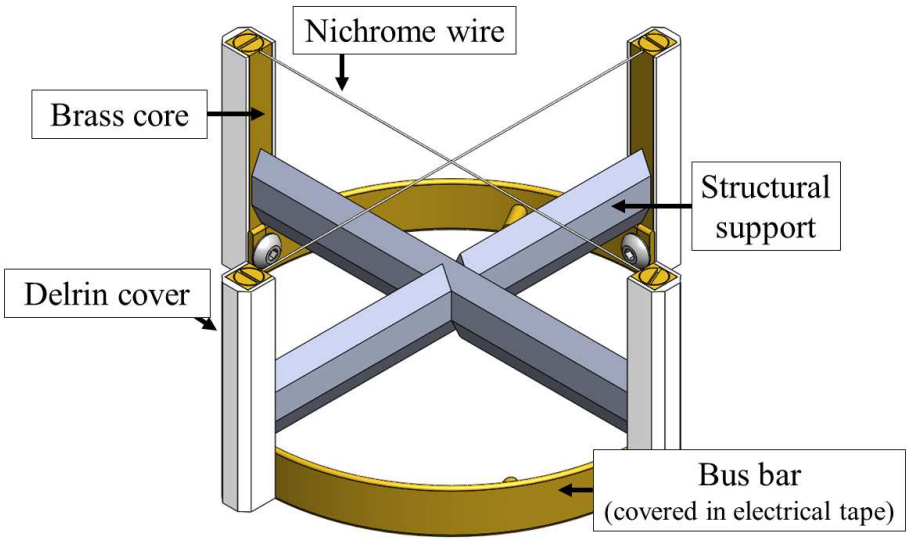

Figure C.6.: Electrical burst system schematic (duplicated from Figure 2.6).

1. **Check resistances before installing nichrome wires**. Check resistance across bus bars through the brass posts (0.3–0.4 Ω on each). Check resistance between capacitor leads and tube (O.L.). This can help diagnose problems if there are issues with electrical connectivity.
2. **Wire the nichrome**. Unscrew the brass screws and remove wire fragments from the previous run. The screw heads have been ground down to not contact

the other side of the transition section when hydraulic pressure is applied, so be careful not to strip the screws. Wrap a length of nichrome around one of the screws and tighten the screw down. Make sure the wire end is not poking out and that the wire sits in the groove. Pull the wire taught to the screw directly across the tube, and wrap it around to remove any slack. Cut the wire so that it will not poke out from under the screw and tighten as with the other side. Repeat for the other two screws. This is typically the most difficult portion of running the shock tube because of the small pieces. Often times it can take a few tries to get the wires properly connecting. Patience helps.

3. **Cut the diaphragm**. Select the diaphragm thickness based on Table 2.1. Place a section of diaphragm material on the cutting board. Cut around the metal template with a razor blade. This does not have to be exact, but cutting an accurate diaphragm reduces the risk of other problems occurring.

Table C.1.: Useful diaphragm pressure differentials (duplicated from Table 2.1)

Diaphragm Type	Typical Useful Pressure Differential, [mbar]
0.31-mil Polyethylene	35 - 200
1-mil Mylar	200 - 415
1.5-mil Mylar	415 - 700
2-mil Mylar	> 700

4. **Place the diaphragm in the shock tube**. Lay the diaphragm on the driven side of the transition section. Try to get it as centered as possible, completely covering the o-ring. If the o-ring is not covered, significant leaks will develop. If the diaphragm does not stick to the tube, apply a small amount of vacuum grease to the o-ring. Make sure there are no wrinkles in the diaphragm as these will cause leaks.
5. **Apply electrical tape over the screws**. Cut two small pieces of electrical tape just large enough to cover the head of the brass screws. Tape one on top

of the other to make a double layer of tape, and attach them to the diaphragm over a screw head. Cover the screw but do not cover where the o-ring from the opposite side will contact the diaphragm (this could cause leaks). Repeat for the other three screw heads.

6. **Close the tube**. Bring the two sides together. You may have to wiggle the two sides to get a good seat. Bring the clamp ring down and close the latch. Wiggle the clamp ring as you bring it down to get a better seat. Applying a lubricant to the exterior of the transition section can make closing the clamp ring easier. Penetrating oil generally works well. If the ring does not close, it is likely because the driver section is not properly seated into the driven section. If this occurs, remove the ring and attempt to shift the driver section into the driven section better. Once the clamp ring is closed, apply 1000 psi to the transition section via the hydraulic hand pump.
7. **Check for electrical connection**. Check the resistance across the burst circuit from the leads at the capacitor ($\approx 1\Omega$). Check the resistance between the capacitor circuit and the shock tube (O.L.). If the multimeter reads a finite value, there is likely electrical contact through the diaphragm from the screws to the shock tube. If the DAQ is not turned on, the resistance will read around 300 KΩ if no other electrical path exists. Section D.8.2 has more detailed electrical-contact troubleshooting instructions.

C.4 Run the Shock Tube

1. **Ensure the valves are working properly**. With the hand valve to the pump closed (valve 1 in Figure C.1), command both automated valves to open to position 1/1000 and then close. Check pressures in the driver and driven sections to make sure they are reasonably close to one another.
2. **Command pressures**. Command pressures in steps of 200 mbar making sure to keep the driven section at a lower pressure than the driver section. This

ensures the diaphragm is only deformed towards the wires and any problems with leaking can be seen as the tube is pumped down. The driven section can take some time to pump down, so it is often easiest to entirely open the valve at pressures lower than 50 mbar until the pressure approaches the desired level.

3. **Charge the capacitor**. Check the resistances from the capacitor again, making sure the multimeter reads O.L between the capacitor and the tube and around 1Ω across the capacitor leads. Turn on the power supply to the capacitor. Click the arm switch on the LabVIEW graphical user interface (GUI). You should hear an audible click when you do this as the charging circuit is switched inside the capacitor. When this is not switched, the capacitor will discharge current across the internal resistor so if left with no command the voltage will be dissipated. It can take a few seconds before the capacitor begins charging. Sometimes the power supply will short itself. If it does not begin charging, turn the power supply off and then on again.

4. **Single the oscilloscopes**. Single the oscilloscopes and set scaling for the run. If you are unsure of the strength of the shock, 10mV per division for static-mounted PCBs and 50 mV for static-mounted Kulites captures most shocks with pressure steps less than 10 mbar. Generally sampling at 25 MS/s works well, as PCBs should be sampled at 10 MHz or higher.

5. **Prepare for burst**. Check the resistances a final time between the tube and capacitor and across the capacitor circuit. Flip the firing switch on the capacitor up. Re-single all oscilloscopes. Turning off the power supply to the capacitor bank once the capacitor bank is charged seems to reduce electrical noise in PCB and Kulite signals, but it is not strictly necessary.

6. **Burst and clean up**. Make sure the pressures are close to desired, and then use the LabVIEW program to initiate the run. When the burst has completed, close the hand valve connected to the vacuum pump inlet (valve 1 in Figure C.1). Record the final pre-shock pressures and save data on the oscilloscopes. Open

the leak valve connected to the driver section (valve 5 in Figure C.1) and allow to return to atmospheric. Release the hydraulic pressure and open the shock tube. If this is the final run, clamp sections back together but do not apply the 1000 psi hydraulic pressure. This ensures the driver section does not rotate or tip in case something bumps it.

7. **Pitot-testing: optional filling procedure**. When testing pitot-mode sensors, especially when they are mounted in the end-plate, diaphragm fragments may disturb the flow near the sensor. This can be remedied by blowing diaphragm fragments upstream after each run, similar to the clearing procedure discussed in Section D.2. After a run, do not return the pressure to atmospheric as normal. Close the vacuum pump inlet valve (valve 1 in Figure C.1) and **completely** open the automated driven valve. Make sure the valve to the black line (valve 2 in Figure C.1) is open. Quickly open the yellow hand valve (valve 4 in Figure C.1). This allows air to leak into the black line and through the automated driven valve, pushing diaphragm fragments upstream to where they can be easily removed. Make sure the vacuum pump is isolated and the automated driven valve completely open before opening the yellow valve. Damage to the pump or valves can occur if these steps are not taken.

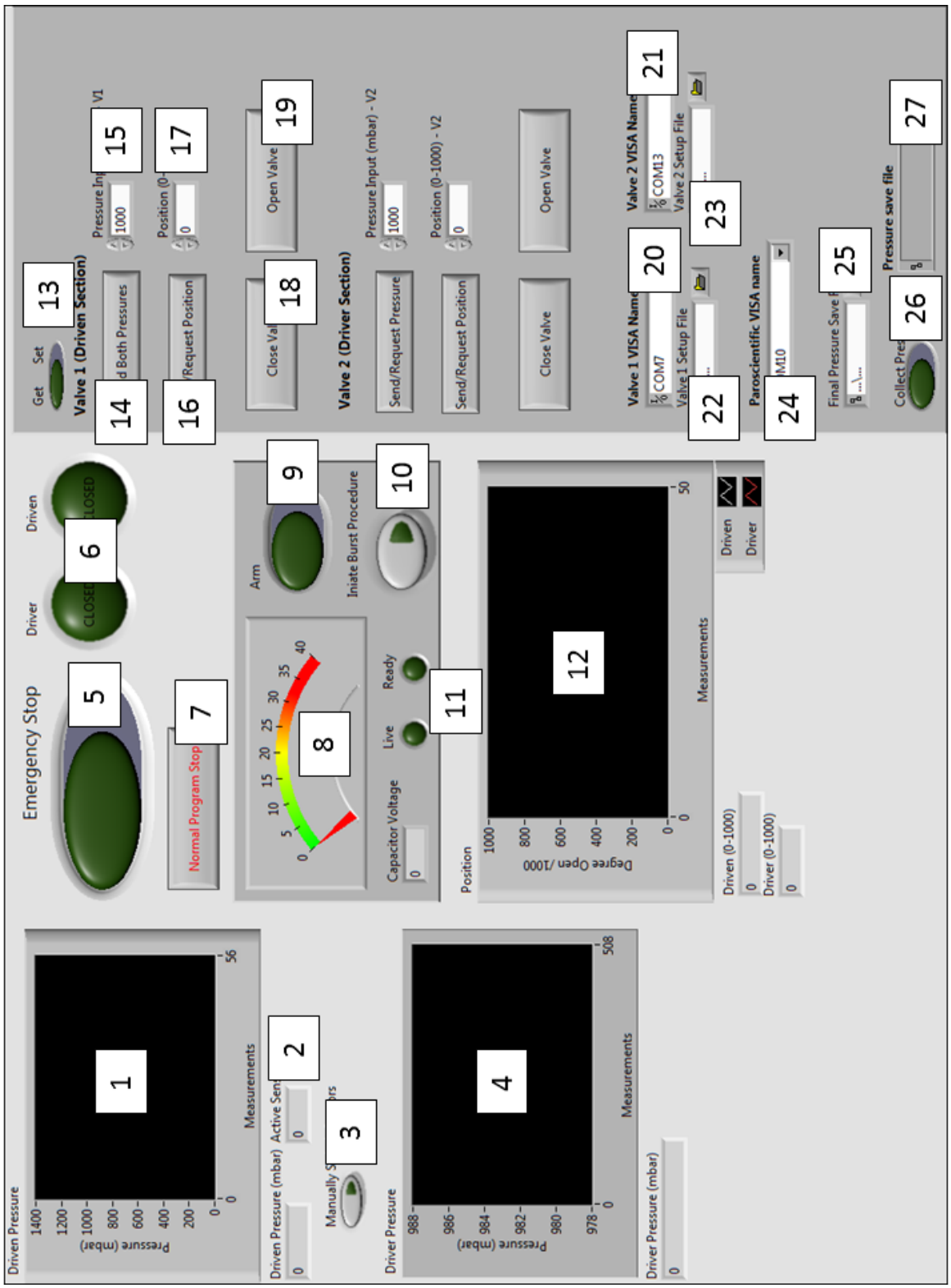

Figure C.7.: LabVIEW VI front panel.

C.5 LabVIEW Control Panel

1. **Driven pressure plot indicator**.
2. **Active driven sensor indicator**. Sensor 1 is higher range (1000 Torr) and sensor 2 is lower range (1 Torr).
3. **Sensor switch control**. Toggle to switch between driven sensors.
4. **Driver pressure plot indicator**.
5. **Emergency stop control**. Toggle to close both valves, begin discharging capacitor, and stop program in case of emergency.
6. **Driver and driven-section valve position indicators**. Indicates when the driver and driven-section valves are any amount open.
7. **Normal program stop control**. Toggle for normal program stop procedure which includes closing both valves, resetting the Paroscientific sensor, and discharging the capacitor.
8. **Capacitor voltage indicator**. Shows current voltage of burst system capacitor bank.
9. **Capacitor arming control**. Toggle to begin charging the burst-system capacitor bank.
10. **Initiate burst procedure control**. Toggle to begin a run when capacitor is fully charged. This closes both valves, records pressures, and discharges the capacitor bank across the nichrome wires.
11. **Live and Ready indicators**. Indicates when the capacitor is above 0.5 Volts (Live), and above 29 Volts with the Arm switch toggled to "on" (Ready). The capacitor bank will not be discharged if the Ready indicator is not on.
12. **Valve position plot indicator**. Shows the driver and driven valve positions out of 1000.

13. **Get/Set control**. In Set mode, below controls can be used to set pressures and positions to the valves. In Get mode, the below controls can be used to return values set to the valves.
14. **Driven section pressure control**. Toggle to send pressure control commands to both driven and driver valves. Driver section controls below.
15. **Driven pressure input**. Input desired driven pressure for pressure control, or returns set pressure for pressure control. Driver section controls below.
16. **Driven section position control**. Toggle to send position control commands to driven valve. Driver section controls below.
17. **Driven section position control**. Input desired driven-section valve opening ratio (out of 1000), or returns set driven-section valve opening ratio. Driver section controls below.
18. **Driven-section close valve**. Toggle to set driven valve position to 0/1000. Driver section controls below.
19. **Driven-section open valve**. Toggle to set driven valve position to 1000/1000. Driver section controls below.
20. **Driven-section valve VISA name**. Select communication name for driven-section valve.
21. **Driver-section valve VISA name**. Select communication name for driver-section valve.
22. **Driven-section valve setup file**. Select setup file for driven-section valve. This is preset and generally should not change.
23. **Driver-section valve setup file**. Select setup file for driver-section valve. This is preset and generally should not change.
24. **Driver-section pressure sensor VISA name**. Select communication name for driver-section pressure sensor.

25. **Final pressure save file**. Select file to write final pre-shock pressures. This is preset and generally should not change.
26. **Collect pressure data control**. Toggle to start or stop collecting pre-run driver and driven pressure data. Data will be written to a file when toggled to "off".
27. **Pressure data save file**. Select file to write pressure data.

D. SHOCK TUBE MAINTENANCE

Sections of this appendix are copied or modified from Appendix A in [3] to provide complete documentation on P3IST maintenance.

D.1 Burst System Maintenance

The electrical burst system does not need to be removed or rebuilt often. Sometimes it is necessary to remove the burst system for routine cleaning or repair. Uninstallation and installation is simple, but can be tricky.

1. Remove the burst system by unclipping the alligator clips attached to the brass rods on the bus bars. When the alligator clips are unfastened, the burst system should slide out easily. If this does not happen, something could be caught. Be careful when taking the burst system out as it is not as rigid without the support of the shock tube.

2. Take the burst system apart. The structural support blades should easily slide away from the brass posts as they are only held together with pins. When the supports are removed, the bus bars can be separated from the brass posts. Figure D.1 shows a zoomed view of one of the brass posts. The screw can be removed from the post, allowing the bus bar and washer to be removed. The washers between the brass posts and bus bars are necessary to conduct current from the bus bars to the brass posts. The washers must be trimmed so that they do not contact the shock-tube structure.

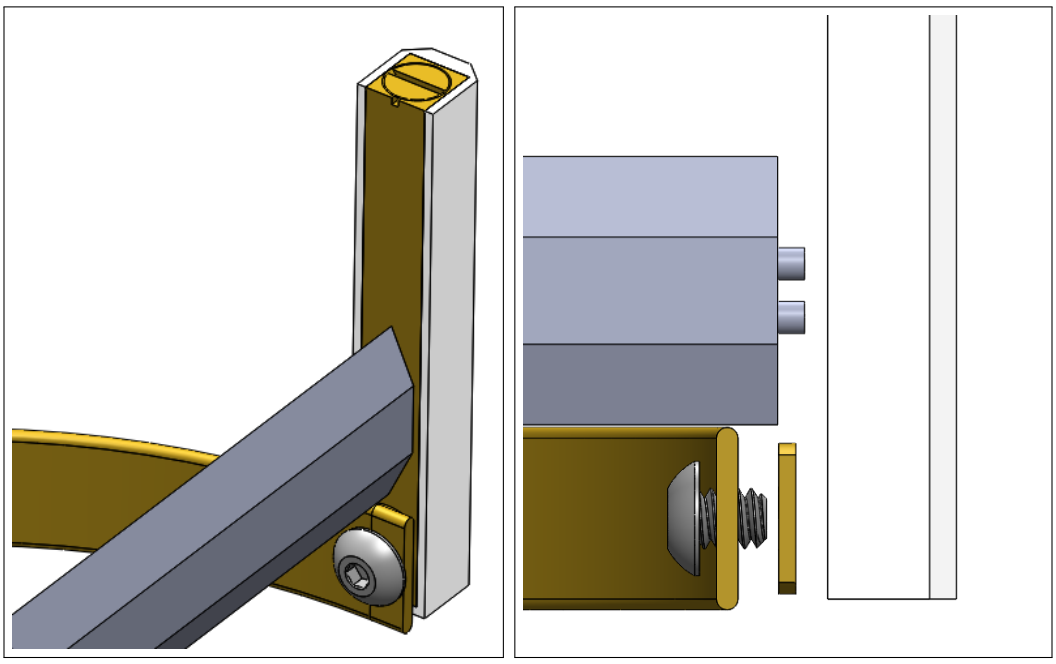

(a) Zoomed view (b) Exploded view

Figure D.1.: Zoomed and exploded views of electrical burst system.

3. Replace any damaged pieces. Make sure the washers make electrical contact between the bus bars and the posts. Make sure the bus bar is completely covered in electrical tape where it contacts the shock tube.
4. Reassemble the burst system in opposite order of disassembly.
5. Check electrical resistances across the bus bars and to the support blades. The resistances from the brass screws across each bus bar should be 0.3–0.4 Ω, and should be the same for each bus bar. If the resistance is higher on one bus bar, the bus bar may not be properly making contact with the brass post.
6. Reinstall the burst system in the shock tube by sliding into the grooves and clipping the alligator clips to the brass posts.

D.2 Clearing the Shock Tube

Clearing the shock tube is a relatively quick way to remove diaphragm and wire fragments in the shock tube. Completely cleaning the shock tube is still necessary, but not as frequently as clearing.

1. Place a 2-mil mylar diaphragm in the tube.
2. Close the tube and apply 1000 psi of clamp pressure.
3. Follow instructions in Appendix C to depressurize the shock tube as normal.
4. When the driven and driver pressures reaches 100 mbar or less, close the inlet valve to the vacuum pump.
5. Fully open both driven and driver-section automated valves. There should be no flow to the vacuum pump, and both sections should be at the same pressure.
6. Quickly open the green hand valve. This will allow air to flow to both driven and driver sections, pushing any debris towards the diaphragm. It is important that both automated valves are completely open before opening the green hand valve. The automated valves are not intended to have high-pressure in an opposite orientation, but will not be damaged if they are completely open.
7. Repeat the depressurization cycle three more times, to ensure all fragments are blown to the diaphragm section of the shock tube.
8. After the fourth repressurization, open the tube as normal.
9. Remove the diaphragm and remove debris from both sections.
10. Check the tube with the flashlight for other debris that got stuck farther down the tube.
11. If debris is found, further clearing cycles will not move it. If the debris is in an unimportant location, it should be dislodged during the next run. If the debris would affect the next run, it should be removed by opening the shock tube at the nearest joint (see Section A.6). Use gloves when opening the shock tube and be careful to clean any hand oils that may get on the interior.

D.3 Cleaning Sections

Cleaning the shock tube interior is necessary if any machining has been done involving the interior (such as adding new sensor locations), or periodically after wire fragments and other debris have accumulated inside. Cleaning is primarily done with the plunger, which is a wooden dowel rod with a small circular wooden plate screwed into the end. A diaper cloth should be folded in thirds, with the two thin flaps overlapping the thick middle, and wrapped around the plate. Another diaper should also be wrapped around the plate, but with only one of the thin flaps. The goal is to have a tight fit in the shock tube, so that it's clear that all parts are being cleaned, but not to make it so tight that the plunger can't be inserted or moved easily. This task can be performed by one person, but it is best to have someone assist.

1. Select which part of the shock tube is to be cleaned. Remove all sensors from that section. If necessary, remove windows and end plate.
2. Use gloves when working with the inside of the shock tube.
3. Open the section on both ends, **UNLESS** that section is the first section or the driver section. **Don't remove the first section or the driver section from the transition sections!** The transition sections require the regular pipe sections for support, and should never be detached unless they're being removed.
   (a) If the final driven section is being cleaned, ensure the tube section will not tip when the clamp is removed. Due to the sensors and valve mounted at the end-plate, the final section can tip towards the downstream side. Lower the more upstream pipe hanger on the final section so there is significant slack. This ensures the section will not tip downstream. Care is required when working with this section.
   (b) Loosen the bolt on the band clamp holding the split clamp rings on. It shouldn't be removed, it just needs to be loosened enough that the band clamp can be moved.

(c) While keeping your hand on the lower split clamp ring, move the band clamp off the rings. Leave it on the shock tube. Some of the split clamp rings will fall immediately when the band clamp is removed, so keep your hand on it to prevent this.

(d) If the lower clamp ring didn't fall, use a screwdriver to pry one half loose, and take it off the joint. Again, keep your hand on the lower clamp ring in case it decides to let go.

(e) Using the rubber mallet, tap the remaining half on each side to loosen it, and take it off.

(f) Repeat for the other side, if applicable.

4. Push one end of the free section to the side until it clears the nearby fixed section. Move the free section towards the fixed section until the two flange rings have cleared each other, then let the free section rest on the fixed section. This angles the free section so you can look through it and insert the plunger.

5. If not already done, wrap the plunger with the diapers. Spray acetone around the widest part until the diaper is wet.

6. Carefully push the plunger into the shock tube. This may require some force, but be careful not to damage the o-rings or dislodge the diapers.

7. Push the plunger all the way to the other side, until it is just about to exit the shock tube. Then pull it back. You may wish to repeat this several times before removing the plunger, depending on how dirty the interior is. If clearing wire fragments, get as many out of the shock tube as possible before pulling the plunger back, and do not repeat. Dragging the wire fragments against the side runs the risk of scratching the tube. Be careful not to scratch or damage the inside of the shock tube with the plunger.

8. Repeat until the tube is clean. Any dirt removed by the diaper will darken the cloth. As the tube gets cleaner, the cloth will need to be changed more often.

9. Unhook the free section from the fixed section.

10. Clean the flat face with acetone.
11. Inspect the o-ring on the other face. You may need to remove, clean (or replace), grease, and re-install the o-ring. You may also need to clean out the groove.
12. When re-installing the o-ring, wear gloves. Apply vacuum grease, and then place one part of the o-ring in the groove. Then, place both of your index fingers next to each other on the installed part. While pressing down, drag your fingers in opposite directions around the circle until they meet again. This method stretches the o-ring evenly and prevents it from popping out due to uneven tension in the rubber.
13. Place the two faces against each other. Check the alignment of the two sections. You want both sections to be centered, and the gap at the top and bottom should be the same length, indicating the angles of the two sections are matched. Otherwise, raise and lower each section (or one end of the sections, in the case of mismatched angles) to fix the discrepancy.
14. Using the mallet, hammer on the top section. Use substantial force, since most of the clamping force is applied this way.
15. Now, hammer on the bottom section. Don't use too much force, or it may fall off again. Be sure that the numbers match and are positioned next to each other. Also, ensure that the gaps on each side are even. Hammer until the bottom section bites, and then stop. You may need to readjust the clamp rings if they became very uneven during the hammering.
16. Hold on to the lower section to ensure it doesn't fall off. Slide the band clamp over the rings. You may need to loosen the nut to get the clamp to fit.
17. Center the band clamp, and tighten the nut.
18. Install the other clamp ring.
19. Repeat the cleaning process for any other sections required.
20. In the case of the last section, the end-plate will need to be removed. This is the same process as for the other joints, but the end plate is slightly thicker, and

it may be more difficult to pry the clamp rings apart. Refer to Section D.4 for instructions on removing and replacing the end-plate.

21. When cleaning the first section with the burst system installed, be careful not to push the plunger into the electrical burst system.

D.4 Installing and Removing Driven-Section End-Plate

The end-plate can be changed for different tests. The pitot end-plate allows for pitot-mounted PCB132 sensor testing, but often has a higher leak rate. The other end-plate may be desired to achieve a lower driven pressure. The end-plate must be removed to clean the final shock tube section. This task can be done by a single person, but it is best to have an assistant.

1. Disconnect the vacuum line from the automated VAT valve.
2. Disconnect the automated valve from the end-plate. Depending on the end-plate, the vacuum sensors may need to be removed first. Be careful to not get any debris into the sensors. Always hold sensors facing downwards so particulate cannot get into the sensing mechanism. When the valve is disconnected, carefully begin loosening the valve mount while keeping a hand on the valve. When the mount is loose enough, carefully move the valve away from the shock tube. Re-tighten the valve mount so it is secure.
3. If vacuum sensors were not already removed, remove them. Cover the sensing mechanism with a flange cap and place on a bench where they will not be damaged.
4. Remove any vacuum piping still attached to the end-plate. If Kulite or PCB132 sensors are installed in the pitot end-plate, they can stay installed. Care must be taken to ensure the sensors and interior of the shock tube are not damaged.

5. Remove the clamp from the end-plate. Follow the procedure in Section D.3 to remove the clamp, but maintain a firm grip on the end-plate. The end-plate can be heavy, so be careful. This can be difficult to do with only one person.
6. Reinstall the end-plate in reverse order to uninstallation. Again, be careful with the end-plate. Always hold the end-plate and lower section of the clamp ring while the band clamp is not in place. The lower section of the clamp ring can fall off without warning if not held in place.
7. When replacing the automated valve and pressure sensors, always keep a hand on the unit until securely mounted.

D.5 Aligning Shock Tube Transition Sections

The clearances for the joint between the transition sections are not large. Because of this, small misalignments between the two pieces result in them getting stuck together. Misalignments often develop because of movement of the supports on the driver section. The alignment can usually be corrected by keeping track of the position of the supports and putting them back when they move. In addition, pulling the driver section forward slowly and waiting for the rollers when they get stuck tends to prevent the supports from moving in the first place. In other situations, misalignments are caused by removing and re-installing sections of the shock tube.

It is important to align the pieces not only in position, but also in angle. When the pieces go together easily but need to be pried apart, they are typically well-aligned positionally but are at different angles to the horizontal. For this reason, the digital protractor is useful when aligning the shock tube, since it is able to measure the angles with high precision.

1. If no major adjustments have been made recently, the sections may not be misaligned. Small amounts of rust can build up on the transition sections and eventually cause the sections to not fit together. Before attempting to realign the sections, try removing rust. First, wipe the contact portions of the transition

section with acetone using a Kimtech wipe. If this does not work, you can lightly sand the transition section with fine-grit sandpaper. If this does not remedy the issue, proceed with the following steps.

2. Adjust the supports closest to the transition sections first. Extend or retract the turnbuckles to adjust. Adjust until they seem lined up visually. The support for the driven transition section is particularly difficult to turn, especially to tighten. It's usually best to adjust the other sections to line up with the driven transition section.
3. Test the alignment by trying to join the sections. Observe where the sections seem to get stuck. When squeezing the sections together, try squeezing harder with one hand and then the other, causing the driver section to rock back and forth. This can make it easier to tell which side is stuck.
4. Adjust accordingly until the sections slide together. Use small adjustments- no more than a quarter of a turn.
5. If the sections slide together roughly, continue adjusting by less than an eighth of a turn each try. If they slide together roughly and get stuck, continue by adjusting the angles. If they slide together and apart smoothly, you are done.
6. The angles can sometimes be adjusted visually, but it is generally easier to start by immediately using the digital protractor.
7. Place the protractor on a machined surface on the driven section. If possible, use the actual driven transition section, but it may be easier to measure on the first tube section.
8. Adjust the protractor until it is lined up on the top or bottom of the shock tube. If the protractor is angled off-centerline or not close enough to vertical, it will affect the measurement.
9. You can either remember the angle that it reads, or re-zero the protractor.
10. Perform the same measurement on the driver section, but do not re-zero.

11. Remove the protractor and place in a safe spot before performing the adjustments.
12. Adjust the far turnbuckle for the driver section. You will need a ladder. Raise or lower the turnbuckle by 1/8 turn increments.
13. Repeat the previous three steps until the angles match within a few tenths of a degree.
14. Check the fit of the sections. If it is still sticking, reduce the angle difference further. Alternatively, try to improve the positional alignment, if joining the sections is also difficult.
15. Continue until the sections join and separate smoothly and without the use of the screwdriver to pry them apart. Occasional use of the screwdriver is normal.

D.6 Installing/Removing Shock Tube Sections

The pipe sections of the shock tube are fairly easy to move, but due to their length, care must be taken not to hit anything when in motion. They are not very heavy and can be picked up by one person, at least briefly. Two people should be able to move one easily. However, the easiest way to move all the pieces is by using the crane. Installing and removing shock tube pieces can be done by one person, but should generally be done by two people. An experienced person could install or remove a piece on their own if it became necessary. Special care must be taken when working with the transition sections, due to their weight and irregular shape. It's recommended that you request help from the machine shop when moving those pieces.

Removing a section is just the reverse of the installation instructions, except that it is slightly more difficult to balance the section properly on the strap. The strap must be installed while the section is still in the pipe hangers. While performing the tests to see if it is balanced properly, it will be pulled to the side. One end or the other will begin to lift further, and come off the pipe hanger earlier. The strap should

be moved away from this side. It can be difficult to tell how severe the imbalance is, but generally if the section appears fairly well-balanced in the hangers, it will be well-balanced when removed from them. Care must be taken when removing the hangers, since the section will want to swing out away from centerline without the hangers to hold it back. One person should hold the section in place while the other removes the hangers. The section can then be slowly allowed to hang straight down. If the imbalance is severe, one person can hold the section level while it is lowered to the platform floor. It can then be readjusted according to the installation method. Make sure diaphragms are in place for the ends of the section when lowering the section on to the cart.

1. Clear any Lista cabinets and other furniture from the area in front of the supersonic tunnel on the side with the BAM6QT vacuum pump.
2. Begin with the section laying flat on a cart. Move the cart next to the supersonic tunnel. Move the schlieren hardware out of the way as much as possible. Keep the section as far away from the I-beam's vertical steel supports as possible, as well. Also, make sure that none of the section is underneath the table for the supersonic tunnel. The axis of the section should be perpendicular to the supersonic tunnel.
3. Move the crane above the section.
4. Get a 6 or 8-foot strap.
5. Wrap the strap around the center of the shock tube section several times. Leave about 1.5 - 2 feet of lead on either side.
6. Attach both of the loops of the strap to the crane's hook.
7. Lift the crane until the shock tube section just starts to lift. Note which side lifts first.
8. Move the straps away from the side that lifted first. Use small adjustments of less than an inch.

9. Repeat the process of lifting and adjusting until the two sides lift nearly simultaneously. The section should be approximately level when only supported by the crane.
10. Have one person keep a hand on one end of the section at all times to prevent it from tipping. Make sure not to stand directly under the section while it is suspended.
11. Start lifting the section. Move the crane as far away from the centerline as possible. The section starts out perpendicular to the supersonic tunnel, and will eventually need to be turned parallel whenever convenient. Keep the section oriented in a way that collisions are easy to prevent.
12. When the section is at about shoulder height, stop lifting and begin moving it towards the platform.
13. When the section is close to the vertical steel support, begin lifting it again. Keep a hand on it the entire time.
14. As the section rises, eventually the person holding the section will need to get on the platform in order to keep a hand on it. To let them get on the platform, the person controlling the crane should hold it while the other person moves.
15. Continue lifting the section until it is clear of the platform railing and other hazards.
16. Rotate the section until it is parallel with the rest of the shock tube, if you haven't already.
17. Begin moving the section over the platform.
18. As the tube clears the platform railing and the working table becomes a hazard, begin moving the section back toward the centerline.
19. Lift the crane chains over the platform railing as necessary.
20. Continue moving the section until it is in the correct axial position and the crane is as close to the centerline as possible. The crane will be prevented from being on

centerline by the I-beam and the wire rope for the counterweight system. Make sure the section is oriented so it will mate properly with the other sections.

21. Remove the u-brackets on the pipe hangers for the section, if they are not already removed.
22. One person should push the section towards the I-beam, while the other person positions the hangers on the section and re-installs the u-brackets so that the section is held by the turnbuckles. The nut for the U-bracket bolt only needs to be finger-tight. Adjust the height of the section as necessary if the hangers do not easily fit over the section.
23. Slowly lower the crane until all the weight is on the turnbuckles. The section will swing down to the centerline. The crane has a tendency to resist lowering, and getting the chain to start moving down may require substantial force.
24. Remove the strap from the crane and the section.
25. Rotate the section until it is properly oriented with the 0° ray on top.
26. Connect the section to the adjacent sections. Be sure to perform any necessary maintenance on the o-rings and sealing surfaces.

D.7 Working with the Transition Sections

The transition sections are more complicated to work with due to their much higher weight as compared to the tube sections, and because of their odd shape which makes locating the CG difficult. However, the straps can be mounted directly behind the flanges. This places the CG behind the strap, forcing the flange into the strap, which is fairly secure. A particular problem is the tendency to swing back to the vertical when the hanger is removed. This tendency is easy to correct with the tube sections, but is substantially more difficult with the heavier transition sections. Additionally, the transition sections need to be suspended from the straps before the joint with the tube section is undone. This means that the swing-back will happen

suddenly, and also that the joint will be under stress as it is disassembled, and that the tube section will tend to fall back into the pipe hanger. It may be useful to have more than two people for this operation.

Additionally, the transition sections are both at least partially suspended off the platform. To make it easier to work with the sections, and to avoid damaging the supersonic tunnel if anything goes wrong, at least one pipe section should be removed first so that the transition sections can be slid back over the platform.

D.8 Troubleshooting

D.8.1 LabVIEW Program Connections

Issues with connectivity when using the LabVIEW VI can be difficult to diagnose due to the limited ability to troubleshoot, especially while running. The following troubleshooting methods should be used if a problem is occuring that stops the VI operation. If issues persist, errors may be solved by resetting equipment. This is especially true for errors involving data overflow from the DAQ.

1. Ensure all equipment is connected and powered. Check all USB connections at the computer and make sure the computer recognizes the equipment plugged in. Check connections between the computer and the piece of equipment. Due to the setup of the P3IST, several connections use long USB cables. If a section is unplugged, this could prevent the computer from finding the piece of equipment.
2. Ensure VISA names are correct in the LabVIEW VI. If the USB cables are plugged in as labeled on the computer and the default VISA names are used, the names are likely correct. To check the VISA name for each piece of equipment, open the Devices and Printers menu through the Control Panel on the computer. Unplug each piece of equipment to identify each one. Right-click on each icon and select properties to see the COM port.
3. Restart the DAQ, VAT valves, and Paroscientific sensor by turning off and on.

4. Unplug everything from the computer and restart.
5. If issues persist there may be something wrong with the LabVIEW communication or the equipment.

D.8.2 Electrical Resistance

There should be no electrical path between the shock tube structure and the burst capacitor bank. If a current path exists, it must be isolated before the shock tube can be run. This issue is one of the most common with the P3IST and can be frustrating to fix.

1. Identify that contact is made by measuring the resistance between the burst capacitor lead and the shock tube. If the resistence is low (0.1–5 Ω), contact is definitely made. If the resistance is around 300 kΩ, The DAQ may not be powered, and the issue is fixed by powering the DAQ. If the resistance is high ($\approx$ 1MΩ) and intermittent, it could be caused by your finger touching the multimeter probe. If the resistance is steadily decreasing, contact is likely made, and is likely at the brass screw heads contacting the driver section.
2. If contact is made, open the shock tube. Completely redo the nichrome wiring paying attention to screwing the screws completely flush with no nichrome wire poking out. Make another diaphragm, paying attention to applying the tape to cover the screw heads. Close the shock tube and apply hydraulic pressure. It is good practice to wait a couple minutes before testing the resistance, since the current path may exist only after the diaphragm has been under compression for a time.
3. If a path still exists, re-open the shock tube. Examine the brass screws. If portions of the face are uneven or if they are becoming stripped, you may need to use a new screw. Before using in the shock tube, the screw must be filed down. Mount the new screw in a bench vise and file the sides and face. The screw should sit somewhat recessed in the burst system, and be flush with the

surface when tightened over wires. This will take some trial and error. Test again, as before.

4. If this does not solve the issue, contact could be made at another point in the curcuit. Remove the burst system, as discussed in Section D.1.
5. Check the resistance between the alligator clips and the shock tube. If a current path exists, it is likely at the Conax compression fittings.
   (a) Isolate the wires and determine where the connection is made.
   (b) Loosen the Conax fitting and remove the wire. It may be necessary to remove the insert holding the Conax fitting.
   (c) Feed another wire through the Conax fitting into the shock tube. Make sure it is a solid-core wire the same gauge as the old wire.
   (d) Solder an alligator clip to the end inside the shock tube. Crimp a ring terminal to the end outside the shock tube.
   (e) Pull slack out of the shock tube so only the minimal amount of wire necessary is in the shock tube. Flatten the wire against the wall. This can be difficult to do with solid-core wire.
   (f) Replace the Conax and attach the ring terminal to the burst capacitor bank.
6. If a path still exists, check the electrical burst insert. Check for any tears in the electrical tape on the bus bars. If necessary rebuild the burst system and replace all electrical tape, following instructions in Section D.1.

E. HELIUM LEAK DETECTOR INSTRUCTIONS

E.1 Background

The GOW-MAC leak detector measures gas at a point using the probe and compares it to gas at a reference location on the system at a port marked "REF". The leak detector can measure Helium, Argon, CO_2, Fluorocarbons, H_2/He, and Refrigerants, so it is necessary to isolate the sensor from these gases if they are not used in leak testing. This is especially relevant to CO_2, as breathing on the probe or reference could influence the reading.

The leak detector reading drifts over time, and it is often necessary to re-zero the dial. Because of this along with uncertainties in probe placement in relation to the measured leak, the leak detector is useful as a qualitative tool to find leaks, but is difficult to use as a quantitative tool to determine their size. Relative size can be easily determined based on comparison to other leaks.

E.2 Operating Instructions

1. **Plug in leak detector**. Select "Line" using the "Mode" button to use line power. Turn on the unit.
2. **Zero initial reading**. The dial will move dramatically when turned on, but after a few seconds should return close to zero. This may not happen if the device is on high sensitivity mode. Use the zero dial to return the indicator to zero while the device is not detecting a leak.
3. **Change settings**. Set the detector to high-sensitivity mode. This allows the detection of smaller leaks, although it makes operation more difficult as small changes can dramatically affect the reading. Low-sensitivity mode can be used

to observe a large leak, but high-sensitivity mode is generally more appropriate. The "Audio" button can be selected to make the device emit a sound when a leak is detected.

4. **Prepare shock tube**. Remove Kulite sensors and Paroscientific sensor. Helium should be safe with the Paroscientific sensor, but over pressurization is not. The Paroscientific sensor has a maximum pressure of 15 psia, and exceeding this pressure can change the calibration or damage the sensor. Kulite sensors have not been damaged by Helium, but Helium diffuses through the sensor diaphragm. This effect changes the Kulite calibration (which eventually resets), but could lead to erroneous measurements if a Kulite sensor is exposed to Helium. The Leybold driven-pressure sensor can perform gas-independent pressure measurements, so should be safe with helium. Plumb the gas container to the shock tube through the driver section leak valve. Use caution when working with compressed gas bottles. Always use proper regulators.

5. **Pressurize the shock tube**. Pressurize the shock tube to 2-5 psig. Only some detection gas is necessary as the leak detector can be very sensitive.

6. **Perform leak detection**. Place the leak detector in a stable unmoving place and begin moving the probe over joints. Take care to not touch the tip of the probe to any heat sources as this influences the reading. This can be seen by placing a finger on the metal housing at the end of the probe. If a leak is detected, remove the probe from the area of interest, allow the indicator to return to zero (or re-zero), and retest the area. Often times on high-sensitivity mode small leaks will seem to appear, but do not return on repeat examination. It is good practice to confirm a leak 3 or more times before determining it is a leak.

E.3 Notes

1. Do not use the leak detector near water vapor. If the detector is used near wet seals, the detector can become contaminated or read lower than usual, skewing results.
2. More detailed instructions are given in the manual, however the instructions here will be sufficient to operate the device.

F. MATLAB SOURCE CODE

The following code is used for processing data obtained with the P3IST. It is based on and modified from codes written by Dennis Berridge, Matt Dally, Ross Carlson, and Ines Esteban.

```
function [shockTime,shockSize,preSh_noise,t2,v2,t0,v0,h2,Hd2,shockInd_gl
    ,t,v] = ...
     LowPassDetectFilter_update(filename,filterWindowSize,level,
         falseWidth,coarseStep,ref)
%%% LowPassDetectFilter_update
%
%%% INPUTS %%%
% filename          = data filename
% filterWindowSize  = window size in which to detect shock, [s]
% level             = minimum level to detect shock, [V]
% falseWidth        = minimum peak width to detect shock, [s]
% coarseStep        = number of indices between each location for
    detection
% ref               = reference sensor (1) or PCB (0)
%
%
%%% OUTPUTS %%%
% shockTime     = detected shock time, [s]
% shockSize     = measured voltage rise, [V]
% preSh_noise   = pre-shock RMS, [V]
% t2            = shortened (filtered) time, [s]
% v2            = shortened filtered signal, [V]
% t0            = shortened time, [s]
% v0            = shortened voltage, [V]
% h2            = filter specifications
% Hd2           = designed filter
```

```
% shockInd_gl    = index of shock location
% t              = raw time signal, [s]
% v              = raw voltage signal, [V]
%
%
%% Load and pre-process data

maxInterval         = 5e-5; % time interval to look for the peak maximum
maxFalsePositives   = 800;  % maximum number of false positives before
    stop

[~,~,ext] = fileparts(filename); % get file extension

% load data from file
switch ext
    case '.mat'
        loaded = load(filename);
        v = loaded.data(:,2);
        t = loaded.data(:,1);
    case '.wfm'
        [v,t] = tekread(filename);
    otherwise
        error('File extension not recongnized. Must be either .mat or .
            wfm')
end

v    = v - mean(v(1:1000));        % remove mean
fs   = round(10/(t(11)-t(1)));     % data sample rate, (samples/s)


%% Process

% set rough-pass moving-average filter for finding shock location
roughpass_freq = .5e6;
roughpass_FREQ = 5*round(fs/roughpass_freq);
```

```
57
58 % Rough-cut low-pass filter the data with a reducing running average
59 [vr,tr] = reducing_mov_filter(v,t,roughpass_FREQ);
60
61 % locate shock in rough-cut low-pass filtered trace
62 [shockInd, shockTime, highInd0, lowInd0] = ...
63     detect_shock(vr,tr,t,level,maxInterval,maxFalsePositives,...
64     falseWidth,coarseStep,filterWindowSize);
65
66 % no shock found, abort, exports NaNs
67 if shockInd == 0
68     shockTime = NaN;
69     shockSize = NaN;
70     preSh_noise = NaN;
71     shockInd = NaN;
72     exportT = NaN;
73     exportV = NaN;
74     warning('No shock found using rough-cut moving average.')
75
76     t2 = NaN;
77     v2 = NaN;
78     v2 = NaN;
79     t0 = NaN;
80     v0 = NaN;
81     h2 = NaN;
82     Hd2 = NaN;
83
84     shockInd_gl = NaN;
85     t = NaN;
86     v = NaN;
87     levelOffset = NaN;
88
89     return
90 end
91
```

```
92 %re-do fine filter only over the period where shock is located
93 t0 = t(lowInd0:highInd0);
94 v0 = v(lowInd0:highInd0);
95 coarseStep = 1;
96
97
98 if ref == 1
99     % IF reference sensor
100
101     % set filter frequencies for reference sensor (Kulite)
102     pass_band = 200e3;
103     stop_band = 300e3;
104
105     % design a filter
106     h3 = fdesign.lowpass('n,fp,fst', 100,pass_band/fs, stop_band/fs);
107     Hd3 = design(h3);
108
109     h2 = h3;
110     Hd2 = Hd3;
111
112     % filter relevant data
113     [v2]            = filter(Hd3,v0);
114     filter_delay    = mean(grpdelay(Hd3))/fs;
115     t2              = t0-filter_delay;
116     delay_ind       = round(filter_delay*fs);
117
118 else
119     % ELSE PCB132
120
121     % high-frequency lowpass filter before roll-off calculation
122     h2 = fdesign.lowpass('fp,fst,ap,ast', 1e6, 1.5e6, .2, 100, fs);
123     Hd2 = design(h2);
124
125     [v2] = filter(Hd2,v0);
126     filter_delay = mean(grpdelay(Hd2))/fs;
```

```
127     t2 = t0-filter_delay;
128
129     %use low-pass data for shock detection
130     [shockInd] = detect_shock(v2,t2,t,level,maxInterval,
            maxFalsePositives,...
131         falseWidth,coarseStep,filterWindowSize);
132     shockInd = shockInd(1);
133
134     % find peak after shock
135     [~,pkI] = findpeaks(v2(shockInd:shockInd+5e-5*fs));
136     shockInd2 = pkI(1)+shockInd;
137
138     % calculate slope coming off of shock peak
139     v_slope = v2(shockInd2:shockInd2+round(3e-6*fs));
140     t_slope = 1:length(v_slope);
141     p = polyfit(t_slope',v_slope,1);
142     back_slope = -p(1)*fs;
143     if back_slope<0
144         back_slope = 0;
145     end
146
147     % apply filter correlation
148     stop_band = (back_slope*.48+150)*1e3;
149     pass_band = stop_band-100e3;
150
151     % stop filter at 300 kHz (processing takes too long)
152     if stop_band<400e3
153         pass_band = 300e3;
154         stop_band = 400e3;
155     end
156
157     % design filter
158     h3 = fdesign.lowpass('fp,fst,ap,ast', pass_band, stop_band, .2, 100,
            fs);
159     Hd3 = design(h3);
```

```
160
161     % apply fine filter based on slope on backside of peak
162     [v2] = filter(Hd3,v0);
163     filter_delay = mean(grpdelay(Hd3))/fs;
164
165     % correct time vector for delay
166     t2 = t0-filter_delay;
167     delay_ind = round(filter_delay*fs);
168
169
170 end
171
172
173 % re-calculate shock position
174 [shockInd, shockTime, highInd, lowInd] = detect_shock(v2,t2,t,level,...
175     maxInterval,maxFalsePositives,falseWidth,coarseStep,filterWindowSize
        );
176
177 shockTime = shockTime(1);
178 shockInd = shockInd(1);
179
180 if ref == 1
181     shockInd_gl = shockInd+lowInd0-delay_ind;
182     shockSize = mean(v(shockInd_gl+(.25e-3*fs):shockInd_gl+(.75e-3*fs)))
        ;
183 else
184     start = round(shockInd-1e-6*fs);
185     last = round(shockInd+2e-6*fs);
186
187     [~,shockInd] = max(v2(start:last));
188     shockInd = shockInd+start;
189     shockInd_gl = shockInd+lowInd0-delay_ind;
190
191     % shock size from max of filtered data in search range
192     shockSize = max(v2(start:last));
```

```
193
194 end
195
196
197
198 %% Pre-Shock Noise
199 % compute RMS over range before shock arrival
200
201 rms_time = [-0.0001, -0.0011];   % take RMS over 1 ms from 0.1 ms before
        shock
202
203 % RMS indices
204 rms_inds = [shockInd_gl+round(fs*rms_time(2)),shockInd_gl+round(fs*
        rms_time(1))];
205 rms_inds(rms_inds<1) = 1;
206
207 % pre-shock noise from RMS
208 preSh_noise = rms(v(rms_inds(1):rms_inds(2)));
209
210
211
212 function [v2,t2] = reducing_mov_filter(v,t,window)
213 %reducing moving average filter
214
215 for ii = 1:round(length(t)/window)
216     ind = round(window*ii-window/2);
217     t2(ii) = t(ind);
218     v2_range = v(floor(ind-window/2+1):floor(ind+window/2));
219     v2(ii) = mean(v2_range);
220 end
221
222 function [ average ] = findmean( lowtime, hightime, t, v )
223 ind = (t>=min([lowtime(1),hightime(1)])) & (t<=max([lowtime(1),hightime
        (1)]));
224 average = mean(v(ind));
```

```
225
226 function [ jumpval ] = findjump( lowtime1, hightime1, lowtime2,
        hightime2, t, v )
227 %finds the value of a jump given an interval for the low value and an
228 %interval for the high value
229 %
230 % lowtime1 = first index below shock loc, used to find mean before shock
231 % hightime1 = second index below shock loc,used to find mean before
        shock
232 % lowtime1 = first index above shock loc, used to find mean after shock
233 % hightime1 = second index above shock loc,used to find mean after shock
234 % t = time data
235 % v = voltage data with detrend (mean of first 300 pts subtracted)
236 %
237 % indecies specified by avgInts in main script
238 %
239
240 low = findmean(lowtime1,hightime1,t,v);
241 high = findmean(lowtime2,hightime2,t,v);
242
243 jumpval = high-low;
```

G. SHOCK TUBE SENSOR MOUNT DRAWINGS

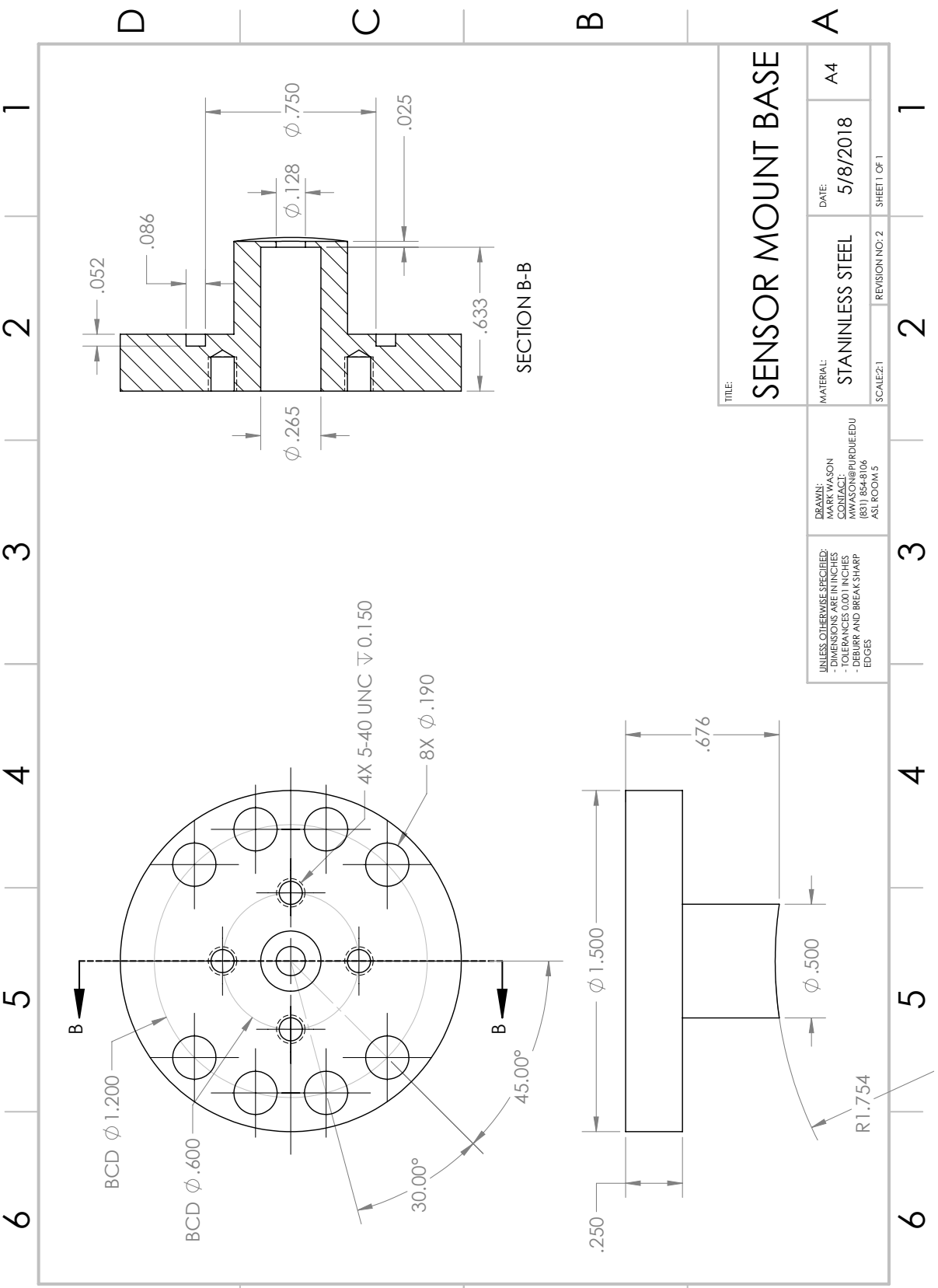
SENSOR MOUNT BASE
TITLE:
MATERIAL:
STANINLESS STEEL
DATE:
5/8/2018
A4
SCALE:2:1
REVISION NO: 2
SHEET 1 OF 1
DRAWN:
MARK WASON
CONTACT:
MWASON@PURDUE.EDU
(831) 854-8106
ASL ROOM 5
UNLESS OTHERWISE SPECIFIED:
- DIMENSIONS ARE IN INCHES
- TOLERANCES 0.001 INCHES
- DEBURR AND BREAK SHARP EDGES
SECTION B-B
.052
.086
ϕ.265
ϕ.128
ϕ.750
.025
.633
4X 5-40 UNC ↧0.150
8X ϕ.190
BCD ϕ1.200
BCD ϕ.600
30.00°
45.00°
B
B
.676
ϕ1.500
ϕ.500
.250
R1.754

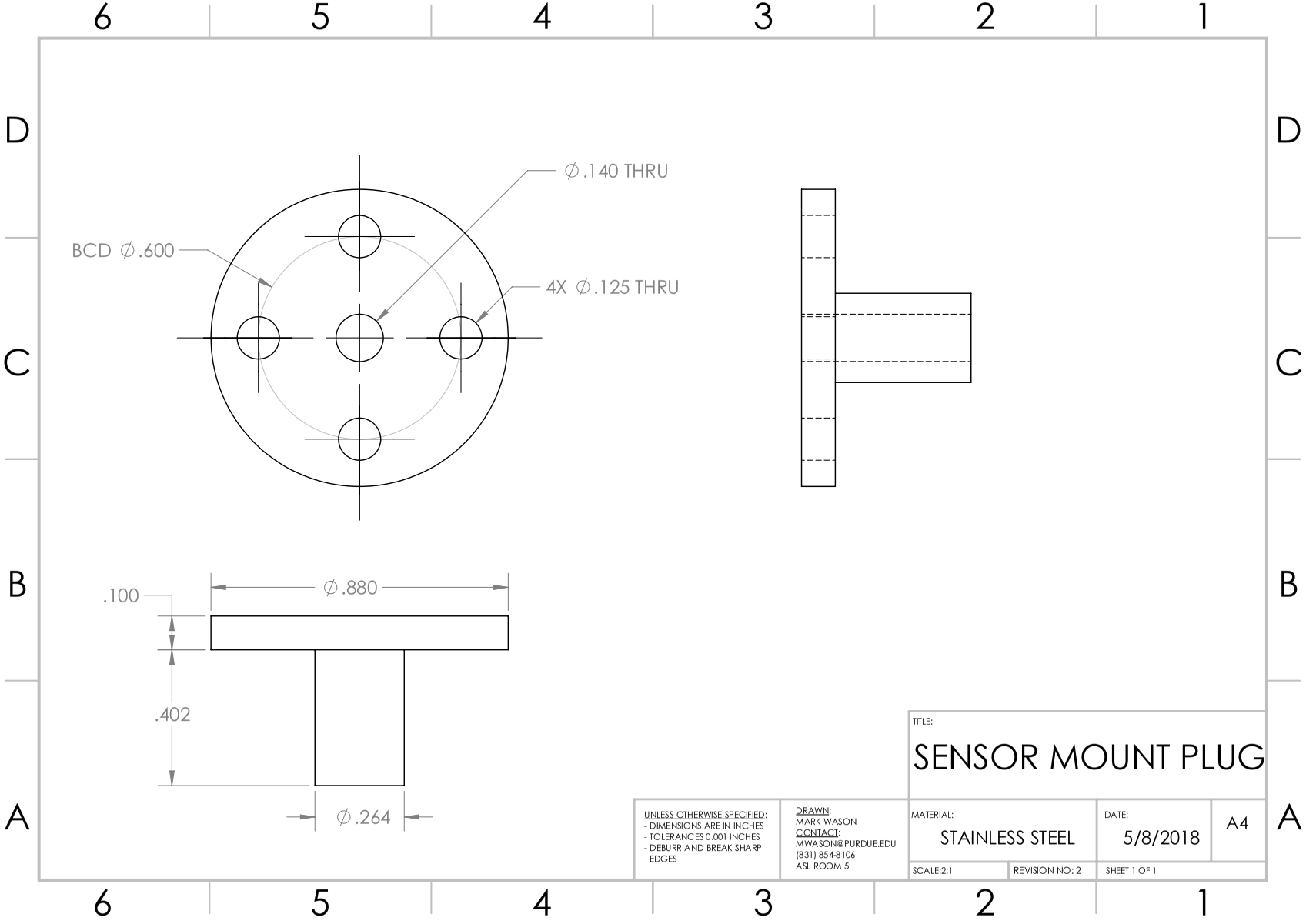
6
5
4
3
2
1
D
C
B
A
∅.140 THRU
BCD ∅.600
4X ∅.125 THRU
.100
∅.880
.402
∅.264
UNLESS OTHERWISE SPECIFIED:
- DIMENSIONS ARE IN INCHES
- TOLERANCES 0.001 INCHES
- DEBURR AND BREAK SHARP EDGES
DRAWN:
MARK WASON
CONTACT:
MWASON@PURDUE.EDU
(831) 854-8106
ASL ROOM 5
TITLE:
SENSOR MOUNT PLUG
MATERIAL:
STAINLESS STEEL
DATE:
5/8/2018
A4
SCALE:2:1
REVISION NO: 2
SHEET 1 OF 1